HIGHER ORDER COMPACT SCHEMES FOR INCOMPRESSIBLE VISCOUS FLOWS ON GEOMETRIES BEYOND RECTANGULAR

SWAPAN KUMAR PANDIT

DEPARTMENT OF MATHEMATICS

INDIAN INSTITUTE OF TECHNOLOGY GUWAHATI

JULY, 2006

HIGHER ORDER COMPACT SCHEMES FOR INCOMPRESSIBLE VISCOUS FLOWS ON GEOMETRIES BEYOND RECTANGULAR

A Thesis Submitted

for the Award of the Degree of

Doctor of Philosophy

by

Swapan Kumar Pandit

to the

DEPARTMENT OF MATHEMATICS

INDIAN INSTITUTE OF TECHNOLOGY GUWAHATI

JULY, 2006

DECLARATION

It is certified that the work contained in this thesis titled **Higher Order Compact Schemes for Incompressible Viscous Flows on Geometries Beyond Rectangular** has been done by me, a student in the department of Mathematics, Indian Institute of Technology, Guwahati under the guidance of Dr. D. C. Dalal and Dr. J. C. Kalita for the award of the degree of Doctor of Philosophy and that this work has not been submitted elsewhere for a degree.

July, 2006

(Swapan Kumar Pandit)
Indian Institute of Technology Guwahati
IIT Guwahati

CERTIFICATE

It is certified that the work contained in the thesis titled **Higher Order Compact Schemes for Incompressible Viscous Flows on Geometries Beyond Rectangular** by **Swapan Kumar Pandit**, a student in the department of Mathematics, Indian Institute of Technology, Guwahati for the award of the degree of Doctor of Philosophy has been carried out under our supervision and that this work has not been submitted elsewhere for a degree.

July, 2006

Dr. Durga Charan Dalal
Associate Professor
Department of Mathematics
Indian Institute of Technology Guwahati

Dr. Jiten Chandra Kalita
Assistant Professor
Department of Mathematics
Indian Institute of Technology Guwahati

Dedicated

to my father
Shri Bijoy Krishna Pandit

and

to the memory of my mother
Late Sumitra Pandit

Acknowledgement

This is the space in my dissertation to serve tribute to those individuals who stood behind me, believed in me, supported me, taught me and contributed in any way (direct or indirect) to overcome the hurdles of one of life's most important challenges. The outcome of this tedious, ritual Ph.D work not only provides newness, usefulness and non-obviousness but also gives the academic excellence, the courage and confidence to carry on the journey on an uneven path of life.

First and foremost, I like to express my sincere gratitude to both of my supervisors **Dr. D. C. Dalal** and **Dr. J. C. Kalita** for their constant help, supervision, and encouragement. I am really grateful to Dr. D. C. Dalal, an ideal man whose kind guidance, assistance, wisdom and emphasis on the value of positive scientific thinking made me realize my true potential. Dr. J. C. Kalita is a man of perfection whose prolific guidance and rational approach helped me to be on the right track and taught me the beauty of research. Their spontaneous help and presence can be cited as an example of lightening candle. It was a great experience and I thoroughly enjoyed working under them.

I owe a huge debt of gratitude to **Dr. Damodar Maity** in the Dept. of Civil Engineering, IITG whose support towards the accomplishment of this research work can not be expressed in a single word or phrase. He first introduced me to this challenging world. His constant inspiration and assistance gave me a lot to fulfill this rare achievement. I am also indebted to **Dr. Anoop Kumar Dass** in the Dept. of Mechanical Engineering, IITG for some valuable discussions which proved very handy in my research. He deserves a special thank. I am obliged to **Dr. M. Guru Prem Prasad** and my doctoral committee members **Dr. R. K. Sinha** and **Dr. S. Natesan** for their kind suggestions during my research period.

Thanks to our former computer lab asst. **Mr. Brijesh Nishad** and new lab assistant **Mr. Shantanu Mazumdar** for arranging more than one computers and giving necessary help for computational work and then there are my fellow dorm residents (**Tarakanta, Safique, Subash, Madhusmita, Bibhas and Dr. Rajesh Kanna**), whom I credit most of all for making me feel at home here. I feel proud of being associated with such friends. I would also like to thank our office staff **Mr. Shreedhar Samal** and **Mr. Manoj Boro** for their help during my research tenure.

I like to express my sincere gratitude to my wife **Ranjana Maity** who predicted me as future researcher in my schooling days. This came true due to her love, patience, constant inspiration and hearty support. She easily kept aside all of my frustrating moments with care. I acknowledge her from the bottom of my heart.

Last but not least, though it is beyond the scope of any acknowledgement for all of my family members whose moral support, hearty wishes, affectionate love, special care and constant source of inspiration made me to accomplish smoothly of this Ph.D work, yet I make an effort to express my heartiest gratitude to them. Especially my father's patience, courageous thought, iron determination and unflinching will help me to overcome all odds in my long journey. During difficult situations he took me under his wings of safety shelter and taught me how to survive against oddness. I am very much thankful to my brother-in-law **Uttam**, **Abanti**, **Puran** and **Swadesh** for their constant support and positive thinking in all respect. In the same vein I would also like to thank my elder sisters **Anjali** and **Dipali**, younger sisters **Shyamali** and **Mitali**, elder brother **Surya** and sister-in-law **Sulochana**. They encouraged and assisted my efforts from the very beginning even if they don't realize it. I often doubt that I could have completed my Ph.D. without their guidance. To them, I extend my highest appreciation.

July, 2006 **(Swapan Kumar Pandit)**

Abstract

In this dissertation, we have proposed a new class of higher order compact (HOC) finite difference schemes for solving the two-dimensional (2D) incompressible viscous flows through geometries beyond rectangular. The proposed schemes are developed for both steady-state and transient flows which are governed by the Navier-Stokes (N-S) equations. All these schemes are fourth order accurate in space while the ones for the transient flows are implicit, and first or second order accurate in time depending on the choice of a weighted average parameter. We have employed these schemes not only on problems having analytical solutions to verify their order of accuracy, efficiency, effectiveness and robustness but also to explore new flow phenomena of some other complicated problems, namely, the lid-driven cavity flow, channel flow with forward and backward constriction, flow in a lateral and symmetric dilated channels, flow through constricted tube etc. They are seen to efficiently capture both steady-state and transient solutions with Dirichlet as well as Neumann boundary conditions. Apart from including all the features of existing HOC schemes, the formulation has the added advantage of capturing transient viscous flows involving free and wall bounded shear layers which invariably contain spatial scale variation. We present both qualitative and quantitative results produced by our schemes on relatively coarser grid for all the test cases and compare them with theoretical predictions, analytical as well as established numerical and experimental results available in the literature. Excellent agreement is obtained in all the cases.

Keywords: Transient HOC, N-S equations, Reynolds number, lid driven cavity flow, symmetric and asymmetric channels, forward and backward constricted channels, lateral and dilated channels, reentrant corner, free and wall bounded shear layers, aneurysm, stenosis.

Contents

List of Figures

List of Tables

Chapter 1

Introduction

1.1 Background

The flow physics related to different physical processes is not always easy to understand. Mathematical modelling of these processes needs more attention to explain the underlying physics. In fact many flows of practical interest such as turbulence, combustion, multiphase flows, etc. are difficult to describe exactly mathematically because of the complex nature of flows. Especially, when many different sub-processes are involved, the mathematical models are useful to understand all the complex interactions of the different subsystems because the main characteristics of mathematical modelling are the quantitative predictions of the outcome of a process. Most of such models consist of sets of partial and ordinary or intrego-differential equations with boundary conditions. As for example, in fluid dynamics, the well known Navier-Stokes (N-S) equations are familiar as the model equations for fluid flow predictions. The N-S equations are seen to describe the flow of a Newtonian fluid quite accurately. These equations are highly non-linear and coupled partial differential equations (PDEs), and are difficult to solve. In most cases governing equations are simplified for the sake of calculations; even then, the simplified equations cannot always be solved analytically. Only in a small number of cases, mostly, fully developed flows in simple geometries, e.g. in pipes, between parallel plates, etc., it is possible to obtain analytical solutions of the N-S equations. These flows are important to understand the fundamentals of fluid dynamics but their practical relevance is limited. In practical situations, to solve most of the fluid flow problems, one has to resort to numerical methods in the absence of analytical ones. Among the popular numerical methods one can cite finite difference (FD), finite volume (FV) and finite element (FE). FD method has been used as a better choice for the solution in the computational domain (problem domain) as the FD method is relatively simple and effective on structured grids. The basic methodology here is, on the rectangular plane geometry, the computational domain is covered by a structured grid. At each grid point, the partial differential equation is approximated by approximating the derivatives appearing in that equation in terms of the nodal values of the functions. The result is one algebraic equation per grid node, in which the values of one variable at that and at a certain number of neighbor nodes appear as unknowns. The resulting system of algebraic equations can then be solved with some matrix solver.

In the FD representation, Taylor series expansion or polynomial fitting is used in general to obtain approximations of the derivatives of the variables at the grid points. The leading term in the truncation error (TE) of this expansion determines the order of accuracy of the scheme. For example, if this TE is asymptotically proportional to h^m, where h is the distance between two successive grid points, the difference scheme is said to be accurate of order m or shortly $O(h^m)$. Over the last few decades, most of the popular finite difference schemes for solving two dimensional (2D) incompressible viscous flows have been either first or second order accurate in space because the lower order schemes are relatively easy to implement and demand less CPU time. They do not always yield desired results on reasonable meshes even if the solution is well behaved. For example, in the case of convection dominated flows, the lower order schemes may produce poor quality results if the mesh is not sufficiently refined. Moreover, in practical situations, most of the flow phenomena require refined mesh to capture the flow physics accurately. This mesh refinement invariably brings in additional points into the system resulting in an increased system size. Consequently, more memory and CPU time are required to solve such problems on a computer. The higher order numerical schemes can be employed to circumvent these limitations. However, the discretization procedure of a higher order scheme is generally associated with large non-compact stencils which increase the band-width of the coefficient matrix of the resulting algebraic system of equations and lead to a large number of arithmetic operations, especially for higher dimensional problems. Thus, neither a lower order accurate scheme on a fine mesh nor a higher order accurate scheme on a non-compact stencil could be computationally effective. In such situations, higher order compact (HOC) finite difference scheme could be the best way to circumvent such problems. The objective of compact scheme is to use information only from the grid points strictly adjacent to the node about which differences are taken. Thus, compactness not only reduces the stencil size of the scheme but it also reduces the difficulty of finding approximations in higher order non-compact scheme near the domain boundaries. In the hierarchy of higher-order methods, compact schemes represent an attractive choice for reducing dispersion and anisotropy errors. This is primarily due to their spectral-like resolution. As a result, the higher order accuracy of the HOC methods together with the compactness of the difference stencils yield highly accurate numerical solutions on relatively coarser grids with greater computational efficiency.

There are several mechanisms through which finite difference schemes can achieve higher-order compactness. Among them Gupta et al's [51] series expansion procedure of the differential equation, Dennis and Hudson's [33] exponential expansion of a definite integral of the convective coefficient of the PDE, Gartland's [43] weighted mean approximation, Noye and Tan's [106] weighted modified PDE method, and high order upwind scheme of Yanwen [154] and Sesterhenn [121] are worth mentioning.

In recent times, another popular approach for finding higher order compactness has been the use of original differential equation to replace the leading truncation error (TE) terms of the standard central difference approximation. Lax and Wendroff [79] first implemented this idea on transient hyperbolic PDEs to raise the temporal accuracy from one to two. Mackinnon and Johnson [93] then implemented this idea for higher order spatial accuracy on steady-state convection-diffusion problems. At about the same time Abarbanel and Kumar [1] independently developed a spatial 4th and temporal 2nd order accurate scheme for Euler equations. These schemes are similar to those developed by Dukowicz [35] though achieved in a different manner. Spotz and Carey [128, 129] have extended the idea in Mackinnon and Johnson to the steady-state streamfunction vorticity formulation of the 2D Navier-Stokes (N-S) equations. Based on their ideas, recently Kalita *et al.* [65] developed a class of transient HOC schemes for the solution of unsteady 2D convection-diffusion equations and extended their study to develop HOC schemes on nonuniform grids without transformation [66]. Unfortunately, these schemes are unable to handle complex geometries beyond rectangular. Although, there exists compact schemes proposed by Lele [81] and the higher order schemes used in Visbal [149] for solving unsteady NS equations on curvilinear and deforming meshes, they could not be termed as compact in true sense [127]; the stencil used in these schemes extends beyond one step length away from the point about which finite differences are taken.

1.2 Motivation

Despite significant progress in computational sciences, challenges persist in the accurate numerical simulation of a broad spectrum of dynamics such as fluid-structure interactions and hemodynamics etc. To resolve these complex flow phenomena more accurately, we need higher accuracy schemes. In addition to this, the fluid domain may contain several high gradient regions and boundary layers. To resolve such flow phenomena accurately we need nonuniform grids. It must be mentioned here that the earlier schemes discussed in the previous section have been typically used to examine the flow fields in cartesian coordinate systems in the simple domains (particularly rectangular) on uniform grids. This is where the motivation to develop HOC schemes on nonuniform grids comes from, that can be used in irregular geometries with curvilinear grid settings.

1.3 Objectives

The aim of the present work is to develop HOC schemes on nonuniform grids not only for linear, nonlinear convection-diffusion equations and incompressible viscous flows governed by N-S equations, but also to develop them so as to make them applicable to rectangular as well as curvilinear coordinate systems. The intension also is to come out of the traditional application on only lid-driven cavity flow to broaden the scope of applicability of HOC algorithms to hitherto less explored problems like symmetric constricted channel flow, asymmetric channel flow, dilated channel flow, blood flow through arterial stenosis, etc. It must be noted that in complex flow domains, the advantages of high-order compact schemes remains to be characterized and also careful analysis of these issues is essential prior to the routine application of compact schemes to practical simulations.

1.4 The Work

Keeping all the ideas related to the above discussions in mind, it is worthwhile mentioning that in the finite difference set-up, constructing a rectangular grid on irregular domains is not an easy task. To circumvent this problem, rather than placing a computational grid on the physical domain, we have adopted a more flexible approach by means of coordinate transformation which can convert a complicated non-orthogonal or orthogonal non-uniform grid into a simple, uniform orthogonal grid. The transformed version of the governing equations are then solved in the computational plane by the higher order compact approximation. The associated methodology is that the space derivatives of the transformed version of the governing equations are approximated by central difference formula and the derivatives appearing in the leading terms in the TE are replaced by the transformed version of the original differential equation. The derivatives appearing due to the above replacement are also approximated again by central difference formula to make the scheme fourth order accurate. In the unsteady case, in addition to the scheme being spatially fourth order accurate, it is second order accurate in time, which can be obtained by introducing an appropriate weighted average parameter. The coefficient matrix resulting from the above HOC schemes that have been developed here, is not usually diagonally dominant and symmetric, and the conventional iterative methods such as Gauss-Seidel, SOR are of little help in solving the resulting system of algebraic equations. It may be pointed out that on uniform grids, some of the associated matrices are symmetric and positive definite, which allows the use of algorithms like conjugate-gradient (CG) [68]. But the transformations to convert nonuniform grids to uniform grids usually lead to non-symmetric matrices, and the biconjugate gradient stabilized method (BiCGStab) [68] is applied to solve the systems. In our work, we have used the above iterative methods without any preconditioning. This mechanism has been adopted throughout the present work. This approach has the added advantage that a range of problems can be solved by supplying the Jacobian of the appropriate approximation to a general N-S solver, and mapping the results back to physical space when the calculation is complete. The advantages of transforming the differential equations by a mapping of non-uniform physical space to a body-fitted uniform orthogonal computational space are: a) the boundaries of the physical space fall on coordinate lines of the computational space and as such boundary conditions can be implemented accurately and easily, b) the finite difference approximations of the exact partial derivatives are obtained on uniform orthogonal grid, and c) grid points can be clustered in a region of large gradients and widely spaced in regions of small gradients. The only disadvantage is that the transformed partial differential equations are more complicated and so are the resulting finite difference equations.

In this work, firstly, we have proposed higher order scheme in the ψ (streamfunction)-ζ (vorticity) formulation of the Navier-Stokes equations to solve steady incompressible viscous flows. The spatial accuracy of the proposed scheme is four. It is seen to efficiently capture steady-state solutions of the N-S equations with Dirichlet as well as Neumann boundary conditions. In this context, we have validated the proposed scheme with the help of several problems which have analytical solutions and benchmark results. We have generalized the scheme in such a way that it can be applied in rectangular cartesian as well as curvilinear coordinate systems. The present method is not only robust as evidenced from computations at higher Reynolds numbers, but also accurate as is seen from comparisons with reliable existing results. The scheme is then modified to capture unsteady phenomena. The transient scheme is first or second order accurate in time depending on the choice of a weighted average parameter. We have applied these class of HOC schemes on some complicated flow problems such as lid-driven cavity flows, symmetric and asymmetric channel flows, lateral and symmetric dilated channel flows and constricted tube flows, etc.

Apart from including the good features of HOC schemes, the formulation has the added advantage of capturing transient viscous flows involving free and wall bounded shear layers which invariably contain spatial scale variation. It is to be noted that all of our computations were carried out on a Pentium 4 based PC with 512 MB RAM.

1.5 Organization of the work

This dissertation is organized in six chapters: in Chapter 2, we describe the development of HOC methodology for 2D steady-state N-S equations in cartesian coordinates on nonuniform grids. We have validated the proposed HOC schemes for rectangular lid-driven cavity problem. Chapter 3 describes the transient HOC schemes for 2D transient N-S equations in cartesian coordinates and its validation for the rectangular lid-driven cavity problem. We have further applied these proposed schemes on some new problems in the subsequent chapters. In Chapters 4, 5 and 6, we present symmetric constricted channel flow problem, asymmetric channel flow problem and dilated channel flow problem respectively. Chapter 7 describes the HOC methodology for 2D steady-state N-S equations in cylindrical coordinates and its application to the constricted tube which is the idealization of blood flows through arterial stenosis. Chapter 8 summarizes and comments on the whole work and discusses scope for future work.

Chapter 2

Time independent high order compact scheme on nonuniform grids

This chapter deals with the formulation of a higher order compact (HOC) scheme in cartesian coordinate systems with non-uniform grids on complex geometries to simulate two-dimensional (2D) steady incompressible viscous flows governed by the Navier-Stokes (N-S) equations [1]. The proposed scheme is fourth order accurate in space.

2.1 Introduction

Over the last few decades, numerical schemes and simulation tools for incompressible flows, as a subset of the computational fluid dynamics (CFD) discipline, have made tremendous progress. Most of these schemes are either first or second-order accurate in space, and generally fail to produce highly accurate results for convection dominated flows unless the mesh is sufficiently refined. The use of higher order numerical methods [51, 52, 64–66, 69, 81, 84, 92, 94, 95, 128, 129, 139] is a recognized technique to circumvent the limitations of standard low-order algorithms for the simulation of various physical phenomena. Higher order discretizations are generally associated with large (non-compact) stencils which increase the band-width of the resulting matrix and as such, leads to a large number of arithmetic operations, especially for higher dimensional problems. On the other hand, higher order compact [51, 52, 64–66, 81, 84, 95, 128, 129] approximations reduce the number of points needed in discretization and consequently reduce computational cost to achieve the

---

[1] This study has been accepted for publication in *Computer & Fluids* [109]

desired accuracy. Owing to all these factors, the last two decades have seen significant research efforts towards the development of higher order compact schemes. Almost all of these efforts involving high order compact schemes [51, 52, 64, 65, 84, 129] have employed simple rectangular uniform space grids for a variety of reasons, such as lack of curvilinear grid techniques and the limited flexibility of the HOC schemes. As such these schemes could not fully exploit the advantages associated with the usage of nonuniform grids, particularly that of mesh grading to resolve smaller scales in the regions of large gradients in the physical domain. Recently, some development of HOC schemes [45,66,129] on nonuniform grids have been seen for the 2D convection-diffusion equations. Of these, the application of first two were limited to only linear problems whereas the last one, which used no transformation from the physical to the computational plane could accurately capture steady incompressible viscous flow governed by N-S equations. However, all those schemes were designed to capture flows only on rectangular domains.

In the present chapter, we propose an HOC scheme that works equally efficiently on problems described on both rectangular as well as other curvilinear coordinate settings. The scheme can be applied to both steady-state convection-diffusion and reaction-diffusion equations, and easily accommodated into solving equations of the N-S type as well with slight adjustment of the convection coefficients. It is fourth order accurate in space and handles both Dirichlet and Neumann boundary conditions with ease. To validate the scheme, it is first applied to a linear and a non linear problem having analytical solutions, and then to the classical lid driven cavity problem. We compare our numerical results with both analytical and established numerical results, and excellent match is obtained in all the cases.

2.2 Mathematical Formulations and Discretization Procedure

2.2.1 Governing Equations

The steady 2D incompressible viscous flows governed by N-S equations in non-dimensional primitive variables (pressure-velocity) formulation can be written as:

$$\frac{\partial u}{\partial x} + \frac{\partial v}{\partial y} = 0, \tag{2.1}$$

$$u\frac{\partial u}{\partial x} + v\frac{\partial u}{\partial y} = -\frac{\partial p}{\partial x} + \frac{1}{Re}\left(\frac{\partial^2 u}{\partial x^2} + \frac{\partial^2 u}{\partial y^2}\right), \tag{2.2}$$

$$u\frac{\partial v}{\partial x} + v\frac{\partial v}{\partial y} = -\frac{\partial p}{\partial y} + \frac{1}{Re}\left(\frac{\partial^2 v}{\partial x^2} + \frac{\partial^2 v}{\partial y^2}\right), \tag{2.3}$$

where Re is the Reynolds number, p is the pressure and u, v are the velocity components along x- and y- directions respectively. Instead of pressure and velocity, the equations can be described by the variables streamfunction $\psi(x, y)$ and vorticity $\zeta(x, y)$, that are defined in terms of u, v as

$$u = \frac{\partial \psi}{\partial y}, \quad v = -\frac{\partial \psi}{\partial x}, \tag{2.4}$$

$$\zeta = \frac{\partial v}{\partial x} - \frac{\partial u}{\partial y}. \tag{2.5}$$

With the introduction of the streamfunction as given in equation (2.4), the conservation of mass is automatically satisfied. Introducing the streamfunction into equation (2.5), a Poisson equation relating the streamfunction and vorticity is found as

$$-\frac{\partial^2 \psi}{\partial x^2} - \frac{\partial^2 \psi}{\partial y^2} = \zeta, \tag{2.6}$$

and eliminating pressure from (2.2) and (2.3), the vorticity equation can be written as

$$-\frac{\partial^2 \zeta}{\partial x^2} - \frac{\partial^2 \zeta}{\partial y^2} + uRe\frac{\partial \zeta}{\partial x} + vRe\frac{\partial \zeta}{\partial y} = 0. \tag{2.7}$$

This ψ-ζ formulation ((2.6) and (2.7)) has major advantages over the primitive variables form: firstly, it satisfies the continuity equation automatically and secondly, it decouples the pressure calculation from the velocity calculation. In the process, it also eliminates two computational difficulties, namely, finding (i) the correct boundary condition for pressure, and (ii) an explicit pressure equation satisfying the incompressibility constraint.

The general form of the equations (2.1)-(2.3) and (2.6), (2.7) can be written as

$$\begin{aligned} \alpha(x,y)\frac{\partial^2 \phi}{\partial x^2} + \beta(x,y)\frac{\partial^2 \phi}{\partial y^2} + \gamma(x,y)\frac{\partial \phi}{\partial x} + \nu(x,y)\frac{\partial \phi}{\partial y} \quad &+ \quad \omega(x,y)\phi \\ &= \quad \theta(x,y), \end{aligned} \tag{2.8}$$

where θ is the source term.

2.2.2 Transformation of the Governing Equations

To carry out the solution of a problem on an irregular domain, a direct transformation from the physical plane to the computational plane may be given generically which must be specified by the analytical relations:

$$\xi \;=\; \xi(x, y), \qquad \eta = \eta(x, y). \tag{2.9}$$

The corresponding inverse transformation of the given transformation may be expressed as

$$x = x(\xi,\eta), \qquad y = y(\xi,\eta). \tag{2.10}$$

It may be noted here that for the transformed plane one can use the direct or inverse transformation to obtain the derivatives/metrics. In what follows, we briefly discuss about the transformation (2.10) from the computational ξ-η plane to the physical x-y plane. Under this transformation, equation (2.8) in the physical plane becomes

$$a\frac{\partial^2\widehat{\phi}}{\partial\xi^2} + g\frac{\partial^2\widehat{\phi}}{\partial\xi\partial\eta} + b\frac{\partial^2\widehat{\phi}}{\partial\eta^2} + c\frac{\partial\widehat{\phi}}{\partial\xi} + d\frac{\partial\widehat{\phi}}{\partial\eta} + p\widehat{\phi} = f, \tag{2.11}$$

in the computational plane where

$$\begin{aligned}
\phi(x,y) &= \widehat{\phi}(\xi,\eta), & a(\xi,\eta) &= \frac{1}{J^2}\left(\widehat{b}_1 x_\eta^2 + \widehat{a}_1 y_\eta^2\right),\\
b(\xi,\eta) &= \frac{1}{J^2}\left(\widehat{b}_1 x_\xi^2 + \widehat{a}_1 y_\xi^2\right), & c(\xi,\eta) &= \frac{\widehat{c}_1}{J}y_\eta - \frac{\widehat{d}_1}{J}x_\eta + R,\\
d(\xi,\eta) &= -\frac{\widehat{c}_1}{J}y_\xi + \frac{\widehat{d}_1}{J}x_\xi + S, & g(\xi,\eta) &= \frac{-2}{J^2}\left(\widehat{a}_1 y_\eta y_\xi + \widehat{b}_1 x_\eta x_\xi\right),\\
p(\xi,\eta) &= \widehat{p}_1(\xi,\eta), & f(\xi,\eta) &= \widehat{f}_1(\xi,\eta),
\end{aligned}$$

with

$$\begin{aligned}
J &= x_\xi y_\eta - y_\xi x_\eta,\\
\alpha(x,y) &= \widehat{a}_1(\xi,\eta), & \beta(x,y) &= \widehat{b}_1(\xi,\eta),\\
\gamma(x,y) &= \widehat{c}_1(\xi,\eta), & \nu(x,y) &= \widehat{d}_1(\xi,\eta),\\
\omega(x,y) &= \widehat{p}_1(\xi,\eta), & \theta(x,y) &= \widehat{f}_1(\xi,\eta),
\end{aligned}$$

and

$$\begin{aligned}
R &= \frac{1}{J^3}\Bigg[-y_\eta\Big((\widehat{b}_1 x_\eta^2 + \widehat{a}_1 y_\eta^2)x_{\xi\xi} - 2(\widehat{a}_1 y_\eta y_\xi + \widehat{b}_1 x_\eta x_\xi)x_{\xi\eta} + (\widehat{b}_1 x_\xi^2 + \widehat{a}_1 y_\xi^2)x_{\eta\eta}\Big)\\
&+ x_\eta\Big((\widehat{b}_1 x_\eta^2 + \widehat{a}_1 y_\eta^2)y_{\xi\xi} - 2(\widehat{a}_1 y_\eta y_\xi + \widehat{b}_1 x_\eta x_\xi)y_{\xi\eta} + (\widehat{b}_1 x_\xi^2 + \widehat{a}_1 y_\xi^2)y_{\eta\eta}\Big)\Bigg],\\
S &= \frac{1}{J^3}\Bigg[y_\xi\Big((\widehat{b}_1 x_\eta^2 + \widehat{a}_1 y_\eta^2)x_{\xi\xi} - 2(\widehat{a}_1 y_\eta y_\xi + \widehat{b}_1 x_\eta x_\xi)x_{\xi\eta} + (\widehat{a}_1 y_\xi^2 + \widehat{b}_1 x_\xi^2)x_{\eta\eta}\Big)\\
&- x_\xi\Big((\widehat{b}_1 x_\eta^2 + \widehat{a}_1 y_\eta^2)y_{\xi\xi} - 2(\widehat{a}_1 y_\eta y_\xi + \widehat{b}_1 x_\eta x_\xi)y_{\xi\eta} + (\widehat{b}_1 x_\xi^2 + \widehat{a}_1 y_\xi^2)y_{\eta\eta}\Big)\Bigg].
\end{aligned}$$

2.2.3 Fourth-order accurate discretization scheme

Assuming the computational domain to be rectangular and constructing on it a uniform rectangular mesh of steps h and k in the ξ- and η- directions respectively, the standard central difference approximation to equation (2.11) at the (i, j)-th node is given by

$$\begin{aligned} a_{i,j}\delta_\xi^2\widehat{\phi}_{i,j} + g_{i,j}\delta_\xi\delta_\eta\widehat{\phi}_{i,j} + b_{i,j}\delta_\eta^2\widehat{\phi}_{i,j} + c_{i,j}\delta_\xi\widehat{\phi}_{i,j} &+ d_{i,j}\delta_\eta\widehat{\phi}_{i,j} + p_{i,j}\widehat{\phi}_{i,j} \\ &- T_{i,j} = f_{i,j}, \end{aligned} \tag{2.12}$$

where $\widehat{\phi}_{ij}$ denotes $\widehat{\phi}(\xi_i, \eta_j)$; δ_ξ, δ_ξ^2 and δ_η, δ_η^2 are the first and second order central difference operators along ξ- and η-directions respectively, and $\delta_\xi\delta_\eta$ is the mixed second order central difference operator. The truncation error T_{ij} is given by

$$\begin{aligned} T_{i,j} = \frac{h^2}{12}\left[a\frac{\partial^4\widehat{\phi}}{\partial\xi^4} + 2g\frac{\partial^4\widehat{\phi}}{\partial\xi^3\partial\eta} + 2c\frac{\partial^3\widehat{\phi}}{\partial\xi^3}\right]_{i,j} &+ \frac{k^2}{12}\left[b\frac{\partial^4\widehat{\phi}}{\partial\eta^4} + 2g\frac{\partial^4\widehat{\phi}}{\partial\xi\partial\eta^3} + 2d\frac{\partial^3\widehat{\phi}}{\partial\eta^3}\right]_{i,j} \\ &+ O(h^4, k^4). \end{aligned} \tag{2.13}$$

To obtain a fourth order spatial compact formulation for (2.11), each of the derivatives of the leading terms of (2.13) are compactly approximated [93] to $O(h^2, k^2)$. In order to accomplish this, the transformed PDE of equation (2.8) i.e equation (2.11) is treated as an auxiliary relation that can be differentiated to obtain expressions for higher derivatives. For example, successive differentiation of (2.11) w.r.t ξ yields

$$\begin{aligned} \frac{\partial^3\widehat{\phi}}{\partial\xi^3} &= \frac{1}{a}\Bigg[\frac{\partial f}{\partial\xi} - \left(\frac{\partial a}{\partial\xi} + c\right)\frac{\partial^2\widehat{\phi}}{\partial\xi^2} - \left(\frac{\partial g}{\partial\xi} + d\right)\frac{\partial^2\widehat{\phi}}{\partial\xi\partial\eta} - g\frac{\partial^3\widehat{\phi}}{\partial\xi^2\partial\eta} - \frac{\partial b}{\partial\xi}\frac{\partial^2\widehat{\phi}}{\partial\eta^2} \\ &- b\frac{\partial^3\widehat{\phi}}{\partial\xi\partial\eta^2} - \frac{\partial c}{\partial\xi}\frac{\partial\widehat{\phi}}{\partial\xi} - \frac{\partial d}{\partial\xi}\frac{\partial\widehat{\phi}}{\partial\eta} - p\frac{\partial\widehat{\phi}}{\partial\xi} - \frac{\partial p}{\partial\xi}\widehat{\phi}\Bigg]. \end{aligned} \tag{2.14}$$

$$\begin{aligned} a\frac{\partial^4\widehat{\phi}}{\partial\xi^4} &= \frac{\partial^2 f}{\partial\xi^2} - \left(\frac{\partial^2 a}{\partial\xi^2} + 2\frac{\partial c}{\partial\xi}\right)\frac{\partial^2\widehat{\phi}}{\partial\xi^2} - \left(2\frac{\partial a}{\partial\xi} + c\right)\Bigg[\frac{1}{a}\Bigg(\frac{\partial f}{\partial\xi} - \left(\frac{\partial a}{\partial\xi} + c\right)\frac{\partial^2\widehat{\phi}}{\partial\xi^2} \\ &- \left(\frac{\partial g}{\partial\xi} + d\right)\frac{\partial^2\widehat{\phi}}{\partial\xi\partial\eta} - g\frac{\partial^3\widehat{\phi}}{\partial\xi^2\partial\eta} - \frac{\partial b}{\partial\xi}\frac{\partial^2\widehat{\phi}}{\partial\eta^2} - b\frac{\partial^3\widehat{\phi}}{\partial\xi\partial\eta^2} - \frac{\partial c}{\partial\xi}\frac{\partial\widehat{\phi}}{\partial\xi} - \frac{\partial d}{\partial\xi}\frac{\partial\widehat{\phi}}{\partial\eta} \\ &- p\frac{\partial\widehat{\phi}}{\partial\xi} - \frac{\partial p}{\partial\xi}\widehat{\phi}\Bigg] - \left(\frac{\partial^2 g}{\partial\xi^2} + 2\frac{\partial d}{\partial\xi}\right)\frac{\partial^2\widehat{\phi}}{\partial\xi\partial\eta} - \left(2\frac{\partial g}{\partial\xi} + d\right)\frac{\partial^3\widehat{\phi}}{\partial\xi^2\partial\eta} \\ &- g\frac{\partial^4\widehat{\phi}}{\partial\xi^3\partial\eta} - \frac{\partial^2 b}{\partial\xi^2}\frac{\partial^2\widehat{\phi}}{\partial\eta^2} - 2\frac{\partial b}{\partial\xi}\frac{\partial^3\widehat{\phi}}{\partial\xi\partial\eta^2} - b\frac{\partial^4\widehat{\phi}}{\partial\xi^2\partial\eta^2} - \frac{\partial^2 c}{\partial\xi^2}\frac{\partial\widehat{\phi}}{\partial\xi} - \frac{\partial^2 d}{\partial\xi^2}\frac{\partial\widehat{\phi}}{\partial\eta} \\ &- p\frac{\partial^2\widehat{\phi}}{\partial\xi^2} - 2\frac{\partial p}{\partial\xi}\frac{\partial\widehat{\phi}}{\partial\xi} - \frac{\partial^2 p}{\partial\xi^2}\widehat{\phi}. \end{aligned} \tag{2.15}$$

In a similar way expressions for $\dfrac{\partial^3 \widehat{\phi}}{\partial \eta^3}$ and $b\dfrac{\partial^4 \widehat{\phi}}{\partial \eta^4}$ can be found. It is seen that the expressions for the fourth order derivatives (for example, see equation (2.15)) contain mixed derivative terms like $\dfrac{\partial^4 \widehat{\phi}}{\partial \xi^3 \partial \eta}$, $\dfrac{\partial^4 \widehat{\phi}}{\partial \xi \partial \eta^3}$ etc. which can not be approximated compactly on the stencil shown in figure 2.1. To overcome this difficulty, the transformation can be chosen as an orthogonal or conformation one such that the coefficient g of the mixed-derivative term appearing in equation (2.11) becomes zero. On considering such a grid or transformation, and using central difference for derivatives, equation (2.11) can be written as

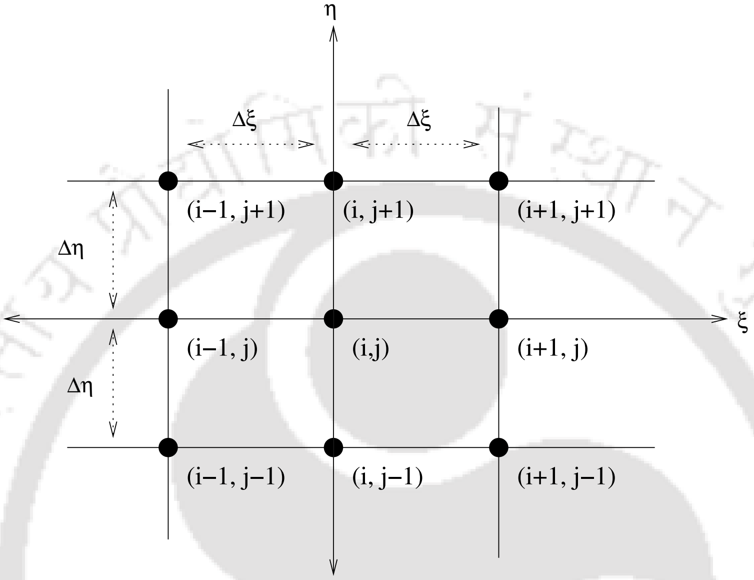

Figure 2.1: *The 9-point HOC stencil.*

$$
\begin{aligned}
& A'_{i,j}\delta_\xi^2\widehat{\phi}_{ij} + G'_{i,j}\delta_\xi\delta_\eta\widehat{\phi}_{i,j} + B'_{i,j}\delta_\eta^2\widehat{\phi}_{i,j} + C'_{i,j}\delta_\xi\widehat{\phi}_{i,j} + D'_{i,j}\delta_\eta\widehat{\phi}_{i,,j} + H'_{i,j}\widehat{\phi}_{i,j} \\
+ \; & \frac{1}{12}\Bigg[\Big(k^2 a_{i,j} + h^2 b_{i,j}\Big)\delta_\xi^2\delta_\eta^2\widehat{\phi}_{i,j} + \Big[h^2 d_{i,j} + k^2\Big(2\delta_\eta a_{i,j} + d^*_{i,j}a_{i,j}\Big)\Big]\delta_\xi^2\delta_\eta\widehat{\phi}_{i,j} \\
+ \; & \Big[k^2 c_{i,j} + h^2\Big(2\delta_\xi b_{i,j} + c^*_{i,j}b_{i,j}\Big)\Big]\delta_\xi\delta_\eta^2\widehat{\phi}_{i,j}\Bigg] = F'_{i,j} + O(h^4, k^4), \qquad (2.16)
\end{aligned}
$$

where

$$
\begin{aligned}
c^*_{i,j} &= \frac{c_{i,j} - 2\delta_\xi a_{i,j}}{a_{i,j}},\\
d^*_{i,j} &= \frac{d_{i,j} - 2\delta_\eta b_{i,j}}{b_{i,j}},\\
A'_{i,j} &= a_{i,j} + \frac{h^2}{12}\left[\left(\delta^2_\xi a_{i,j} + 2\delta_\xi c_{i,j} + p_{i,j}\right) + c^*_{i,j}\left(\delta_\xi a_{i,j} + c_{i,j}\right)\right] + \frac{k^2}{12}\left[d^*_{i,j}\delta_\eta a_{i,j} + \delta^2_\eta a_{i,j}\right],\\
B'_{i,j} &= b_{i,j} + \frac{h^2}{12}\left[c^*_{i,j}\delta_\xi b_{i,j} + \delta^2_\xi b_{i,j}\right] + \frac{k^2}{12}\left[\left(\delta^2_\eta b_{i,j} + 2\delta_\eta d_{i,j} + p_{i,j}\right) + d^*_{i,j}\left(\delta_\eta b_{i,j} + d_{i,j}\right)\right],\\
C'_{i,j} &= c_{i,j} + \frac{h^2}{12}\left[\delta^2_\xi c_{i,j} + 2\delta_\xi p_{i,j} + c^*_{i,j}\left(\delta_\xi c_{i,j} + p_{i,j}\right)\right] + \frac{k^2}{12}\left[\delta^2_\eta c_{i,j} + d^*_{i,j}\delta_\eta c_{i,j}\right],
\end{aligned}
$$

$$
\begin{aligned}
D'_{i,j} &= d_{i,j} + \frac{h^2}{12}\left[\delta^2_\xi d_{i,j} + c^*_{i,j}\delta_\xi d_{i,j}\right] + \frac{k^2}{12}\left[\delta^2_\eta d_{i,j} + 2\delta_\eta p_{i,j} + d^*_{i,j}\left(\delta_\eta d_{i,j} + p_{i,j}\right)\right],\\
G'_{i,j} &= \frac{h^2}{12}\left[2\delta_\xi d_{i,j} + c^*_{ij} d_{i,j}\right] + \frac{k^2}{12}\left[2\delta_\eta c_{i,j} + d^*_{i,j} c_{i,j}\right],\\
H'_{i,j} &= p_{i,j} + \frac{h^2}{12}\left[\delta^2_\xi p_{i,j} + c^*_{i,j}\delta_\xi p_{i,j}\right] + \frac{k^2}{12}\left[\delta^2_\eta p_{i,j} + d^*_{i,j}\delta_\eta p_{i,j}\right],\\
F'_{i,j} &= f_{i,j} + \frac{h^2}{12}\left[\delta^2_\xi f_{i,j} + c^*_{i,j}\delta_\xi f_{i,j}\right] + \frac{k^2}{12}\left[\delta^2_\eta f_{i,j} + d^*_{i,j}\delta_\eta f_{i,j}\right],
\end{aligned}
$$

Thus equation (2.16) becomes the $O(h^4, k^4)$ HOC finite difference approximation for (2.11) on the transformed plane. The order of accuracy is preserved in the physical plane if the transformation function is smooth enough [24, 56].

The discretized form of (2.16) can now be written as

$$
\sum_{k_1=-1}^{1}\sum_{k_2=-1}^{1} w_{i+k_1,j+k_2}\ \widehat{\phi}_{i+k_1,j+k_2} = 24F'_{i,j}, \tag{2.17}
$$

where

$$
w_{i+k_1,j+k_2} = \frac{1}{h^2k^2} r_{i+k_1,j+k_2},
$$

with

$$
\begin{aligned}
r_{i-1,j-1} &= \left(6hkG'_{i,j} + 2X_{i,j} - kY_{i,j} - hZ_{i,j}\right),\\
r_{i,j-1} &= \left(24h^2B'_{i,j} - 12h^2kD'_{i,j} - 4X_{i,j} + 2kY_{i,j}\right),\\
r_{i+1,j-1} &= \left(-6hkG'_{i,j} + 2X_{i,j} - kY_{i,j} + hZ_{i,j}\right),
\end{aligned}
$$

$$
\begin{aligned}
r_{i-1,j} &= \Big(24k^2A'_{i,j} - 12hk^2C'_{i,j} - 4X_{i,j} + 2hZ_{i,j}\Big),\\
r_{i,j} &= \Big(-48k^2A'_{i,j} - 48h^2B'_{i,j} + 24h^2k^2H'_{i,j} + 8X_{i,j}\Big),\\
r_{i+1,j} &= \Big(24k^2A'_{i,j} + 12hk^2C'_{i,j} - 4X_{i,j} - 2hZ_{i,j}\Big),\\
r_{i-1,j+1} &= \Big(-6hkG'_{i,j} + 2X_{i,j} + kY_{i,j} - hZ_{i,j}\Big),\\
r_{i,j+1} &= \Big(24h^2B'_{i,j} + 12h^2kD'_{i,j} - 4X_{i,j} - 2kY_{i,j}\Big),\\
r_{i+1,j+1} &= \Big(6hkG'_{i,j} + 2X_{i,j} + kY_{i,j} + hZ_{i,j}\Big),
\end{aligned}
$$

with

$$
\begin{aligned}
X_{i,j} &= h^2b_{i,j} + k^2a_{i,j},\\
Y_{i,j} &= h^2d_{i,j} + k^2(2\delta_\eta a_{i,j} + d^*_{i,j}a_{i,j}),\\
Z_{i,j} &= h^2(2\delta_\xi b_{i,j} + c^*_{i,j}b_{i,j}) + k^2c_{i,j}.
\end{aligned}
$$

Here, (2.17) represents the system of algebraic equations.

2.3 Solution of algebraic systems

We now discuss the solution of algebraic systems associated with the newly proposed finite difference approximations. The system of equations (2.17) can be written in matrix form as

$$A\mathbf{\Phi} = \mathbf{f}, \tag{2.18}$$

where the coefficient matrix A is an asymmetric sparse matrix. For a grid of size $m \times n$, A is of size $mn \times mn$ and $\mathbf{\Phi}$ and $\mathbf{f}$ are mn-component vectors.

The next step now is to solve the system of equations (2.18) with iterative methods. As the coefficient matrix A is not generally diagonally dominant, conventional iterative methods such as Gauss-Seidel cannot be used. On uniform grids, some of the associated matrices are symmetric and positive definite, which allows algorithms like conjugate-gradient (CG) [68] to be used. As nonuniform grid invariably leads to non-symmetric matrices, in order to solve these systems, the biconjugate gradient stabilized method (BiCGStab) [68, 118, 150] is used here without preconditioning.

To solve the N-S equations representing incompressible viscous flows by using the proposed scheme, we have used the ψ-ζ formulations and employed an outer-inner iteration procedure. In an outer cycle, we solve the transformation of (2.7) using (2.17) with $\alpha = -1$, $\beta = -1$, $\gamma = uRe$, $\nu = vRe$, $\omega = 0$, $\theta = 0$ in (2.8). Then we solve the transformation of (2.6) using (2.17) with $\alpha = -1$, $\beta = -1$, $\gamma = 0$, $\nu = 0$, $\omega = 0$, $\theta = \zeta$ in (2.8). For both the vorticity and streamfunction equation, BiCGStab is used, which constitutes the inner iterations. Once (2.6) is solved, u and v in (2.4) are calculated in the following way:

$$\begin{aligned}
u_{i,j} &= \left(\frac{\partial\psi}{\partial y}\right)_{i,j} \\
&= \left(-\frac{x_\eta}{J}\frac{\partial\psi}{\partial\xi}+\frac{x_\xi}{J}\frac{\partial\psi}{\partial\eta}\right)_{i,j} \\
&= \left[-\frac{x_\eta}{J}\left(\delta_\xi\psi-\frac{h^2}{6}\frac{\partial^3\psi}{\partial\xi^3}\right)+\frac{x_\xi}{J}\left(\delta_\eta\psi-\frac{k^2}{6}\frac{\partial^3\psi}{\partial\eta^3}\right)\right]_{i,j}+O(h^4,k^4) \\
&= \Bigg[-\frac{x_\eta}{J}\Bigg\{\delta_\xi\psi-\frac{h^2}{6}\Bigg(\frac{1}{a}\Bigg[\delta_\xi f-\Big(\delta_\xi a+c\Big)\Big(\delta_\xi^2\psi\Big)-\Big(\delta_\xi g+d\Big)\Big(\delta_\xi\delta_\eta\psi\Big) \\
&- g\Big(\delta_\xi^2\delta_\eta\psi\Big)-\Big(\delta_\xi b\Big)\Big(\delta_\eta^2\psi\Big)-b\Big(\delta_\xi\delta_\eta^2\psi\Big)-\Big(\delta_\xi c\Big)\Big(\delta_\xi\psi\Big)-\Big(\delta_\xi d\Big)\Big(\delta_\eta\psi\Big) \\
&- p\Big(\delta_\xi\psi\Big)-\psi\Big(\delta_\xi p\Big)\Bigg]\Bigg)\Bigg\}+\frac{x_\xi}{J}\Bigg\{\delta_\eta\psi-\frac{k^2}{6}\Bigg(\frac{1}{b}\Bigg[\delta_\eta f-\Big(\delta_\eta b+d\Big)\Big(\delta_\eta^2\psi\Big) \\
&- \Big(\delta_\eta g+c\Big)\Big(\delta_\xi\delta_\eta\psi\Big)-g\Big(\delta_\xi\delta_\eta^2\psi\Big)-\Big(\delta_\eta a\Big)\Big(\delta_\xi^2\psi\Big)-a\Big(\delta_\xi^2\delta_\eta\psi\Big) \\
&- \Big(\delta_\eta c\Big)\Big(\delta_\xi\psi\Big)-\Big(\delta_\eta d\Big)\Big(\delta_\eta\psi\Big)-p\Big(\delta_\eta\psi\Big)-\psi\Big(\delta_\eta p\Big)\Bigg]\Bigg)\Bigg\}\Bigg]_{i,j} \\
&+ O(h^4,k^4), \qquad (2.19)
\end{aligned}$$

Likewise,

$$\begin{aligned}
v_{i,j} &= \left(-\frac{\partial\psi}{\partial x}\right)_{i,j} \\
&= \left(-\frac{y_\eta}{J}\frac{\partial\psi}{\partial\xi}+\frac{y_\xi}{J}\frac{\partial\psi}{\partial\eta}\right)_{i,j} \\
&= \left[-\frac{y_\eta}{J}\left(\delta_\xi\psi-\frac{h^2}{6}\frac{\partial^3\psi}{\partial\xi^3}\right)+\frac{y_\xi}{J}\left(\delta_\eta\psi-\frac{k^2}{6}\frac{\partial^3\psi}{\partial\eta^3}\right)\right]_{i,j}+O(h^4,k^4) \\
&= \Bigg[-\frac{y_\eta}{J}\Bigg\{\delta_\xi\psi-\frac{h^2}{6}\Bigg(\frac{1}{a}\Bigg[\delta_\xi f-\Big(\delta_\xi a+c\Big)\Big(\delta_\xi^2\psi\Big)-\Big(\delta_\xi g+d\Big)\Big(\delta_\xi\delta_\eta\psi\Big) \\
&- g\Big(\delta_\xi^2\delta_\eta\psi\Big)-\Big(\delta_\xi b\Big)\Big(\delta_\eta^2\psi\Big)-b\Big(\delta_\xi\delta_\eta^2\psi\Big)-\Big(\delta_\xi c\Big)\Big(\delta_\xi\psi\Big)-\Big(\delta_\xi d\Big)\Big(\delta_\eta\psi\Big)
\end{aligned}$$

$$
\begin{aligned}
- &\; p\Big(\delta_\xi\psi\Big) - \psi\Big(\delta_\xi p\Big)\Big]\Big]\Big)\Big\} + \frac{y_\xi}{J}\Big\{\delta_\eta\psi - \frac{k^2}{6}\Big(\frac{1}{b}\Big[\delta_\eta f - \Big(\delta_\eta b + d\Big)\Big(\delta_\eta^2\psi\Big) \\
- &\; \Big(\delta_\eta g + c\Big)\Big(\delta_\xi\delta_\eta\psi\Big) - g\Big(\delta_\xi\delta_\eta^2\psi\Big) - \Big(\delta_\eta a\Big)\Big(\delta_\xi^2\psi\Big) - a\Big(\delta_\xi^2\delta_\eta\psi\Big) \\
- &\; \Big(\delta_\eta c\Big)\Big(\delta_\xi\psi\Big) - \Big(\delta_\eta d\Big)\Big(\delta_\eta\psi\Big) - p\Big(\delta_\eta\psi\Big) - \psi\Big(\delta_\eta p\Big)\Big]\Big)\Big\}\Big]_{i,j} \\
+ &\; O(h^4, k^4).
\end{aligned}
\tag{2.20}
$$

Here a, b, c, d, g and p are the coefficients, and f is the source term in the equation (2.11) for ψ. We utilize a relaxation parameter ϵ for the inner iteration cycles for both ζ and ψ. For larger values of Reynolds number, we needed in general smaller values of ϵ.

2.4 Numerical Test Cases

We validate the proposed scheme on three test cases of which one is linear and two are non-linear. These are (i) a linear convection-diffusion problem, (ii) a problem governed by N-S equations with a constructed analytical solution and (iii) the lid-driven cavity flow problem. Problem (i) and (ii) have analytical solutions, so Dirichlet boundary conditions are used while for the problem (iii), both Dirichlet and Neumann boundary conditions are applied.

2.4.1 Test case 1: Linear convection-diffusion

Firstly we consider a problem governed by the linear 2D convection-diffusion that was also numerically solved in [51]. Here the equation is of the form (2.8) in a square $0 \le x, y \le 1$ with the coefficients as follows:

$$
\begin{aligned}
\alpha(x,y) &= -1, & \beta(x,y) &= -1, \\
\gamma(x,y) &= -Rex, & \nu(x,y) &= Rey, \\
\omega(x,y) &= 0,
\end{aligned}
$$

and

$$\theta(x,y) = e^{x+y}[xy(6 - 2x - 2xy - 2y) + xyRe(x^2 - y^2 - x^2y + xy^2)].$$

The boundary conditions are

$$
\begin{aligned}
\phi(x,0) &= \phi(x,1) = 0, & 0 \le x \le 1 \\
\phi(0,y) &= \phi(1,y) = 0. & 0 \le y \le 1
\end{aligned}
$$

The exact solution of this problem is given by

$$\phi_{ex} = xy(1-x)(1-y)e^{x+y}. \tag{2.21}$$

Because of the presence of large gradients near the top and right walls (at $x = 1$ and $y = 1$) of the problem domain (see the numerical solution in figure 2.2(b)), we generate the grid (see figure 2.2(a)) in such a way that points are clustered in those regions. We have used the following transformations

$$x = \xi + \frac{\lambda}{\pi}\sin(\pi\xi), \tag{2.22}$$

$$y = \eta + \frac{\lambda}{\pi}\sin(\pi\eta), \tag{2.23}$$

where λ, the stretching parameter $(0 \leq \lambda < 1)$, determines the degree of clustering near the boundaries. Here $\lambda = 0$ indicates a uniform grid.

(a) (b)

Figure 2.2: *For problem 1: 41 × 41 Grids, λ=0.5 (a) physical plane and (b) Contour plot of numerical solution at Re=100.*

Table 2.1 shows maximum errors in ϕ for $0 \leq Re \leq 250$ on different meshes e.g. 21×21, 41×41 with different λ. The last column shows the estimated orders of accuracy (O(A)), which is calculated by the following formula (2.24).

$$O(A) = \frac{ln(E_1/E_2)}{ln2}, \tag{2.24}$$

where
$E_1 = \phi - \phi_M; \qquad E_2 = \phi - \phi_F.$

Table 2.1: *Problem 1: maximum absolute errors and convergence rates of* ϕ *for different Re* ($0 \leq Re \leq 250$)*, stretching ratio* λ ($\lambda = 0.0, 0.2, 0.5$ *and* 0.7)*, and mesh size (21 × 21 and 41 × 41).*

Re	λ	Maximum absolute errors		Rate
		21× 21	41× 41	
0.0	0.0	5.972163(-7)	4.792009(-8)	3.64
	0.2	7.380441(-7)	5.404933(-8)	3.77
	0.5	2.329631(-6)	1.439459(-7)	4.02
	0.7	1.366644(-5)	8.303628(-7)	4.04
	0.9	1.426221(-4)	8.327804(-6)	4.10
10.0	0.0	6.495213(-6)	4.162546(-7)	3.96
	0.2	4.253100(-6)	2.718492(-7)	3.97
	0.5	4.574328(-6)	2.880939(-7)	3.99
	0.7	1.312638(-5)	7.927363(-7)	4.05
	0.9	1.457512(-4)	8.436668(-6)	4.11
50.0	0.0	6.376308(-5)	4.021584(-6)	3.99
	0.2	3.653922(-5)	2.299240(-6)	3.99
	0.5	5.088935(-5)	3.198843(-6)	3.99
	0.7	7.559852(-5)	4.656992(-6)	4.02
	0.9	1.012255(-4)	6.158866(-6)	4.04
100.0	0.0	1.381619(-4)	9.135107(-6)	3.92
	0.2	8.318824(-5)	5.268395(-6)	3.98
	0.5	1.188183(-4)	7.417254(-6)	4.00
	0.7	1.771463(-4)	1.131675(-5)	3.97
	0.9	2.492911(-4)	1.525042(-5)	4.03
250.0	0.0	3.276991(-4)	2.375178(-5)	3.77
	0.2	2.132622(-4)	1.422608(-5)	3.91
	0.5	3.190254(-4)	2.054453(-5)	3.96
	0.7	5.027599(-4)	3.205554(-5)	3.97
	0.9	7.169570(-4)	4.445088(-5)	4.01

Here ϕ, ϕ_F, ϕ_M stand for exact solution, the solution on a fine grid and the solution on a coarse grid with half of the numbers of points in each direction respectively. One can clearly see from Table 2.1 that the error decays as $O(h^4)$ as expected. It may be pointed out that the computed rate deviates from fourth order rate for uniform meshes ($\lambda = 0$) are due to insufficient points in high gradient regions in the problem domain. It can not be accurately resolved unless the grid is fine enough.

2.4.2 Test case 2: 2D N-S equations with a constructed solution

Next we take a problem in the domain ($0 \leq x, y \leq 1$) governed by the N-S equations in streamfunction-vorticity formulations ((2.6) and (2.7)) with a known constructed solution in [45]. Here the vorticity equation (2.7) contains a source function θ which is given by the following expression:

$$\theta = -\frac{p^4(e^{-px} + e^{-py} - 4e^{-p(x+y)})}{(1-e^{-p})^2} - Re\frac{p^4 e^{-p(x+y)}(e^{-px} - e^{-py})}{(1-e^{-p})^4},$$

where p is a constant. The exact solutions are

$$\begin{aligned}\psi &= \frac{(1-e^{-px})(1-e^{-py})}{(1-e^{-p})^2}, \qquad \zeta = \frac{p^2(e^{-px}+e^{-py}-2e^{-p(x+y)})}{(1-e^{-p})^2}.\\ u &= \frac{pe^{-py}(1-e^{-px})}{(1-e^{-p})^2}, \qquad v = -\frac{pe^{-px}(1-e^{-py})}{(1-e^{-p})^2}.\end{aligned}$$

For both ψ and ζ, there exist boundary layers near the bottom and left boundary (shown in figure 2.3(b)). To resolve this layer we have used a non-uniform clustered


(a)
(b)

Figure 2.3: *For problem 2: 41 × 41 Grids, (λ=0.6) (a) physical plane and (b)Contour plot of vorticity at Re=100.*

Table 2.2: *Problem 2: maximum absolute errors and convergence rates of ψ for different Res ($0 \leq Re \leq 100$), stretching ratios λ ($\lambda = 0.0, 0.2, 0.6$ and 0.9), and mesh sizes (21 × 21, 41 × 41 and 81 × 81.)*

Re	λ	Max (ψ) 21 × 21	Max (ψ) 41 × 41	Rate(ψ)	Max (ψ) 81 × 81	Rate(ψ)
1	0.0	8.533237(-4)	5.363826(-5)	3.99	3.359854(-6)	4.00
	0.2	2.760385(-4)	1.735080(-5)	3.99	1.084940(-6)	4.00
	0.6	1.584300(-4)	1.007031(-5)	3.98	6.313645(-7)	4.00
	0.9	2.297964(-3)	1.288683(-4)	4.16	7.841111(-6)	4.04
10	0.0	1.982106(-3)	1.228728(-4)	4.01	7.665783(-6)	4.00
	0.2	8.821008(-4)	5.460008(-5)	4.01	3.407415(-6)	4.00
	0.6	1.924951(-4)	1.179163(-5)	4.03	7.334939(-7)	4.01
	0.9	1.131330(-3)	6.882639(-5)	4.04	4.293485(-6)	4.00
100	0.0	2.114424(-2)	1.195317(-3)	4.14	7.007112(-5)	4.09
	0.2	1.007629(-2)	5.161778(-4)	4.29	3.092081(-5)	4.06
	0.6	2.378835(-3)	1.269820(-4)	4.23	7.868219(-6)	4.01
	0.9	3.732115(-3)	1.960301(-4)	4.25	1.223926(-5)	4.00

grid (shown in figure 2.3(a)) which is obtained by the following transformations

$$x = \xi - \frac{\lambda}{\pi}\sin(\pi\xi), \tag{2.25}$$

$$y = \eta - \frac{\lambda}{\pi}\sin(\pi\eta). \tag{2.26}$$

Where λ is defined as in test case 1. Also a larger value of p indicates a steeper boundary layer. In all the calculations we have considered p=10. In table 2.2, the maximum errors of streamfunction (ψ) have been presented on three grid sizes 21 × 21, 41 × 41 and 81 × 81 which in turn measure the order of accuracy of the proposed scheme for this non-linear problem as in test case 1 (see equation (2.24)). This table clearly demonstrates that the order of accuracy (rate) is approximately O(h^4) as expected.

2.4.3 Test case 3: Lid-driven cavity problem

We now move to the classical lid-driven cavity problem. This problem with aspect ratio K=1 (K=$\frac{D_1}{D_2}$, where D_1 and D_2 are the depth and width of the cavity), over the years, has become the most frequently used benchmark problem for the assessment of numerical methods, particularly the steady-state solution of the incompressible fluid flows governed by the N-S equations [14, 18, 19, 46, 65, 66, 72, 120, 148]. In contrast to the fairly large number of studies conducted in square lid-driven cavity, relatively less number of investigations have been carried out for flow in a rectangular cavity. The effects of geometry on the vortex structure in the rectangular cavity were studied in [96, 108, 125, 141]. This problem is of great scientific interest because it displays almost all fluid mechanical phenomena for incompressible viscous flows in the simplest of geometric settings. The geometry and the boundary conditions have been shown in the figure 2.4 where the top wall is moving and the remaining three walls are stationary. No slip boundary conditions have been employed on three stationary walls. The moving wall generates vorticity which diffuses inside the cavity and this diffusion is the driving mechanism of the flow. At high Re ($Re = (U/\nu)$L, U is the lid velocity, L is the cavity width and ν is the kinematic viscosity of the enclosed fluid in motion), several secondary and tertiary vortices begin to appear, whose characteristics depend on Re. Because of the presence of large gradients near the walls, we generate a centro-symmetric grid (see the physical plane in figure 2.5(a)) and the corresponding uniform grid in the computational plane in figure 2.5(b)) with clustering near the

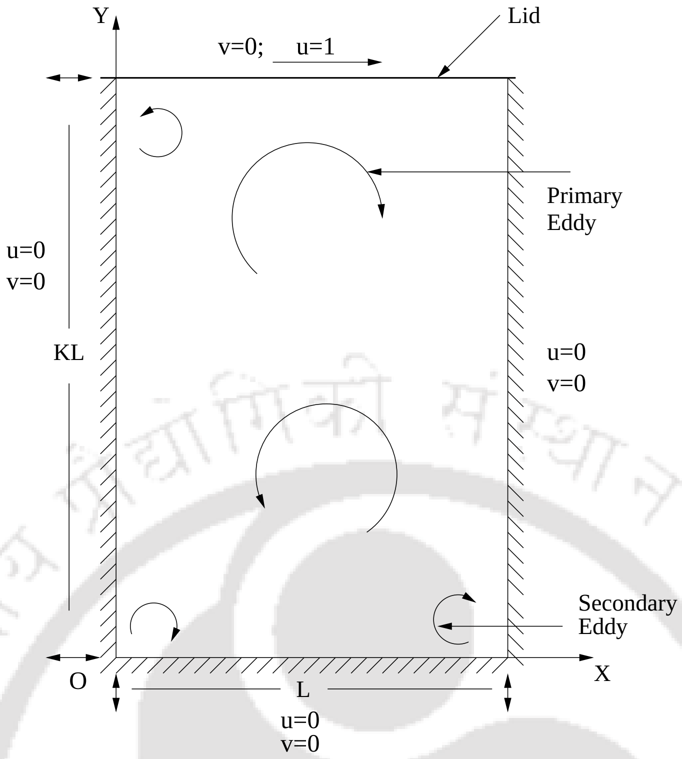

Figure 2.4: *The lid-driven cavity flow configuration with boundary conditions.*

walls using the stretching functions

$$x = \xi - \frac{\lambda}{\theta_1}\sin(\theta_1\xi),$$
$$y = \eta - \frac{\lambda}{\theta_2}\sin(\theta_2\eta),$$

where λ, the stretching parameter ($0 \leq \lambda < 1$), determines the degree of clustering and the proper choice of θ_1 and θ_2 correspond the clustering near the boundaries (see figure 2.5(a). It can be noted that $\lambda = 0$ indicates uniform grid (see figure 2.5(b)).

Boundary conditions:

No-slip boundary conditions have been employed on the three stationary walls. Boundary conditions for velocity on the top wall is given by $u = 1$, $v = 0$. On all other walls of the cavity the velocities are zero ($u = v = 0$). In the ψ-ζ setting used here, streamfunction values on all the four walls are zero ($\psi = 0$).

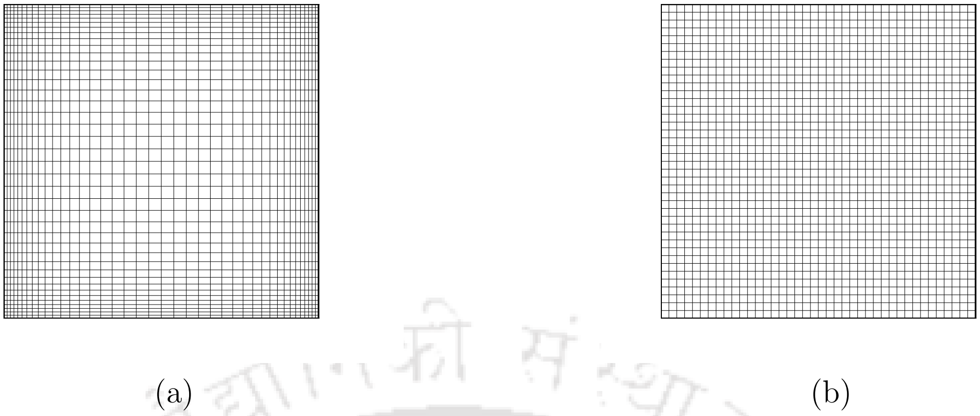
(a) (b)

Figure 2.5: *(a) For problem 2: 41 × 41 Grids, (a) physical plane (λ=0.6) and (b) computational plane.*

We now proceed to develop HOC wall boundary conditions for vorticity ζ in the following manner:

In the physical plane, the velocity on the left wall, where the index for x-direction is 0 and j is the y-direction index varying from 0 to $y_{\max}$, on using forward difference, we have

$$\begin{aligned} v_{0,j} &= -\frac{\partial\psi}{\partial x}\Big|_{0,j}, \\ &= -\delta_x^+\psi_{0,j} + \frac{\Delta x}{2}\frac{\partial^2\psi}{\partial x^2}\Big|_{0,j} + \frac{(\Delta x)^2}{6}\frac{\partial^3\psi}{\partial x^3}\Big|_{0,j} + O((\Delta x)^3), \end{aligned} \tag{2.27}$$

where Δx is the distance between the left wall and the first point closest to it in the physical plane. Using the fact that $\dfrac{\partial^2\psi}{\partial y^2} = 0$ on a vertical wall, from the Poisson equation (2.6), we have

$$\frac{\partial^2\psi}{\partial x^2}\Big|_{0,j} = -\zeta_{0,j}, \qquad \frac{\partial^3\psi}{\partial x^3}\Big|_{0,j} = -\frac{\partial\zeta}{\partial x}\Big|_{0,j}.$$

With this and using the fact that the vertical velocity on the left wall is zero, (2.27) can be written in the computational plane as

$$0 = -\frac{1}{x_\xi}\delta_\xi^+\psi_{0,j} - \frac{1}{2}hx_\xi\zeta_{0,j} - \frac{1}{6}h^2x_\xi\delta_\xi^+\zeta_{0,j} + O(h^3),$$

where we have used the fact that

$$\Delta x = x_\xi d\xi + x_\eta d\eta,$$

in which $d\xi = h$; $d\eta = k$ are the uniform step lengths in the ξ and η directions respectively in the computational plane. The vorticity at the other boundaries can be approximated in a similar way.

The vorticity at the corners has been approximated using a second order accurate formula as was done by Spotz [127]. It may be mentioned that the use of higher order formulas at the corners result in oscillatory solutions in their neighbourhoods which was also observed in references [65, 127].

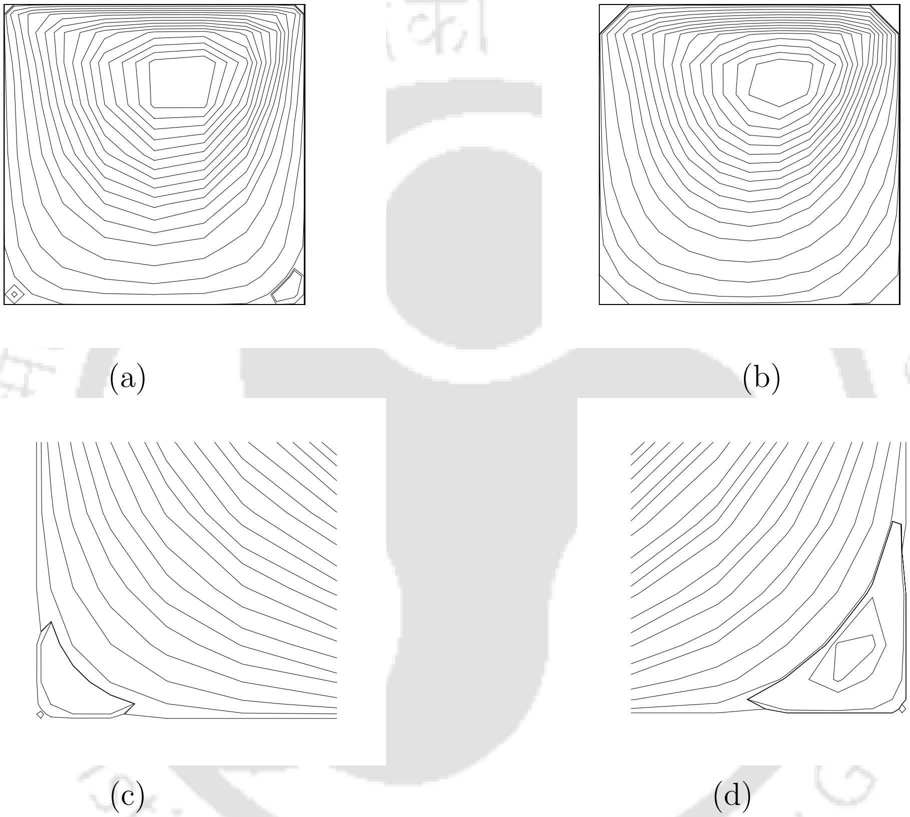

Figure 2.6: *For the lid-driven square cavity flow problem,* $Re = 100$*: streamlines computed on a* 11×11 *grid with (a) the present scheme* ($\lambda = 0.7$)*, (b) reference [128]; appearance of tertiary vortex on a* 21×21 *grid,* ($\lambda = 0.95$)*: (c) bottom left and (d) bottom right.*

Results for square cavity (Aspect ratio=1.0)

We now present the steady-state solutions produced by the proposed scheme for this problem in tables 2.3-2.9 and figures 2.6-2.11. Figure 2.6 shows the good effects of clustering: figures 2.6(a) and (b) respectively show computed steady-state streamlines for $Re = 100$ on clustered nonuniform ($\lambda = 0.7$) and a uniform 11×11 grid. It clearly shows that on a grid of this size, a uniform grid cannot produce the secondary corner vortices at the bottom whereas this can be resolved easily on the nonuniform grid. Likewise figures 2.6(c) and (d) show the bottom left and bottom right corners of the cavity, where we were able to capture even the tertiary vortices on a grid as coarse as 21×21 with $\lambda = 0.95$. In table 2.3 we demonstrate the effect of the stretching parameter λ on the computed solutions. It is seen from table 2.3 (a) that with increasing λ, the minimum streamfunction value and the vorticity at the mid-point of the moving wall deviate from the benchmark results in [46]. This is due to the fact that severe clustering at the walls takes away some significant points from the interior and high-gradient vorticity regions are not necessarily aligned to the walls. In addition to this one can see from the table 2.3 (b) that the location of the primary vortex center for $Re = 2000$ varies with λ, with slight variation in the ψ_{min} value. Next, we try to find an optimal λ value which will guarantee the most accurate resolution of the flow with minimal computational effort. It is numerically experimented and found that for $\lambda < 0.6$, bottom left (BL) tertiary vortex could not be captured for $Re = 2000$. This phenomenon has been observed for $\lambda \geq 0.6$ (see figure 2.7). It is also seen that for $\lambda \geq 0.6$ the ψ_{min} value deviates from the numerical result in [53]. Again from figure 2.7 we see that with $\lambda = 0.6$, all the flow characteristics including the tertiary

Table 2.3: *Lid-driven cavity flow problem: effects of the stretching parameter for (a) Re=400 on a 41 × 41 grid and (b) Re=2000 on a 61 × 61 grid.*

(a)

λ	Present		Ref. [46]	
	ψ_{min}	$\zeta(0.5, 1)$	ψ_{min}	$\zeta(0.5, 1)$
0.6	-0.112	-9.99162	-0.114	-10.0545
0.7	-0.111	-9.96032		
0.8	-0.110	-9.89285		
0.9	-0.108	-9.64820		

(b)

λ	Present			[53]	
	ψ_{min}	Primary vortex center (x,y)	BL tertiary vortex	ψ_{min}	Primary vortex center (x,y)
0.0	-0.114274	(0.5167, 0.5667)	-	-0.118	(0.5250, 0.5500)
0.3	-0.115965	(0.5217, 0.5648)	-	-	-
0.4	-0.116151	(0.5233, 0.5466)	-	-	-
0.5	-0.116096	(0.5250, 0.5499)	-	-	-
0.6	-0.115701	(0.5266, 0.5532)	develops	-	-
0.7	-0.114892	(0.5283, 0.5565)	do	-	-
0.8	-0.113530	(0.5300, 0.5598)	do	-	-

corner vortices could be easily captured which $0.2 \leq \lambda \leq 0.5$ could not do so. Also with values of $\lambda > 0.6$, the size of the top left vortex was seen to decrease as severe clustering at the walls with higher λ values takes away some significant points from the interior. Therefore, for most of the computations in this problem, we have used $\lambda = 0.6$. In table 2.4, we present our grid independence data for u, v, ψ and ζ for $Re = 100$, 400 and 1000, and compare them with those of ref. [18,46,92]. It confirms that our coarse grids are enough to produce more accurate results.

Table 2.4: *Lid-driven cavity flow problem: grid independence study of the steady-state data at the center of the cavity.*

Re	Present				
	Grid	Velocity		ψ	ζ
		u	v		
100	21 × 21	-0.20453	0.05508	-0.06486	-1.12965
	129 × 129 [46]	-0.20581 [46]	0.05454 [46]		
	31 × 31	-0.20701	0.05643	-0.06574	-1.15390
	41 × 41	-0.20791	0.05691	-0.06608	-1.16268
	61 × 61	-0.20859	0.05725	-0.06633	-1.16910
	81 × 81	-0.20883	0.05738	-0.06642	-1.17141
	89 × 89 [92]				-1.17441 [92]
400	41 × 41	-0.11829	0.05373	-0.10457	-2.42382
	61 × 61	-0.11578	0.05242	-0.10603	-2.42169
	81 × 81	-0.11529	0.05217	-0.10636	-2.42178
	121 × 121	-0.11510	0.05208	-0.10653	-2.42236
1000	41 × 41	-0.07142	0.02831	-0.10924	-2.01695
	61 × 61	-0.06467	0.02639	-0.11462	-2.05602
	81 × 81	-0.06298	0.02598	-0.11582	-2.06287
	121 × 121	-0.06226	0.02583	-0.11633	-2.06575
	160 × 160 [18]	-0.06206 [18]	0.02578 [18]		-2.06722 [18]

Table 2.5 compares our primary vortex data for $100 \leq Re \leq 5000$ with the benchmark results in [46] as well as other established results [14,18,19,53,57,72,120, 148]. In table 2.6 and 2.7, we provide the secondary vortex data for the same range of Reynolds numbers at the two bottom corners and at the top left corner whereas in table 2.8, we present the tertiary vortex data for the bottom corners. In all these tables, we compare them with the references cited above and excellent match was observed in all the cases.

In figure 2.8, we present comparisons of the horizontal velocities along the vertical centerline and the vertical velocities along the horizontal centerline of the square cavity for Reynolds numbers ranging from 100 to 5000 and compare our data with those of Ghia *et al.* [46]. While the data for [46] were obtained using 129 × 129 and 257 × 257 grids, our data are obtained using a 21 × 21 grid ($Re = 100$), a 41 × 41 grid ($Re = 400$), a 61 × 61 grid ($Re = 1000$), 101 × 101 grid ($Re = 3200$) and a 121 × 121 grid ($Re = 5000$). In each case, our velocity profiles exhibit a perfect match with Ghia's results.

In figure 2.9, we compare our data of the horizontal vorticities along the vertical centerline and the vertical vorticities along the horizontal centerline of the square

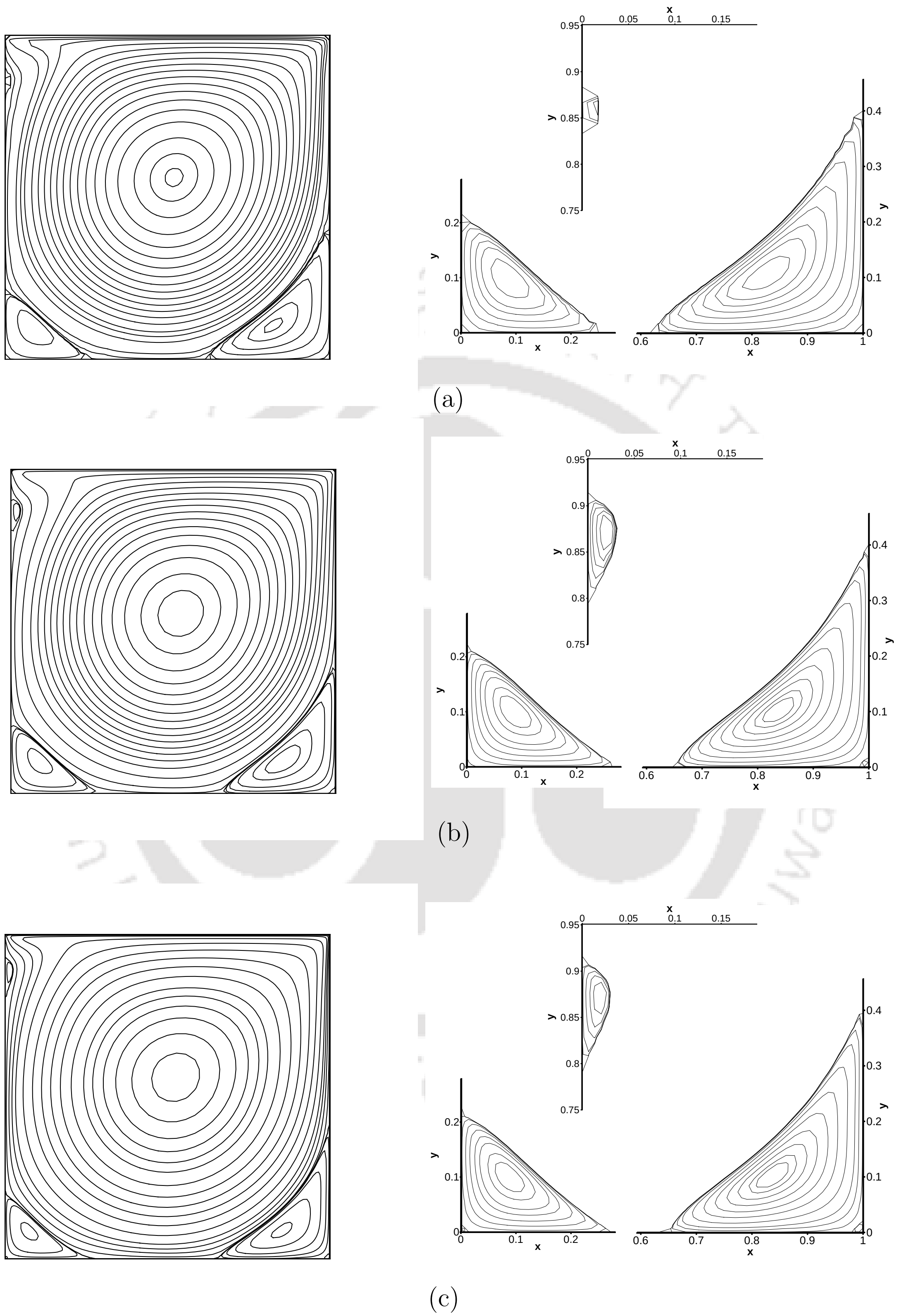

(a)

(b)

(c)

Figure 2.7: *For caption see next page.*

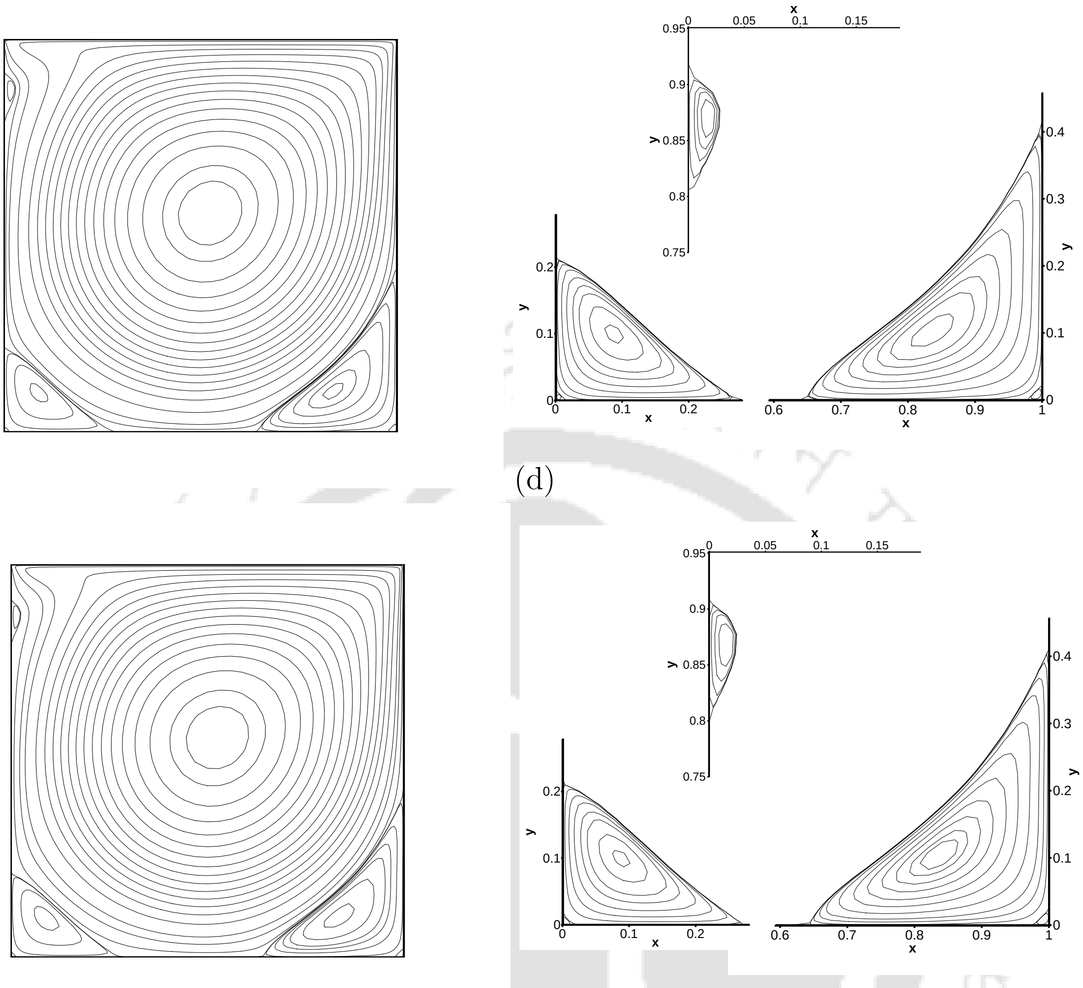

(d)

(e)

Figure 2.7: *For the lid-driven square cavity flow problem,* *Re* = 2000, *on* 61 × 61 *grid, stream line contours for:* *(a)* $\lambda = 0.0$, *(b)* $\lambda = 0.5$, *(c)* $\lambda = 0.6$, *(d)* $\lambda = 0.7$ *and (e)* $\lambda = 0.8$.

cavity on a grid 61 × 61 for Reynolds number 1000 with those of [20] on a grid 1024 × 1024. Here also, our coarse grid results are in excellent match with the extremely fine grid results of ref. [20].

In figure 2.10, we exhibit the well known streamlines and corresponding vorticity contours for $1000 \leq Re \leq 5000$. All of these graphs exhibit the typical separations and secondary vortices at the bottom corners of the cavity as well as at the top left

Table 2.5: *Strength and Location of the Centers of Primary Vortex for the lid-driven square cavity problem.*

Re	Ref.	ψ_{min}	x	y
100	[46]	-0.103	0.6172	0.7344
	[53]	-0.103	0.6125	0.7375
	[57]	-0.103	0.6196	0.7373
	[120]	-0.103	0.6167	0.7417
	[148]	-0.103	0.6188	0.7375
	Present	-0.103	0.6183	0.7273
400	[46]	-0.114	0.5547	0.6055
	[57]	-0.112	0.5608	0.6078
	[53]	-0.113	0.5500	0.6125
	[120]	-0.113	0.5571	0.6071
	[148]	-0.114	0.5563	0.6000
	Present	-0.113	0.5532	0.6055
1000	[18]	-0.119	0.5308	0.5652
	[19]	-0.116	0.5313	0.5586
	[46]	-0.118	0.5313	0.5625
	[53]	-0.117	0.5250	0.5625
	[57]	-0.118	0.5333	0.5647
	[120]	-0.116	0.5286	0.5643
	[148]	-0.117	0.5438	0.5625
	Present	-0.118	0.5399	0.5598
2000	[53]	-0.118	0.5250	0.5500
	[57]	-0.120	0.5255	0.5490
	[148]	-0.112	0.5250	0.5500
	Present	-0.119	0.5200	0.5598
3200	[46]	-0.120	0.5165	0.5469
	[53]	-0.122	0.5188	0.5438
	[72]	-0.115	—	—
	Present	-0.120	0.5160	0.5479
5000	[14]	-0.122	0.5113	0.5283
	[19]	-0.114	0.5156	0.5313
	[46]	-0.119	0.5117	0.5352
	[53]	-0.122	0.5125	0.5375
	[57]	-0.121	0.5176	0.5373
	[72]	-0.112	—	—
	[148]	-0.092	0.5125	0.5313
	Present	-0.119	0.5133	0.5399

of the square cavity.

In figure 2.11, we have presented the convergence histiry of the ζ errors on a 41 $\times$ 41 grid. As expected, the convergence for large Reynolds numbers requires more number of iterations; in table 2.9, we present the convergence data (and CPU time) for these cases.

Table 2.6: *Strength and Location of the Centers of Secondary Vortex: Bottom of the lid-driven square cavity.*

		Bottom Left			Bottom Right		
Re	Ref.	ψ_{max}	x	y	ψ_{max}	x	y
100	[19]	1.63e-6	0.0313	0.0391	1.23e-5	0.9453	0.0625
	[46]	1.75e-6	0.0313	0.0391	1.25e-5	0.9453	0.0625
	[53]	1.83e-6	0.0375	0.0375	1.45e-5	0.9375	0.0625
	[57]	1.72e-6	0.0392	0.0353	1.22e-5	0.9451	0.0627
	[120]	2.05e-6	0.0333	0.0250	1.32e-5	0.9417	0.0500
	[148]	1.94e-6	0.0375	0.0313	1.14e-5	0.9375	0.0563
	Present	1.72e-6	0.0316	0.0316	1.23e-5	0.9425	0.0575
400	[46]	1.42e-5	0.0508	0.0469	6.42e-4	0.8906	0.1250
	[53]	1.30e-5	0.0500	0.0500	6.48e-4	0.8875	0.1250
	[57]	1.30e-5	0.0549	0.0510	6.19e-4	0.8902	0.1255
	[120]	1.45e-5	0.0500	0.0429	6.44e-4	0.8857	0.1143
	[148]	1.46e-5	0.0500	0.0500	6.45e-4	0.8875	0.1188
	Present	1.38e-5	0.0528	0.0439	6.35e-4	0.8908	0.1233
1000	[18]	2.33e-4	0.0833	0.0781	1.73e-3	0.8640	0.1118
	[19]	3.25e-4	0.0859	0.0820	1.91e-3	0.8711	0.1094
	[46]	2.31e-4	0.0859	0.0781	1.75e-3	0.8594	0.1094
	[53]	2.02e-4	0.0875	0.0750	1.70e-3	0.8625	0.1125
	[57]	2.22e-4	0.0902	0.0784	1.69e-3	0.8667	0.1137
	[120]	2.17e-4	0.0857	0.0714	1.70e-3	0.8643	0.1071
	[148]	2.24e-4	0.0750	0.0813	1.74e-3	0.8625	0.1063
	Present	2.24e-4	0.0811	0.0811	1.72e-3	0.8577	0.1092
2000	[53]	8.58e-4	0.0875	0.1000	2.41e-3	0.8375	0.1000
	[57]	7.26e-4	0.0902	0.1059	2.44e-3	0.8471	0.0980
	[148]	6.90e-4	0.0875	0.1063	2.60e-3	0.8375	0.0938
	Present	6.65e-4	0.0899	0.0993	2.48e-3	0.8455	0.0993
3200	[46]	9.78e-4	0.0859	0.1094	3.14e-3	0.8125	0.0859
	[53]	1.03e-3	0.0813	0.1188	2.86e-3	0.8125	0.0875
	Present	9.80e-4	0.0794	0.1175	2.84e-3	0.8247	0.0863
5000	[14]	1.37e-3	0.0725	0.1370	3.07e-3	0.8041	0.0725
	[19]	2.22e-3	0.0664	0.1484	4.65e-3	0.8301	0.0703
	[46]	1.36e-3	0.0703	0.1367	3.08e-3	0.8086	0.0742
	[53]	1.32e-3	0.0750	0.1313	2.96e-3	0.8000	0.0750
	[57]	1.35e-3	0.0784	0.1313	3.03e-3	0.8078	0.0745
	[148]	1.67e-3	0.0625	0.1563	5.49e-3	0.8500	0.0813
	Present	1.16e-3	0.0782	0.1307	3.09e-3	0.8006	0.0782

Table 2.7: *Strength and Location of the Centers of Secondary Vortex: Top left side wall of the lid-driven square cavity.*

Re	Ref.	ψ_{min}	x	y
2000	[53]	-1.22e-4	0.0375	0.8875
	Present	-7.36e-5	0.0260	0.8804
3200	[46]	-7.28e-4	0.0547	0.8984
	[53]	-7.33e-4	0.0563	0.9000
	Present	-5.91e-4	0.0491	0.8988
5000	[14]	-1.45e-3	0.0635	0.9092
	[19]	-1.75e-3	0.0625	0.9102
	[46]	-1.46e-3	0.0625	0.9102
	[53]	-1.54e-3	0.0688	0.9125
	[57]	-1.40e-3	0.0667	0.9059
	Present	-1.24e-3	0.0624	0.9101

Table 2.8: *Strength and Location of the Centers of Tertiary Vortex: Bottom of the lid-driven square cavity.*

		Bottom Left			Bottom Right		
Re	Ref.	ψ_{min}	x	y	ψ_{min}	x	y
2000	Present	-1.59e-8	0.0050	0.0050	-7.52e-8	0.9899	0.0101
3200	[46]	-6.33e-8	0.0078	0.0078	-2.52e-7	0.9844	0.0078
	[53]	-3.74e-8	0.0063	0.0063	-2.37e-7	0.9875	0.0125
	Present	-2.32e-8	0.0040	0.0080	-1.93e-7	0.9879	0.0121
5000	[14]	-6.67e-8	0.0079	0.0079	-1.43e-6	0.9786	0.0188
	[19]	-2.33e-7	0.0117	0.0098	-2.47e-5	0.9668	0.0293
	[46]	-7.09e-8	0.0117	0.0078	-1.43e-6	0.9805	0.0195
	[53]	-5.15e-8	0.0063	0.0063	-1.70e-6	0.9750	0.0188
	Present	-4.52e-8	0.0067	0.0067	-1.45e-6	0.9795	0.0205

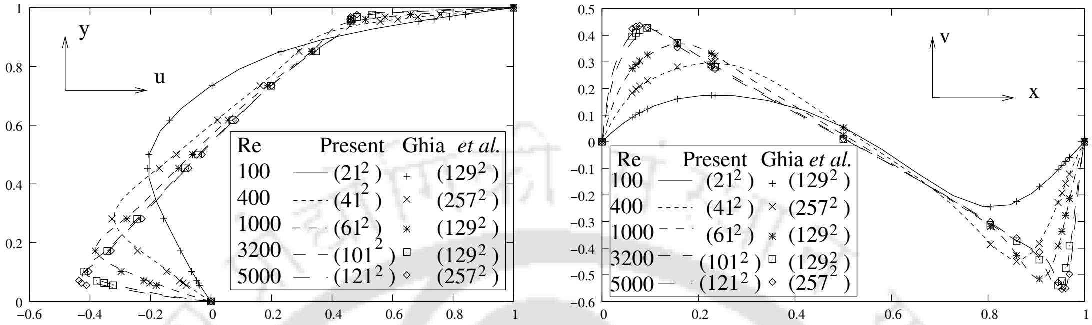

(a) (b)

Figure 2.8: *For the lid-driven square cavity flow problem: comparisons of steady-state (a) horizontal velocity along the vertical centerline and (b) vertical velocity along horizontal centerline from Re* = 100 *to Re* = 5000.

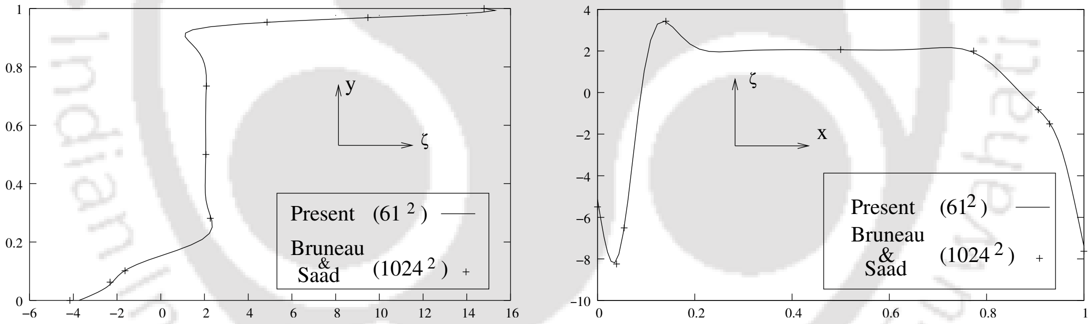

(a) (b)

Figure 2.9: *For the lid-driven square cavity flow problem: comparisons of steady-state (a) horizontal vorticity along the vertical centerline and (b) vertical vorticity along horizontal centerline for Re* = 1000.

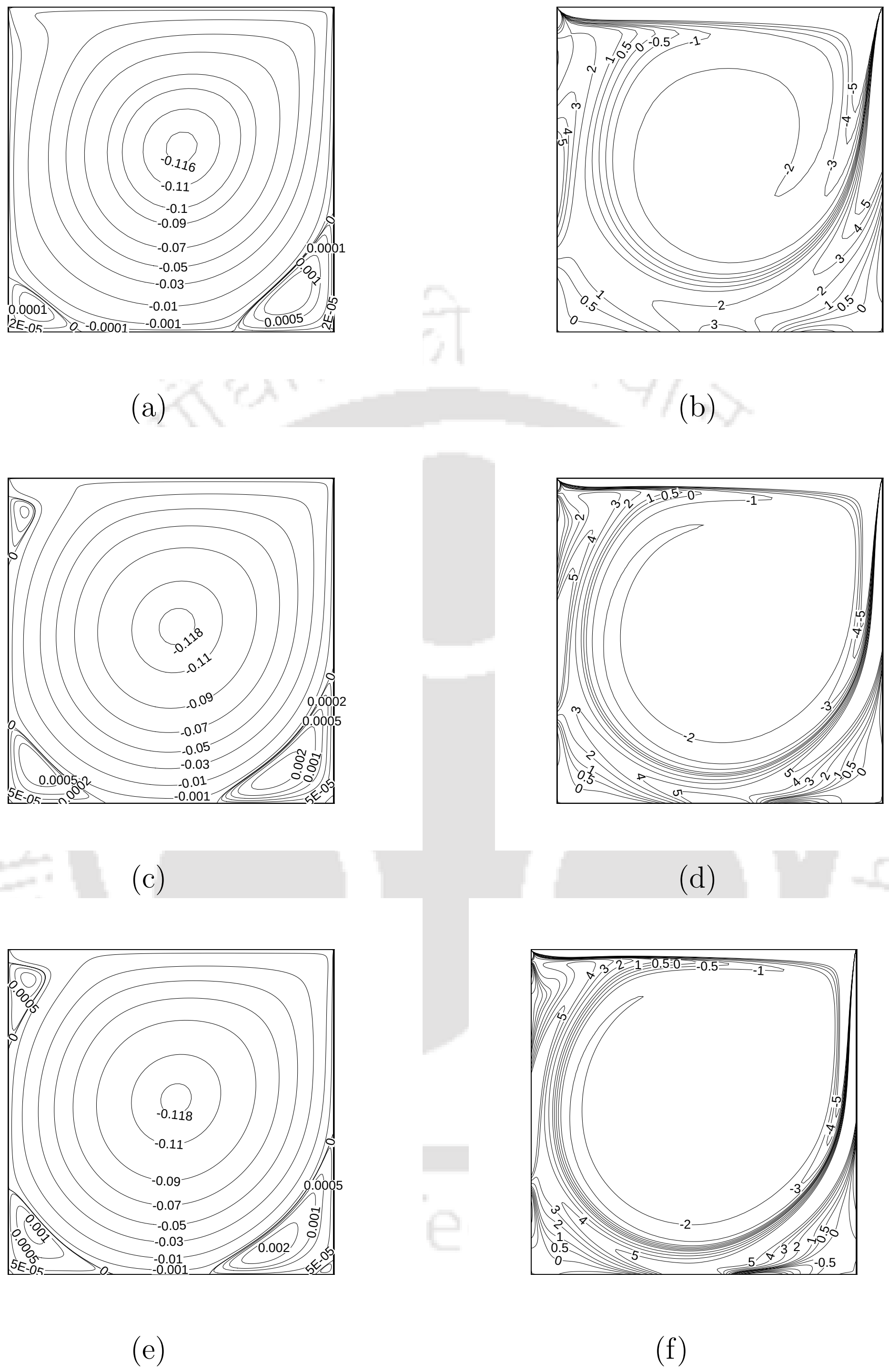

(a) (b)

(c) (d)

(e) (f)

Figure 2.10: *For the lid-driven square cavity flow problem: comparisons of steady-state streamfunction contour: (a) Re* = 1000 *on 61* × *61, (c) Re* = 3200 *on 101* × *101 and (e) Re* = 5000 *on 121* × *121; vorticity contour: (b) Re* = 1000 *on 61* × *61, (d) Re* = 3200 *on 101* × *101 and (f) Re* = 5000 *on 121* × *121.*

Table 2.9: *Convergence data and relaxation parameter for the lid-driven square cavity problem on a 41 × 41 grid in a PC with pentium 4 processor and 512 mB RAM.*

Re	Present		
	CPU(s)	Iterations	Relaxation parameter (inner (ζ), inner (ψ))
100	12.225	225	(0.125, 0.2)
400	26.109	378	(0.1, 0.2)
1000	45.124	481	(0.1, 0.2)
2000	116.167	1361	(0.08, 0.175)

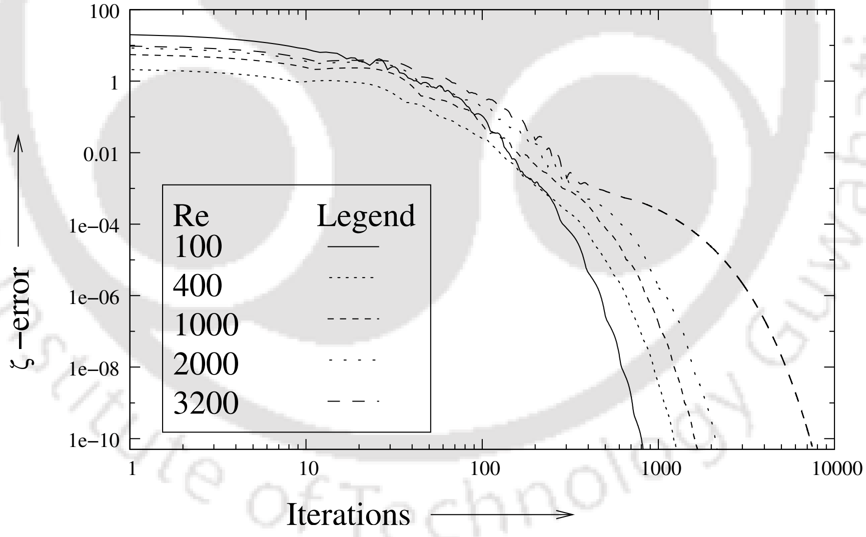

Figure 2.11: *Convergence history of the ζ-error till steady-state for the lid-driven square cavity flow on a 41 × 41 grid on a Pc with pentium 4 processor and 512 mB RAM.*

Results for rectangular cavity (Aspect ratio≠1.0)

In this section, we now present the steady-state solutions produced by the proposed scheme for the rectangular cavity in table 2.10 and figures 2.12-2.16. In table 2.10 we have presented the location of the centers of first and second large vortices and corresponding $\psi_{\min}$ values thereat for different aspect ratios and compared those with the results available in the literature [19,28,53,111]. An excellent agreement has been found. It may be seen from these figures that a series of successive, counter rotating vortices are formed below the moving lid. All the figures (2.12)-(2.15) represent the streamline contours and corresponding vorticity contours. These figures show the effect of Reynolds number on the vortex structure in the cavity.

Table 2.10: *Problem 2: Lid-driven rectangular cavity flow problem: strength and location of the center of first and second large vortices.*

Aspect ratio	Re	Ref.	First large vortex			Second large vortex		
			$\psi_{\min}$	x	y	$\psi_{\min}$	x	y
0.5	100	[28]	-0.0747	0.6642	0.3275	-	-	-
	41 × 21	Present	-0.0746	0.6561	0.3281	-	-	-
	400 61 × 31	Present	-0.0810	0.7043	0.3027	-	-	-
	1000	[28]	-0.0782	0.7010	0.2799	0.0043	0.1868	0.2391
	61 × 31	Present	-0.0788	0.7043	0.2766	0.0041	0.1899	0.2234
1.5	50	[111]	-0.0912	0.5781	1.2578	-	-	-
	41 × 61	Present	-0.1019	0.5795	1.2682	-	-	-
	400	[111]	-0.1084	0.5625	1.1172	6.41e-3	0.4453	0.3906
	41 × 61	Present	-0.1137	0.5399	1.1241	7.57e-3	0.4205	0.4091
	1000	[111]	-0.1134	0.5352	1.0820	1.09e-2	0.3007	0.4179
	81 × 121	Present	-0.1144	0.5399	1.0851	7.74e-3	0.3439	0.3950
2	100	[19]	-0.1033	0.6172	1.7344	7.83e-4	0.5391	0.5859
		[53]	-0.1031	0.6125	1.7375	5.23e-4	0.5625	0.6000
	41 × 81	Present	-0.1041	0.6184	1.7386	8.1e-4	0.5399	0.5798
	400	[19]	-0.1124	0.5547	1.5938	9.09e-3	0.4297	0.8125
		[53]	-0.1131	0.5500	1.6125	8.02e-3	0.4375	0.8625
	41 × 81	Present	-0.1132	0.5399	1.6107	8.97e-3	0.4205	0.8410
	1000	[19]	-0.1169	0.5273	1.5625	0.0148	0.3516	0.7891
		[53]	-0.1182	0.5250	1.5875	0.0125	0.3250	0.8750
	61 × 121	Present	-0.1180	0.5266	1.5816	0.0133	0.3439	0.8410

In figure 2.12 we have presented results for aspect ratio 0.5. It is seen that for $Re = 0.01$ the flow in the cavity is characterized by a symmetric pattern of the vortex structure, which consists of one large vortex (first primary vortex) and a pair of bottom corner vortices (secondary vortices). The corner vortices are the primary vortices from the Moffatt [101] sequence. It is experimented that this symmetric flow pattern almost remains unchanged till to $Re < 1$. With the increase in Re, the center of the large vortex moves from the vertical centerline of the cavity, and the symmetric flow pattern is perturbed due to the inertia force effect. When $Re > 50$, the size of the left bottom corner vortex increases remarkably with increasing Re and ultimately forms a secondary large vortex with a new vortex at the left bottom corner. The new vortex is the secondary vortex from the Moffatt sequence.

In figure 2.13 we have presented the results for $Re = 1000$ with aspect ratios

$0.6 \le \mathrm{K} < 1$. It shows the changes of size of the secondary large vortex at the left corner and the development of the right bottom secondary corner vortex. With the increase in aspect ratio, it is seen that the size of the second large vortex as well as the left corner secondary vortex decreases and the size of the bottom right corner vortex increases. For an aspect ratio K≈0.85 (figure is not shown) a symmetry in size in the two bottom corners appears.

Figure 2.14 shows the evolution of vortex structures with aspect ratios $1.1 \le$ K≤ 1.25. When K$= 1.1$, due to the inertia effect, the size of the bottom right corner vortex is larger than that of left corner vortex. As K increases, the attachment point of the left secondary vortex and separation point of the right secondary vortex on the bottom wall approach each other and meet together to form a stagnation point. From numerical experiments it is seen that the stagnation point is not at the center of the bottom wall. It is also noticed that the merging process of the centers of the two bottom corner vortices is completed for K=1.25 and forms a second large vortex. It may be mentioned here that the development of the second large vortex (second primary vortex) is a function of aspect ratio (K). Further, increase in K shows the gradual development of a pair of new bottom corner vortices. It is noticed that the maximum size of the first large vortex decreases with the increase in aspect ratio.

Figure 2.15 shows the constant streamfunction and corresponding vorticity contours for different Res with aspect ratio K$= 2.0$. It reveals that though the center of the first large vortex is offset towards the top right corner for $Re = 100$, with increasing Re, it moves downwards, while the center of the second large vortex shifts from right to left. Again, as Re increases the size of the first large vortex decreases and the second large vortex increases. It is also seen that with the increase in Re, the size of the bottom left secondary vortex increases compared to bottom right secondary vortex. From vorticity contours the change of vortex line patterns are evident. With the increase in Re a vortex core is developed in the upper half of the cavity indicating the viscous effects are confined to the thin boundary layers close to the walls.

Figure 2.16 shows the evolution of vortex structures for low Re ($Re = 0.01$). As K increases, the separation point of the left bottom corner vortex and the attachment point of the right bottom corner vortex on the bottom wall approach each other. They meet at above the center position of the bottom wall, while the primary large vortex reaches its vertical length approximately 1.63 [111] (measured from the top moving wall to the lowest point on the separation line with respect to bottom wall in figure for aspect ratio 1.65). Finally, when the aspect ratio attained a certain critical value, the bottom two corner vortices coalesce and forms a second primary eddy. Such a critical aspect ratio was found to be in the range 1.75 <K< 1.80.

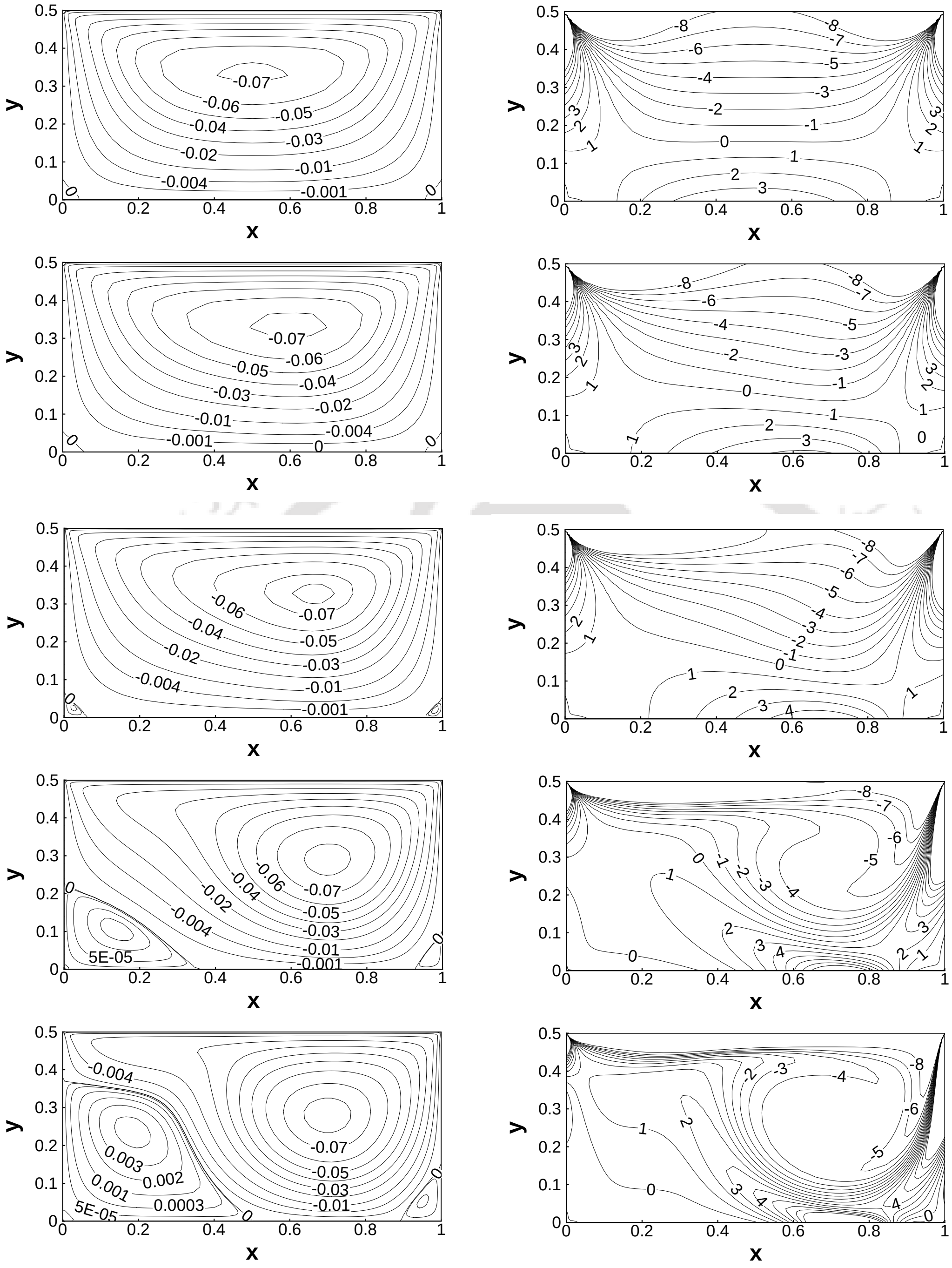

Figure 2.12: *For rectangular lid driven cavity flow: Streamline contours and corresponding vorticity contours for aspect ratio 0.5, and Re=0.01, 50, 100, 400 and 1000 with λ=0.6.*

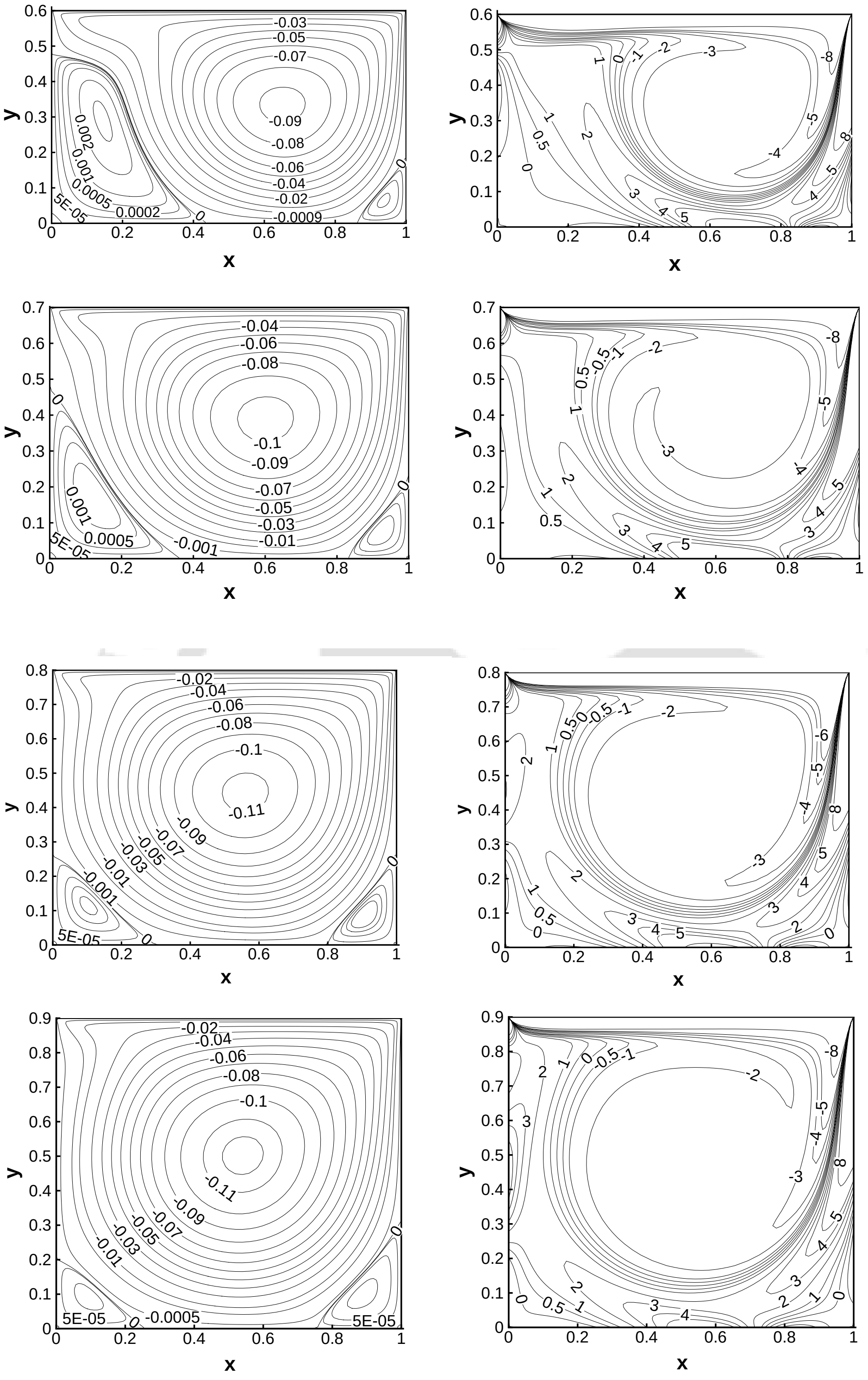

Figure 2.13: *For rectangular lid driven cavity flow: Streamline contours and corresponding vorticity contours for different aspect ratios 0.6, 0.7, 0.8 and 0.9 with Re=1000, and λ=0.6.*

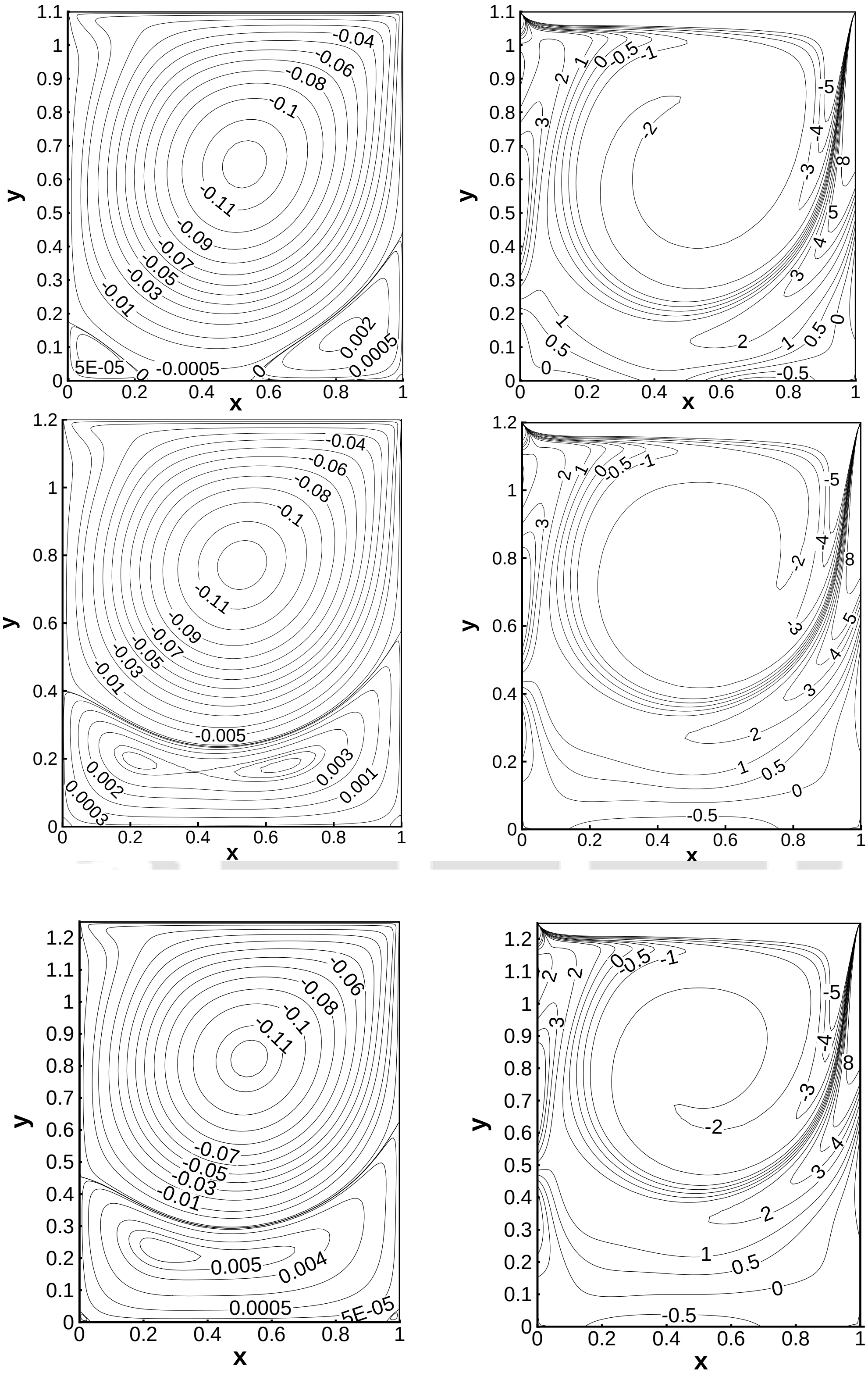

Figure 2.14: *For rectangular lid driven cavity flow: Streamline contours and corresponding vorticity contours for different aspect ratios 1.1, 1.2 and 1.25 with Re=1000, and λ=0.6.*

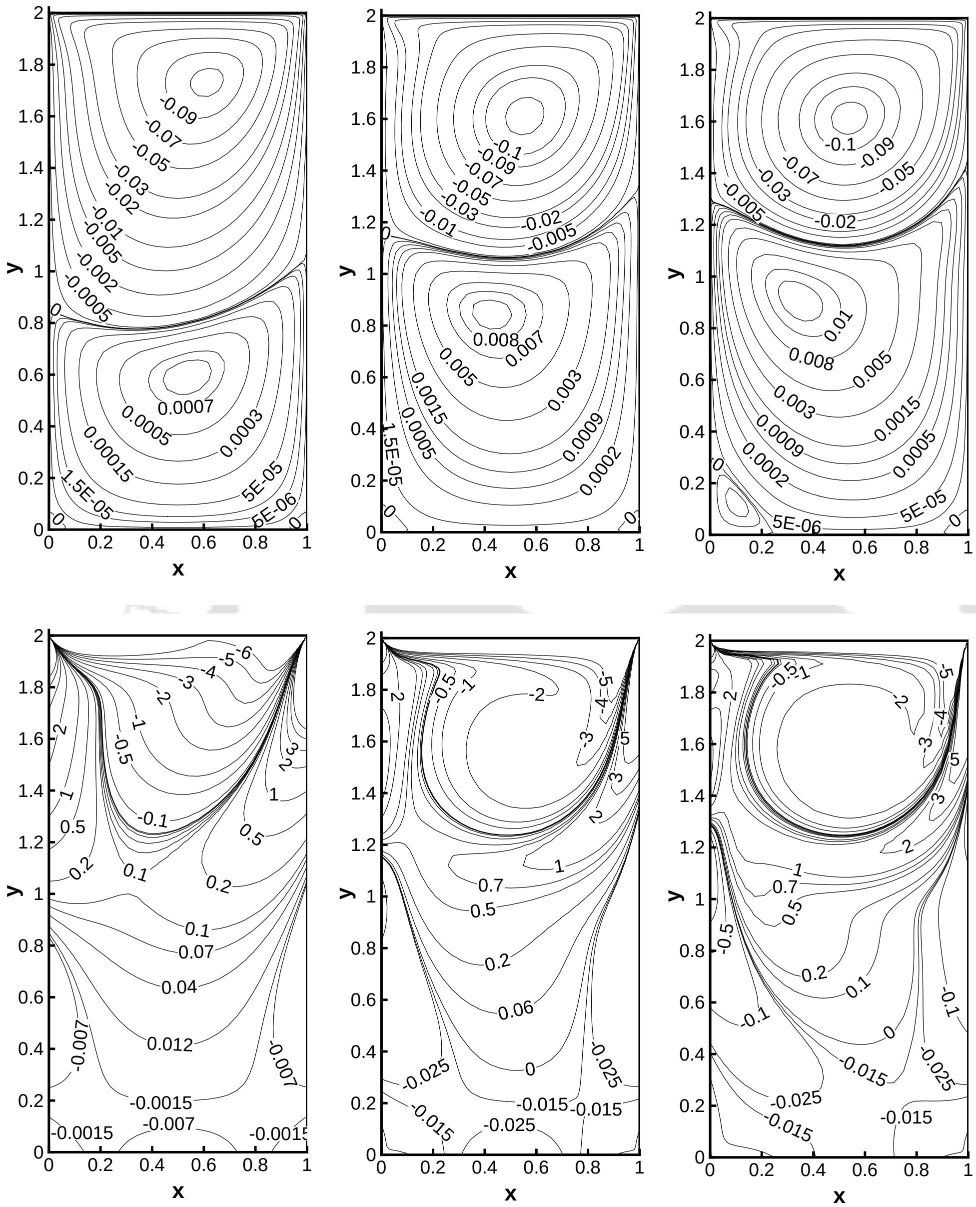

Figure 2.15: *For rectangular lid driven cavity flow: Streamline contours and corresponding vorticity contours for aspect ratio 2.0 with different Re=100, 400 and 1000, and λ=0.6.*

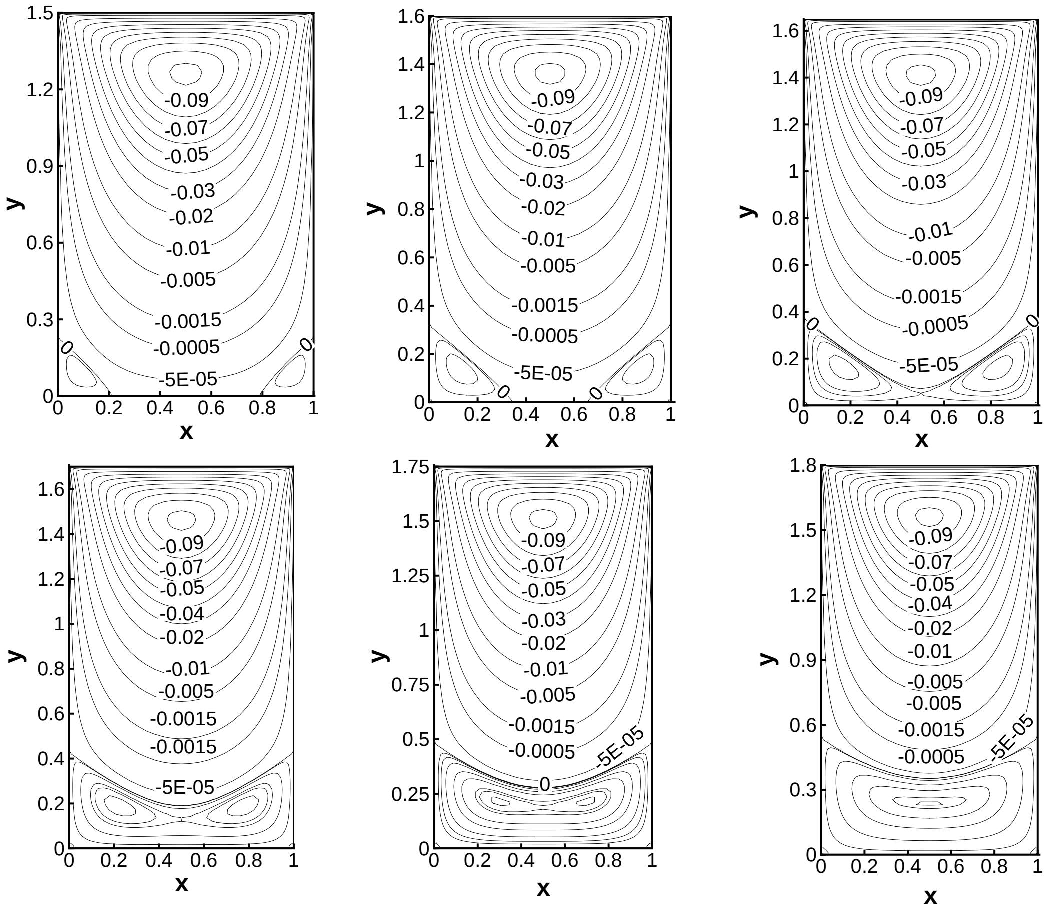

Figure 2.16: *For rectangular lid driven cavity flow: Streamline contours for Re* = 0.01 *with aspect ratio 1.5, 1.6, 1.65, 1.7, 1.75 and 1.8, and* λ*=0.6.*

2.5 Conclusions

In this work, we introduce a new HOC formulation for solving incompressible viscous flow problems governed by the N-S equations on nonuniform grids. The scheme is fourth order accurate in space. Both Dirichlet and Neumann boundary conditions can easily be incorporated into the scheme. To bring out different aspects of the scheme, we employed it to compute the steady-state solutions of a linear convection-diffusion problem, a problem governed by N-S equations with a constructed analytical solution and the 2D lid-driven cavity flow problem. We provided ample numerical evidence to prove its superiority over other established results. The robustness of the scheme is illustrated by its applicability to problems of varying physical complexities, represented among others, by Reynolds numbers ranging from 0.01 to 5000 in the cavity problem. We found that the accuracy of the numerical solutions depend not only on the order of accuracy of the scheme, but also on a number of other factors such as different stretching parameter values, the tolerance of the iterative procedure, etc. The results obtained in all the test cases on relatively coarser grids are in excellent agreement with the analytical as well as established numerical results as the grid is nonuniform, underlining the high accuracy of the scheme. The scheme has the added advantage of being used in non-rectangular physical domains such as constricted tube which is presented in chapter 7. Thus, it has very good potential for efficient application to many problems of incompressible viscous flows on complex geometries. In the next chapter, we will present the extension of the proposed HOC scheme to transient N-S equations.

Chapter 3

A transient higher order compact scheme on nonuniform grids

In this chapter, an extension of the proposed HOC scheme in the previous chapter for steady flow to a transient one has been made. It describes the formulation of a class of transient high order compact (HOC) finite difference schemes for solving the two-dimensional (2D) unsteady Navier-Stokes (N-S) equations on irregular geometries [1]. Apart from including the good features of HOC schemes, the formulation has the added advantage of capturing transient viscous flows involving free and wall bounded shear layers which invariably contain spatial scale variation. However, the power of the scheme is better realized when it is used to solve three pertinent fluid flow problems, namely, the flow in (1) a symmetric channel with both forward and a backward constriction, (2) an asymmetric constricted channel with different aspect ratios and (3) a lateral and symmetric dilated channel.

3.1 Introduction

The governing equations representing the 2D unsteady incompressible viscous flow of a fluid are the N-S equations which, in non-dimensional primitive variables formulation can be written as

$$\frac{\partial u}{\partial x} + \frac{\partial v}{\partial y} = 0, \tag{3.1}$$

$$\frac{\partial u}{\partial t} + u\frac{\partial u}{\partial x} + v\frac{\partial u}{\partial y} = -\frac{\partial p}{\partial x} + \frac{1}{Re}\nabla^2 u, \tag{3.2}$$

$$\frac{\partial v}{\partial t} + u\frac{\partial v}{\partial x} + v\frac{\partial v}{\partial y} = -\frac{\partial p}{\partial y} + \frac{1}{Re}\nabla^2 v, \tag{3.3}$$

---

[1] This study has been published in *Journal of Computational Physics* [110]

where Re is the Reynolds number, p is the pressure and u, v are the velocity components along x- and y-directions respectively. The streamfunction $\psi(x, y, t)$ and the vorticity $\zeta(x, y, t)$ can be defined as

$$u = \frac{\partial \psi}{\partial y}, \qquad v = -\frac{\partial \psi}{\partial x}, \tag{3.4}$$

and

$$\zeta = \frac{\partial v}{\partial x} - \frac{\partial u}{\partial y}. \tag{3.5}$$

With these, the streamfunction-vorticity (ψ-ζ) form of the N-S equations (3.1)-(3.3) can be written as

$$-\frac{\partial^2 \psi}{\partial x^2} - \frac{\partial^2 \psi}{\partial y^2} = \zeta, \tag{3.6}$$

$$Re\frac{\partial \zeta}{\partial t} - \frac{\partial^2 \zeta}{\partial x^2} - \frac{\partial^2 \zeta}{\partial y^2} + uRe\frac{\partial \zeta}{\partial x} + vRe\frac{\partial \zeta}{\partial y} = 0. \tag{3.7}$$

The past few decades have seen the development of many numerical schemes [10, 14, 19, 20, 27, 45, 52, 65–67, 69, 72, 78, 81, 82, 84, 93–95, 120, 129, 139, 148] to solve the N-S equations both in the primitive variables ((3.1)-(3.3)) as well as ψ-ζ ((3.6), (3.7)) formulations. Of late, HOC finite difference schemes [51, 52, 64–66, 81, 84, 85, 92, 93, 129] for the computation of incompressible viscous flows are gaining popularity because of their advantages associated with high order accuracy coupled with compact difference stencils. However, most of these HOC approaches are confined to steady flow calculations [52, 81, 84, 92, 93] mostly on uniform space grids. As such these schemes could not fully exploit the advantages associated with nonuniform space grids, particularly that of mesh grading to resolve smaller scales in the regions of large gradients in the physical domain. Recently, Spotz and Carey [128], Zhang *et al.* [45], and, Kalita *et al.* [66] have developed some HOC schemes on nonuniform grids for the 2D convection-diffusion equations. Of these, the application of first two were limited to only linear problems whereas the last one, which used no transformation from the physical to the computational plane, could accurately capture steady incompressible viscous flows governed by N-S equations. Also, whenever there have been attempts to develop HOC schemes for the transient flows, these are confined invariably to uniform space grids [10, 46, 65, 85].

In this chapter we propose an HOC scheme for the transient, spatially second order quasi-linear partial differential equation without the mixed derivative term. Like its steady-state counterpart the scheme which can be applied to both convection-diffusion and reaction-diffusion equations, can also be easily accommodated into solving equations of the N-S type with slight adjustment of the convection coefficients. It may be noted that application of all the schemes mentioned in the previous paragraph was almost confined only to rectangular physical domains. The proposed scheme works equally efficiently on problems described on both rectangular as well as other curvilinear coordinate settings. It is implicit, second order accurate in time and fourth order accurate in space. It handles both Dirichlet and Neumann boundary conditions with ease. To validate the scheme, it is first applied to the problem of flow decayed by viscosity having analytical solutions and, then to the classical lid-driven cavity problem. We compare our numerical results with both analytical and established numerical results, and excellent match is obtained in all the cases.

3.2 Basic formulations and Discretization Procedure

All the equations (3.1)-(3.3) and (3.6), (3.7) can be put under the same umbrella of the two dimensional time dependent second degree equation

$$\begin{aligned} l\frac{\partial\phi}{\partial t}+\alpha(x,y,t)\frac{\partial^2\phi}{\partial x^2}+\beta(x,y,t)\frac{\partial^2\phi}{\partial y^2} &+ \gamma(x,y,t)\frac{\partial\phi}{\partial x}+\nu(x,y,t)\frac{\partial\phi}{\partial y}\\ &+ \omega(x,y,t)\phi=\theta(x,y,t), \end{aligned} \tag{3.8}$$

where l is constant and θ is the source term.

3.2.1 Transformation of the Governing Equations

We now briefly discuss the transformation

$$x = x(\xi,\eta,t), \qquad y=y(\xi,\eta,t), \tag{3.9}$$

from the physical x-y plane to the computational ξ-η plane which is used to convert a complicated grid into a simple, uniform cartesian grid. Under this transformation, equation (3.8) in the physical plane becomes

$$l\frac{\partial\widehat{\phi}}{\partial t}+a\frac{\partial^2\widehat{\phi}}{\partial\xi^2}+g\frac{\partial^2\widehat{\phi}}{\partial\xi\partial\eta}+b\frac{\partial^2\widehat{\phi}}{\partial\eta^2}+c\frac{\partial\widehat{\phi}}{\partial\xi}+d\frac{\partial\widehat{\phi}}{\partial\eta}+p\widehat{\phi}=f, \tag{3.10}$$

in the computational plane where

$$\begin{aligned} a(\xi,\eta,t) &= \frac{1}{J^2}\left(\widehat{b_1}x_\eta^2+\widehat{a_1}y_\eta^2\right), \qquad b(\xi,\eta,t)=\frac{1}{J^2}\left(\widehat{b_1}x_\xi^2+\widehat{a_1}y_\xi^2\right),\\ c(\xi,\eta,t) &= \frac{\widehat{c_1}}{J}y_\eta-\frac{\widehat{d_1}}{J}x_\eta+R, \qquad d(\xi,\eta,t)=-\frac{\widehat{c_1}}{J}y_\xi+\frac{\widehat{d_1}}{J}x_\xi+S,\\ g(\xi,\eta,t) &= \frac{-2}{J^2}\left(\widehat{a_1}y_\eta y_\xi+\widehat{b_1}x_\eta x_\xi\right), \qquad p(\xi,\eta,t)=\widehat{p_1}(\xi,\eta,t),\\ f(\xi,\eta,t) &= \widehat{f_1}(\xi,\eta,t), \end{aligned} \tag{3.11}$$

with

$$\begin{aligned} \alpha(x,y,t) &= \widehat{a}_1(\xi,\eta,t), \qquad \beta(x,y,t) = \widehat{b}_1(\xi,\eta,t),\\ \gamma(x,y,t) &= \widehat{c}_1(\xi,\eta,t), \qquad \nu(x,y,t) = \widehat{d}_1(\xi,\eta,t),\\ \omega(x,y,t) &= \widehat{p}_1(\xi,\eta,t), \qquad \theta(x,y,t) = \widehat{f}_1(\xi,\eta,t), \end{aligned}$$

and the expressions for J, R, S are same as in section 2.2.1.

3.2.2 Discretization in the transformed plane

Assuming the transformed domain to be rectangular and constructing on it a uniform rectangular mesh of steps h and k in the ξ- and η-directions respectively, the standard central difference approximation to equation (3.10) at the (i,j)-th node (the stencil is similar to the one at the n or $(n+1)$-th time level shown in figure 3.1) is given by

$$\begin{aligned} l\delta_t^+\widehat{\phi}|_{i,j}^n + a_{i,j}\delta_\xi^2\widehat{\phi}_{i,j}^n &+ g_{i,j}\delta_\xi\delta_\eta\widehat{\phi}_{i,j}^n + b_{i,j}\delta_\eta^2\widehat{\phi}_{i,j}^n + c_{i,j}\delta_\xi\widehat{\phi}_{i,j}^n + d_{i,j}\delta_\eta\widehat{\phi}_{i,j}^n\\ &+ p_{i,j}\widehat{\phi}_{i,j}^n - T_{i,j}^n = f_{i,j}^n, \end{aligned} \tag{3.12}$$

where $\widehat{\phi}_{i,j}$ denotes $\widehat{\phi}(\xi_i,\eta_j)$; δ_ξ, δ_ξ^2 and δ_η, δ_η^2 are the first and second order central difference operators along ξ- and η-directions respectively, and $\delta_\xi\delta_\eta$ is the mixed second order central difference operator. The truncation error $T_{i,j}^n$ is given by

$$\begin{aligned} T_{i,j}^n = \frac{h^2}{12}\left[a\frac{\partial^4\widehat{\phi}}{\partial\xi^4} + 2g\frac{\partial^4\widehat{\phi}}{\partial\xi^3\partial\eta} + 2c\frac{\partial^3\widehat{\phi}}{\partial\xi^3}\right]_{i,j}^n &+ \frac{k^2}{12}\left[b\frac{\partial^4\widehat{\phi}}{\partial\eta^4} + 2g\frac{\partial^4\widehat{\phi}}{\partial\xi\partial\eta^3} + 2d\frac{\partial^3\widehat{\phi}}{\partial\eta^3}\right]_{i,j}^n\\ &+ O(\Delta t, h^4, k^4). \end{aligned} \tag{3.13}$$

To obtain a fourth order spatial compact formulation for (3.12), each of the derivatives of the leading terms of (3.13) are compactly approximated [93] to $O(\Delta t, h^2, k^2)$. In order to accomplish this, the original PDE of equation (3.10) is treated as an auxiliary relation that can be differentiated to obtain expressions for higher derivatives. For example, successive differentiation of (3.10) w.r.t ξ yields

$$\begin{aligned} \frac{\partial^3\widehat{\phi}}{\partial\xi^3} = \frac{1}{a}\Bigg[\frac{\partial f}{\partial\xi} &- \left(\frac{\partial a}{\partial\xi} + c\right)\frac{\partial^2\widehat{\phi}}{\partial\xi^2} - \left(\frac{\partial g}{\partial\xi} + d\right)\frac{\partial^2\widehat{\phi}}{\partial\xi\partial\eta} - g\frac{\partial^3\widehat{\phi}}{\partial\xi^2\partial\eta} - \frac{\partial b}{\partial\xi}\frac{\partial^2\widehat{\phi}}{\partial\eta^2}\\ &- b\frac{\partial^3\widehat{\phi}}{\partial\xi\partial\eta^2} - \frac{\partial c}{\partial\xi}\frac{\partial\widehat{\phi}}{\partial\xi} - \frac{\partial d}{\partial\xi}\frac{\partial\widehat{\phi}}{\partial\eta} - p\frac{\partial\widehat{\phi}}{\partial\xi} - \frac{\partial p}{\partial\xi}\widehat{\phi} - l\frac{\partial\widehat{\phi}_t}{\partial\xi}\Bigg], \end{aligned} \tag{3.14}$$

and

$$
\begin{aligned}
a\frac{\partial^4\widehat{\phi}}{\partial\xi^4} &= \frac{\partial^2 f}{\partial\xi^2} - \left(\frac{\partial^2 a}{\partial\xi^2} + 2\frac{\partial c}{\partial\xi}\right)\frac{\partial^2\widehat{\phi}}{\partial\xi^2} - \left(2\frac{\partial a}{\partial\xi} + c\right)\bigg[\frac{1}{a}\bigg(\frac{\partial f}{\partial\xi} - \left(\frac{\partial a}{\partial\xi} + c\right)\frac{\partial^2\widehat{\phi}}{\partial\xi^2} \\
&- \left(\frac{\partial g}{\partial\xi} + d\right)\frac{\partial^2\widehat{\phi}}{\partial\xi\partial\eta} - g\frac{\partial^3\widehat{\phi}}{\partial\xi^2\partial\eta} - \frac{\partial b}{\partial\xi}\frac{\partial^2\widehat{\phi}}{\partial\eta^2} - b\frac{\partial^3\widehat{\phi}}{\partial\xi\partial\eta^2} - \frac{\partial c}{\partial\xi}\frac{\partial\widehat{\phi}}{\partial\xi} - \frac{\partial d}{\partial\xi}\frac{\partial\widehat{\phi}}{\partial\eta} \\
&- p\frac{\partial\widehat{\phi}}{\partial\xi} - \frac{\partial p}{\partial\xi}\widehat{\phi} - l\frac{\partial\widehat{\phi}_t}{\partial\xi}\bigg] - \left(\frac{\partial^2 g}{\partial\xi^2} + 2\frac{\partial d}{\partial\xi}\right)\frac{\partial^2\widehat{\phi}}{\partial\xi\partial\eta} - \left(2\frac{\partial g}{\partial\xi} + d\right)\frac{\partial^3\widehat{\phi}}{\partial\xi^2\partial\eta} \\
&- g\frac{\partial^4\widehat{\phi}}{\partial\xi^3\partial\eta} - \frac{\partial^2 b}{\partial\xi^2}\frac{\partial^2\widehat{\phi}}{\partial\eta^2} - 2\frac{\partial b}{\partial\xi}\frac{\partial^3\widehat{\phi}}{\partial\xi\partial\eta^2} - b\frac{\partial^4\widehat{\phi}}{\partial\xi^2\partial\eta^2} - \frac{\partial^2 c}{\partial\xi^2}\frac{\partial\widehat{\phi}}{\partial\xi} - \frac{\partial^2 d}{\partial\xi^2}\frac{\partial\widehat{\phi}}{\partial\eta} \\
&- p\frac{\partial^2\widehat{\phi}}{\partial\xi^2} - 2\frac{\partial p}{\partial\xi}\frac{\partial\widehat{\phi}}{\partial\xi} - \frac{\partial^2 p}{\partial\xi^2}\widehat{\phi} - l\frac{\partial^2\widehat{\phi}_t}{\partial\xi^2}. \qquad (3.15)
\end{aligned}
$$

Expressions for $\dfrac{\partial^3\widehat{\phi}}{\partial\eta^3}$ and $b\dfrac{\partial^4\widehat{\phi}}{\partial\eta^4}$ can be found in a similar way. It is seen that the expressions for the fourth order derivatives (for example, see equation (3.15)) contain mixed derivative terms like $\dfrac{\partial^4\widehat{\phi}}{\partial\xi^3\partial\eta}$, $\dfrac{\partial^4\widehat{\phi}}{\partial\xi\partial\eta^3}$ etc. which cannot be approximated compactly on the stencil shown in figure 3.1. As mentioned in chapter 2, this difficulty could be overcome by choosing an orthogonal or conformal mapping. On considering such a grid or transformation, and using central difference for space derivatives

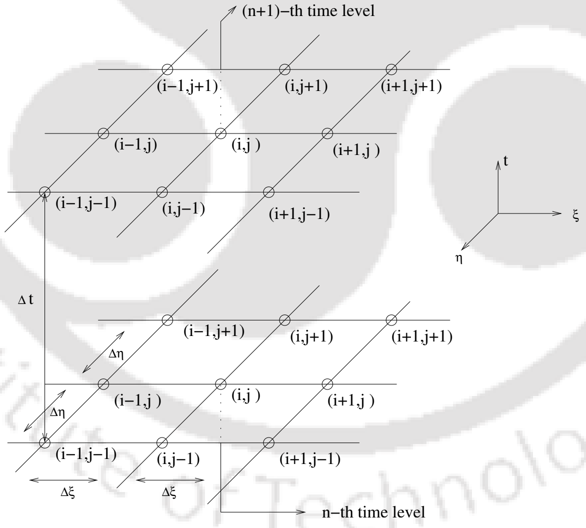

Figure 3.1: *The unsteady HOC computational (9,9) stencil in $\xi\eta t$-space.*

and forward temporal difference with uniform step length Δt, equation (3.12) can be written as

$$
\begin{aligned}
& l\Bigg\{\delta_t^+\widehat{\phi}_{i,j}^n + \overbrace{\frac{h^2}{12}\Big(\delta_\xi^2\delta_t^+\widehat{\phi}_{i,j}^n + c_{i,j}^*\delta_\xi\delta_t^+\widehat{\phi}_{i,j}^n\Big) + \frac{k^2}{12}\Big(\delta_\eta^2\delta_t^+\widehat{\phi}_{i,j}^n + d_{i,j}^*\delta_\eta\delta_t^+\widehat{\phi}_{i,j}^n\Big)}\Bigg\} \\
+ & \ A_{i,j}'\delta_\xi^2\widehat{\phi}_{ij}^n + G_{i,j}'\delta_\xi\delta_\eta\widehat{\phi}_{i,j}^n + B_{i,j}'\delta_\eta^2\widehat{\phi}_{i,j}^n + C_{i,j}'\delta_\xi\widehat{\phi}_{i,j}^n + D_{i,j}'\delta_\eta\widehat{\phi}_{i,j}^n + H_{i,j}'\widehat{\phi}_{i,j}^n \\
+ & \ \frac{1}{12}\Bigg[\Big(k^2a_{i,j} + h^2b_{i,j}\Big)\delta_\xi^2\delta_\eta^2\widehat{\phi}_{i,j}^n + \Big\{h^2d_{i,j} + k^2\Big(2\delta_\eta a_{i,j} + d_{i,j}^*a_{i,j}\Big)\Big\}\delta_\xi^2\delta_\eta\widehat{\phi}_{i,j}^n \\
+ & \ \Big\{k^2c_{i,j} + h^2\Big(2\delta_\xi b_{i,j} + c_{i,j}^*b_{i,j}\Big)\Big\}\delta_\xi\delta_\eta^2\widehat{\phi}_{i,j}^n\Bigg] = F_{i,j}' + O(\Delta t, h^4, k^4), \qquad (3.16)
\end{aligned}
$$

where

$$
\begin{aligned}
c_{i,j}^* &= \frac{c_{i,j} - 2\delta_\xi a_{i,j}}{a_{i,j}}, \\
d_{i,j}^* &= \frac{d_{i,j} - 2\delta_\eta b_{i,j}}{b_{i,j}},
\end{aligned}
$$

with

$$
\begin{aligned}
A_{i,j}' &= a_{i,j} + \frac{h^2}{12}\Bigg[\Big(\delta_\xi^2a_{i,j} + 2\delta_\xi c_{i,j} + p_{i,j}\Big) + c_{i,j}^*\Big(\delta_\xi a_{i,j} + c_{i,j}\Big)\Bigg] \\
&+ \frac{k^2}{12}\Big[d_{i,j}^*\delta_\eta a_{i,j} + \delta_\eta^2a_{i,j}\Big], \\
B_{i,j}' &= b_{i,j} + \frac{h^2}{12}\Big[c_{i,j}^*\delta_\xi b_{i,j} + \delta_\xi^2b_{i,j}\Big] + \frac{k^2}{12}\Bigg[\Big(\delta_\eta^2b_{i,j} + 2\delta_\eta d_{i,j} + p_{i,j}\Big) \\
&+ d_{i,j}^*\Big(\delta_\eta b_{i,j} + d_{i,j}\Big)\Bigg], \\
C_{i,j}' &= c_{i,j} + \frac{h^2}{12}\Big[\delta_\xi^2c_{i,j} + 2\delta_\xi p_{i,j} + c_{i,j}^*\Big(\delta_\xi c_{i,j} + p_{i,j}\Big)\Big] + \frac{k^2}{12}\Big[\delta_\eta^2c_{i,j} + d_{i,j}^*\delta_\eta c_{i,j}\Big], \\
D_{i,j}' &= d_{i,j} + \frac{h^2}{12}\Big[\delta_\xi^2d_{i,j} + c_{i,j}^*\delta_\xi d_{i,j}\Big] + \frac{k^2}{12}\Big[\delta_\eta^2d_{i,j} + 2\delta_\eta p_{i,j} + d_{i,j}^*\Big(\delta_\eta d_{i,j} + p_{i,j}\Big)\Big], \\
G_{i,j}' &= \frac{h^2}{12}\Big[2\delta_\xi d_{i,j} + c_{i,j}^*d_{i,j}\Big] + \frac{k^2}{12}\Big[2\delta_\eta c_{i,j} + d_{i,j}^*c_{i,j}\Big], \\
H_{i,j}' &= p_{i,j} + \frac{h^2}{12}\Big[\delta_\xi^2p_{i,j} + c_{i,j}^*\delta_\xi p_{i,j}\Big] + \frac{k^2}{12}\Big[\delta_\eta^2p_{i,j} + d_{i,j}^*\delta_\eta p_{i,j}\Big], \\
F_{i,j}' &= f_{i,j} + \frac{h^2}{12}\Big[\delta_\xi^2f_{i,j} + c_{i,j}^*\delta_\xi f_{i,j}\Big] + \frac{k^2}{12}\Big[\delta_\eta^2f_{i,j} + d_{i,j}^*\delta_\eta f_{i,j}\Big].
\end{aligned}
$$

We now introduce a weighted average parameter μ through the approximation of the time derivative $\dfrac{\partial\widehat{\phi}}{\partial t}$ such that $t_\mu = (1-\mu)t^{(n)} + \mu t^{(n+1)}$ where $0 \le \mu \le 1$. Varying μ yields different schemes of different time accuracies. With these, equation (3.16) can be put in the form

$$
\begin{aligned}
\sum_{k_1=-1}^{1}\sum_{k_2=-1}^{1} w_{i+k_1,j+k_2}\ \widehat{\phi}^{(n+1)}_{i+k_1,j+k_2} &= \sum_{k_1=-1}^{1}\sum_{k_2=-1}^{1} w'_{i+k_1,j+k_2}\ \widehat{\phi}^{(n)}_{i+k_1,j+k_2} \\
&+ 24\Delta t\left(\mu F^{(n+1)}_{i,j} + (1-\mu)F^{(n)}_{i,j}\right), \qquad (3.17)
\end{aligned}
$$

where
$w_{i+k_1,j+k_2} = \mu\dfrac{\Delta t}{h^2k^2} r_{i+k_1,j+k_2} + q_{i+k_1,j+k_2}$,
and
$w'_{i+k_1,j+k_2} = (\mu-1)\dfrac{\Delta t}{h^2k^2} r_{i+k_1,j+k_2} + q_{i+k_1,j+k_2}$,

with

$$
\begin{array}{rcll}
r_{i-1,j-1} &=& (6hkG'_{i,j} + 2X_{i,j} - kY_{i,j} - hZ_{i,j}), & q_{i-1,j-1} = 0, \\
r_{i,j-1} &=& (24h^2B'_{i,j} - 12h^2kD'_{i,j} - 4X_{i,j} + 2kY_{i,j}), & q_{i,j-1} = l(2 - kd^*_{i,j}), \\
r_{i+1,j-1} &=& (-6hkG'_{i,j} + 2X_{i,j} - kY_{i,j} + hZ_{i,j}), & q_{i+1,j-1} = 0, \\
r_{i-1,j} &=& (24k^2A'_{i,j} - 12hk^2C'_{i,j} - 4X_{i,j} + 2hZ_{i,j}), & q_{i-1,j} = l(2 - hc^*_{i,j}), \\
 & & & \\
r_{i,j} &=& (-48k^2A'_{i,j} - 48h^2B'_{i,j} + 24h^2k^2H'_{i,j} + 8X_{i,j}), & q_{i,j} = 16l, \\
r_{i+1,j} &=& (24k^2A'_{i,j} + 12hk^2C'_{i,j} - 4X_{i,j} - 2hZ_{i,j}), & q_{i+1,j} = l(2 + hc^*_{i,j}), \\
r_{i-1,j+1} &=& (-6hkG'_{i,j} + 2X_{i,j} + kY_{i,j} - hZ_{i,j}), & q_{i-1,j+1} = 0, \\
r_{i,j+1} &=& (24h^2B'_{i,j} + 12h^2kD'_{i,j} - 4X_{i,j} - 2kY_{i,j}), & q_{i,j+1} = l(2 + kd^*_{ij}) \\
r_{i+1,j+1} &=& (6hkG'_{i,j} + 2X_{i,j} + kY_{i,j} + hZ_{i,j}), & q_{i+1,j+1} = 0,
\end{array}
$$

in which

$$
\begin{aligned}
X_{i,j} &= h^2b_{i,j} + k^2a_{i,j}, \\
Y_{i,j} &= h^2d_{i,j} + k^2(2\delta_\eta a_{i,j} + d^*_{i,j}a_{i,j}), \\
Z_{i,j} &= h^2(2\delta_\xi b_{i,j} + c^*_{i,j}b_{i,j}) + k^2c_{i,j}.
\end{aligned}
$$

Thus equation (3.17) becomes the $O((\Delta t)^s, h^4, k^4)$ HOC finite difference approximation for (3.8) on the transformed plane. It should be noted that for $\mu = 0$, the computational stencil requires nine points at the n-th and five points at $(n+1)$-th time level resulting in what may be termed as a (9, 5) scheme. Similarly $\mu = 0.5$ and

$\mu = 1$ yields a (9, 9) and a (5, 9) scheme respectively. It is worthwhile mentioning that these schemes are implicit due to the terms under the brace in equation (3.16). The temporal order of accuracy s is two for the (9, 9) scheme and one for the other two. Throughout our computations, we have used the (9, 9) scheme (see the corresponding stencil on figure 3.1). As the scheme is implicit and some stability analysis of this kind of scheme has been already done in [65], so a separate analysis has not been made in this study. It is worth mentioning that our scheme is unconditionally stable.

NOTE: If the grid is non orthogonal, the magnitude of the coefficients of mixed derivatives relative to the coefficients of the diagonal derivatives depend on the angles between the grid lines and on the grid aspect ratio. When the angle between grid lines is small and the aspect ratio large, the coefficients of mixed derivative (off-diagonal terms) may be larger than the coefficients of the derivative with respect to single variable (diagonal terms). This can lead to numerical problems (poor convergence, oscillations in the solution etc.). If the nonorthogonality and aspect ratio make the coefficients of the mixed derivatives much smaller compared to those of the diagonal derivatives, the effect of mixed derivative terms become negligible. Hence those terms can be ignored [41].

3.3 Solution of algebraic systems

Equation (3.17) can now be evaluated in terms of system of equations which can be written in a matrix form as follows:

$$A\Phi^{n+1} = f(\Phi^n), \tag{3.18}$$

where A is a nine diagonal asymmetric sparse matrix. The solution procedure is similar to the one discussed for the steady-state case in section 2.3 except the convergence criteria. Here we have defined the steady-state solutions through time marching process. The convergence criteria for time marching steady-state solutions is, for all the grid points,

$$\max|\Phi^{n+1} - \Phi^n| < Tol, \tag{3.19}$$

where Φ^{n+1} and Φ^n stand for solution at $(n+1)$-th and n-th time step respectively, and Tol is the limit for convergence. We consider the outer iteration cycle at every time step. In an outer cycle, we solve first the transformation of (3.7) using (3.17). Here, one more additional coefficient in comparison with vorticity equation in steady formulation ($l = Re$ due to unsteady term $\dfrac{\partial \zeta}{\partial t}$) has been accommodated, Then we solve the transformation of (3.6) using its steady-state form.

3.4 Numerical Test cases

The test cases chosen for the proposed extension are (i) the flow decayed by viscosity and (ii) the lid-driven cavity flow problem. Problem (i) has analytical solutions, so Dirichlet boundary conditions are used for it while for the problem (ii), both Dirichlet and Neumann boundary conditions are applied. For the first problem, we use exact initial data and for the second one, where steady-state is arrived at in a time marching fashion, zero initial data was used in all the computations.

3.4.1 Test case 1:

Firstly we consider the problem of flow decayed by viscosity [30,64,139,154] governed by equations (3.1)-(3.3) in the square $0 \leq x, y \leq \pi$ with the following initial conditions

$$u(x,y,0) = -\cos(x)\sin(y) \;\text{ and }\; v(x,y,0) = \sin(x)\cos(y). \tag{3.20}$$

The exact solution of this problem is given by

$$u(x,y,t) = -\cos(x)\sin(y)e^{-\frac{2t}{Re}} \;\text{ and }\; v(x,y,t) = \sin(x)\cos(y)e^{-\frac{2t}{Re}}. \tag{3.21}$$

The initial and boundary conditions for the ψ-ζ formulations of these equations can be easily derived from the exact solution.

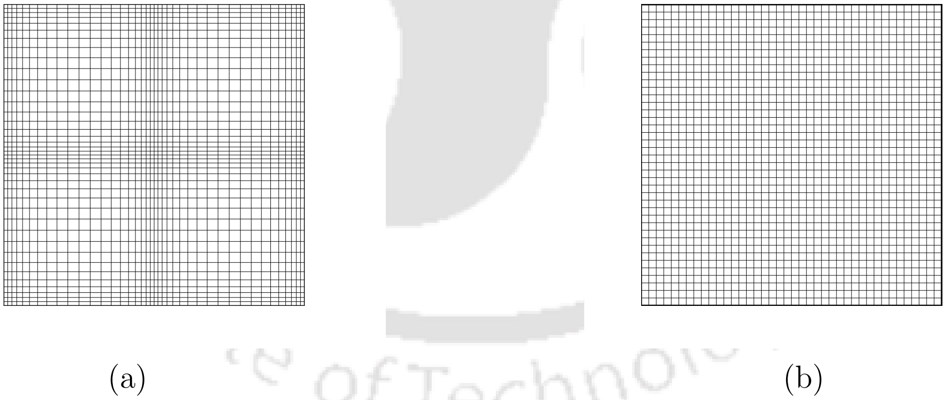
(a) (b)

Figure 3.2: *For problem 1: 41 × 41 grids, (a) physical plane ($\lambda = 0.5$) and (b) computational plane.*

As the flow is characterized by a number of free shear layers, in order to resolve the flow accurately, we have generated the grid in such a way (see figure 3.2) that

Table 3.1: *Grid independence study for problem 1: numerical and exact values of (a)* ψ *and* ζ*, and (b)* u *and* v *at the point* $(\frac{\pi}{4}, \frac{\pi}{10})$ *for different Res at different time stations* $t = 1, 10$ *and grid sizes with* $\Delta t = 0.01$ *and* $\lambda = 0.5$.

(a)

t	Re	Stream-function (ψ)			Exact	Vorticity (ζ)			Exact
		21 × 21	41 × 41	81 × 81		21 × 21	41 × 41	81 × 81	
1.0	100	0.680621	0.679970	0.679934	0.679932	1.361058	1.359910	1.359866	1.359864
	400	0.691508	0.690313	0.690214	0.690208	1.385520	1.380628	1.380417	1.380416
	1000	0.693919	0.692480	0.692296	0.692282	1.394472	1.385375	1.384579	1.384563
10.0	100	0.568445	0.567849	0.567815	0.567813	1.136711	1.135682	1.135630	1.135627
	400	0.660942	0.659928	0.659811	0.659804	1.323536	1.319808	1.319613	1.319608
	1000	0.681361	0.680119	0.679937	0.679918	1.368113	1.360586	1.359864	1.359837

(b)

t	Re	velocity (u)			Exact	velocity (v)			Exact
		21 × 21	41 × 41	81 × 81		21 × 21	41 × 41	81 × 81	
1.0	100	-0.129682	-0.134237	-0.134474	-0.134489	0.682061	0.680064	0.679940	0.679932
	400	-0.128669	-0.135917	-0.136486	-0.136522	0.692395	0.690369	0.690219	0.690208
	1000	-0.127638	-0.135865	-0.136851	-0.136932	0.694413	0.692454	0.692296	0.692282
10.0	100	-0.108007	-0.112084	-0.112299	-0.112312	0.569634	0.567926	0.567820	0.567813
	400	-0.123506	-0.129804	-0.130466	-0.130508	0.661914	0.659969	0.659815	0.659804
	1000	-0.126156	-0.133403	-0.134383	-0.134486	0.682178	0.680092	0.679935	0.679918

maximum number of points gets allocated to those regions. To generate the grid we have used the following stretching functions:

$$x = \xi - \frac{\lambda}{4}\sin(4\xi), \qquad y = \eta - \frac{\lambda}{4}\sin(4\eta).$$

Here, the parameter $\lambda \in [0, 1)$ determines the degree of clustering with greater value of λ indicating more number of grid points at specified locations. The stretching function constructed in the present case generates a centro-symmetric distribution of points with clustering along the centerlines.

We present our results computed on different grid sizes for different Reynolds number in tables 3.1, 3.2 and figure 3.3. In table 3.1(a), we show the values of ψ, ζ for time $t = 1.0$ and 10.0 at the point $\left(\frac{\pi}{4}, \frac{\pi}{10}\right)$, whereas table 3.1(b) shows variation in u and v at same time stations. It is obvious from the table that our numerical results are grid independent and they are in excellent agreement with the analytical ones. In table 3.2, we present the maximum absolute errors of ψ, ζ, u and v for $Re = 100$ on three different grid sizes 21×21, 41×41 and 81×81 at $t = 1.0$ and 10.0. This table clearly demonstrates that with grid refinement, the error decays with $O(h^4)$ as expected.

In figure 3.3(a) and (b), we show the numerical and analytical results using streamlines for $Re = 1000$ on a 81×81 grid and figures 3.3(c) and (d) show the corresponding vorticity contours at time $t = 10.0$ for the same Reynolds number. All these figures indicate a very close match of the numerical solutions with the exact ones including excellent resolution of the shear layers.

Table 3.2: *Problem 1: maximum absolute errors and convergence rates of (a) ψ, (b) ζ, (c) u and (d) v for $Re = 100$ at two time stations $t = 1$ and $t = 10$ ($\Delta t = 0.01$ and $\lambda = 0.5$).*

(a)

t	Grid	ψ	Rate(ψ)
		Max (ψ)	
1.0	21 × 21	1.367266(-3)	
	41 × 41	8.604717(-5)	3.99
	81 × 81	5.222722(-6)	4.04
10.0	21 × 21	1.480007(-3)	
	41 × 41	9.345349(-5)	3.99
	81 × 81	5.646347(-6)	4.05

(b)

t	Grid	ζ	Rate (ζ)
		Max (ζ)	
1.0	21 × 21	9.765736(-3)	
	41 × 41	6.572612(-4)	3.89
	81 × 81	4.070853(-5)	4.01
10.0	21 × 21	1.150130(-2)	
	41 × 41	8.085744(-4)	3.83
	81 × 81	4.990446(-5)	4.02

(c)

t	Grid	u	Rate (u)
		Max (u)	
1.0	21 × 21	2.185866(-2)	
	41 × 41	1.890278(-3)	3.53
	81 × 81	1.328059(-4)	3.83
10.0	21 × 21	1.871943(-2)	
	41 × 41	1.596069(-3)	3.55
	81 × 81	1.114534(-4)	3.84

(d)

t	Grid	v	Rate (v)
		Max (v)	
1.0	21 × 21	2.166603(-2)	
	41 × 41	1.877177(-3)	3.53
	81 × 81	1.323446(-4)	3.83
10.0	21 × 21	1.812902(-2)	
	41 × 41	1.569013(-3)	3.53
	81 × 81	1.105766(-4)	3.83

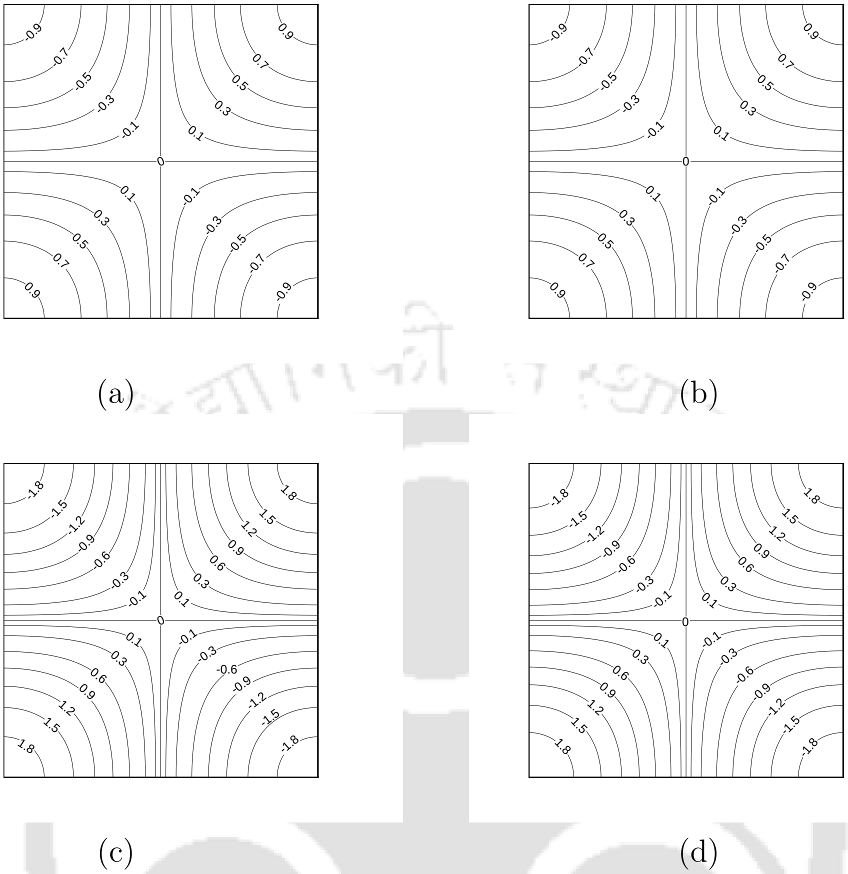

(a) (b)

(c) (d)

Figure 3.3: *For problem 1, at t=10, Re=1000, ($\Delta t = 0.01$, $\lambda = 0.5$), on grid size 81 × 81: streamlines (a) exact and (b) numerical, and vorticity contours (c) exact and (d) numerical.*

3.4.2 Test case 2: The lid-driven cavity problem

Next we consider the classical 2D lid-driven cavity problem. The basic problem is same as discussed in section 2.4.3. It is worthwhile mentioning that there is a limited literature concerning the evolution of vortex structures and the related issues in a lid-driven cavity [19,31,54,111,122]. Shankar [122] analyzed the Stokes flow in a deep cavity and found that the primary eddy structure is related to the corner eddy. Most of the facts that happen in cavity flow can be found in [122]. He concluded that very little work has been done on flow in a deep cavity for higher *Re*s. Miller [97] studied shallow cavity (aspect ratio<1) flow and observed that the nature of the boundary conditions affect the predicted vortex structures.

In this section, we have produced and discussed both the steady-state and transient results for different aspect ratios ($K = \frac{D_1}{D_2}$, where D_1 and D_2 are the depth and width of the cavity) in a time marching fashion. The boundary conditions for vorticity have been treated in the same way as in section 2.4.3 for the problem of lid-driven cavity. Here it is noted that the final form of the vorticity boundary conditions become time dependent as the flow variables (ψ, ζ, u, v) in this study are time dependent. In an outer temporal cycle, the convergence criteria of the solution of $\Phi(\psi, \zeta)$ is, for all the grid points,

$$\max |\Phi^{n+1} - \Phi^n| < 0.5 \times 10^{-6}, \tag{3.22}$$

where Φ^{n+1} and Φ^n stand for the solution at two consecutive time levels. The nonuniform grid is generated as in chapter 2 for lid-driven cavity problem. We have considered the same optimal λ (degree of clustering, $\lambda = 0.6$) for all the calculations as discussed in section 2.3.4. It can be seen an excellent agreement through the comparison of our steady-state results obtained in a time marching manner to the steady-state results presented in chapter 2 for the same problem.

Here, we have presented extensively the evolution of vortex structures in a cavity with different aspect ratios. It shows clearly how the large vortex structures (other than first primary vortex) are generated from the corner vortices in the intermediate steps.

Results for lid-driven square cavity problem (Aspect ratio=1.0)

We now present the time-marching steady-state and the transient solutions produced by the proposed scheme for this problem in tables 3.3-3.6 and figures 3.4-3.8.

In table 3.3, we present grid independence results obtained in time marching steady-state manner for flow variables u, v, ψ and ζ for $Re = 100$ and 1000, and compare them with the numerical data available in the literature [18, 46, 92]. Table 3.4 and 3.5 show the comparison with the calculated primary, secondary and tertiary vortex data for different Res ($100 \leq Re \leq 5000$) with the numerical results available in the literature [20, 46, 57, 72]. An excellent agreement is found.

Figure 3.4 shows the wall vorticity values for different Res ($100 \leq Re \leq 5000$) on different sizes of grid. It reveals that the use of a coarser grid is sufficient to capture the flow phenomena accurately if the grid is nonuniform and thereby confirms that our formulation on nonuniform grids yield quantitatively accurate solutions.

In table 3.6, we present the convergence data (and CPU time) on a 61× 61 grid till steady-state where steady-state was assumed to reach when

Table 3.3: *Lid-driven square cavity flow problem: grid independence study of the steady-state data at the center of the cavity.*

Re	Present					Reference			
	Grid	Velocity		ψ	ζ	Grid	Velocity		ζ
		u	v				u	v	
100	21 × 21	-0.20424	0.05489	-0.06468	-1.12383	129 [46]	-0.20581 [46]	0.05454 [46]	-
	31 × 31	-0.20690	0.05636	-0.06566	-1.15113	-	-	-	-
	41 × 41	-0.20785	0.05688	-0.06600	-1.16012	-	-	-	-
	61 × 61	-0.20851	0.05729	-0.06619	-1.16404	-	-	-	-
	81 × 81	-0.20882	0.05738	-0.06641	-1.17101	89 [92]	-	-	-1.17442 [92]
1000	41 × 41	-0.07180	0.02810	-0.10858	-2.01270	-	-	-	-
	61 × 61	-0.06469	0.02638	-0.11463	-2.05634	-	-	-	-
	81 × 81	-0.06304	0.02600	-0.11585	-2.06441	-	-	-	-
	101 × 101	-0.06253	0.02587	-0.11622	-2.06661	160 [18]	-0.06206 [18]	0.02578 [18]	-2.06722 [18]
	121 × 121	-0.06189	0.02582	-0.11587	-2.05344	-	-	-	-

Table 3.4: *Lid-driven square cavity flow problem: steady-state primary vortex data for* $100 \leq Re \leq 5000$.

Re	variables	Ghia et al. [46], (1982)	Kim and Moin [72], (1985)	Bruneau and Saad [20], (2005)	Present($\lambda = 0.6$)
100	ψ_{min}	-0.103	-0.103		-0.103
	$\zeta_{v,c}$	-3.166	-3.177	-	-3.1397
	x,y	(0.6172, 0.7344)	-	-	(0.6183, 0.7273)
	grid	129 × 129	65 × 65	-	41 × 41
400	ψ_{min}	-0.114	-0.112	-	-0.1135
	$\zeta_{v,c}$	-2.295	-2.260	-	-2.2920
	x,y	(0.5547, 0.6055)	-	-	(0.5532, 0.6055)
	grid	257 × 257	65 × 65	-	61 × 61
1000	ψ_{min}	-0.118	-0.116	-0.1189	-0.1183
	$\zeta_{v,c}$	-2.050	-2.026	-2.0674	-2.0659
	x,y	(0.5313, 0.5625)	-	(0.5313, 0.5654)	(0.5399, 0.5598)
	grid	129 × 129	97 × 97	1024 × 1024	81 × 81
2000	ψ_{min}	-	-	-	-0.1182
		-	-	-	(-0.120) [57]
	$\zeta_{v,c}$	-	-	-	-1.9453
	x,y	-	-	-	(0.5200, 0.5598)
	grid	-	-	-	81 × 81
3200	ψ_{min}	-0.120	-0.115	-	-0.1193
	$\zeta_{v,c}$	-1.989	-1.901	-	-1.9399
	x,y	(0.5165, 0.5469)	-	-	(0.5160, 0.5479)
	grid	129 × 129	97 × 97	-	101 × 101
5000	ψ_{min}	-0.119	-0.112	-0.1219	-0.1204
	$\zeta_{v,c}$	-1.860	-1.812	-1.9322	-1.9708
	x,y	(0.5117 ,0.5352)		(0.5147, 0.5352)	(0.5133,0.5399)
	grid	257 × 257	97 × 97	1024 × 1024	121 × 121

$$\max|\zeta^{(n+1)} - \zeta^{(n)}| < 5 \times 10^{-6}.$$

Here, $\zeta^{(n+1)}$ and $\zeta^{(n)}$ stand for solutions at $(n+1)$-th and n-th time steps respectively and we have used the computed solution for a lower *Re* as the initial guess for a higher *Re*. We also compare our CPU times with that for the scheme presented in [65], which used direct discretization on a uniform Cartesian grid. Although the CPU time taken by our scheme is more than the CPU time taken for direct discretization on a uniform Cartesian grid (presented here within parentheses), our scheme has the advantage of working equally well in domains beyond rectangular whereas the scheme in [65] is limited to rectangular domain only. It is worthwhile mentioning that coarser uniform

Table 3.5: *Lid-driven square cavity flow problem: steady-state secondary and tertiary vortex data for* $100 \leq Re \leq 5000$.

				Re		
Vortex	Property	100	400	1000	3200	5000
Secondary	ψ_{max}	—	—	—	5.91e-4	1.27e-3
TL		—	—	—	(7.28e-4)	(1.46e-3)
	Location x, y	—	—	—	0.0491, 0.8988	0.0624, 0.9101
		—	—	—	(0.0547, 0.8984)	(0.0625, 0.9125)
	H_L	—	—	—	0.0838	0.1153
		—	—	—	(0.0859)	(0.1211)
	V_L	—	—	—	0.2054	0.2678
		—	—	—	(0.2057)	(0.2693)
BL	ψ_{max}	2.06e-6	1.37e-5	2.12e-4	8.92e-4	1.23e-3
		(1.75e-6)	(1.42e-5)	(2.31e-4)	(9.78e-4)	(1.36e-3)
	Location x, y	0.0316, 0.0316	0.0528, 0.0439	0.0840, 0.0727	0.0794, 0.1175	0.0727, 0.1384
		(0.0313, 0.0391)	(0.0508, 0.0469)	(0.0859, 0.0781)	(0.0859, 0.1094)	(0.0703, 0.1367)
	H_L	0.0834	0.1301	0.2288	0.3002	0.3310
		(0.0781)	(0.1273)	(0.2188)	(0.2844)	(0.3184)
	V_L	0.0835	0.1093	0.1665	0.2462	0.2840
		(0.0781)	(0.1081)	(0.1680)	(0.2305)	(0.2643)
BR	ψ_{max}	1.22e-5	6.35e-4	1.75e-3	2.85e-3	3.16e-3
				(1.73e-3)*		(3.07e-3)*
		(1.25e-5)	(6.42e-4)	(1.75e-3)	(3.14e-3)	(3.08e-3)
	Location x, y	0.9526, 0.0638	0.8908, 0.1233	0.8616, 0.1092	0.8247, 0.0863	0.8005, 0.0782
				(0.8643, 0.1123)*		(0.8057, 0.0732)*
		(0.9453, 0.0625)	(0.8906, 0.1250)	(0.8594, 0.1094)	(0.8125, 0.0859)	(0.8086, 0.0742)
	H_L	0.1334	0.2723	0.3191	0.3589	0.3816
		(0.1328)	(0.2617)	(0.3034)	(0.3406)	(0.3565)
	V_L	0.1612	0.3193	0.3685	0.4204	0.4457
		(0.1484)	(0.3203)	(0.3536)	(0.4102)	(0.4180)
Tertiary	ψ_{min}	—	—		-5.87e-8	-2.16e-8
BL		—	—	—	(-6.33e-8)	(-7.08e-8)
	Location x, y	—	—	0.0059, 0.0060	0.0080, 0.0080	0.0060, 0.0080
		—	—	—	(0.0078, 0.0078)	(0.0117, 0.0078)
	H_L	—	—	0.0156	0.0168	0.0152
		—	—	—	(0.0254)	(0.0156)
	V_L	—	—	0.0175	0.0160	0.0165
		—	—	—	(0.0234)	(0.0163)
Tertiary	ψ_{min}	-1.25e-9	-4.81e-8	-1.10e-7	-2.77e-7	-1.26e-6
BR		—	(-8.91e-8)	(-9.32e-8)	(-2.52e-7)	(-1.46e-6)
	Location x, y	0.9974,0.0057	0.9933, 0.0067	0.9933, 0.0067	0.9879, 0.0121	0.9795, 0.0170
			(0.9922, 0.0078)	(0.9922, 0.0078)	(0.9844, 0.0078)	(0.9805, 0.0195)
	H_L	0.0081	0.0152	0.0078	0.0240	0.0559
		—	(0.0156)	(0.0078)	(0.0254)	(0.0528)
	V_L	0.0075	0.0156	0.0087	0.0226	0.0448
		—	(0.0156)	(0.0078)	(0.0234)	(0.0417)
Grid Size (present)		41 × 41	61 × 61	61 × 61	101 × 101	121 × 121
Ghia et al.		(129 × 129)	(257 × 257)	(129 × 129)	(129 × 129)	(257 × 257)
* Bruneau and Saad	-	-	-	(1024 × 1024)	-	(1024 × 1024)

grid used in [65] could not capture the flow patterns for higher *Re*s accurately.

Table 3.6: *Convergence data and relaxation parameter for the lid-driven square cavity problem on a 61 × 61 grid in a PC with pentium 4 processor and 512 mB RAM.*

Re	CPU(s)	Relaxation parameter (inner (ζ), inner (ψ))
100	116.585 (64.926)	(0.725, 0.9)
400	261.197 (126.972)	(0.425, 0.625)
1000	782.034 (372.254)	(0.5, 0.6)

In figures 3.5 and 3.6, we show the time-wise evolution of the streamlines for

Figure 3.4: *Lid-driven square cavity flow problem: comparison of wall vorticity for (a) Re=100 and 400, and (b) Re=1000, 3200 and 5000.*

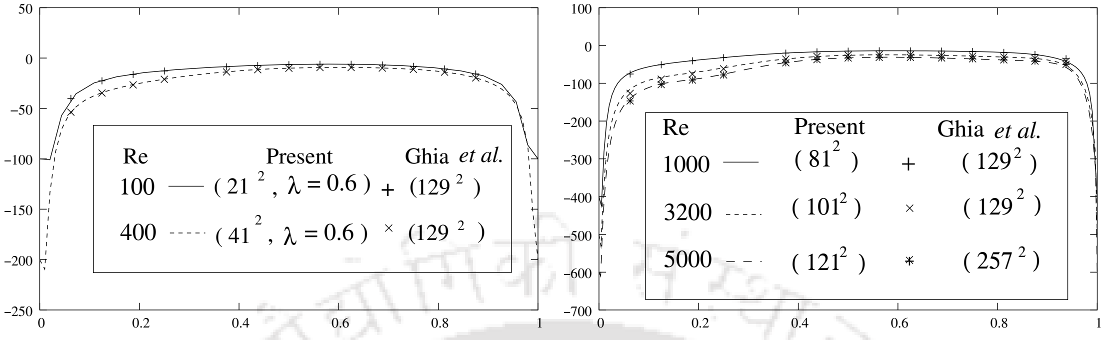

(a) (b)

Re = 1000 and 3200 till the steady-state is reached (on a 81 × 81 and 101 × 101 grid respectively). These figures show that our scheme excellently captures the formation of the secondary and tertiary vortices as time progresses. In a similar note, the adjacent tables show the time evolution of the ψ-ζ data at different time stations for *Re* = 1000 and 3200 respectively on a 81×81 and 101×101 grid. We have compared the transient data presented in figure 11 with the same given in [31].

Figures 3.7 and 3.8 respectively show the horizontal velocity along the vertical centerline and vertical velocity along the horizontal centerline at instant $t = 20.0$, captured with five different time steps $\Delta t = 0.05$, 0.02, 0.01, 0.005 and 0.001 for *Re* = 5000. These profiles captured on a grid of size 121 × 121 clearly exemplifies the good effects of the implicitness of our scheme which allows time step as coarse as $\Delta t = 0.02$ to achieve time-grid-independence (hence time-accuracy).

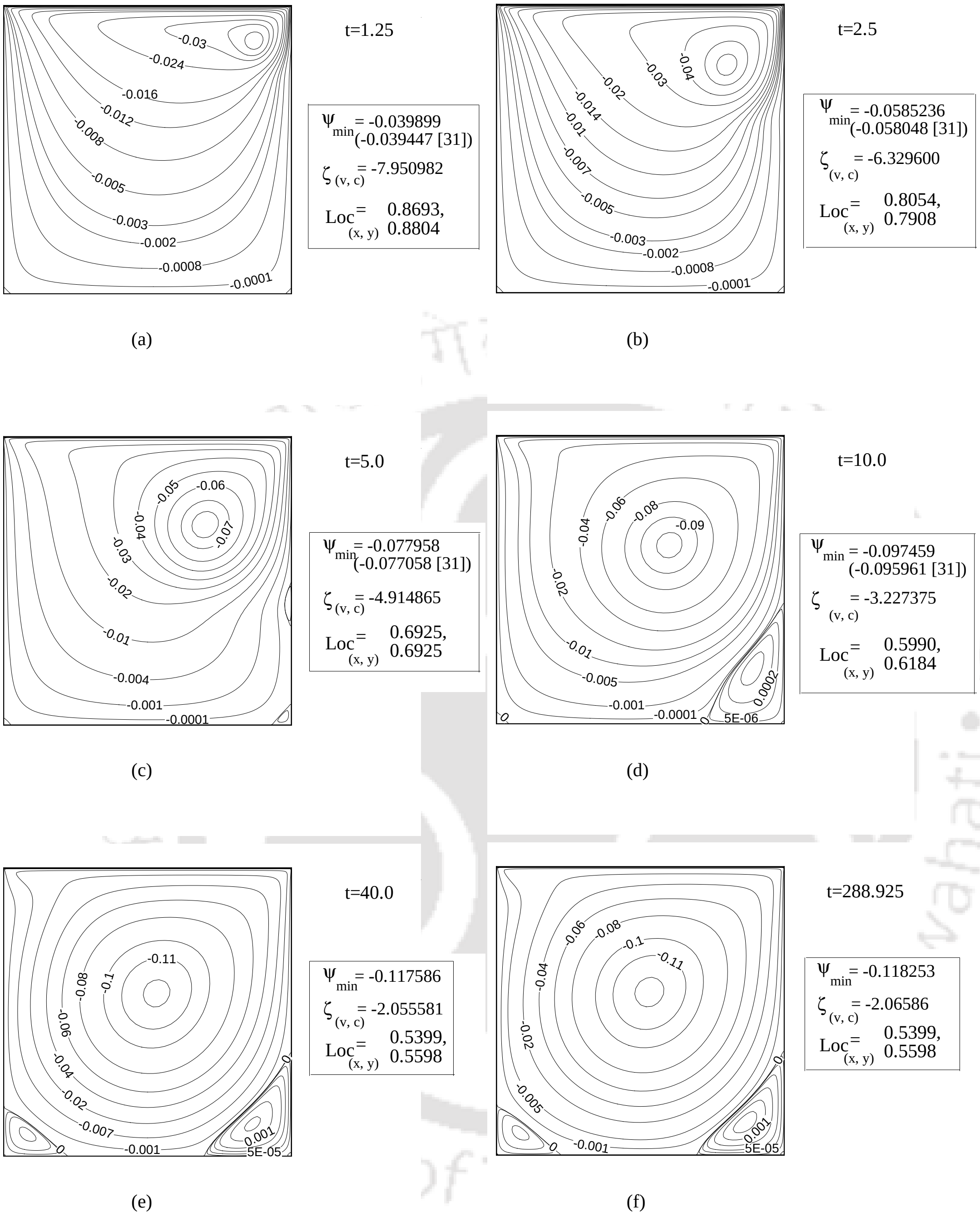

Figure 3.5: *Evolution of streamlines at different time stations for the lid-driven cavity flow for Re* = 1000 *on a grid 81* × *81* (λ = 0.6)*: (a) t=1.25 (b) t=2.5 (c) t=5.0 (d) t=10.0 (e) t=40.0 (f) t=288.925 (steady-state).*

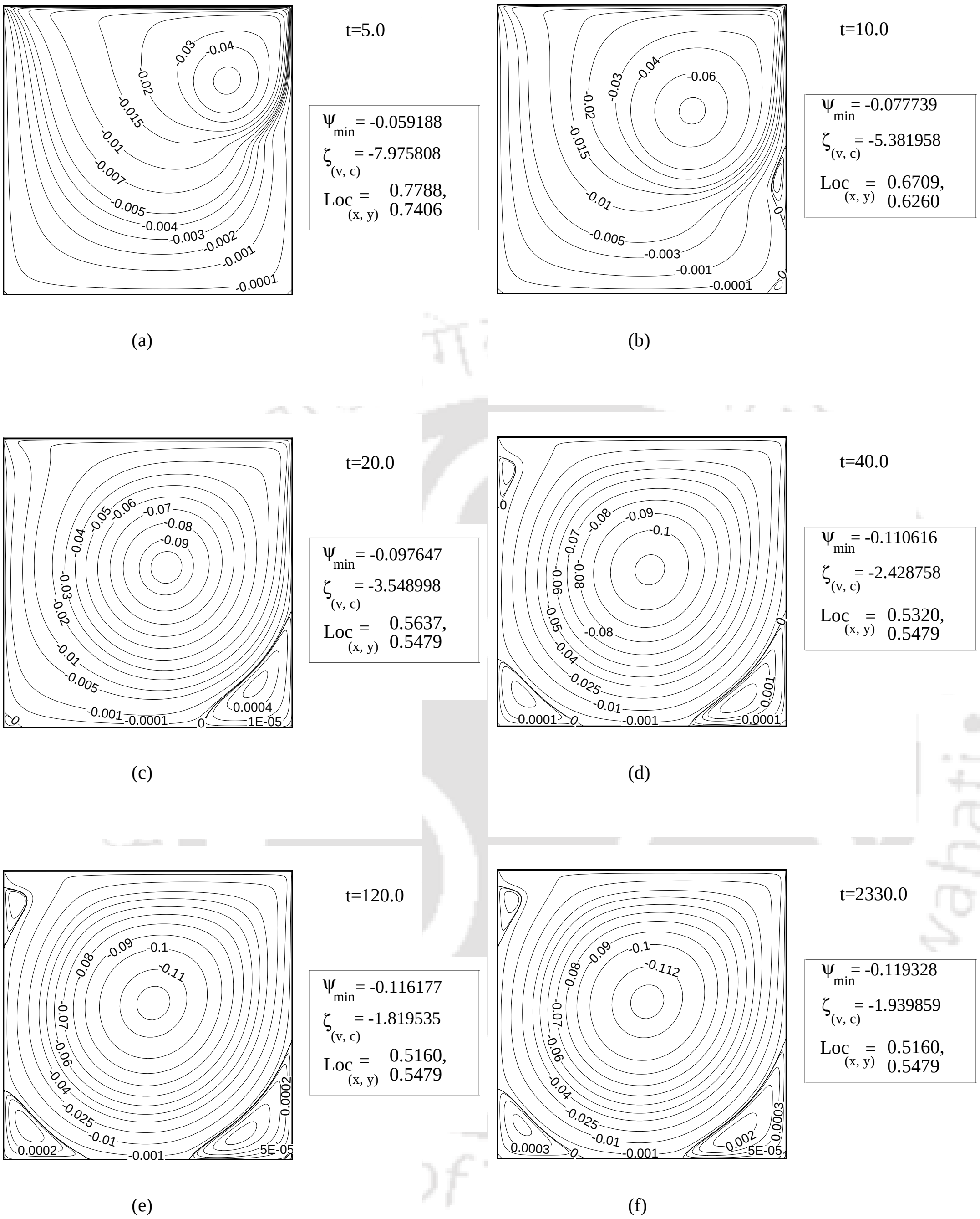

(a) (b)

(c) (d)

(e) (f)

Figure 3.6: *Evolution of streamlines at different time stations for the lid-driven cavity flow for Re* $= 3200$ *on a grid* 101×101 $(\lambda = 0.6)$*: (a) t=5.0 (b) t=10.0 (c) t=20.0 (d) t=40.0 (e) t=120.0 (f) t=2330.0 (steady-state).*

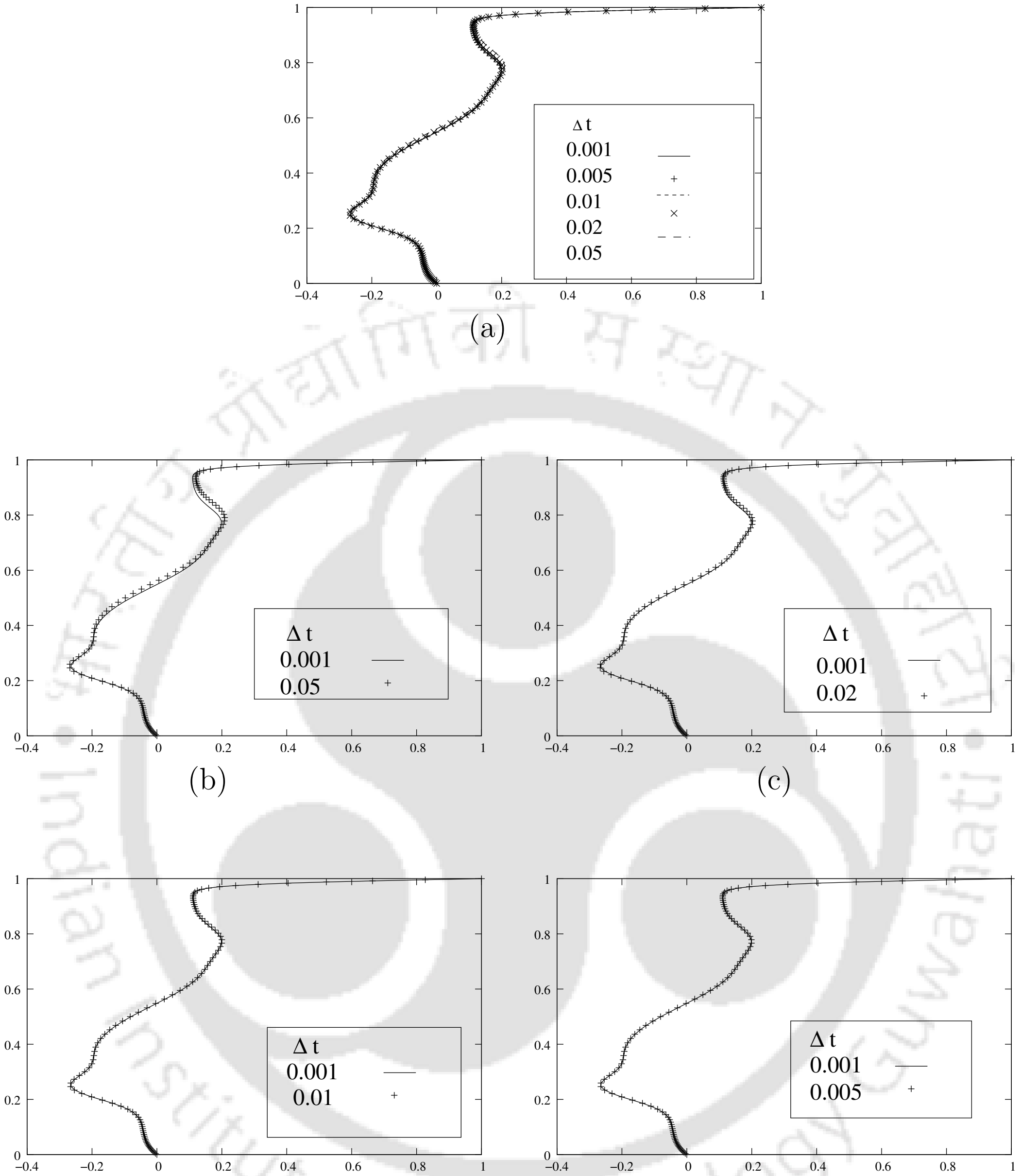

(a)

(b)

(c)

(d)

(e)

Figure 3.7: *Temporal grid independence study, horizontal velocity along the vertical centerline for Re* = 5000 *at time station* t = 20 *(*λ*=0.6) for lid-driven square cavity flow: (a)* Δt*=0.05,* Δt*=0.02,* Δt*=0.01,* Δt*=0.005,* Δt*=0.001, (b)* Δt*=0.001,* Δt*=0.05, (c)* Δt*=0.001,* Δt*=0.02, (d)* Δt*=0.001,* Δt*=0.01 and (e)* Δt*=0.001,* Δt*=0.005.*

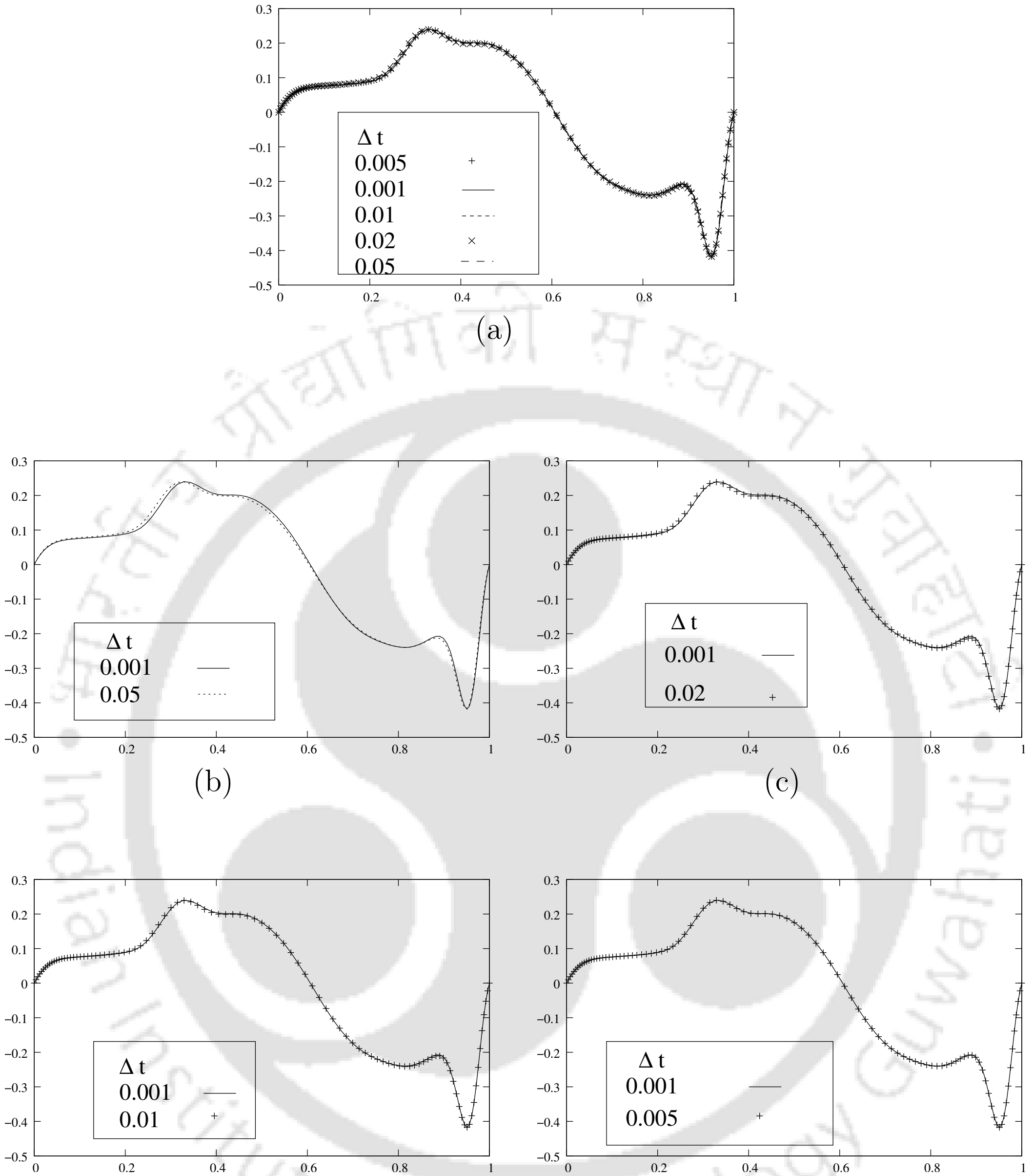

(a)

(b) (c)

(d) (e)

Figure 3.8: *Temporal grid independence study, vertical velocity along the horizontal centerline for Re* = 5000 *at time station t* = 20 *(λ=0.6) for lid-driven square cavity flow: (a) Δt=0.05, Δt=0.02, Δt=0.01, Δt=0.005, Δt=0.001, (b) Δt=0.001, Δt=0.05, (c) Δt=0.001, Δt=0.02, (d) Δt=0.001, Δt=0.01 and (e) Δt=0.001, Δt=0.005.*

Results for rectangular cavity (Aspect ratio≠1.0)

In this section, we now present the transient solutions produced by the proposed scheme for the rectangular cavity (both shallow and deep cavity) having aspect ratio other than 1.0 in figures 3.9-3.14. The streamline contours show the dramatic extent of the effects of vortices that starts to develop along the right or left wall. These figures also show that the first large vortex shrinks at first as time evolves but beyond a certain time, the shrinkage is insignificant. Again, it may be observed from these figures that a series of successive, counter-rotating vortices are formed below the moving lid. In the case of deep cavity, the center of the primary vortex does not reach the geometric center of the cavity due to evolution of large vortices other than first large vortex (primary vortex) at higher *Re*s. Thus, the rectangular cavity gives rise to some more interesting flow phenomena in comparison with the flow structure in the square lid-driven cavity. It is to be noted here that the effect of the Reynolds number on the flow structures in the rectangular cavity for different aspect ratios is still not fully understood. For instance, when the inertial force is involved, what is the flow structure in a deep cavity? How does the inertia force affect the flow structure as *Re* increases? As time evolves, distribution of inertial forces in the cavity is not symmetrical. Due to this fact, high velocity gradient regions develop which causes eddy formation. In addition to this it is numerically experimented and found that the vortex formation occurs almost immediately but the amplitudes develop much more slowly. In the following we discuss the evolution of flow structures for different aspect ratios.

Aspect ratio=0.5, $Re = 1000$

In figures 3.9, we show the time-wise evolution of the streamlines for aspect ratio 0.5 for $Re = 1000$ (on 81×41 grid). It is seen that at the early stage (see figure at t=1.25) of the fluid motion the primary vortex occupies almost the whole area of the cavity with two small vortices (secondary vortices) at two bottom corners. Then, the size of the right bottom corner vortex increases in comparison with left bottom corner vortex (see figure at t=4.0 and 5.0). But further increase in time shows that the size of the left vortex increases rapidly while the bottom right corner vortex maintains almost same size. In addition to this, the center of the primary vortex shifts down towards left and finally settles down at a stationary position. In the intermediate steps the left corner vortex splits up into two vortices and then they coalesce in a short time. Towards steady-state two large vortices along with two bottom corner vortices develop in the cavity (see figure at t=20.0).

Aspect ratio=0.5, $Re = 3200$

For $Re = 3200$ (on 101×51 grid), the transient flow characteristics are almost same with those for $Re = 1000$. It is numerically experimented, and can be seen from figure 3.10 that more computational time is required for higher Res to reach steady-state solutions. It is noted here that in both the cases ($Re = 1000$ and 3200) the second large vortex is generated from left corner vortex. The size of the right bottom corner vortex is larger than that of the left bottom corner vortex which is due to inertia effect.

Aspect ratio=2.0, $Re = 1000$

When the aspect ratio of the cavity increases, additional dynamical information on basic eddy formation, growth, separation, and reintegration in the flow domain has been found (see figure 3.11 for $Re = 1000$ with aspect ratio 2.0). The evolution of the vortex structures is completely different from those in case of aspect ratio 0.5. In the early stage of the flow development, early distortion of the outer streamline contours along the right wall near the lid has been seen. As a result a small eddy is evolved on the right wall (see figure at t=7.5). As time progresses the growth and movement of this wall eddy is evident. Meanwhile, it meets with right corner vortex and then with left one. These three secondary vortices finally form a massive recirculating region in the lower half occupying more than 50% of the area of the cavity, and called second large vortex (second primary vortex). It is also observed that when flow approaches towards steady state, the center of the second large vortex drifts along (see figure at t=25.0) left wall (see figure at t=40.0). These vortex dynamics have been also observed by Gustafson and Halasi [54] for $Re = 2000$.

Aspect ratio=2.0, $Re = 3200$

Further increase in Re (see figure 3.12 for $Re = 3200$) adds some new flow features due to increase in inertia force effect in the cavity with aspect ratio 2.0. The change in the flow patterns in comparison with figure 3.11 is observed after t=220.0. Then another vortex slowly develops at the top of the left wall (see figure at t=240.0). As time evolves, this vortex increases up to a certain size. The center of the second large vortex is offset towards the left wall with slight distortion of its outer streamline contours towards that left wall. Another wall eddy develops just above the left bottom corner eddy and immediately it merges with the bottom left corner eddy. Later there is a coalescence with bottom right corner eddy. Towards steady-state (see figure at t=1300.0) a third large vortex develops near the bottom wall with the two small vortices at the left and right bottom corners.

Aspect ratio=3.0, $Re = 3200$

In comparison with the transient flow structures in a cavity with aspect ratio 2.0, similar flow phenomena have been noticed for aspect ratio 3.0 (see figure 3.13). The steady-state results contain three large vortices with two bottom corner vortices and a top left vortex. The main differences are the strength and the size of the vortices.

Aspect ratio=5.0, $Re = 3200$

Further with increase in aspect ratio one can see some more interesting intermediate steps for the development of vortex structures. The evolution of second and third vortices followed almost same intermediate steps as discussed for aspect ratio 3.0. Then the size of the bottom left and right corner vortices are found to be symmetric with respect to each other, and the center of the third large vortex moves slowly towards left wall. With these, the reattachment point of the left corner vortex and the separation point of the right corner vortex approach each other. These vortices merge together. In the process of evolution, a large fourth vortex forms. Finally, the steady-state flow domain consists of four large vortices with a top left vortex and two bottom corner vortices.

The above facts can be explained on the basis of velocity. Velocity in the cavity decreases towards bottom with increase in depth. The deeper the cavity, the smaller the velocity in the region of bottom wall will be i.e the flow near the bottom wall in a deep cavity is closer to the Stokesian limit, and is dominated by viscous force over inertia force.

The above discussions reveal that when the cavity becomes infinitely deep, beyond a certain distance from the moving wall, the flow field consists of a series of counter rotating vortices. The number of such vortices depends on both *Re* and aspect ratios.

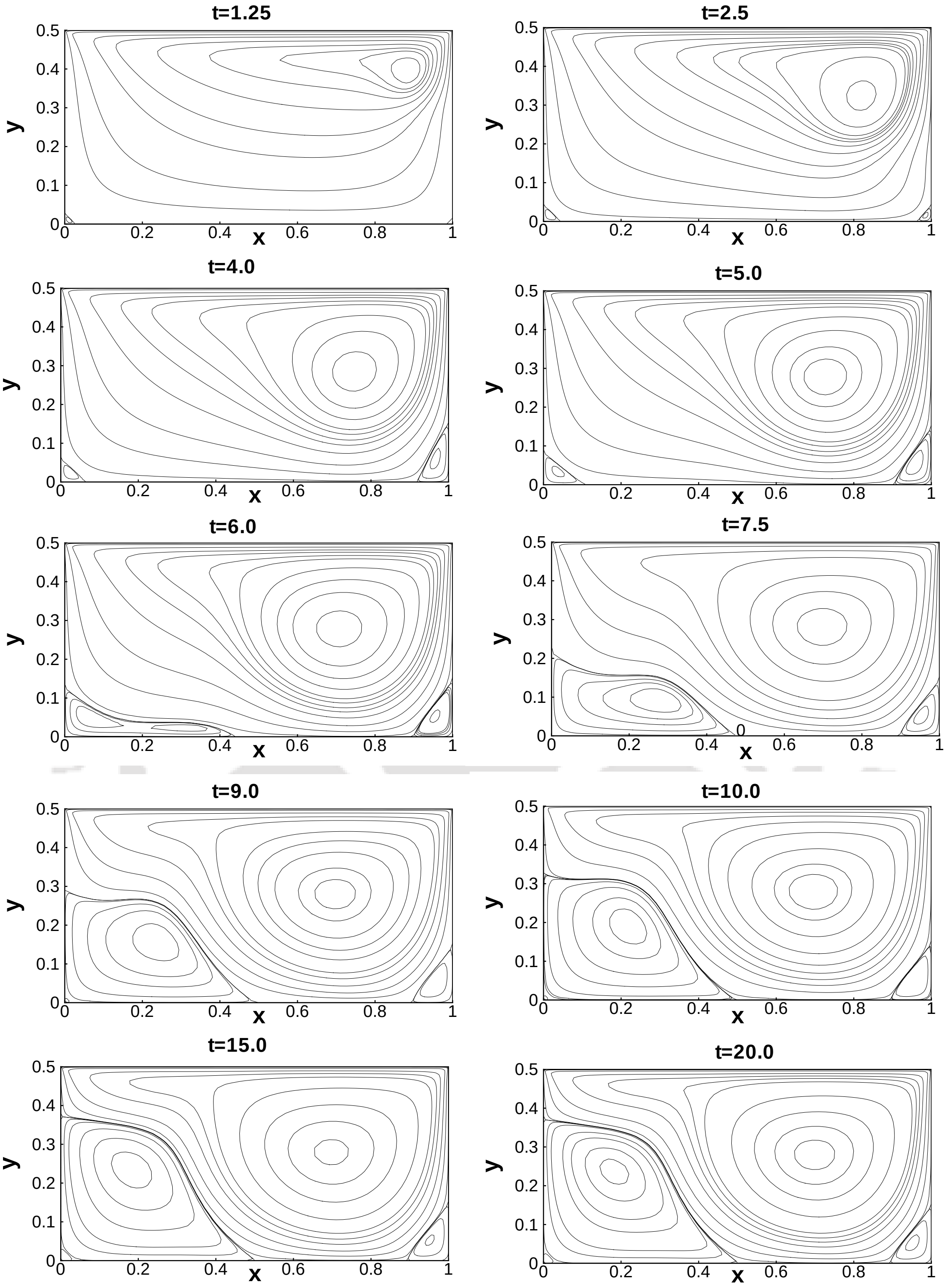

Figure 3.9: *Lid-driven rectangular cavity flow problem: evolution of streamlines at different time stations for the lid-driven cavity flow with aspect ratio 0.5 for* $Re = 1000$ *on a grid* 81×41 $(\lambda = 0.6)$.

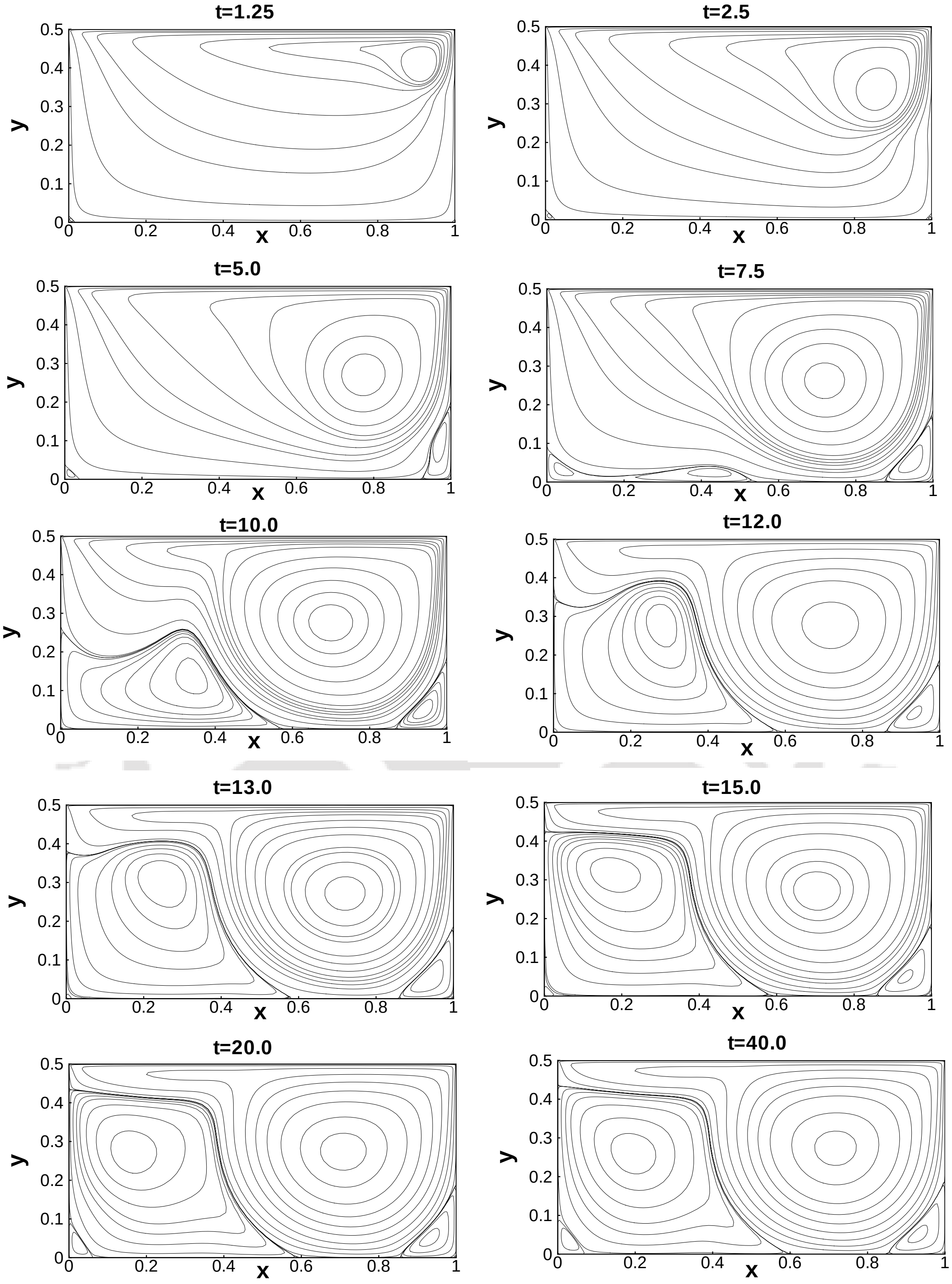
t=1.25 t=2.5
t=5.0 t=7.5
t=10.0 t=12.0
t=13.0 t=15.0
t=20.0 t=40.0

Figure 3.10: *Lid-driven rectangular cavity flow problem: evolution of streamlines at different time stations for the lid-driven cavity flow with aspect ratio 0.5 for* $Re = 3200$ *on a grid* 101×51 $(\lambda = 0.6)$.

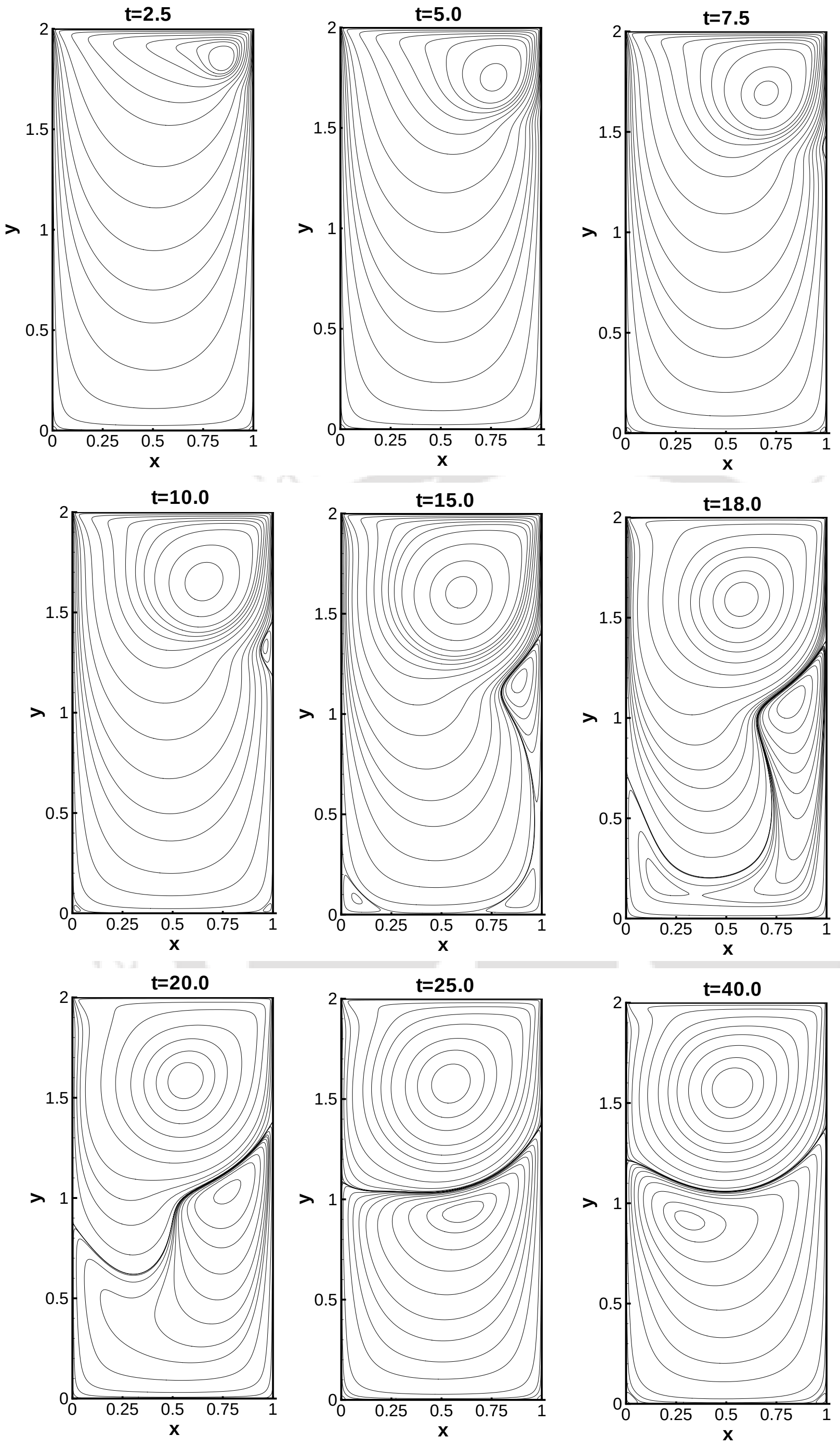

Figure 3.11: *Lid-driven rectangular cavity flow problem: evolution of streamlines at different time stations for the lid-driven cavity flow with aspect ratio 2.0 for* $Re = 1000$ *on a grid 101 × 201 (*$\lambda = 0.6$*).*

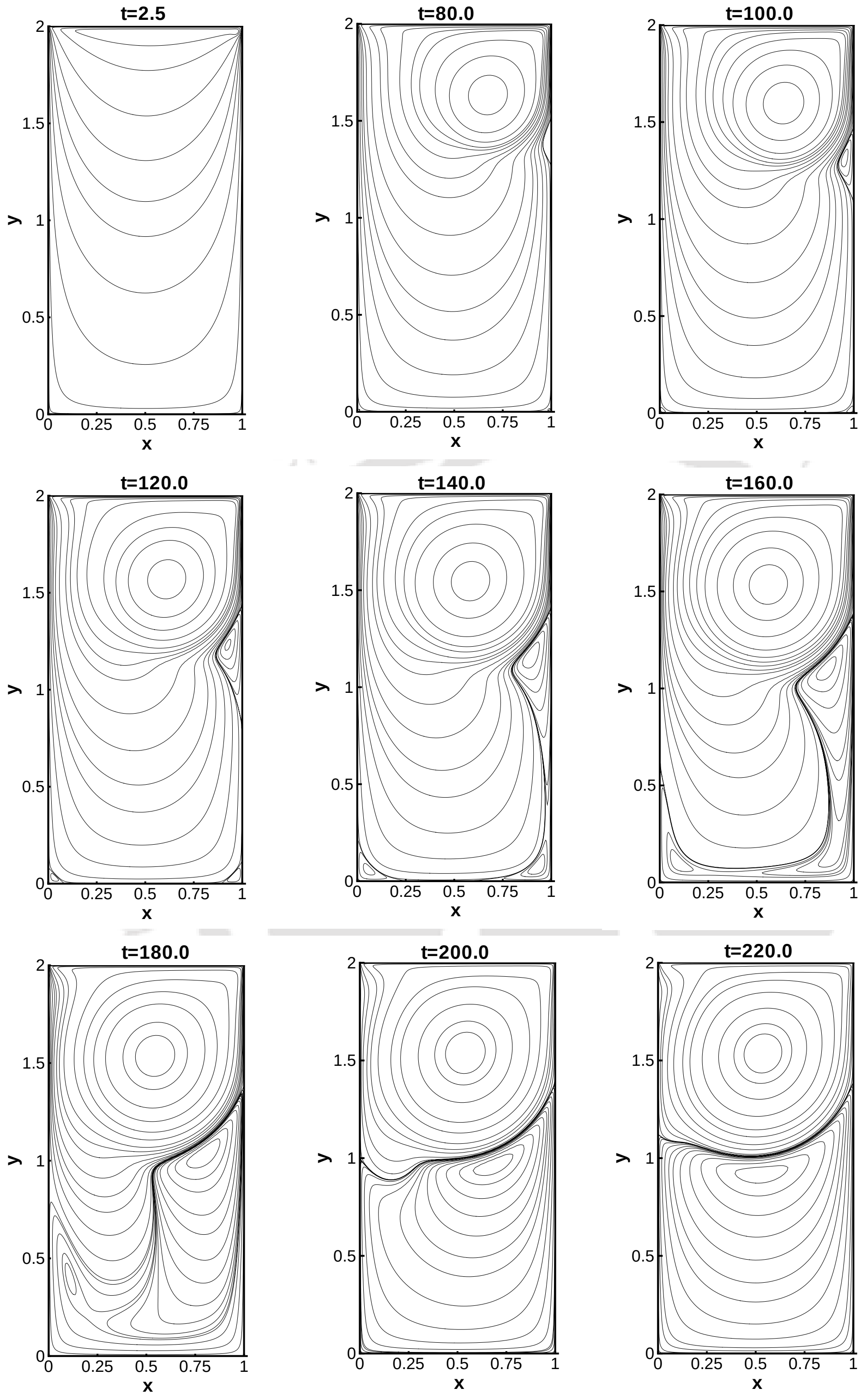

Figure 3.12: *For caption see next page.*

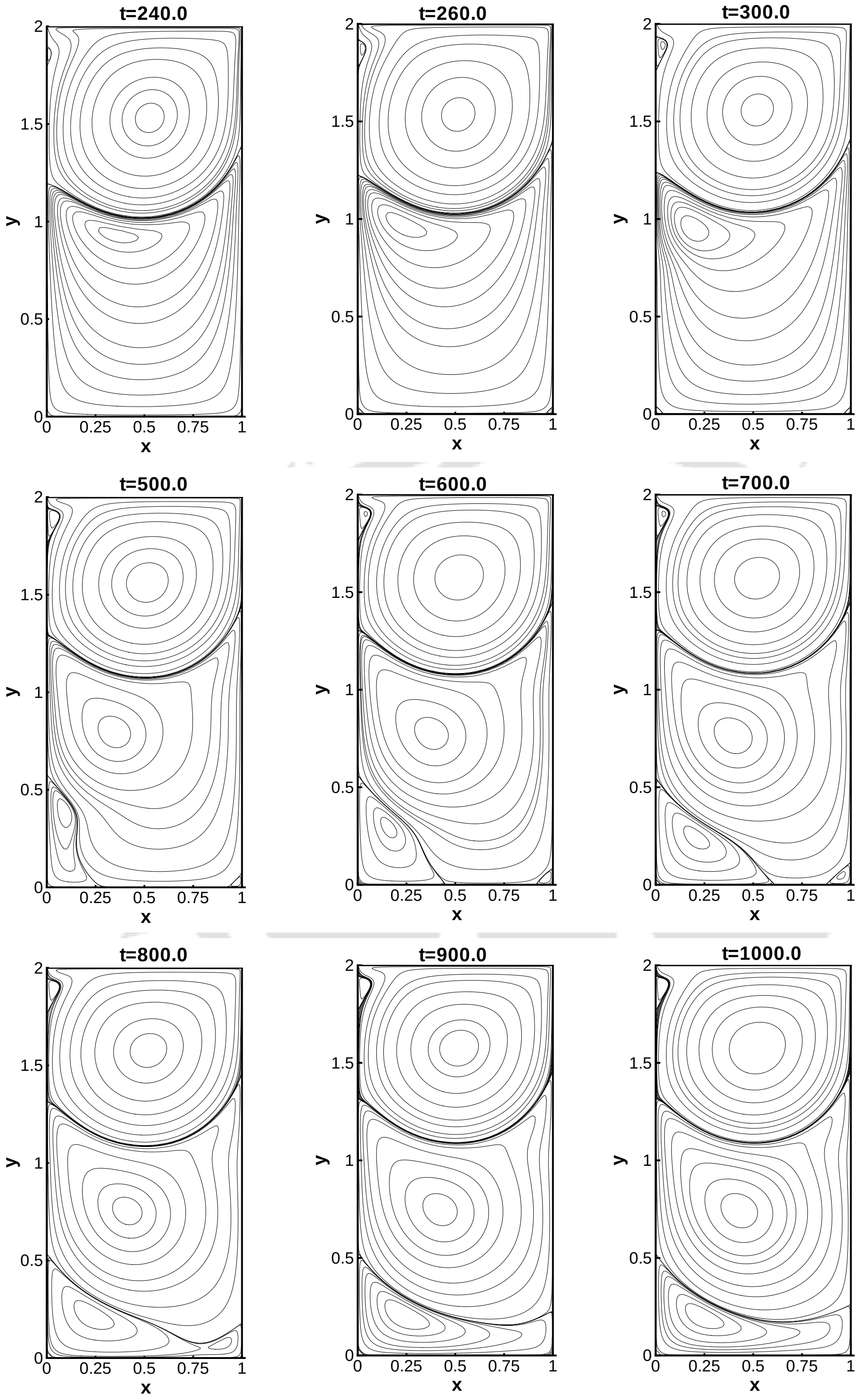

Figure 3.12: *For caption see next page.*

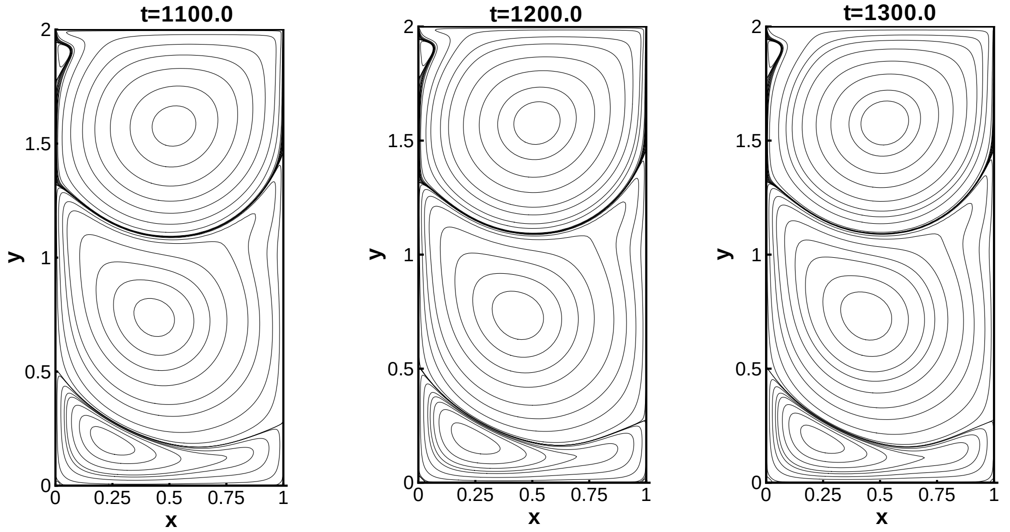

Figure 3.12: *Lid-driven rectangular cavity flow problem: evolution of streamlines at different time stations for the lid-driven cavity flow with aspect ratio 2.0 for* $Re = 3200$ *on a grid* 101×201 $(\lambda = 0.6)$.

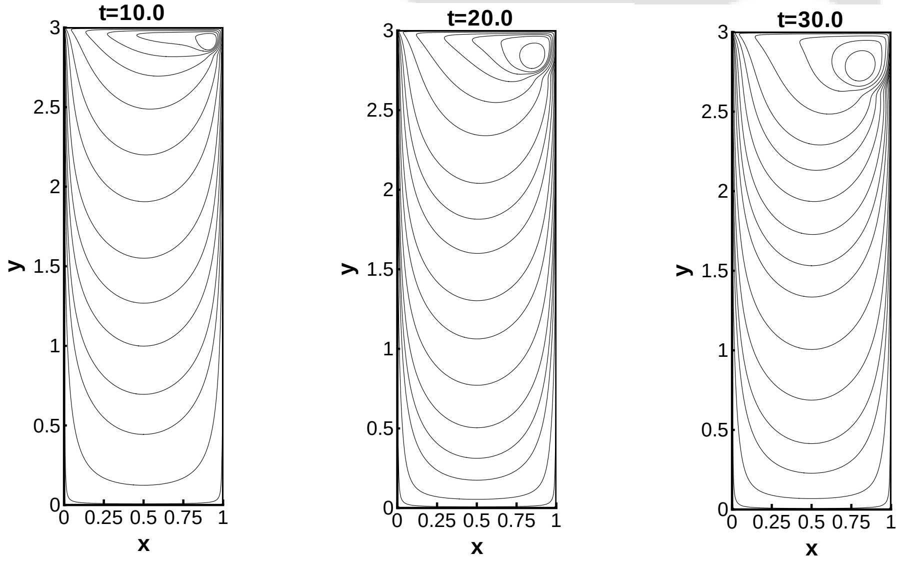

Figure 3.13: *For caption see next page.*

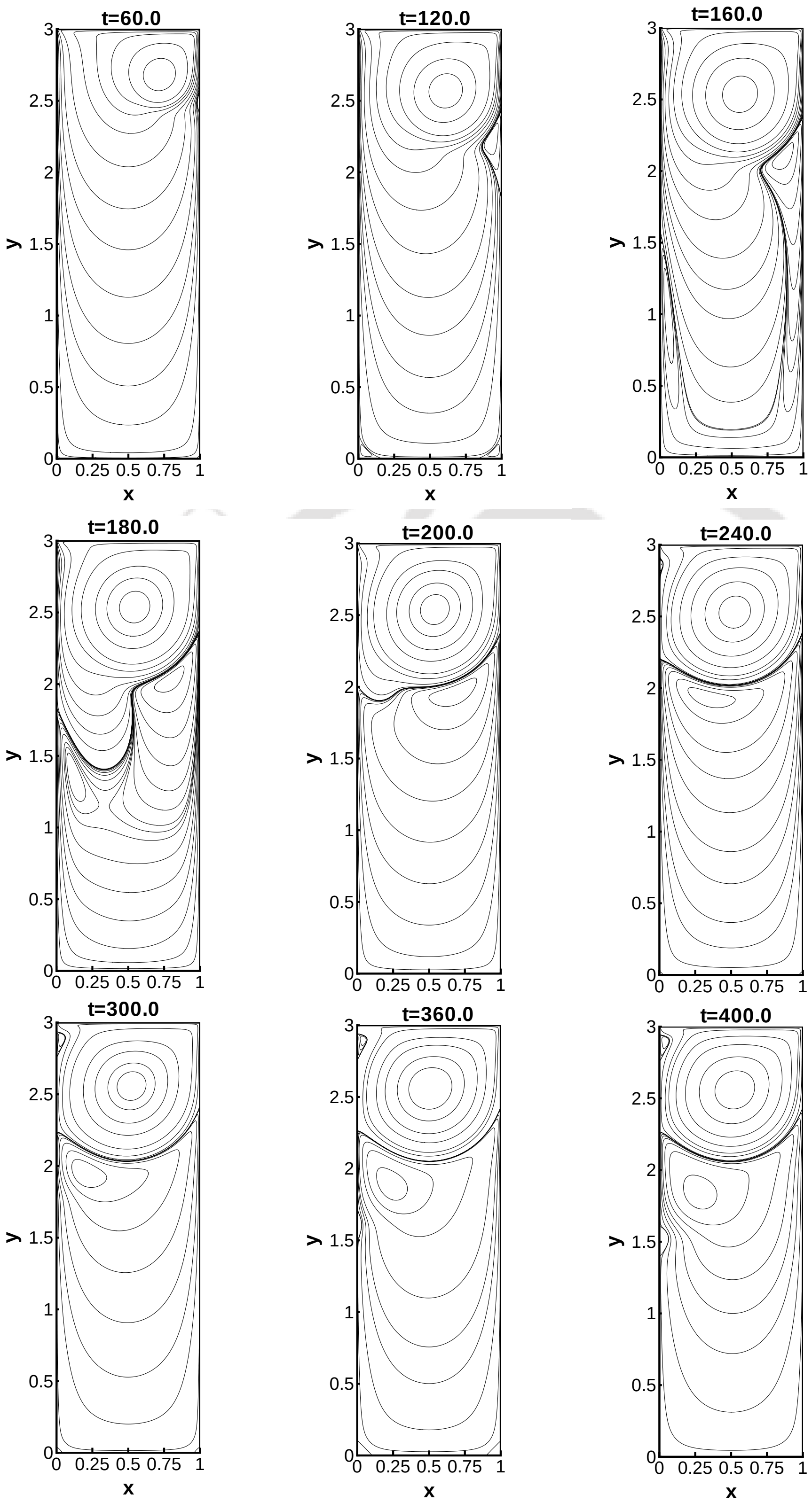

Figure 3.13: *For caption see next page.*

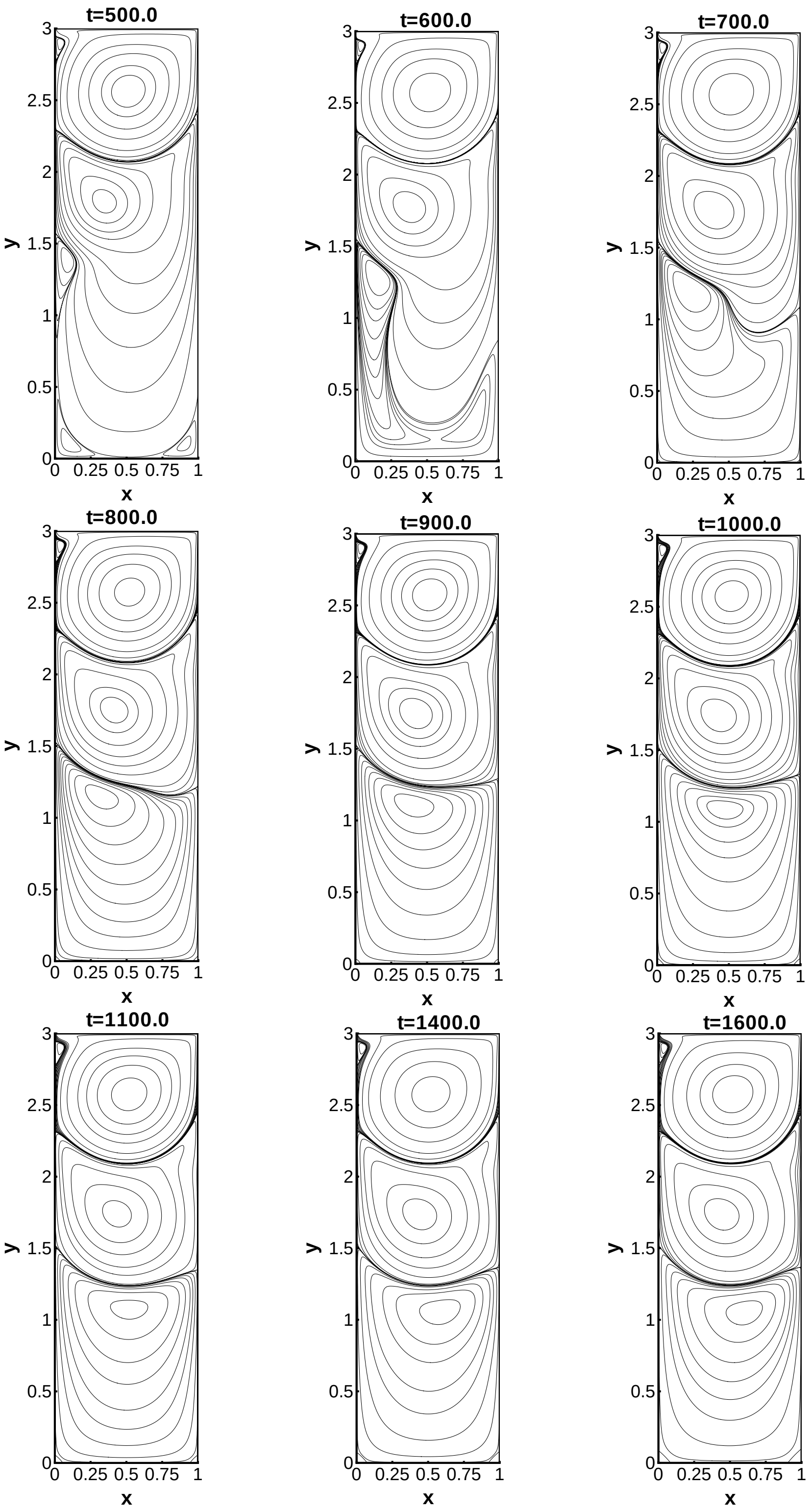

Figure 3.13: *Lid-driven rectangular cavity flow problem: evolution of streamlines at different time stations for the lid-driven cavity flow with aspect ratio 3.0 for Re* $= 3200$ *on a grid 101* $\times$ *301* ($\lambda = 0.6$).

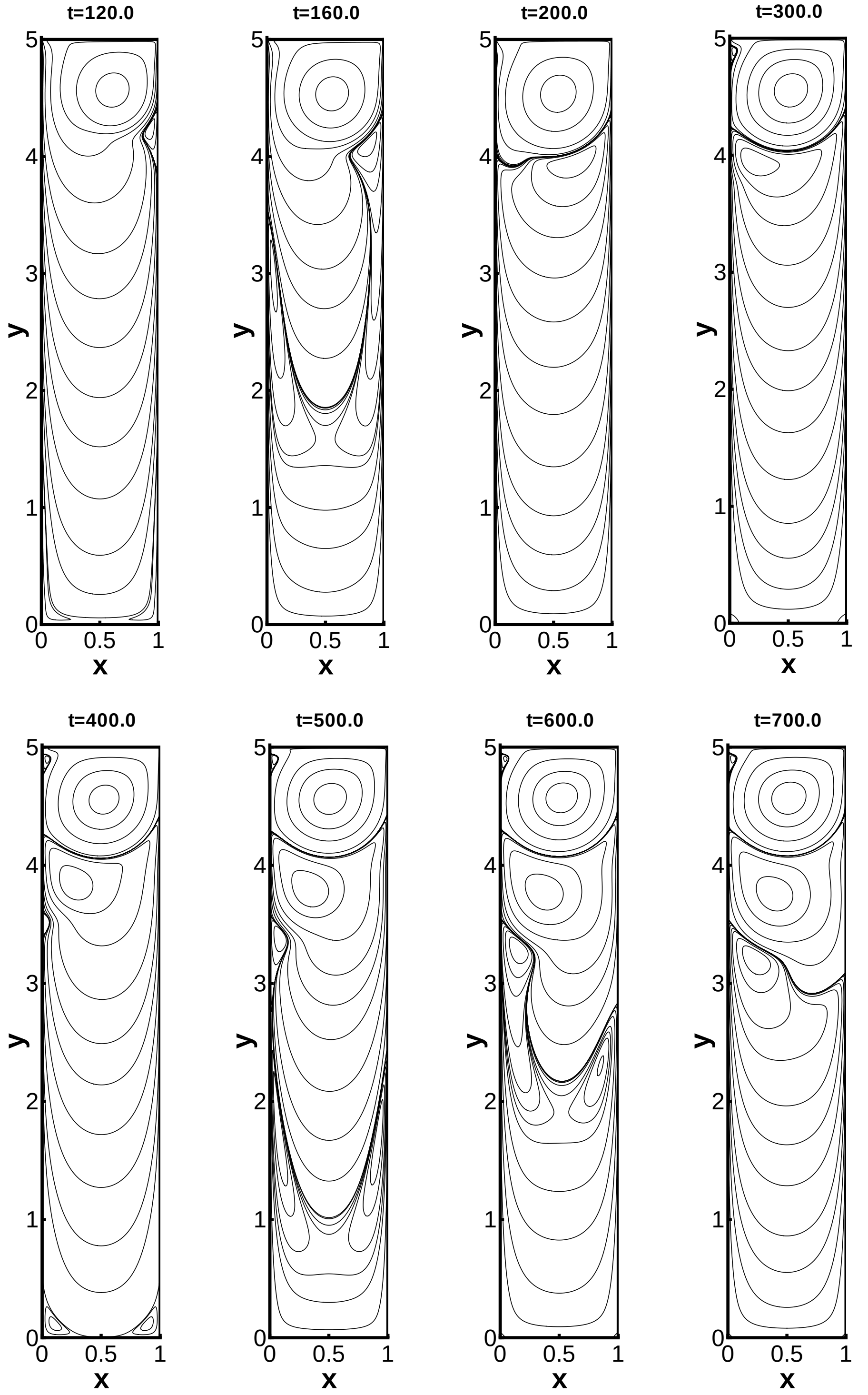

Figure 3.14: *For caption see next page.*

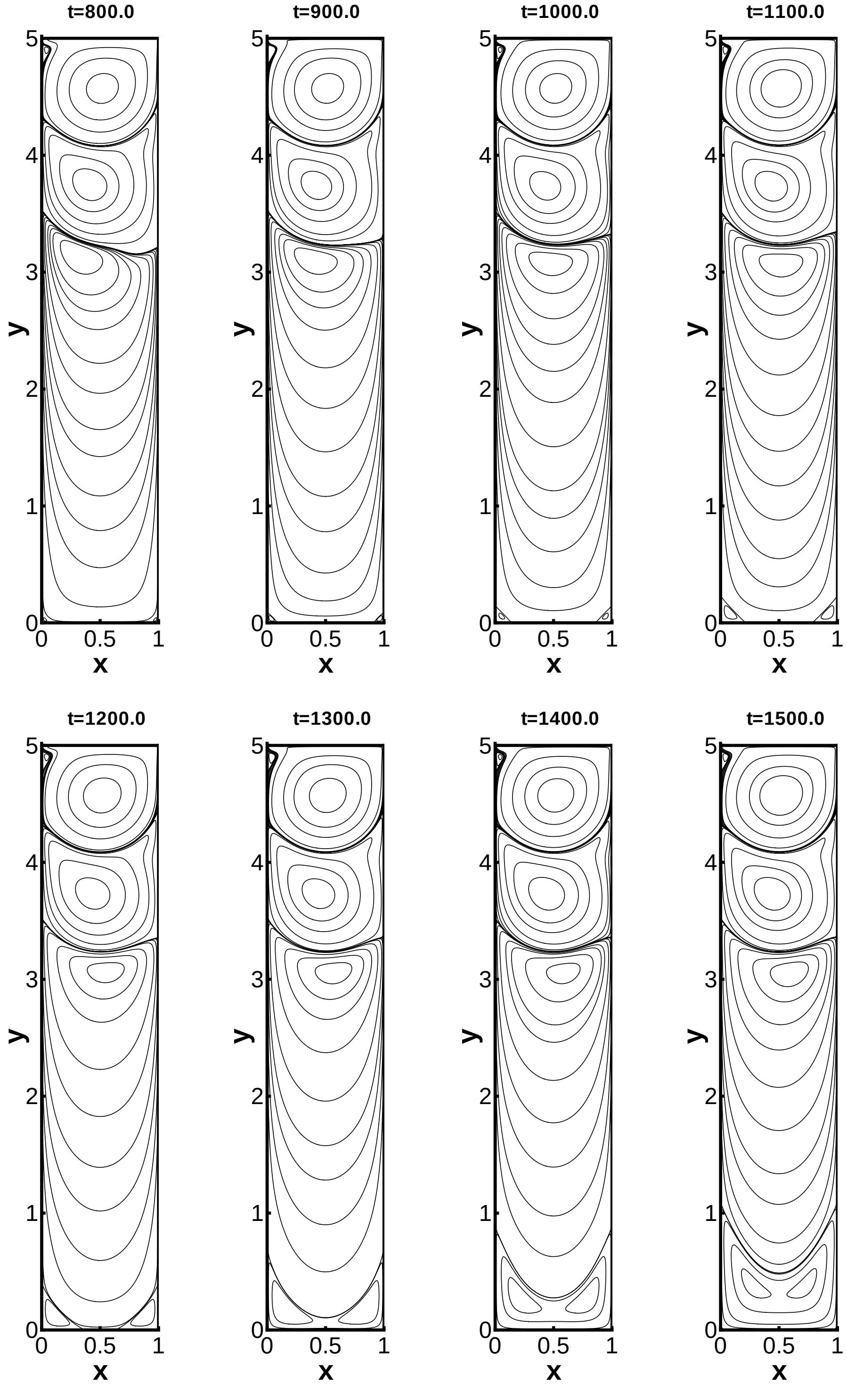

Figure 3.14: *For caption see next page.*

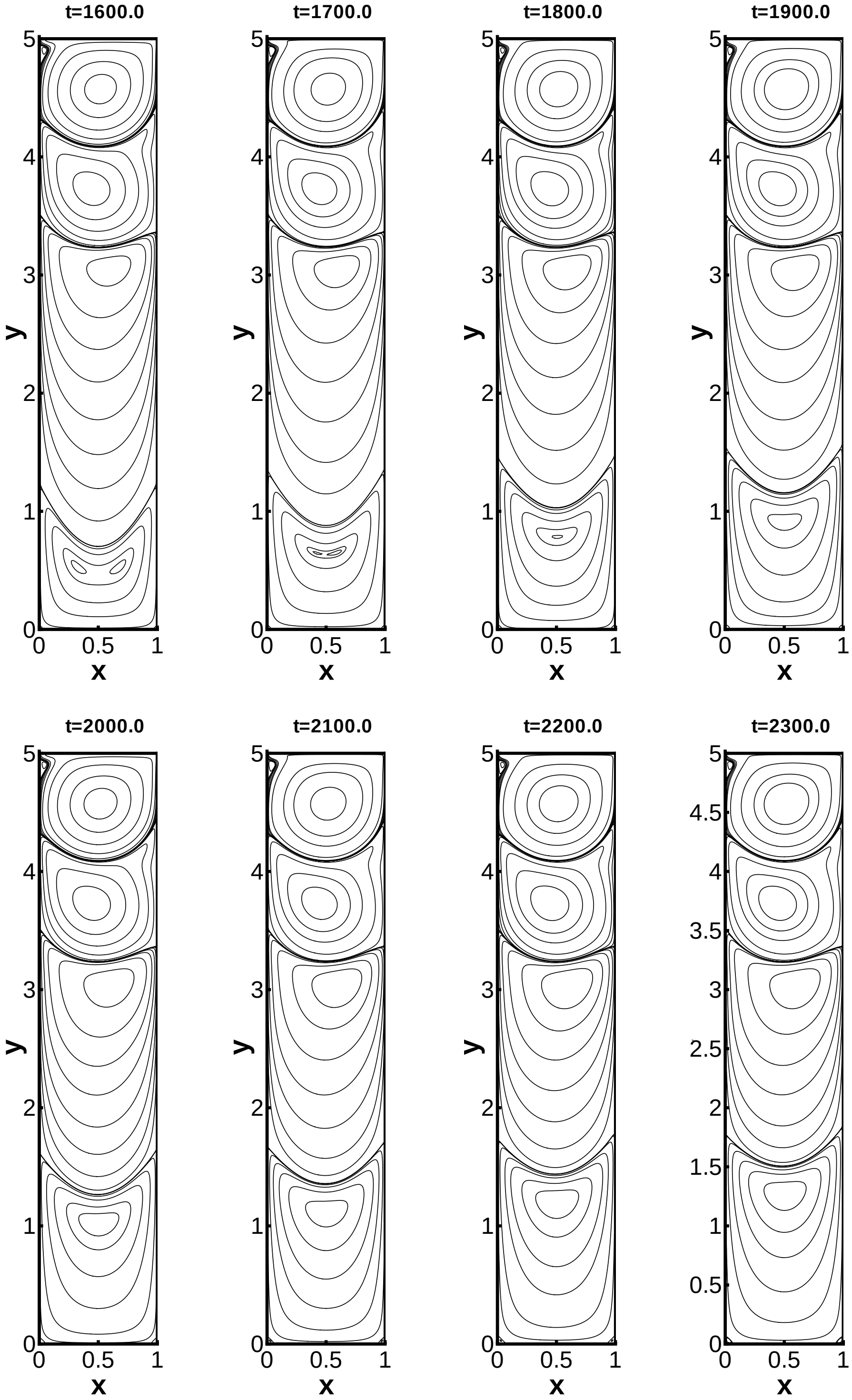

Figure 3.14: *Lid-driven rectangular cavity flow problem: evolution of streamlines at different time stations for the lid-driven cavity flow with aspect ratio 5.0 for* $Re = 3200$ *on a grid 101* × *501* ($\lambda = 0.6$).

3.5 Conclusions

In this chapter, we developed a new HOC formulation for solving unsteady incompressible viscous flow problems governed by the N-S equations on nonuniform grids. The scheme is implicit, second order accurate in time and fourth order accurate in space. It is seen to efficiently capture both transient and steady-state solutions of the N-S equations with Dirichlet as well as Neumann boundary conditions. Despite the presence of singularities at the top corners, our numerical results exhibited no oscillation (as was seen for the simulations utilizing the steady-state equations in chapter 2). The use of BiCGStab algorithm for solving the algebraic systems arising at every time level, makes the implicit procedure computationally efficient even in capturing transient solutions. Since the proposed scheme is higher order accurate, it demands lesser number of grid points than other popular schemes to reach the desired accuracy. To bring out different aspects of the scheme, we employed it to compute the transient solutions of the flow decayed by viscosity and the time marching steady-state as well as transient solutions of the 2D lid-driven cavity flow. The robustness of the scheme has been presented for wide range of Reynolds numbers ranging from 100 to 5000 in the cavity problem. The results obtained on relatively coarser grids, are in excellent agreement with the analytical as well as the established numerical results as the grid is nonuniform, underlining the high accuracy of the scheme. The implicit nature of the scheme is fully exploited in arriving at the steady-state results for the lid-driven cavity where time-steps as high as 0.05 have been employed for some of the computations. This is the first study in our knowledge where we have presented transient solutions in a rectangular cavity for higher aspect ratios and higher Res, which in turn produce some new flow features. The present scheme has the added advantage of being used in non-rectangular physical domains, it has very good potential for efficient application to many problems of incompressible viscous flows on complex geometries as can be seen in the next few chapters. The present scheme can be used for curvilinear coordinates also. So far we have not come across any work on transient HOC scheme on nonuniform curvilinear grids and our work in the subsequent chapters could be the first one of this kind.

Chapter 4

Incompressible viscous flow in a channel with sudden contraction or expansion

4.1 Introduction

The study of flows in presence of obstructions varying from different types of blocking or various constrictions such as a valve to an orifice (which are widely used in a pipe line systems) is of practical importance. This is due to the fact that situations such as these are prone to accumulate high shear stress resulting from flow disturbances. The outcome of such studies is of great importance in the field of physiological fluid flows. Moreover, a reduction in cross sectional area caused by constriction brings about an increase in flow resistance. The dependency of resistance on the flow rate is an important factor in the design of pumping devices. Flow phenomena in such problems resemble the classic example of the flow through channel with both forward and backward constrictions with re-entrant corner which are important in both engineering and biomechanics. The richness and complexity of the flow patterns occur in both the cases even in a relatively simplest of geometrical settings. There has been extensive studies in the last two decades on the flow through asymmetric and symmetric channels with sudden expansion or contraction that include uniform, nonuniform and pseudospectral grids. The most common amongst them is the study of backward facing step flow [8, 36, 146]. Both experimental and numerical results for the flow in a symmetric channel with right angled as well as 45^0 angled expansion can be found in references [29, 36–38, 130, 137] for different expansion ratios. In these studies, the development of asymmetric flow patterns with increase of Reynolds number in a symmetrical channel has been justified. This phenomenon is explained by Coanda effect [153]. In addition to this the causes of instability occurring in this channel flow have been analyzed in [17, 124, 137]. It must be mentioned that these studies have made a significant stride towards the understanding of flow physics in a channel with backward expansion.

In this chapter, we consider the flow in an symmetric constricted channel with different shapes of reentrant corners in two forms, namely, (i) the forward [94, 95] and (ii) the backward constricted channel. The first one is formed as a result of contraction and the second one results from expansion. The channels are nonuniform in cross section both at the proximal and distal side of the corner (throat). The schematic flow diagrams and corresponding boundary conditions for both the cases are shown in figures 4.1(a) and 4.1(b).

We extensively discuss how the nonuniform channel geometry with a re-entrant corner with different shapes affects the flow in a restrictive way. We also present numerical results for the flow through symmetric nonuniform rigid channel having varying degrees of constriction, either forward or backward, over a wide range of Reynolds numbers ($1 \leq Re \leq 1000$ and $1 \leq Re \leq 500$ are studied for forward and backward constricted channel respectively).

4.2 Governing equations

The governing equations for the cases considered here are the N-S equations for the 2D unsteady incompressible viscous flows, which in non-dimensional primitive variable formulation can be written as

$$\frac{\partial u}{\partial x} + \frac{\partial v}{\partial y} = 0, \tag{4.1}$$

$$\frac{\partial u}{\partial t} + u\frac{\partial u}{\partial x} + v\frac{\partial u}{\partial y} = -\frac{\partial p}{\partial x} + \frac{1}{Re}\nabla^2 u, \tag{4.2}$$

$$\frac{\partial v}{\partial t} + u\frac{\partial v}{\partial x} + v\frac{\partial v}{\partial y} = -\frac{\partial p}{\partial y} + \frac{1}{Re}\nabla^2 v, \tag{4.3}$$

where u, v are velocities along x-, y-directions respectively, p is the pressure, t is the time and Re is the Reynolds number given by $Re = \frac{Lu_0}{\nu}$, where L is the unperturbed channel width at the inlet, u_0 is the average velocity at the entrance and ν is the kinematic viscosity.

To eliminate p, we may introduce streamfunction $\psi(x, y, t)$ and vorticity $\zeta(x, y, t)$ in terms of u and v as

$$u = \frac{\partial \psi}{\partial y}, \qquad v = -\frac{\partial \psi}{\partial x}, \tag{4.4}$$

and

$$\zeta = \frac{\partial v}{\partial x} - \frac{\partial u}{\partial y}. \tag{4.5}$$

With these, the streamfunction-vorticity (ψ-ζ) form of the N-S equations (4.1)-(4.3) can be written as

$$-\frac{\partial^2\psi}{\partial x^2} - \frac{\partial^2\psi}{\partial y^2} = \zeta, \tag{4.6}$$

$$Re\frac{\partial\zeta}{\partial t} - \frac{\partial^2\zeta}{\partial x^2} - \frac{\partial^2\zeta}{\partial y^2} + uRe\frac{\partial\zeta}{\partial x} + vRe\frac{\partial\zeta}{\partial y} = 0. \tag{4.7}$$

4.3 Boundary Conditions

The top and bottom walls in both the cases are considered as fixed rigid ones throughout the channel and the usual no-slip condition is imposed thereat

$$u = v = 0. \tag{4.8}$$

Because of the symmetry of the flow about the horizontal centerline, we use

$$v = \frac{\partial u}{\partial y} = 0, \tag{4.9}$$

thereat. At the entrance, a parabolic velocity profile is prescribed:

$$\begin{aligned} u &= c_1(1 - c_2y^2), \\ v &= 0, \end{aligned} \tag{4.10}$$

where c_1 and c_2 are constants. The boundary conditions for ψ and ζ can be easily obtained from the equations (4.4) and (4.5). At the outlet, fully developed flow is considered.

4.4 Mesh Structure

We are considering forward and backward constricted channels, both of which have reentrant corners. To resolve the flow accurately at such corners we have incorporated the grid given in figures 4.2(a) and 4.2(b). The mesh structure for such a situation may be provided through a conformal transformation [94] which maps the actual nonuniform geometry (physical domain) (see figure 4.2 (a) and (b)) to a uniform rectangular geometry (computational domain) (see figure 4.2(c)) as follows:

$$z = w(A + B\tanh(w)), \tag{4.11}$$

where $z = x + iy$ and $w = \xi + i\eta$ ($i = \sqrt{-1}$) with

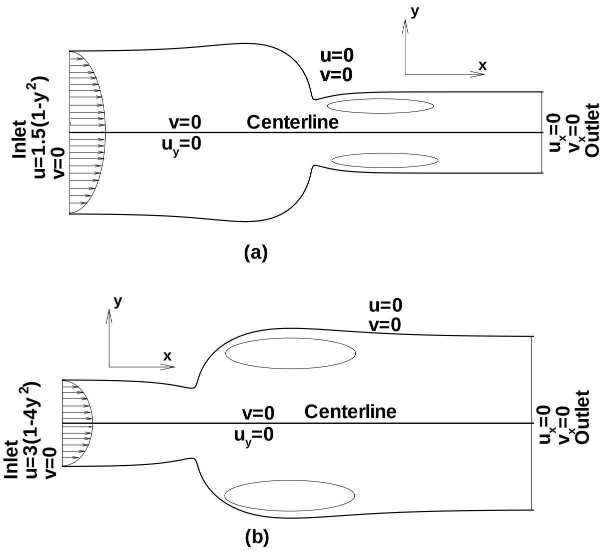

Figure 4.1: *(a) Forward (physical) and (b) backward (physical) constricted channel flow configuration with boundary conditions.*

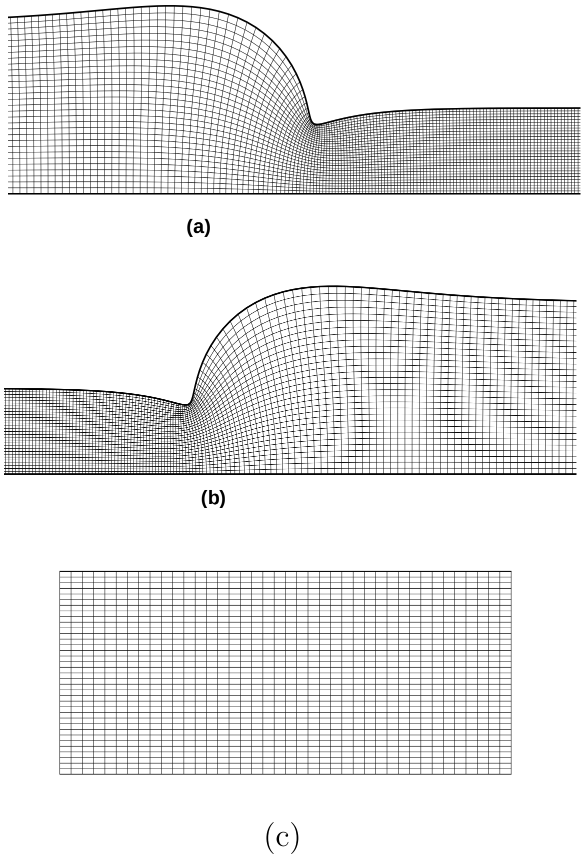

Figure 4.2: *Mesh structure for (a) forward (physical) constricted channel, (b) backward (physical) constricted channel and (c) mesh structure in computational plane.*

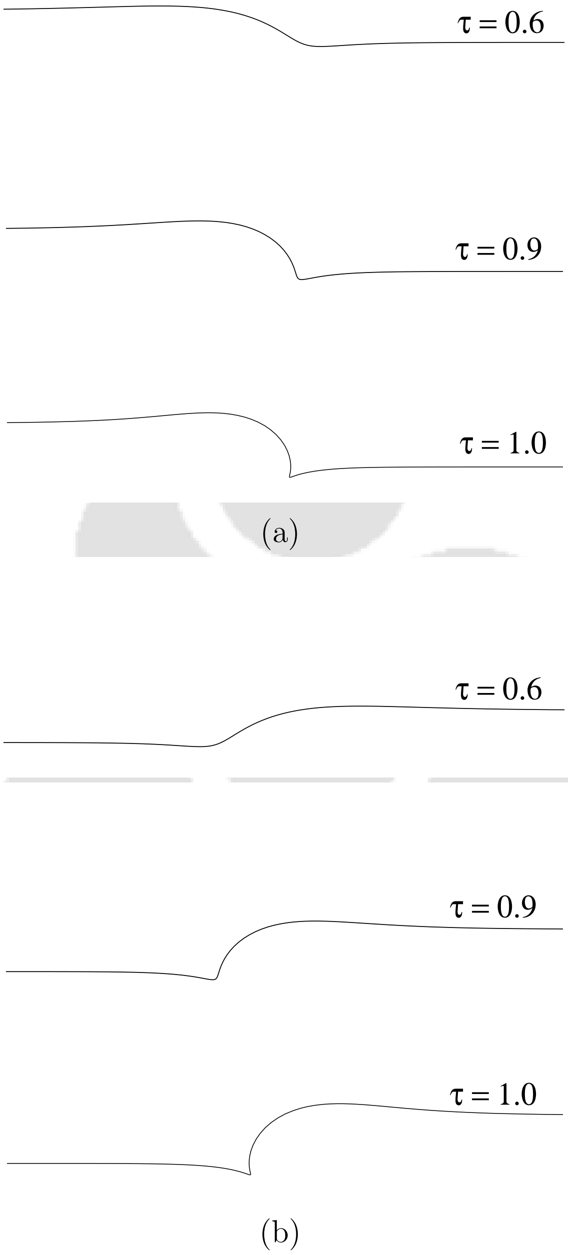

Figure 4.3: *Top boundaries for different degrees of sharpness of constriction in a (a) forward and (b) backward constricted channel.*

$$x = A\xi + \frac{B}{H}[\xi \sinh(2\xi) - \eta \sin(2\eta)], \tag{4.12}$$

$$y = A\eta + \frac{B}{H}[\eta \sinh(2\xi) + \xi \sin(2\eta)]. \tag{4.13}$$

Here $H = \cosh(2\xi)+\cos(2\eta)$; (ξ, η) are the coordinates in the computational plane. A and B are constants defined by $A = \dfrac{r_i + r_o}{2\tau}$, $B = \dfrac{r_o - r_i}{2\tau}$ where $2r_i$, $2r_o$ respectively are the inlet and outlet heights of the constricted channel and τ is a parameter controlling the smoothness as well as sharpness of the constriction: an increasing value of τ indicating a sharp corner. In the present computation, we have taken $r_i = 1$ and $r_o = 0.5$ for the channel with forward constriction [figure 4.1(a)], and $r_i = 0.5$ and $r_o = 1.0$ for the backward one [figure 4.1(b)]. We present the mesh distributions in figure 4.2(a) and 4.2(b). The varying shapes of the top boundary due to the above fixed inlet and outlet radii, and different choices of the degrees of sharpness of the constriction are shown in figure 4.3. One can see smooth corner for $\tau = 0.6$. But a slight variation in the value of τ can drastically change the sharpness of the corner as can be seen for $\tau = 0.9$ and $\tau = 1.0$.

4.5 Discretization and Related Issues

At the interior, to discretize equation (4.7) for ζ, we use the recently developed HOC scheme on irregular domains for 2D transient convection-diffusion (details can be found in section 3.2.2), whereas for ψ (equation (4.6)), we use its steady-state form. For the Neumann conditions at the outlet and the horizontal centerline, we use a one-sided five point formula prescribed in [143]. For example, for a typical flow variable ϕ (which may represent u, v, ψ or ζ) at the outlet (denoted by the index b along x-axis), we use

$$\phi_{b,j} = 0.04\left[48\phi_{b-1,j} - 36\phi_{b-2,j} + 16\phi_{b-3,j} - 3\phi_{b-4,j} - 12h\left(\frac{\partial \phi}{\partial y}\right)_{b,j}\right] + O(h^5),$$

where h is the x-step length in the physical plane. Finally, after discretization, the resulting matrix equation for ζ may be written as

$$A\mathbf{\Phi^{n+1}} = \mathbf{f}(\mathbf{\Phi^{n}}), \tag{4.14}$$

where the coefficient matrix A is an asymmetric sparse matrix with at most nine non-zero entries in each row. For a grid of size $m \times n$, A has dimension mn, and $\mathbf{\Phi^{n+1}}$ and $\mathbf{f}(\mathbf{\Phi^{n}})$ are mn-component vectors. To solve the system of equation (4.14)

Biconjugate Gradient Stabilized method (BiCGStab) [68,118,150] has been employed without any preconditioning. Steady state was assumed to reach when the following condition is satisfied,

$$\max|\zeta^{(n+1)} - \zeta^{(n)}| < 10^{-6}. \tag{4.15}$$

Here, $\zeta^{(n)}$ denotes numerical value of ζ at n-th time level.

NOTE: In addition to grid step and the tolerance of the iterative procedure, the position of upstream and the downstream boundary affect the correctness of the numerical solution. We have numerically experimented and found that the minimum inlet distance from the throat should be $x \approx -8$ and -10 for forward and backward constricted channel respectively to eliminate the throat effect at the inlet. And to get fully developed flow at the outlet for Reynolds numbers up to $Re = 1000$ (for $\tau = 0.6$), $Re = 750$ (for $\tau = 0.9$) and $Re = 500$ (for $\tau = 1.0$) we experimented and found a common minimum distance from the throat as $x \approx 25$ in the case of forward constricted channel whereas for backward constricted channel we experimented and found the distances as $x \approx 45$ for Reynolds numbers up to $Re = 500$ (for $\tau = 0.6$), and $x \approx 30$ up to $Re = 250$ (for $\tau = 0.9$ and 1.0). However, these distances depend on the parameters (Re, width of the channel). In all the computations, we have used step lengths $\Delta\xi = \frac{1}{20}, \frac{1}{25}, \frac{1}{30}$ and $\frac{1}{40}$ along the horizontal, and $\Delta\eta = \frac{1}{30}$ and $\frac{1}{40}$ along the vertical direction in the computational plane for the corner flow geometry defined by $\tau = 0.6,\ 0.9$ and 1.0, and time step $\Delta t = 0.001$ in all the cases.

4.6 Results and Discussions

4.6.1 General flow behavior study

Generally, flows in constricted channel develop closed separation bubbles (also called as recirculation zones or vortex) immediate after the channel throat. In addition to the appearance of vortices, some more complex flow phenomena are usually seen in the case of transient flows, which do not occur in the case of steady flows. Locating centers of such vortices are difficult from the vorticity field since there is no unique relation between vorticity contours and separated recirculating zones. The strength of a vortex is defined by the difference between the Max (ψ) in the calculated region and ψ at the wall, and its center is defined by the point at which ψ attains its maximum value. Besides the formation of a strong vortex there exists a large velocity gradient in the flow field, this combination could cause several new phenomena. Therefore, it is important to study the flow characteristics. A description of the various possible steady state laminar flow patterns is perhaps best rendered by a display of streamlines and vorticity contours for different degrees of constrictions as well as flow parameters.

In the following two subsections, we have presented results of numerical solutions of the N-S equations for unsteady flow in a nonuniform rigid channel with a forward constriction or backward constriction having a smooth corner with increasing sharpness. Extensive set of model cases have been considered to study the numerical and physical aspects of the flow.

4.6.2 Flow in a channel with forward constriction

In this section, numerical study of flows in a symmetric channel with forward constriction has been presented. Numerical results are compared with that of Mancera et al. [94, 95] and they are in excellent agreement. As they do not give numerical data in a tabular form, the graphical results were optically scanned to produce the cited quantities. Three model cases have been considered as given in table 4.1. We have restricted our study up to $Re = 1000$. The channel geometries used in [94, 95] are closely approximated by our models given in table 4.1. It should be mentioned that for all the models convergent solutions have been obtained over a wide range of Reynolds numbers. Time marching steady state results with zero initial condition have also been presented in the form of tables (table 4.3 and 4.5) as well as in the form of figures (figure 4.4 - 4.9).

Table 4.1: *Geometries of forward constricted channel and Reynolds number range studies.*

Model	Degrees of constriction (τ)	Reynolds number range for calculations	Computed separation Reynolds number
M_1	0.6	1-1000	no separation
M_2	0.9	1-750	168.0
M_3	1.0	1-500	separation is seen for $Re = 1$

Table 4.2: *Location of the corner (x, y_{min}) in the forward constricted channel for different τ.*

τ	(x, y_{min})
0.6	(0.940104, 0.436011)
0.7	(0.750907, 0.428928)
0.8	(0.635091, 0.418853)
0.9	(0.530827, 0.404055)
1.0	(0.450649, 0.381584)

Table 4.3: *Separation and reattachment points in the forward constricted channel flow for $\tau = 0.9$ and 1.0.*

τ	Re	Separation points (x,y)	Reattachment points (x,y)
0.9	170	(0.65909, 0.42473)	(0.87626, 0.45733)
	250	(0.57916, 0.41010)	(1.25243, 0.485207)
	500	(0.53085, 0.40407)	(2.25000, 0.49930)
	750	(0.51741, 0.40409)	(3.33335, 0.49997)
1.0	50	(0.51349, 0.40068)	(0.64651, 0.43568)
	100	(0.46394, 0.38384)	(1.17478, 0.48834)
	250	(0.45065, 0.38158)	(2.64998, 0.49993)
		(0.456, 0.383) [94]	(2.55, 0.499) [94]
	500	(0.45065, 0.38158)	(5.27500, 0.50000)

Table 4.4: *Vortex center in the forward constricted channel flow for $\tau = 0.9$ and 1.0.*

τ	Re	Vortex center (x,y)	Max(ψ)
0.9	250	(0.8283, 0.4258)	1.00085
	500	(1.1198, 0.4105)	1.00896
	750	(1.4326, 0.4084)	1.01778
1.0	100	(0.6759, 0.3964)	1.00381
	250	(1.0674, 0.3684)	1.02781
	500	(1.6519, 0.3645)	1.04359

Flow in a forward constricted channel is symmetric which is shown in figure 4.4. Therefore, we have considered one half planar area (upper half plane) of the forward constricted channel for the numerical calculations.

It has been numerically experimented that no separation zone is formed in the range of the Reynolds numbers studied (given in table 4.1) for model $M_1(\tau = 0.6)$, whereas in model $M_2(\tau = 0.9)$ separation starts to occur at approximately $Re = 168$ and in the case of model $M_3(\tau = 1.0)$ separation is seen for Reynolds number as low as 1.

In figure 4.5, the first column illustrates the curves of constant streamfunction for a fixed τ ($\tau = 0.8$) with different Re values and the second column represents the same for a fixed Re with different degrees of constriction. It is evident that there is no separation zone even for $Re = 500$ in the geometry defined by $\tau = 0.6, 0.7$ respectively whereas a small recirculation zone develops in the case of $\tau = 0.8$. It is

Table 4.5: *Error analysis of the constricted channel flow problem for different Res* ($\tau = 0.6$).

Re		Errors		Order
		$\|\phi_M - \phi_C\|_\infty$	$\|\phi_F - \phi_M\|_\infty$	
1.0	ψ	1.705187e-03	1.111000e-04	3.94
	ζ	1.124975e-02	7.101000e-04	3.43
	u	2.822500e-03	7.080000e-04	3.99
	v	3.531502e-03	2.238000e-04	3.98
10.0	ψ	3.060635e-03	2.008000e-04	3.93 (3.60 [95])
	ζ	2.208857e-02	1.371000e-03	4.01 (3.75 [95])
	u	1.892129e-02	1.232800e-03	3.94
	v	1.216307e-02	7.870000e-04	3.95
100.0	ψ	8.086469e-03	6.353000e-04	3.67 (1.48 [95])
	ζ	4.897917e-02	2.998200e-03	4.03 (3.69 [95])
	u	8.545852e-02	7.047700e-03	3.60
	v	5.004434e-02	4.070300e-03	3.62

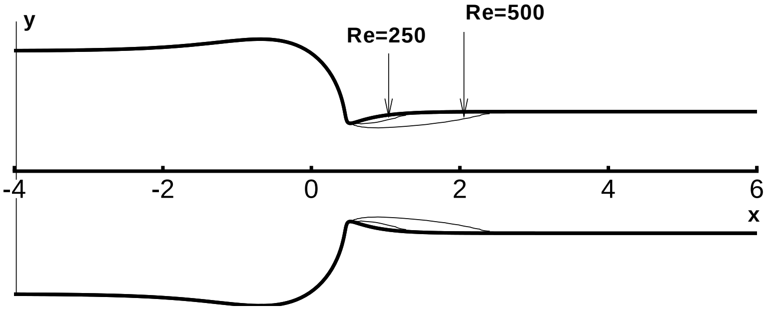

Figure 4.4: *separation lines in the forward constricted channel flow defined by* $\tau = 0.9$ *for Re=250 and 500.*

also seen that in the case of $\tau = 0.8$, even for higher *Res* (e.g. *Re*=750, 1000) the size of the recirculation region is small in compared to lower *Re* (e.g. *Re*=500) in the case of model $M_2(\tau = 0.9)$ and $M_3(\tau = 1.0)$. The above facts conclude that the corner sharpness is more important for the development of corner vortex than velocity (or

Re).

In figure 4.6, we have presented the corresponding vorticity contours for figure 4.5. It shows the existence of several high gradient regions around the throat in the flow domain. It can be emphasized that changes in area around the throat of the channel due to different degrees of sharpness could be the main reason for the flow disturbance and the generation of different sizes of vortices.

Separation and reattachment points for different *Re*s are presented in the table 4.3 for $\tau = 0.9$ and $\tau = 1.0$ respectively. For $Re = 250$ in the case of $\tau = 1.0$, we have compared our results with [94] (given in table 4.3) and an excellent agreement has been found. It is seen that the separation length increases with the increase in *Re*s for both the model cases. In comparison to table 4.2 it is also seen that in the case of model $M_2(\tau = 0.9)$, the separation point occurs in the downstream side of the corner for *Re* as large as 500 but for higher *Re* (say $Re = 750$) separation point occurs just immediately before the corner whereas in the case of model $M_3(\tau = 1.0)$, the separation point starts to occur at corner for $250 \leq Re \leq 500$.

In table 4.4, the center of the vortex and its strength have been presented for different *Re*s with different degrees of constriction. It reveals that for a fixed *Re* the center of the vortex shifts towards downstream with the increase in degrees of constriction and the same phenomenon occurs for a fixed τ with increase in *Re*.

As no analytical solution exists for the problem, in order to estimate the grid convergence rate for this problem, we compute the steady-state solution on three different grid sizes 161×16, 321×31 and 641×61 (denoted by C, M and F respectively). Then the formula for grid convergence rate of a variable ϕ (which represents u, v, ψ or ζ here) is

$$\alpha_R = \frac{\ln\left((\|\phi^M - \phi^C\|_\infty)/(\|\phi^F - \phi^M\|_\infty)\right)}{\ln 2}, \tag{4.16}$$

where

$$\|\phi^F - \phi^M\|_\infty = \max_{i,j} |\phi^F_{i,j} - \phi^M_{i,j}|. \tag{4.17}$$

We present these results in table 4.5 for three Reynolds numbers, namely, 1, 10, 100. All the flow variables show approximately a fourth order grid convergence as expected. We have compared our computed grid convergence rate based on maximum error with those in [95] (presented here within parentheses).

Figure 4.7 shows the variation of centerline velocity with axial location for the model $M_1(\tau = 0.6)$, $M_2(\tau = 0.9)$ and $M_3(\tau = 1.0)$ for different *Re*s. It has been seen that the peak velocity occurs after the throat. It is also noticed that with the increase in degrees of sharpness of the reentrant corner the peak velocity value increases. Another important observation is that for degree of sharpness $\tau = 0.6$, the change in velocity pattern is quite different from the other patterns for $\tau = 0.9$ and

$\tau = 1.0$ respectively. The related physics of such flow patterns needs more discussion.

Since there is no reliable experimental method to determine wall shear-stress near the recirculation zone, we try to get some information about wall shear stress (wall-vorticity value) theoretically. Figure 4.8(a) shows the changes in wall vorticity along the x-direction for different Res in the case of model $M_1(\tau = 0.6)$. It may be mentioned that no separation region has been noticed even for Re as large as 1000 for model $M_1(\tau = 0.6)$. Peak shear stress value occurs at $x = 0.683569$ even with increase in Re. Likewise, in the case of model $M_2(\tau = 0.9)$ (can be seen from figure 4.8(b)), the peak shear stress occurs at the same point ($x = 0.485673$) just immediately before the corner (throat) even with increase in Re. For model $M_3(\tau = 1.0)$ peak shear stress value occurs at the corner (not shown in picture). Thus, it can be stated that for forward constricted channel peak shear stress values occur at the corner or near to the corner along upstream. In addition to this it is also seen that the region of recirculation increases with increase in Re (which is evident from the negative values of shear stress). That is a central jet, issued from the constriction, creates a potential core bounded by a shear layer which links up to the wall by a recirculation zone. The rapid increase in wall vorticity with Re for the sharp constriction is quite apparent.

Figure 4.9 shows the vector plots of the flow field. A parabolic flow was prescribed at the inlet. As soon as it reaches the throat of the constriction, the flow profile is changed to a blunt shaped non-parabolic profile with a negative flow zone near the wall. This figure also reveals that the profile slowly regains the parabolic shape as it moves along the downstream. The negative velocity near the wall indicates the existence of separation zone.

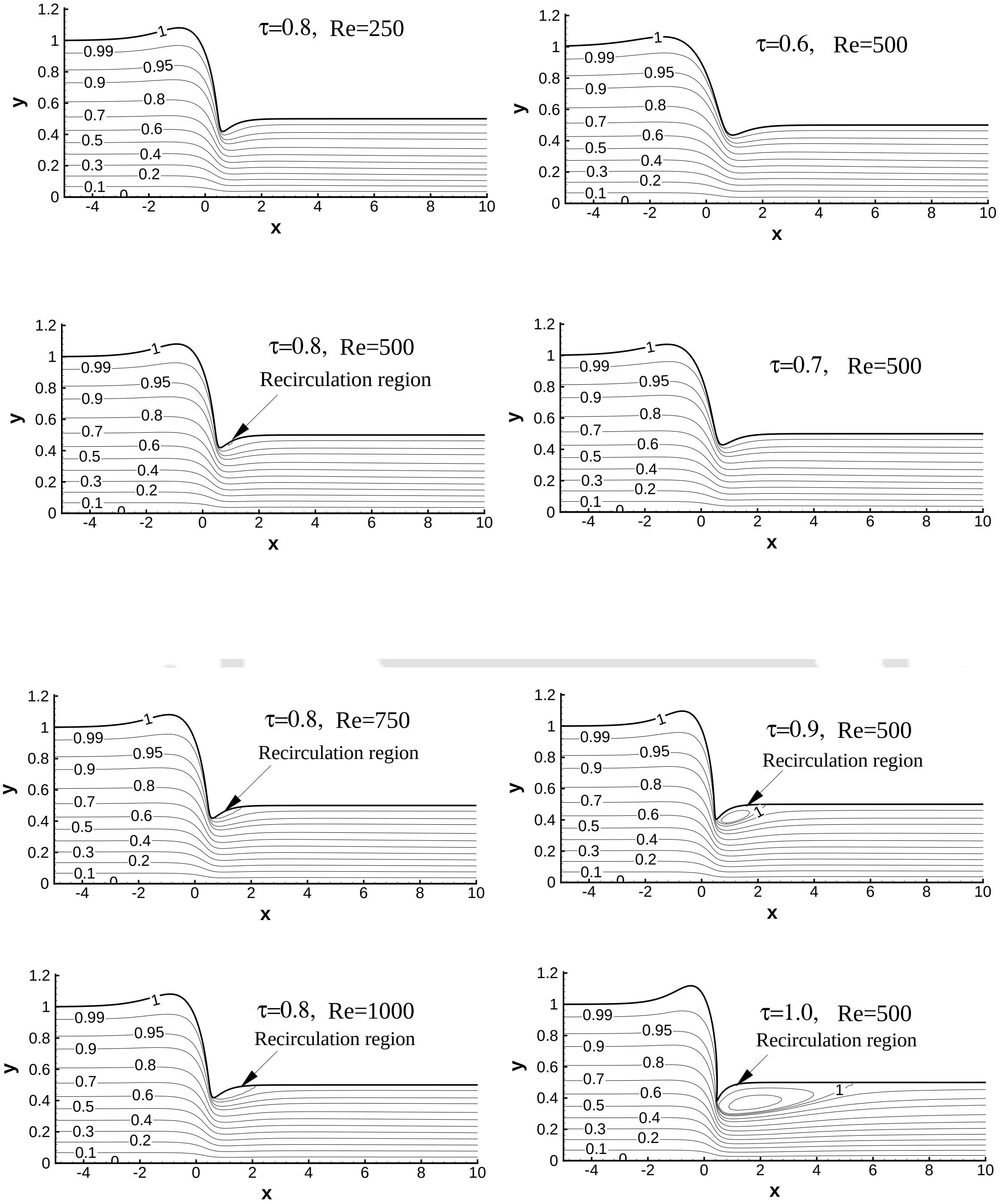

Figure 4.5: *In a forward constricted channel: the first column corresponds to streamline contour for fixed* $\tau = 0.8$ *with different* Re *and the second column corresponds to streamline contour for* $Re = 500$ *with different* τ.

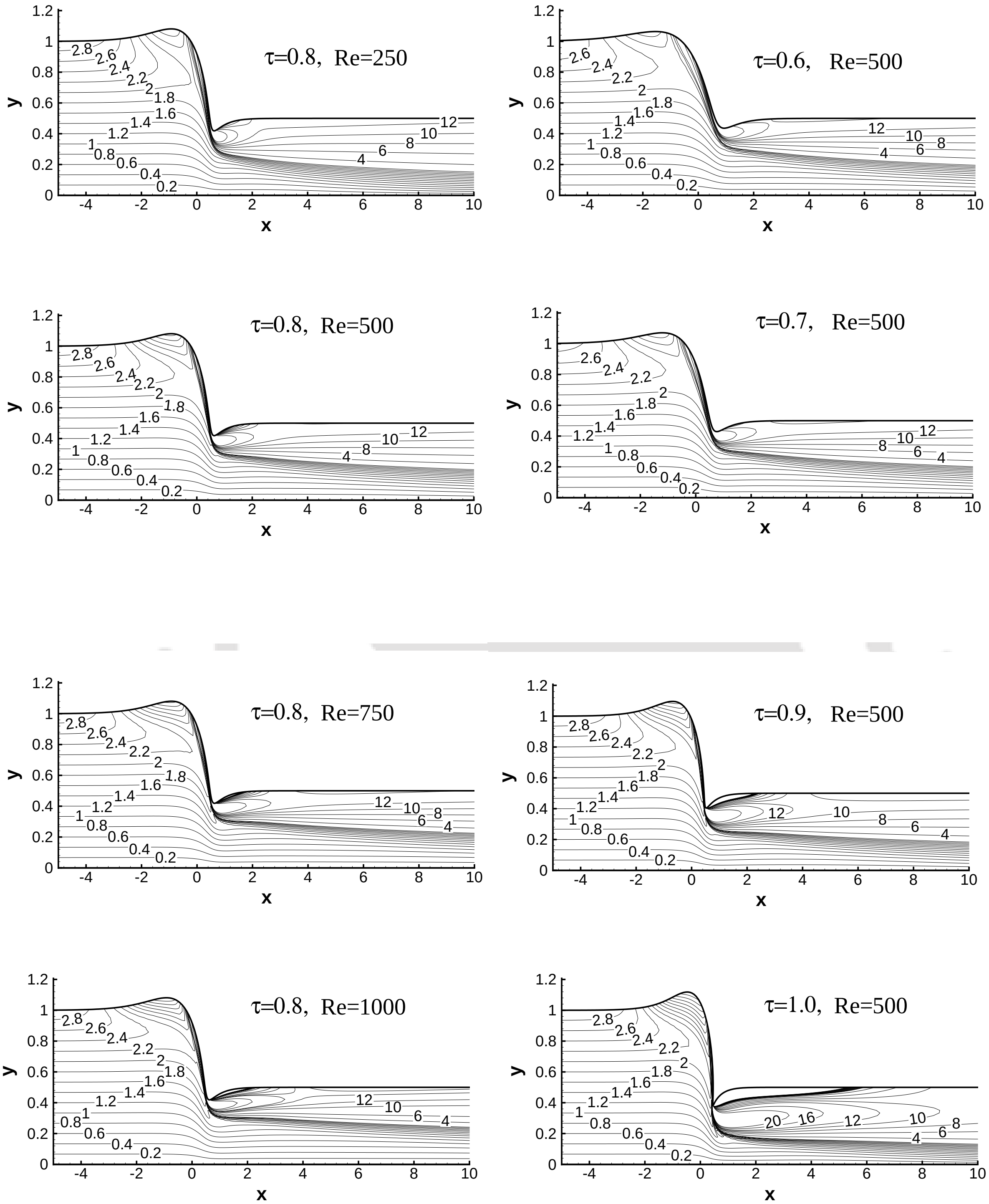

Figure 4.6: *In a forward constricted channel: the first column corresponds to vorticity contour for fixed* $\tau = 0.8$ *with different* Re *and the second column corresponds to vorticity contour for* $Re = 500$ *with different* τ.

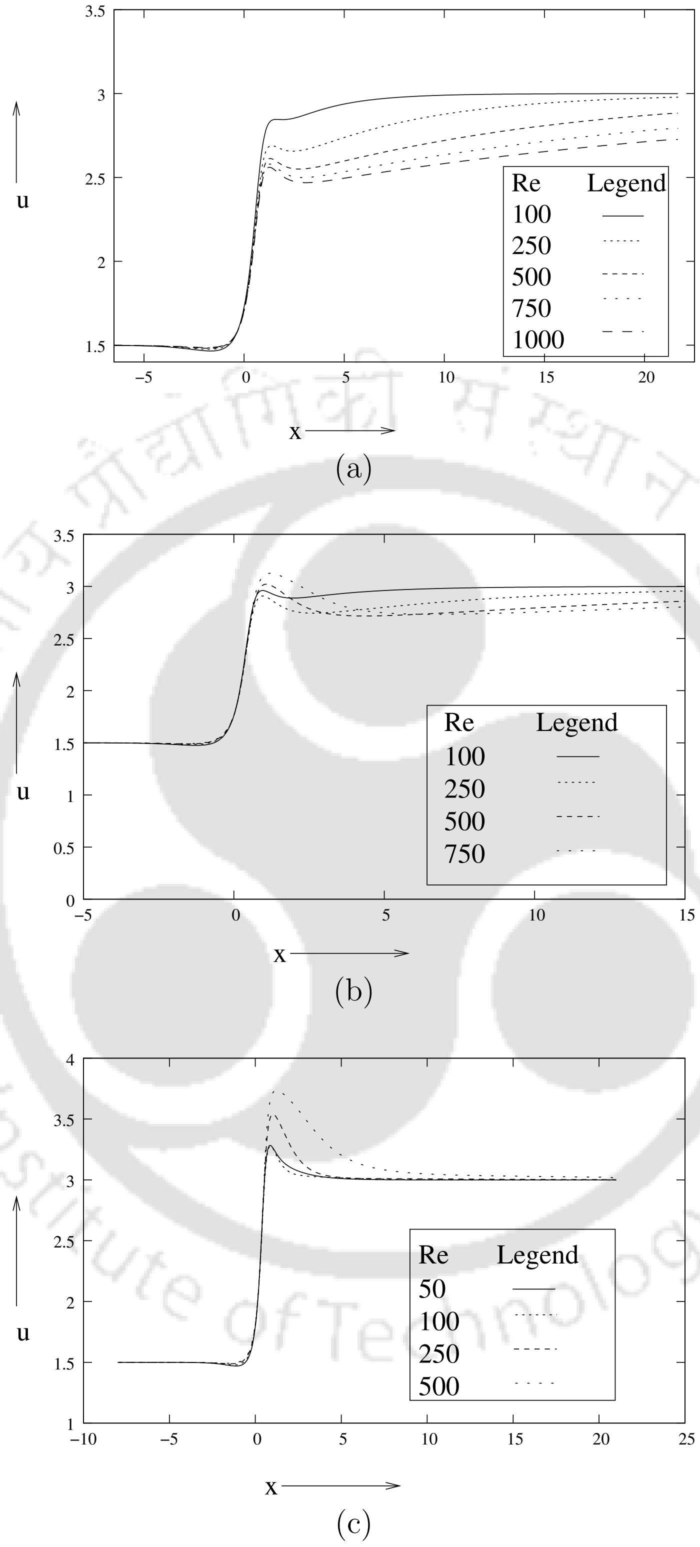

Figure 4.7: *In a forward constricted channel: centerline axial velocity for (a)* $\tau = 0.6$, *(b)* $\tau = 0.9$ *and (c)* $\tau = 1.0$.

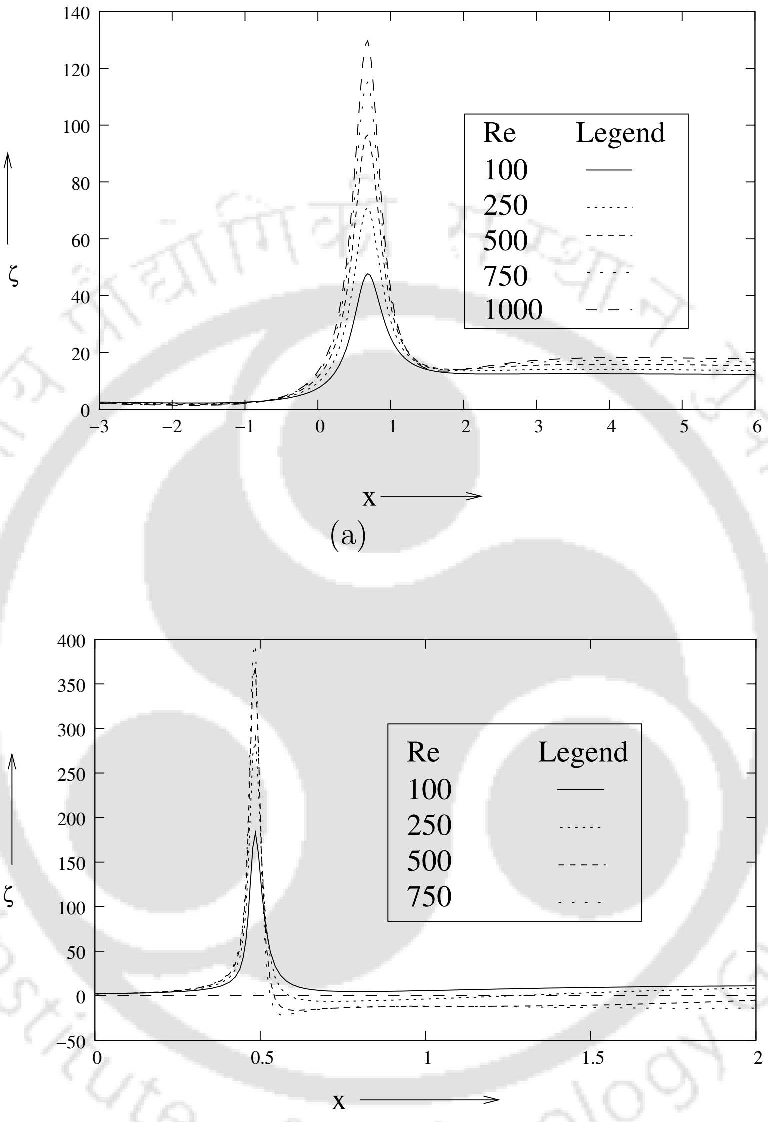

(b)

Figure 4.8: *In a forward constricted channel: wall vorticity for (a)* $\tau = 0.6$ *and (b)* $\tau = 0.9$.

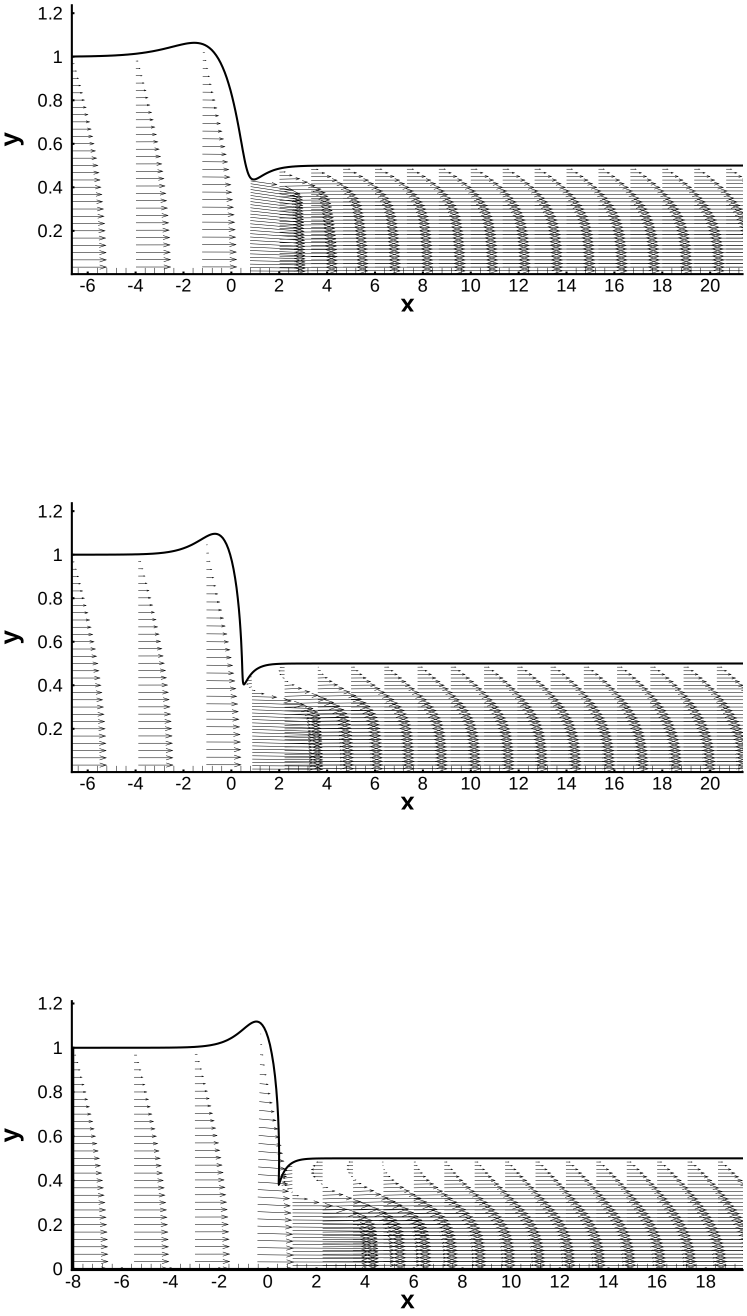

(c)

Figure 4.9: *In a forward constricted channel: velocity profile for (a)* $\tau = 0.6, Re = 1000$*, (b)* $\tau = 0.9, Re = 750$ *and (c)* $\tau = 1.0, Re = 500$.

4.6.3 Flow in a channel with backward constriction

Numerical results for flow in a channel with backward constriction have been presented in this section. The degree of sharpness of the corner has been considered same as in the case of forward constricted channel. Table 4.6 shows the range of Reynolds numbers studied and the critical *Res* for flow separation for different values of τ (called as model m_1, m_2 and m_3).

Table 4.6: *Geometries of backward constricted channel and Reynolds number range studied.*

Model	τ	Reynolds number range for calculations	Computed separation Reynolds number
m_1	0.6	1-500	15.0
m_2	0.9	1-250	4.0
m_3	1.0	1-250	separation is seen for $Re = 1$

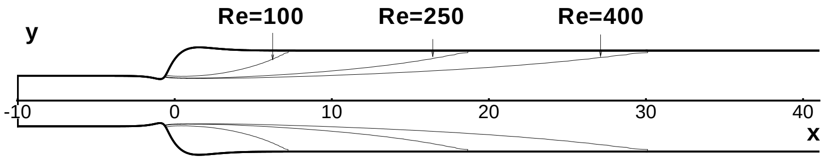

Figure 4.10: *Separation lines in the backward constricted channel flow geometry defined by $\tau = 0.6$ for Re=100, 250 and 400.*

It is worthwhile mentioning that for a prescribed parabolic flow at the inlet and symmetric flow boundary condition at the centerline, we observed a symmetric flow behaviour (shown in figure 4.10) in the backward constricted channel. Our observations concur with those made by Pedrizzetti [112]. However, it differs with the observations made in the studies of [38,130,137] where occurrence of flow asymmetry has been discussed. This difference between these two sets of observations may be due to the use of different channel geometries (right angled and 45^0 sloped expansion) and different inlet flow condition (oscillatory flow) used by [38, 130, 137].

Table 4.7: *Vortex center of the backward constricted channel flow for* $\tau = 0.6, 0.9$ *and 1.0.*

τ	Re	Vortex center (x,y)	Max(ψ)
0.6	50	(1.0697, 0.7319)	1.0310
	100	(1.7848, 0.7035)	1.0556
	250	(3.0080, 0.6450)	1.0687
0.9	50	(0.9178, 0.6716)	1.0871
	100	(1.4778, 0.6428)	1.0966
	250	(3.0330, 0.6162)	1.0929
1.0	50	(0.8919, 0.6383)	1.1208
	100	(1.4081, 0.6030)	1.1214
	250	(3.5194, 0.6013)	1.1125

Table 4.7 shows the vortex center and the maximum value of ψ for all three model cases. It is seen from this table that in each model the center of the vortex moves towards downstream with the increase in *Re*. It is also noticed that for fixed lower *Re* ($Re = 50, 100$), the center of the vortex moves towards upstream with increase in degrees of constriction and for $Re = 250$ it moves towards downstream. It is because of the fact that up to a certain *Re*, τ becomes responsible for shifting the vortex center towards upstream for a fixed *Re*. Beyond that τ acts differently.

In table 4.8, we have presented the separation and reattachment points for all the three model cases. It is seen that for model $m_1(\tau = 0.6)$ and $m_2(\tau = 0.9)$, as *Re* increases the separation point moves slightly towards the upstream and the reattachment point moves towards downstream whereas for model $m_3(\tau = 1.0)$ the separation point almost remains unchanged though the reattachment point moves towards downstream, which can be observed from figure 4.11(a), 4.12(a) and 4.13(a) respectively. As a result the large amplitude vortex develops in the downstream side of the corner in all cases. It is also seen that for model $m_1(\tau = 0.6)$ a large vortex develops even for *Re* as small as 50. The increase in area just after the constriction in the case of backward constricted channel flow causes pressure loss which brings out a large recirculation region.

Figures 4.14 and 4.15 show a time-wise evolution of the streamlines for $Re = 100$ in the case of model $m_1(\tau = 0.6)$ and $m_2(\tau = 0.9)$ respectively. For the model

Table 4.8: *Separation and reattachment points for the backward constricted channel flow for* $\tau = 0.6, 0.9$ *and 1.0.*

τ	Re	Separation points (x,y)	Reattachment points (x,y)
0.6	50	(-0.4940, 0.5600)	(3.5680, 1.0199)
	100	(-0.5677, 0.5186)	(7.2497, 1.0005)
	250	(-0.6188, 0.4939)	(18.6667, 1.0000)
0.9	50	(-0.4728, 0.4317)	(4.2593, 1.0010)
	100	(-0.4777, 0.4239)	(8.5000, 1.0000)
	250	(-0.4857, 0.4151)	(21.6668, 1.0000)
1.0	50	(-0.4478, 0.3829)	(4.7600, 1.0002)
	100	(-0.4479, 0.3829)	(9.4000, 1.0000)
	250	(-0.4478, 0.3829)	(23.2800, 1.0000)

$m_1(\tau = 0.6)$ at t=2.5, there is a small separated region in the downstream of the throat with a strong vortex at $x \approx 1$(given in figure 4.14). As time evolves the separated region becomes larger with a weaker vortex at $x \approx 2$, which can be seen from the figure 4.14. At t=20.0, the flow becomes nearly steady by forming a large vortex. On the other hand for the model $m_2(\tau = 0.9)$, (given in figure 4.15) intermediate flow features become more complicated. The separation region increases gradually with time. At t=2.5 a small separation region evolves with a strong vortex at x $\approx$ 0. As time passes (say t=5.0 or 10.0), the vortex grows and splits into a number of smaller vortices. When flow approaches the steady state (say at t=20.0), these small vortices coalesce and formed a larger separated region.

The centerline velocity data has been presented in figure 4.16 for each model with different Res. It shows that for each model the peak of the centerline velocity occurs just immediately after the throat for lower Res and the peak shifts slightly towards downstream with the increase in Re. It is also noticed that in each model for lower Res the centerline velocity decreases sharply up to a small distance along the downstream just after reaching its peak value and then it behaves asymptotically to attain a constant value (for example, it is 1.5 for $Re = 50$) whereas for higher Res, this decrease is linear from its peak value. This could be explained as follows. For a model, at lower Re the size of the vortex is smaller in comparison with the size of the vortex in higher Re. However, this vortex behaves as an obstacle. After the throat, the velocity gradient is high for a smaller vortex compared to larger vortex. For larger one the velocity gradient is dying out slowly. This fact causes the decrease in centerline velocity sharply for smaller one and linearly for larger one.

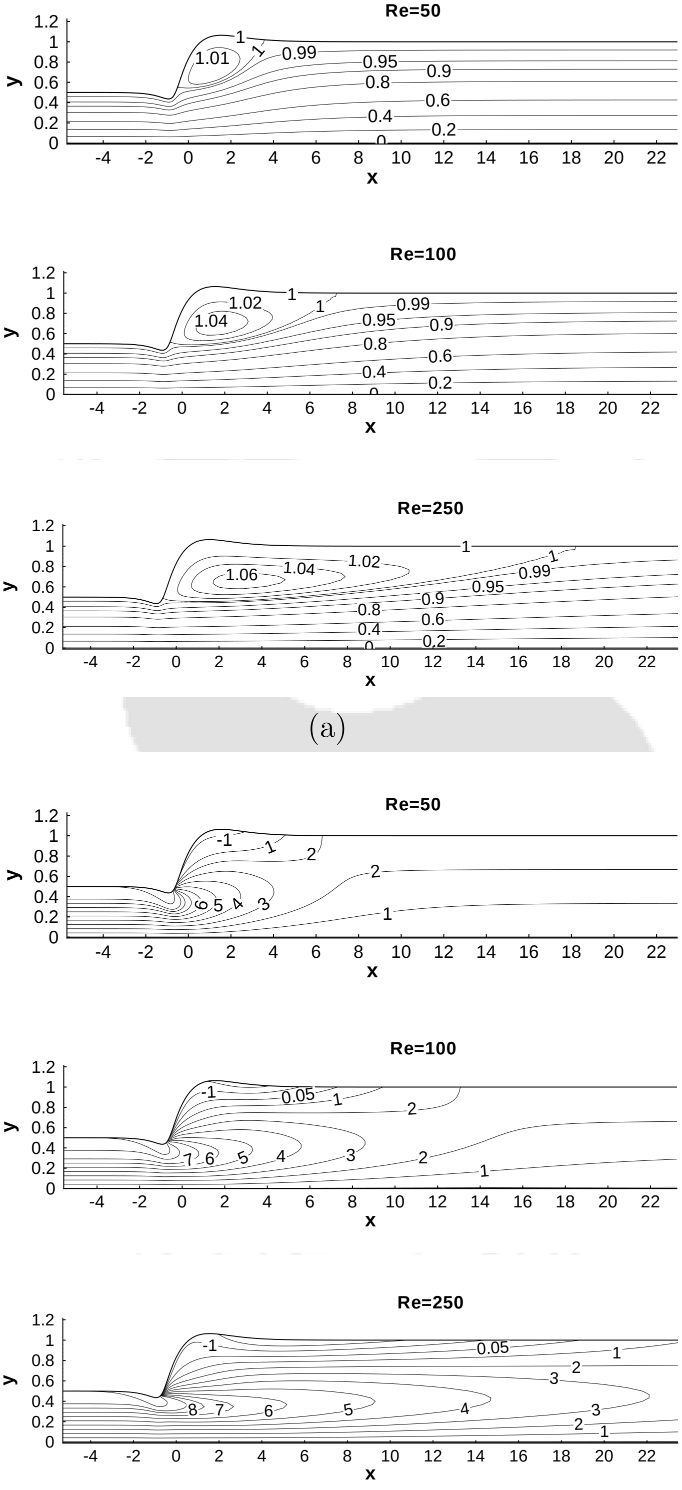

(a)

(b)

Figure 4.11: *In a backward constricted channel: (a) streamline-contours and (b) corresponding vorticity contours for* $\tau = 0.6$.

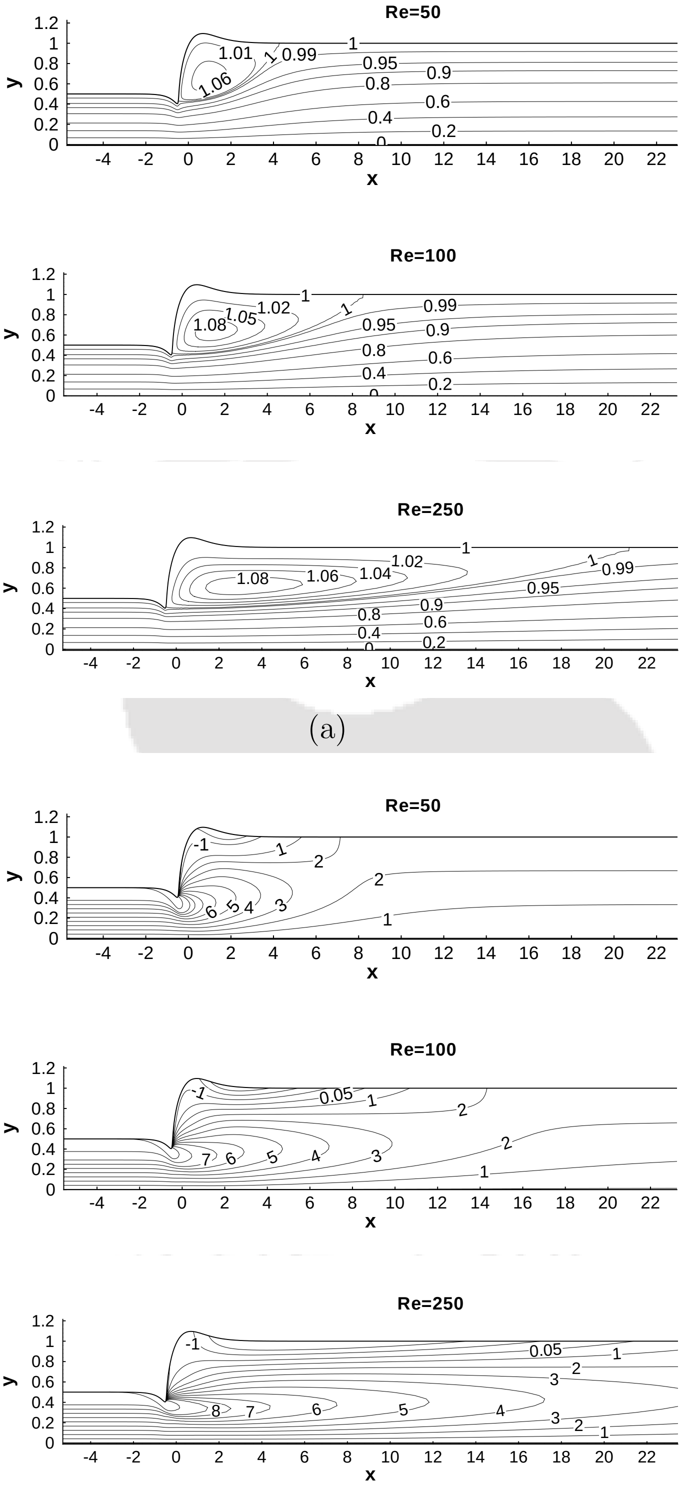

(a)

(b)

Figure 4.12: *In a backward constricted channel: (a) streamline-contours and (b) corresponding vorticity contours for* $\tau = 0.9$.

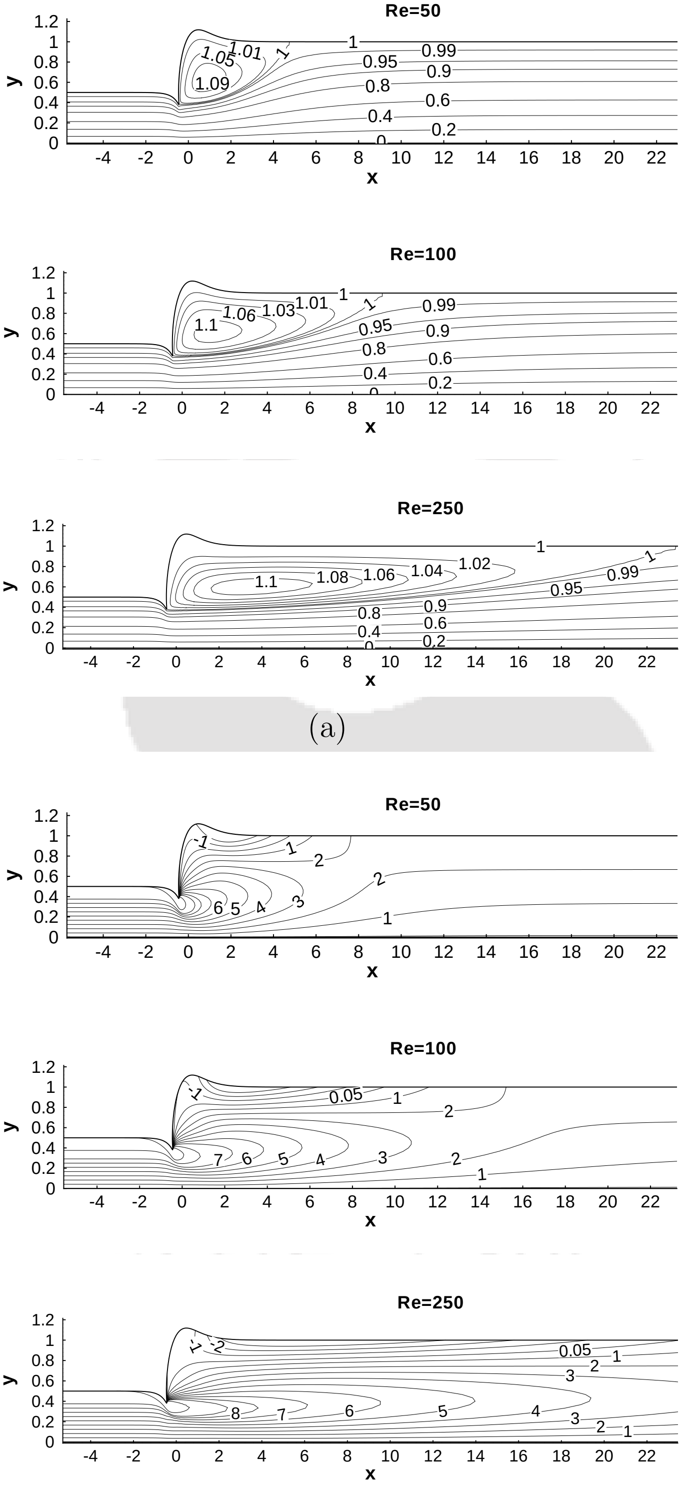

Figure 4.13: *In a backward constricted channel: (a) streamline-contours and (b) corresponding vorticity contours for* $\tau = 1.0$.

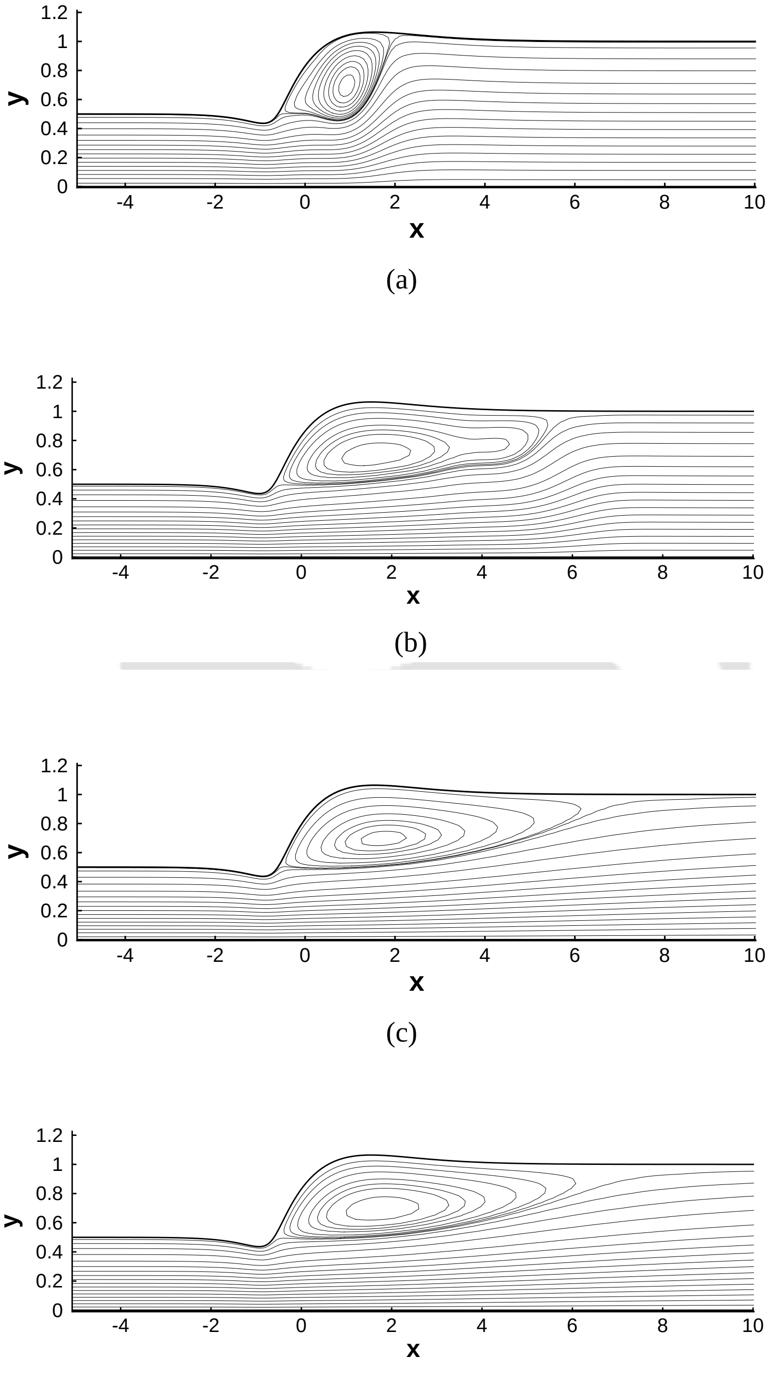

Figure 4.14: *Time evolution for* $\tau = 0.6$, $Re = 100$ *at (a) t=2.5, Max*(ψ) $= 1.13756$, *(b) t=5.0, Max*(ψ) $= 1.05486$, *(c) t=10.0, Max*(ψ) $= 1.05534$ *and (d) t=20.0, Max*(ψ) $= 1.05525$ *in a backward constricted channel.*

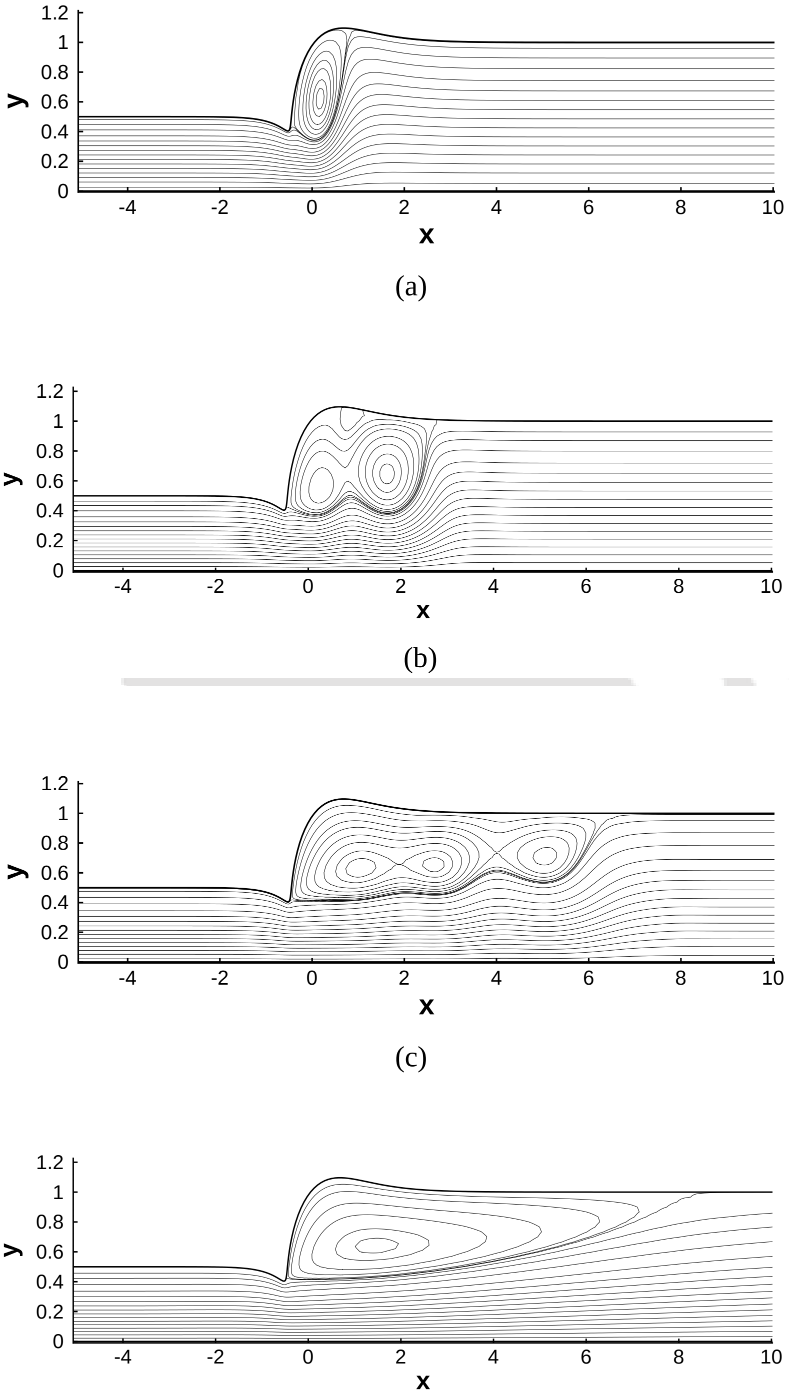

(a)

(b)

(c)

(d)

Figure 4.15: *Time evolution for* $\tau = 0.9$, *Re* $= 100$ *at (a) t=2.5, Max*$(\psi) = 1.33982$, *(b) t=5.0, Max*$(\psi) = 1.25592$, *(c) t=10.0, Max*$(\psi) = 1.10354$ *and (d) t=20.0, Max*$(\psi) = 1.09789$ *in a backward constricted channel.*

In figure 4.17 we have presented magnified view (see figures 4.17 (a), (b) and (c)) of the change in shear stress values for $Re = 250$ in each model in a small neighborhood of the reentrant corner. Also we have presented the wall shear stress (wall vorticity) values for each model with different Res (see figures 4.17 (a′), (b′) and (c′)). From figures 4.17 (a), (b) and (c) respectively for models $m_1(\tau = 0.6)$, $m_2(\tau = 0.9)$ and $m_3(\tau = 1.0)$, it is seen that around the throat, the change in shear stress values is sharp with the increase in degrees of constriction. In each of the three models the maximum shear stress value occurs just immediately before the corner. In figures 4.17(a′) and (b′) it has been noticed that with the increase in Re the location of the peak shear stress shifts slightly to upstream and it occurs at the onset of the corner whereas figure 4.17(c′)) for model $m_3(\tau = 1.0)$ shows that the peak shear stress values occur at the same point. In addition to this, it is noticed that the peak value of the wall shear stress increases significantly with the increase in degrees of constriction. As in the case of forward constricted channel, the negative vorticity values in figures 4.17 (a′), (b′) and (c′) represent the regions of flow separation.

Figure 4.18 shows the vector plots of the flow field. Like forward constricted channel a parabolic flow was prescribed at the inlet. It retains the parabolic shape at the throat with a negative velocity zone in the expansion region. As the profile moves along the downstream, slowly the parabolic part is extended vertically and the negative flow zone is reduced. Finally after some distance negative zone disappears and a parabolic velocity profile is regained in downstream of the channel.

In comparison of the flow field in the backward constricted channel with the same in the forward constricted channel, it is noticed that for a fixed Re the area of the negative velocity zone i.e separation zone in backward constricted channel is greater than that in the forward constricted channel. It is because of the fact that after the throat the upstream flux in the forward constricted channel reduces substantially along downstream due to contraction. Again, after the throat of the forward constricted channel geometry at $\tau = 0.9$ and 1.0, a small area increased, for which a small vortex forms. In the case of backward constricted channel, after the throat the upstream flux diffuses in an expanded large region which causes high pressure drops resulting a large separation zone.

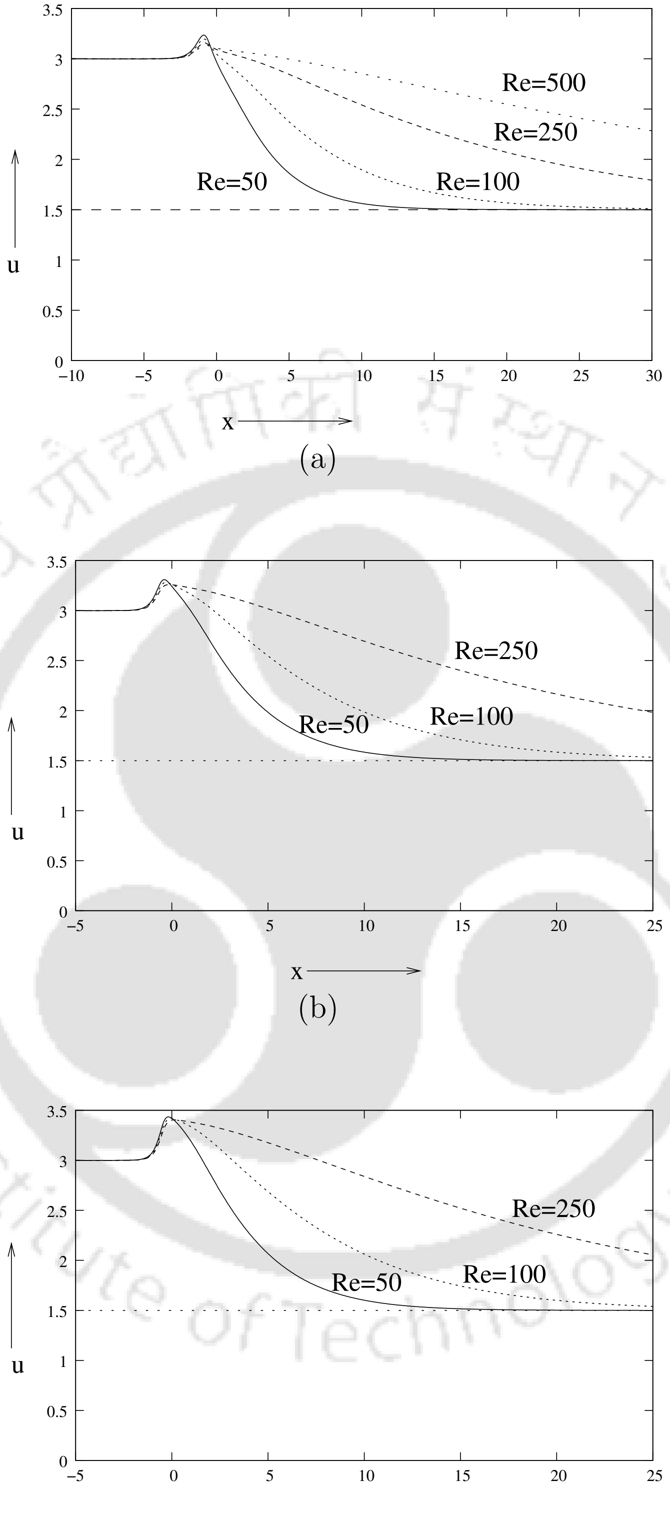

(c)

Figure 4.16: *In a backward constricted channel: centerline axial velocity for (a)* $\tau = 0.6$, *(b)* $\tau = 0.9$ *and (c)* $\tau = 1.0$.

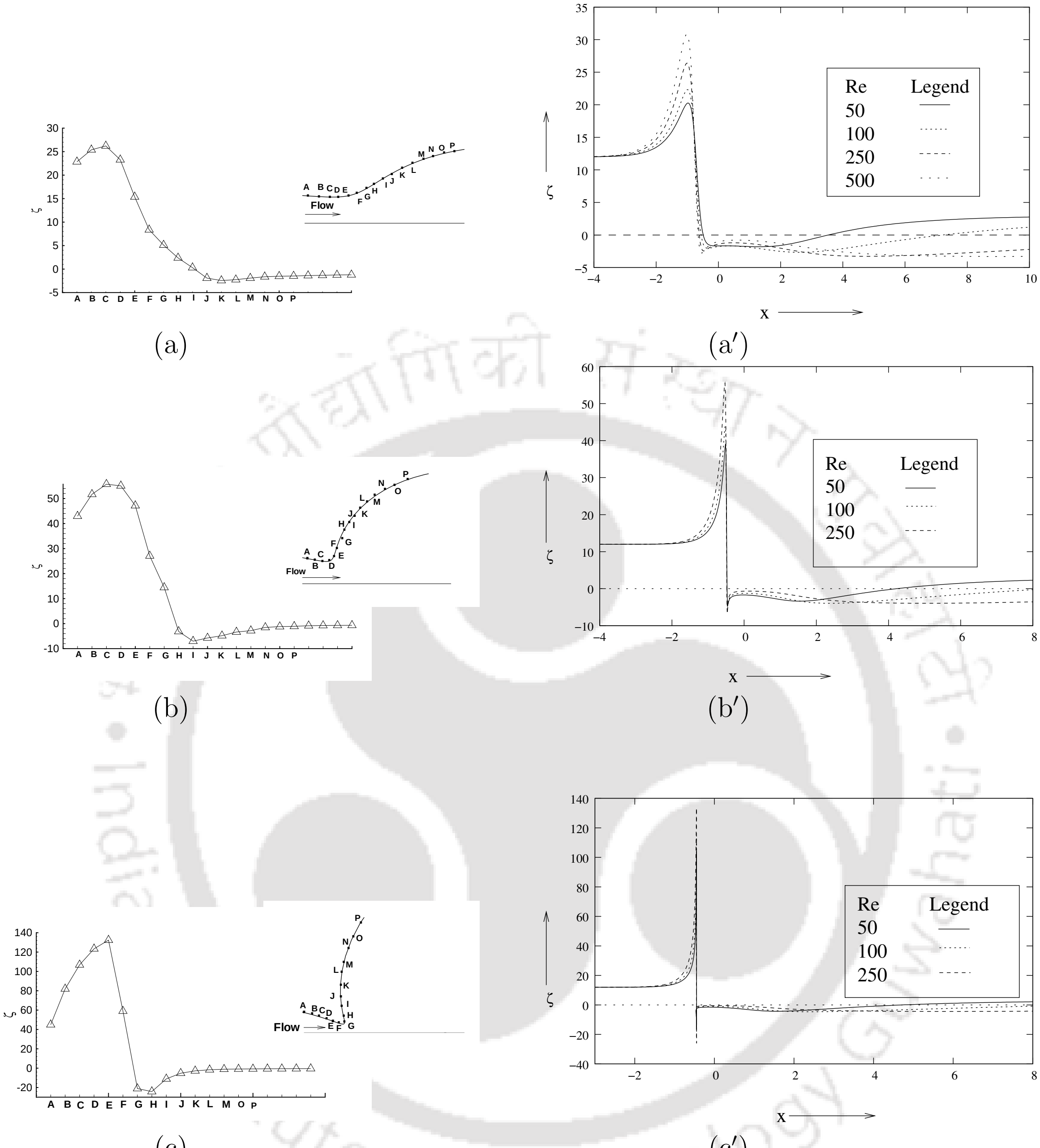

Figure 4.17: *in a backward constricted channel, wall shear-stress: (a), (b) and (c) respectively present the magnified view of the wall shear stress at the top wall around the throat for* $Re = 250$ *with* $\tau = 0.6$, $\tau = 0.9$ *and* $\tau = 1.0$, *and (a′), (b′) and (c′) respectively present the change of wall shear stress in a large part of the domain for different Res and different* τ ($\tau = 0.6$, $\tau = 0.9$ *and* $\tau = 1.0$).

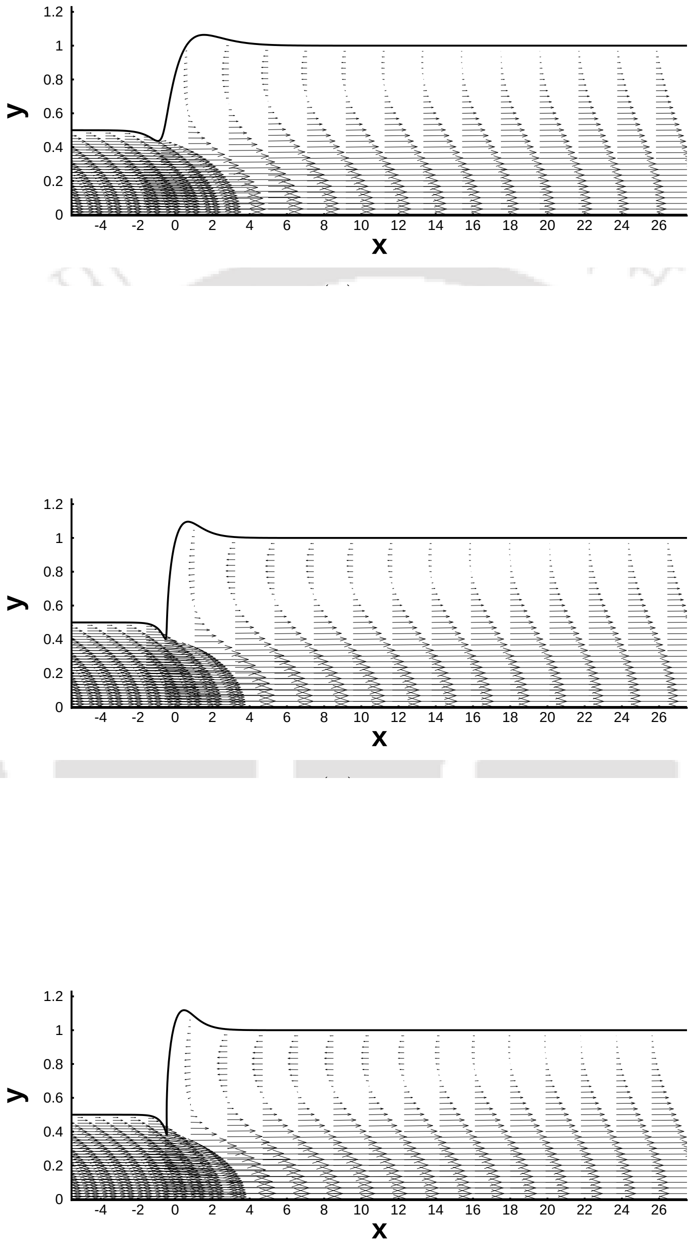

(c)

Figure 4.18: *In a backward constricted channel: velocity profile for Re* = 250 *(a)* $\tau = 0.6$, *(b)* $\tau = 0.9$ *and (c)* $\tau = 1.0$.

4.7 Conclusions

In this chapter, a comparison study has been made between the transient flows in an symmetric channel with both forward and backward constriction. The governing equations have been solved using proposed higher order compact (HOC) schemes presented in chapter 3. We have explored in detail the related issues. Some interesting features of the flow in both the channel geometries have been presented. The channel geometry as well as sharpness of the throat of the channel are the important parameters to control the strength and size of the separation zone without modifying the general flow patterns. Generally, flow separation takes place at the corner or along downstream of the corner. For flow through a channel with forward constriction, it can be mentioned that flow separation does not occur for $\tau \leq 0.7$ even at higher Res (say Re=1000) but flow separation has been observed at the throat when $Re = 500, \tau = 0.8$. The size of the vortex developed in the forward constricted channel flow is small compared to that in backward constricted channel flow. In the case of backward constricted channel there is a sudden change in shear stress values from positive to negative whereas in the case of forward constricted channel this change is smooth. The parabolic flow profile prescribed at the inlet of the forward constricted channel becomes blunter (non-parabolic) near the throat and in the case of backward constricted channel, the shape of the flow profile at the inlet is maintained along the downstream. The axial symmetry in the flow pattern has been noticed throughout the channel. It can also be pointed out that the generation of a series of vortices [146] has not been observed in this study because of using symmetric boundary condition. However, the present study enriches various aspects of channel flows and provides a good opportunity to encompass in detail the flow patterns. As we have produced the steady state convergent results for a wide range of Reynolds numbers and an excellent agreement with [94] demanding that our code is correct and has the capability to produce highly accurate results for complex geometries beyond rectangular. The present chapter in conjunction with our previous chapter focuses on the robustness of our recently proposed scheme in chapter 3. In the next chapter we have discussed incompressible viscous flows in an asymmetric channel.

Chapter 5

Dynamical flow characteristics of incompressible viscous flows through asymmetric channels

5.1 Introduction

The past several years have seen a significant research efforts to solve the incompressible viscous channel flows governed by Navier-Stokes equations. In many channel flow systems, the development of recirculation region due to a sudden large scale nonuniform expansion of the flow passages (i.e. flow phenomena in an asymmetric channel with backward constriction) play an important role which is of practical as well as of theoretical interests. Among such channels, the classic backward facing step flow has been prescribed as benchmark problems. The importance of such flow phenomena has been studied both in numerically [2, 8, 11, 38, 74, 75, 116] and experimentally [3, 8, 40, 44, 47]. In most of these studies, a right angled shaped step and steady flow conditions were considered. In comparison with the flow domain of the symmetric sudden expansion channel which consists of only one separated region in the downstream of the step, it is worthwhile mentioning that the flow domain of asymmetric backward-facing step flow develops more than one recirculation zone depending on Res and aspect ratios. Besides these step channels there exist other kinds of channel geometries which consist of gradual contraction followed by an expansion in a large region of flow domain by forming mild, moderate and severe sharp corner. Nowadays, technological interest and practical applications of these type of channel geometries are increasing in the field of designing of water channels, heat transfer performance of electronic chips and flow behaviors in diffusers etc. It is indicated the need of a better understanding of the effects of expansion ratios and the sharpness of the corners in the asymmetric channel with backward constriction.

Therefore, the present study focuses on the unsteady flow phenomena in an asymmetric nonuniform rigid channel with backward constriction having mild, moderate and severe sharp corners. The present study in conjunction with our previous work focussing on the transient flow analysis for the asymmetric channel and the robustness of our proposed scheme in chapter 3.

In this chapter, numerical solutions are performed to quantify the effects of the corner geometries (mild, moderate and severe sharp corner) upon the flow characteristics (stream lines, size and intensity of recirculation vortices) in asymmetric channels with expansion ratios ($= D = \frac{D_1}{D_2}$, where D_1 and D_2 are the inlet and outlet radius of the channel) 1:2 and 1:4. The parameters studied include Reynolds numbers (Re), degrees of constriction (τ) and channel expansion ratios (D).

5.2 The problem

We consider incompressible viscous fluid flows in an asymmetric channel with backward constriction having mild, moderate and severe reentrant corners. The nonuniform geometry is formed as a result of gradual contraction and then expansion. The schematic flow diagrams and corresponding boundary conditions are shown in figure 5.1(a). To resolve the flow accurately at the reentrant corner of the backward constricted channel, we have used the grid given in figure 5.1(b). The comparatively large spacing of the grid near the expansion region after the throat caused no problems as the flow is not particularly vigorous there. The mesh structure for such a situation may be provided through a conformal transformation [94] which maps the actual nonuniform geometry (physical domain) to a uniform rectangular geometry (computational domain) as follows:

$$z = w(A + B\tanh(w)),$$

where $z = x + iy$ and $w = \xi + i\eta$ ($i = \sqrt{-1}$)
with (The derivation given in Appendix J)

$$x = A\xi + \frac{B}{H}[\xi\sinh(2\xi) - \eta\sin(2\eta)],$$
$$y = A\eta + \frac{B}{H}[\eta\sinh(2\xi) + \xi\sin(2\eta)].$$

Here $H = \cosh(2\xi) + \cos(2\eta)$; A and B are the constants. The constants A and B are defined by $A = \dfrac{r_i + r_o}{2\tau}$, $B = \dfrac{r_o - r_i}{2\tau}$ where r_i and r_o respectively are the inlet and outlet radii of the channel with τ controlling the smoothness and the degree of sharpness of the constriction; a higher value of τ indicates a more sharper corner. We

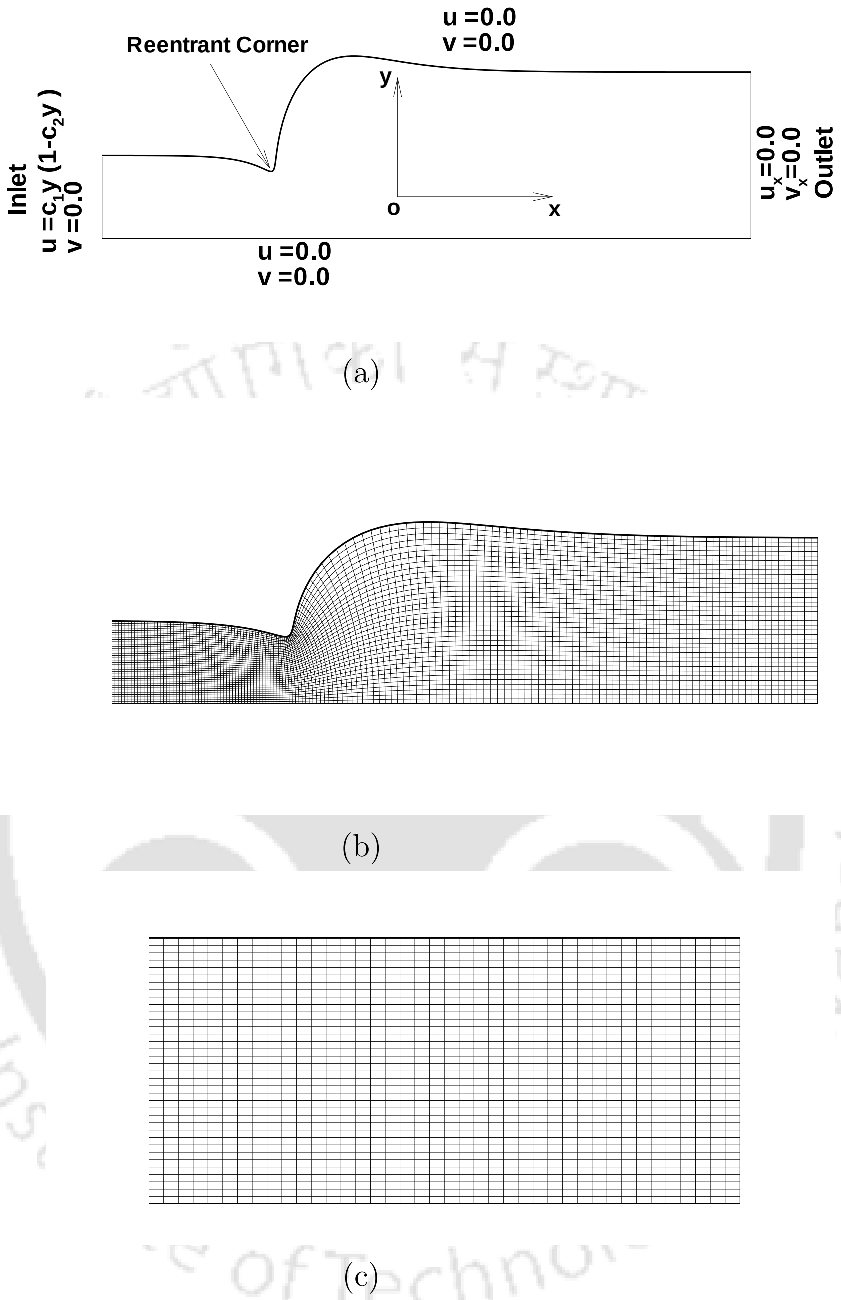

(a)

(b)

(c)

Figure 5.1: *(a) Backward (physical) constricted channel geometry with boundary conditions, (b) associated mesh structure in physical plane and (c) corresponding mesh structure in computational plane.*

define the corners correspond to $\tau = 0.6$ as mild, $\tau = 0.9$ as moderate and $\tau = 1.0$ as severe sharp corner. To obtain the geometry in the physical plane for $\tau = 0.6$ we have used $-12.0 \leq \xi \leq 28.0$, $0.0 \leq \eta \leq 0.6$; for $\tau = 0.9$ we have used $-18.0 \leq \xi \leq 32.0$, $0.0 \leq \eta \leq 0.9$; and for $\tau = 1.0$ we have used $-20.0 \leq \xi \leq 30.0$, $0.0 \leq \eta \leq 1.0$. In the present computation for a channel with expansion ratio 1:2, the inlet and the outlet radii are taken as $r_i = 0.5$ and $r_o = 1.0$ respectively whereas for expansion ratio 1:4, the inlet and the outlet radii are taken as $r_i = 0.25$ and $r_o = 1.0$ respectively. We present the mesh distributions in physical plane and computational plane as in figure 5.2(b) and (c) respectively.

The governing equations for the 2D unsteady incompressible viscous asymmetric channel flows are the N-S equations, which in non-dimensional primitive variable formulation can be written as

$$\frac{\partial u}{\partial x} + \frac{\partial v}{\partial y} = 0, \tag{5.1}$$

$$\frac{\partial u}{\partial t} + u\frac{\partial u}{\partial x} + v\frac{\partial u}{\partial y} = -\frac{\partial p}{\partial x} + \frac{1}{Re}\nabla^2 u, \tag{5.2}$$

$$\frac{\partial v}{\partial t} + u\frac{\partial v}{\partial x} + v\frac{\partial v}{\partial y} = -\frac{\partial p}{\partial y} + \frac{1}{Re}\nabla^2 v, \tag{5.3}$$

where u, v are velocities along x-, y-directions respectively, p is the pressure, t is the time and Re is the Reynolds number given by $Re = \dfrac{Lu_0}{\nu}$, where L is the unperturbed channel width at the outlet, u_0 is the average velocity at the entrance and ν is the kinematic viscosity.

To eliminate p, we may introduce streamfunction $\psi(x, y, t)$ and vorticity $\zeta(x, y, t)$ in terms of u and v as

$$u = \frac{\partial \psi}{\partial y}, \qquad v = -\frac{\partial \psi}{\partial x}, \tag{5.4}$$

and

$$\zeta = \frac{\partial v}{\partial x} - \frac{\partial u}{\partial y}. \tag{5.5}$$

With these, the streamfunction-vorticity (ψ-ζ) form of the N-S equations (5.1)-(5.3) can be written as

$$-\frac{\partial^2 \psi}{\partial x^2} - \frac{\partial^2 \psi}{\partial y^2} = \zeta, \tag{5.6}$$

$$Re\frac{\partial \zeta}{\partial t} - \frac{\partial^2 \zeta}{\partial x^2} - \frac{\partial^2 \zeta}{\partial y^2} + uRe\frac{\partial \zeta}{\partial x} + vRe\frac{\partial \zeta}{\partial y} = 0. \tag{5.7}$$

The boundary conditions at top and bottom walls in both the cases (aspect ratio 1:2 and 1:4) are the usual no-slip condition which follow

$$u = v = 0. \tag{5.8}$$

At the entrance, a parabolic velocity profile is prescribed:

$$\begin{aligned} u &= c_1 y(1 - c_2 y), \\ v &= 0, \end{aligned} \tag{5.9}$$

where c_1 and c_2 are constants. The boundary conditions for ψ and ζ can be easily obtained using (5.4) and (5.5). At the outlet, fully developed flow is considered.

5.3 Discretization and Related Issues

The governing N-S equations (5.6, 5.7) in $\psi - \zeta$ variables maintain their forms under a conformal transformation. We have followed the same discretization procedure as discussed in section 3.2.2. We use a Crank-Nicholson type scheme which is second order accurate in time. For the Neumann boundary conditions at the outlet, we use an one-sided five point formula [143]

$$\phi_{b,j} = 0.04\left[48\phi_{b-1,j} - 36\phi_{b-2,j} + 16\phi_{b-3,j} - 3\phi_{b-4,j} - 12h\left(\frac{\partial \phi}{\partial y}\right)_{b,j}\right] + O(h^5),$$

where h is the x-step length in the physical plane and ϕ (which may represent u, v, ψ or ζ) is a typical flow variable and the index b ($x_{\max}$) along x-axis denotes the outlet boundary whereas j is the y-direction index varying from 0 to $y_{\max}$. We have numerically experimented and found the minimum inlet distance $x \approx -10$ from the throat such that the throat effects on the inlet flow profile are negligible. In order to get the fully developed flow at the outlet, the length of the channel has been found out through numerical experiments for different flow conditions and sharpness of the corner. Flow simulations are carried out using grid steps $\Delta\xi = \dfrac{1}{20}$ and $\dfrac{1}{30}$ along the horizontal and $\Delta\eta = \dfrac{1}{40}$ along the vertical direction in the computational plane for the corner flow geometry defined by $\tau = 0.6,\ 0.9$ and 1.0. Both the steady-state results (which are produced in a time marching fashion) and the transient results have been produced with a time step $\Delta t = 0.001$ in all the cases. The governing equations are highly nonlinear and the use of nonuniform grid invariably leads to non-symmetric matrices. In order to solve these systems, we use the biconjugate gradient stabilized method (BiCGStab) [68,118,150] without preconditioning. Steady-state was assumed to reach when the following condition is satisfied:

$$\max|\zeta^{(n+1)} - \zeta^{(n)}| < 10^{-6} \tag{5.10}$$

where $\zeta^{(n)}$ denotes numerical value of ζ at n-th time level.

5.4 Results and Discussions

In the following two subsections, we have presented steady-state and transient solutions of the N-S equations for unsteady flow in a nonuniform rigid asymmetric channel with backward constriction for different expansion ratios and different degrees of constrictions. These results show the combined effects of Reynolds number, the aspect ratios and sharpness of the corners on the vortex structures for flows in the asymmetric channels.

5.4.1 Expansion ratio 1:2

Like axisymmetric channel flow problems discussed in previous chapter, we have considered here three model cases depending on the degrees of constriction. In table 5.1 we have cited the location of the corner of the asymmetric channel geometry for these defined degrees of constriction. We have restricted our study up to $Re = 750$.

Table 5.1: *Location of the corner* (x, y_{min}) *in the asymmetric backward constricted channel for different* τ*.*

Model	τ	(x, y_{min})
M_1	0.6	(-0.940104, 0.436011)
M_2	0.9	(-0.530827, 0.404055)
M_3	1.0	(-0.450649, 0.381584)

Table 5.2: *Geometries of asymmetric backward constricted channel and Reynolds number range studies.*

Model	Degree of constriction (τ)	Reynolds number range for calculations	Computed separation Reynolds number
M_1	0.6	1 - 750	80
M_2	0.9	1 - 750	19
M_3	1.0	1 - 500	4

Time marching steady state solutions with zero initial condition have been presented in the form of tables (table 5.2 - 5.4) as well as in the form of figures (figure 5.2 - 5.8) whereas the transient solutions have been shown in figures 5.9.

In table 5.2 we have presented critical Re values at which separation starts to occur for different degrees of sharpness of the corner. It has been numerically experimented and found that for $\tau = 0.6, 0.9$ and 1.0 the critical Re values are 80, 19 and 4 respectively. It shows that as degrees of constriction increase the critical Re values fall rapidly.

Figure 5.2 illustrates the curves of constant streamfunction for $\tau = 0.6$ with different Re values. It is seen that there is no separation zone at $Re = 50$. Only one recirculation region (primary vortex) develops just immediate after the throat and adjacent to the top wall for $Re = 100$ and 250. It is also seen that streamlines are slightly perturbed adjacent to the bottom wall after the throat for $Re = 250$. This could be the indication of the development of another separation zone (called secondary vortex). This prediction comes true with further increase in Re (see figure 5.2 for $Re = 500$). As Re increases the size of the two recirculation zones increase (see figure 5.2 for $Re = 750$).

In figures 5.3 and 5.4 for $\tau = 0.9$ and 1.0 respectively, almost the same flow phenomena are observed as in figure 5.2. One important observation is that the secondary vortex develops at a lower Reynolds number in comparison with the figure 5.2. In addition to this, it has also been noticed that the sizes of the vortices increase with the increase in degrees of sharpness of the corner.

Table 5.3: *Separation and reattachment points for the large vortex nearer to the top boundary of the asymmetric channel with expansion ratio 1:2 for different degrees of constrictions.*

τ	Re	Separation points (x, y)	Reattachment points (x, y)	Max(ψ))
0.6	50	-	-	0.5000
	100	(-0.3878, 0.6251)	(0.7235, 1.0196)	0.5010
	250	(-0.5845, 0.5097)	(3.0575, 1.0302)	0.5261
	500	(-0.6188, 0.4939)	(4.6618, 1.0075)	0.5385
	750	(-0.6515, 0.4803)	(5.3309, 1.0039)	0.5400
0.9	50	(-0.4705, 0.4363)	(0.7879, 1.0949)	0.5163
	100	(-0.4776, 0.4240)	(1.6502, 1.0472)	0.5444
	250	(-0.4857, 0.4151)	(3.1111, 1.0061)	0.5581
	500	(-0.4856, 0.4150)	(4.3317, 1.0008)	0.5556
	750	(-0.4857, 0.4152)	(5.1669, 1.0007)	0.5559
1.0	50	(-0.4474, 0.3835)	(1.0097, 1.0837)	0.5484
	100	(-0.4474, 0.3835)	(1.7972, 1.0284)	0.5716
	250	(-0.4474, 0.3836)	(3.1003, 1.0037)	0.5729
	500	(-0.4474, 0.3835)	(4.2502, 1.0003)	0.5697

From table 5.3, it is seen that for $Re = 50$, no separation occurs at $\tau = 0.6$ but

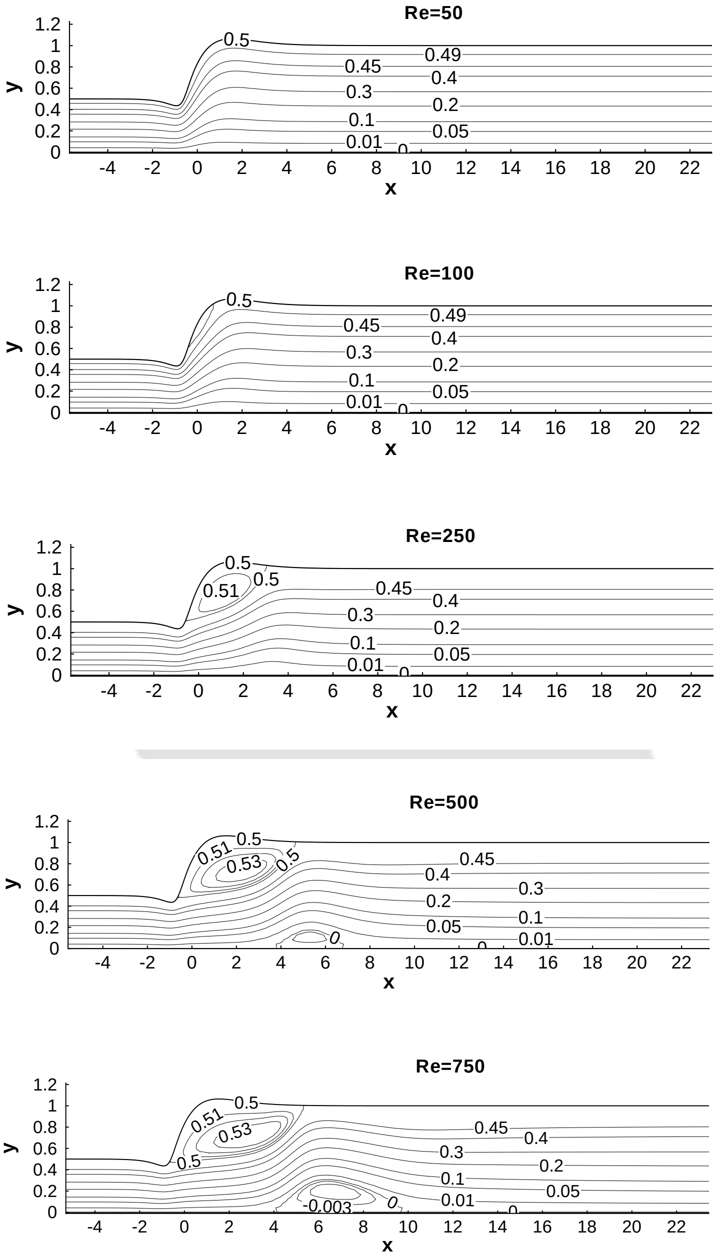

Figure 5.2: *In the asymmetric backward constricted channel (expansion ratio 1:2): streamline contours at* $\tau = 0.6$ *for Re=50, 100, 250, 500 and 750.*

separation is prominent for other two cases ($\tau = 0.9$ and 1.0). This could be explained by seeing the changes of maximum ψ values. If there is no separation zone in the flow domain, the maximum ψ value always occurs at the top boundary in steady-state

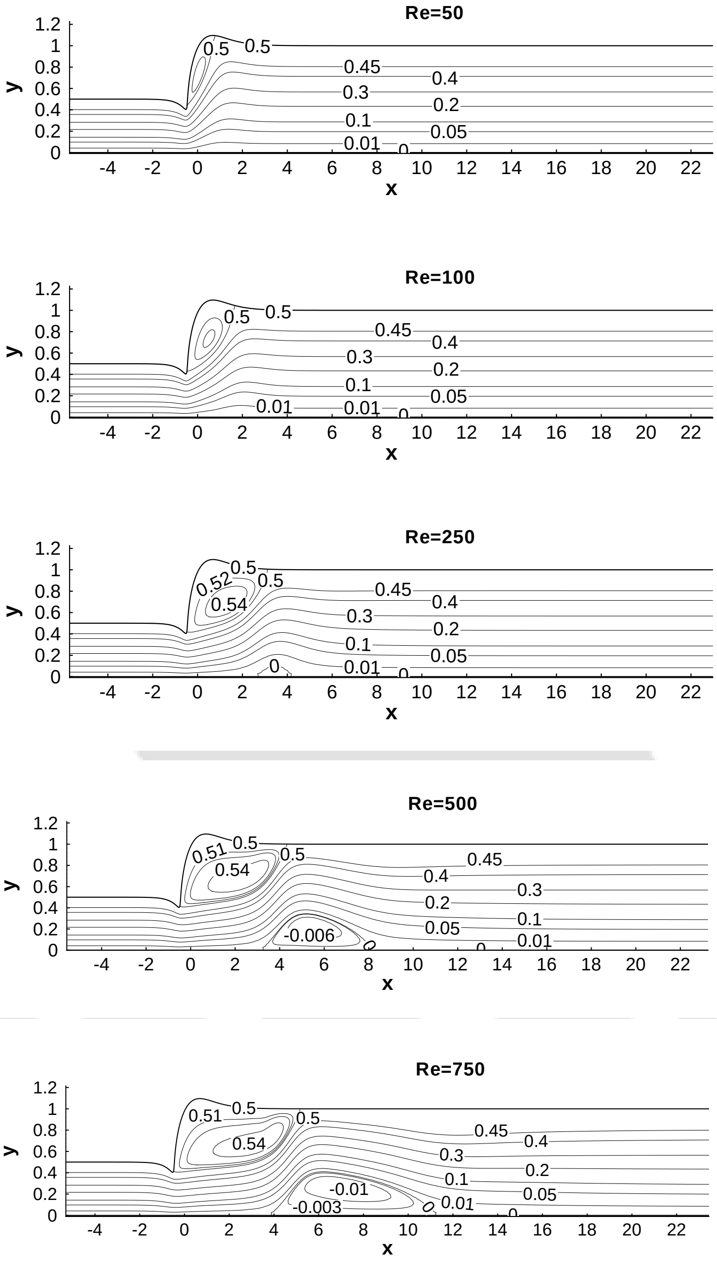

Figure 5.3: *In the asymmetric backward constricted channel (expansion ratio 1:2): streamline contours at* $\tau = 0.9$ *for Re=50, 100, 250, 500 and 750.*

solution for a prescribed parabolic profile at the inlet. For $Re = 50$ with degree of constriction $\tau = 0.6$, the maximum ψ value (0.5) occurs at the top boundary. This fact confirms that there is no separation, whereas change in maximum ψ value (e.g.

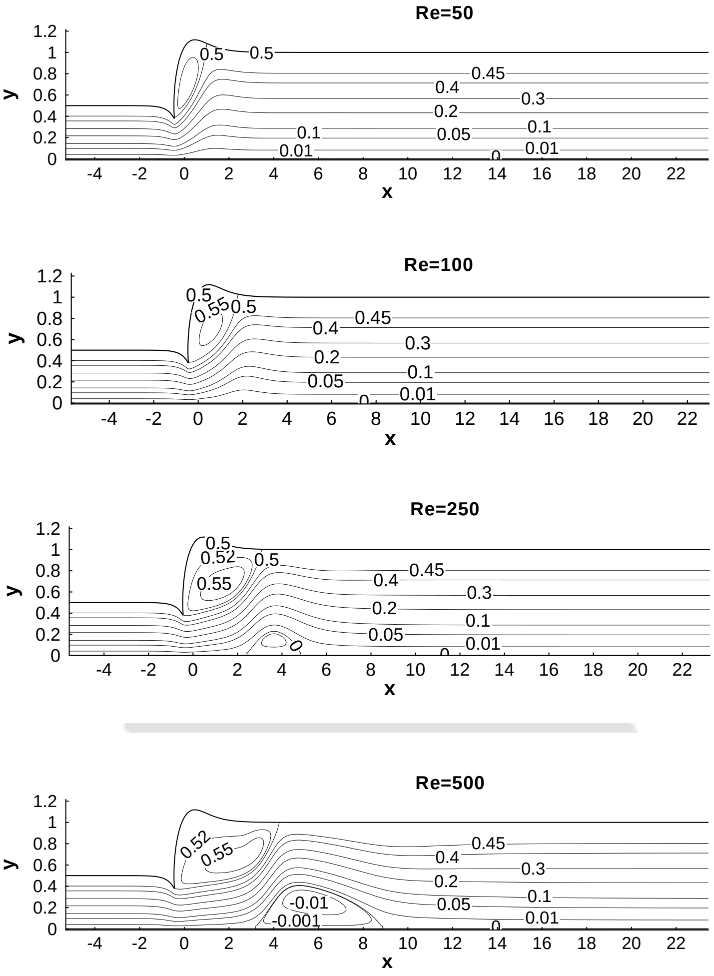

Figure 5.4: *In the asymmetric backward constricted channel (expansion ratio 1:2): streamline contours at* $\tau = 1.0$ *for Re=50, 100, 250 and 500.*

for $Re = 50$, max ψ=0.5163 at $\tau = 0.9$ and 0.5484 at $\tau = 1.0$) demands the existence of flow separation zone in the flow domain. For each of the models M_1 ($\tau = 0.6$), M_2 ($\tau = 0.9$) and M_3 ($\tau = 1.0$) flow separation starts at the downstream of the throat. Moreover, with the increase in Re beyond critical values, the first model M_1 ($\tau = 0.6$) reveals that separation point approaches towards throat along upstream but for higher degrees of constriction the general tendency is that the separation starts at same location. It is also seen that for a fixed value of τ, as Re increases the length of the separation region increases.

Table 5.4 presents abscissa of the points of separation and the points of reattach-

Table 5.4: *Separation points for the second vortex nearer to the bottom boundary of the asymmetric channel with expansion ratio 1:2 for different degrees of constrictions.*

τ	Re	abscissa of separation points	abscissa of reattachment points
0.6	500	3.8143	6.7491
	750	4.1522	9.6671
0.9	250	2.7121	4.1655
	500	3.2733	8.1111
	750	3.8872	11.2225
1.0	250	2.4405	4.8003
	500	3.1973	8.8500

ment for the secondary vortex. It is noticed that for a fixed τ both the separation point and the reattachment point shift towards the downstream direction with the increase in Re. This is due to the fact that as Re increases the size of the first large vortex increases. As a result, when fluid is about to cross the first large vortex, pressure gradient again increases causing further separation. On the contrary, for a fixed Re, the separation point shifts towards the upstream and the reattachment point shifts towards the downstream with the increase in τ. This is because of higher degrees of constriction resulting early separation.

Figure 5.5 shows the vorticity contours for $Re = 250$ and 500 at $\tau = 0.6, 0.9$ and 1.0. For each Re, it is observed that almost same patterns occur for different constrictions with a slight variation of vortex lines. Difference is observed at the secondary vortex zone. It is also noticed that the core vortex lines move along the downstream and diffuse in the downstream direction after traversing a small distance away from the top and bottom vortex depending on Res and degrees of constriction. The length of the core regions increase with the increase in Res.

It is seen from figure 5.6, describing the curves of lower wall shear-stress values that the minimum lower wall shear stress value decreases with increase in degrees of constriction as well as increase in Re. Another important observation is that the maximum lower wall shear-stress value may not always negative (it is negative for lower Res and positive for higher Res). It is also observed that for a fixed Re in each model the maximum wall shear stress value occurs near the downstream of the reattachment point of the primary vortex.

In figure 5.7 we have presented upper wall shear stress for the three models. For $Re = 250$, it is seen from figures 5.7 (a), (b) and (c) (magnified view around the corner) in models $m_1(\tau = 0.6)$, $m_2(\tau = 0.9)$ and $m_3(\tau = 1.0)$ respectively, that the shear stress value changes remarkably (the wall share stress value changes sharply) around the corner for model $m_3(\tau = 1.0)$. In models $m_1(\tau = 0.6)$ and $m_2(\tau = 0.9)$ the maximum shear stress value occurs at the corner whereas in model $m_3(\tau = 1.0)$ it occurs at the proximal lip of the corner which is just upstream of the separation point of the primary vortex. Figures 5.7 (a′), (b′) and (c′) show the changes of wall shear stress values in a wide range of flow domain. From figures 5.7 (a′) and (b′), it has been noticed that with the increase in Re the location of the minimum wall shear-stress value shifts towards the downstream of the separation points for higher Res whereas for lower Res it occurs closed to the separation point along downstream. For figure 5.7 (c′) the minimum wall shear-stress value is at the separation points for all Res which could be due to the severe sharpness of the corner.

Figure 5.8 shows the velocity flow fields. A parabolic flow was prescribed at the inlet. The flow retains its parabolic shape up to the throat. As soon as it departs the throat of the constriction, the core flow maintains the parabolic shape and the flow profiles in the regions near the top and bottom walls are distorted due to development of reverse flow zone. The negative velocity near the wall indicates the existence of a separation zone which are already discussed earlier. As the profile moves along the downstream, slowly the parabolic part is extended vertically and the negative flow zone is going to be reduced. Finally after some distance negative zone disappears and a parabolic velocity profile is regained along the downstream of the channel.

In figures 5.9 we have shown the time-wise evolution of the streamlines for $Re = 250$ with $\tau = 0.9$. It is noticed that at t=1.25, there is a small separated region attached to the throat, which is adjacent to the top wall in the flow domain. As time evolves another vortex (secondary vortex) develops at the bottom wall and moves along downstream. They elongate first and then split into two or more. In addition to this slight perturbation of the streamlines occurs closed to the top wall developing one more top wall vortex. Towards steady-state, it dissipates and smears out. It is also seen that after a while (see t=20.0) the vortices adjacent to the top wall coalesce to form a first large vortex. Further increase in time reveals that one of the bottom wall vortices moves towards downstream and smear out there. Finally at steady-state condition, the flow domain consists of two large vortices, of which one adjacent to the top wall and other one adjacent to the bottom wall.

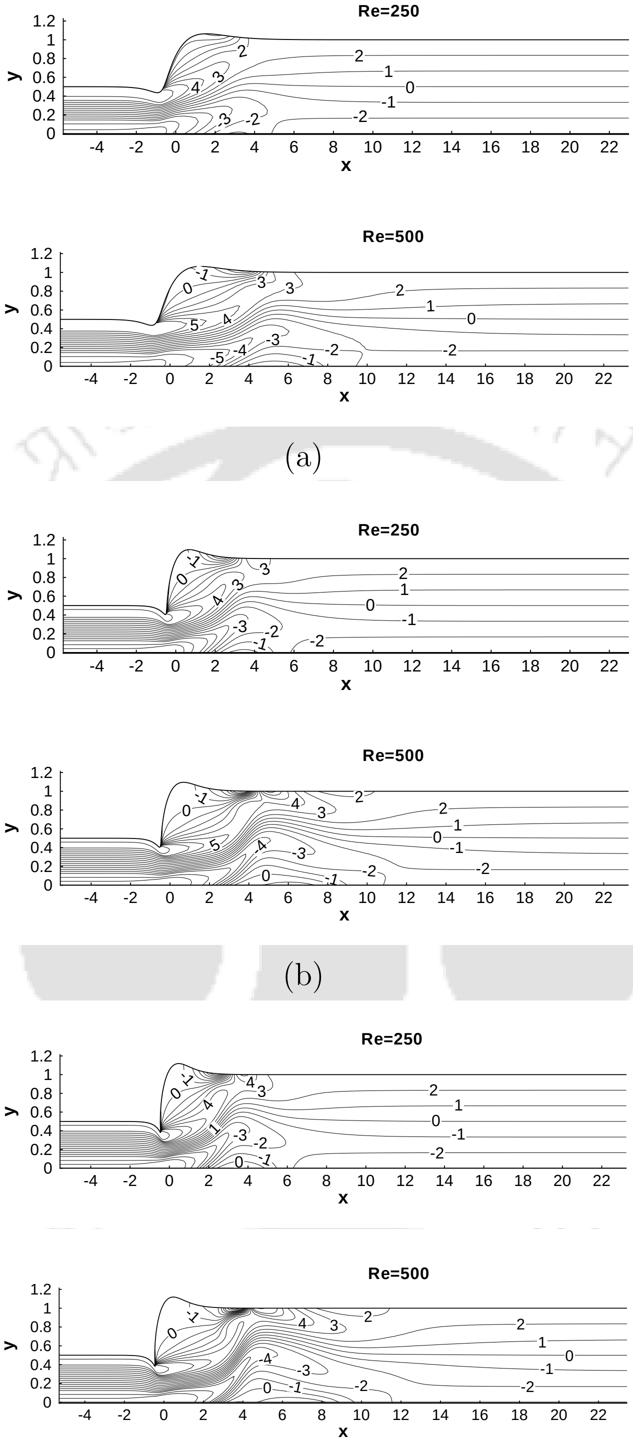

(a)

(b)

(c)

Figure 5.5: *In the asymmetric backward constricted channel (expansion ratio 1:2): vorticity contours for* $Re = 250, 500$ *at (a)* $\tau = 0.6$, *(b)* $\tau = 0.9$ *and (c)* $\tau = 1.0$.

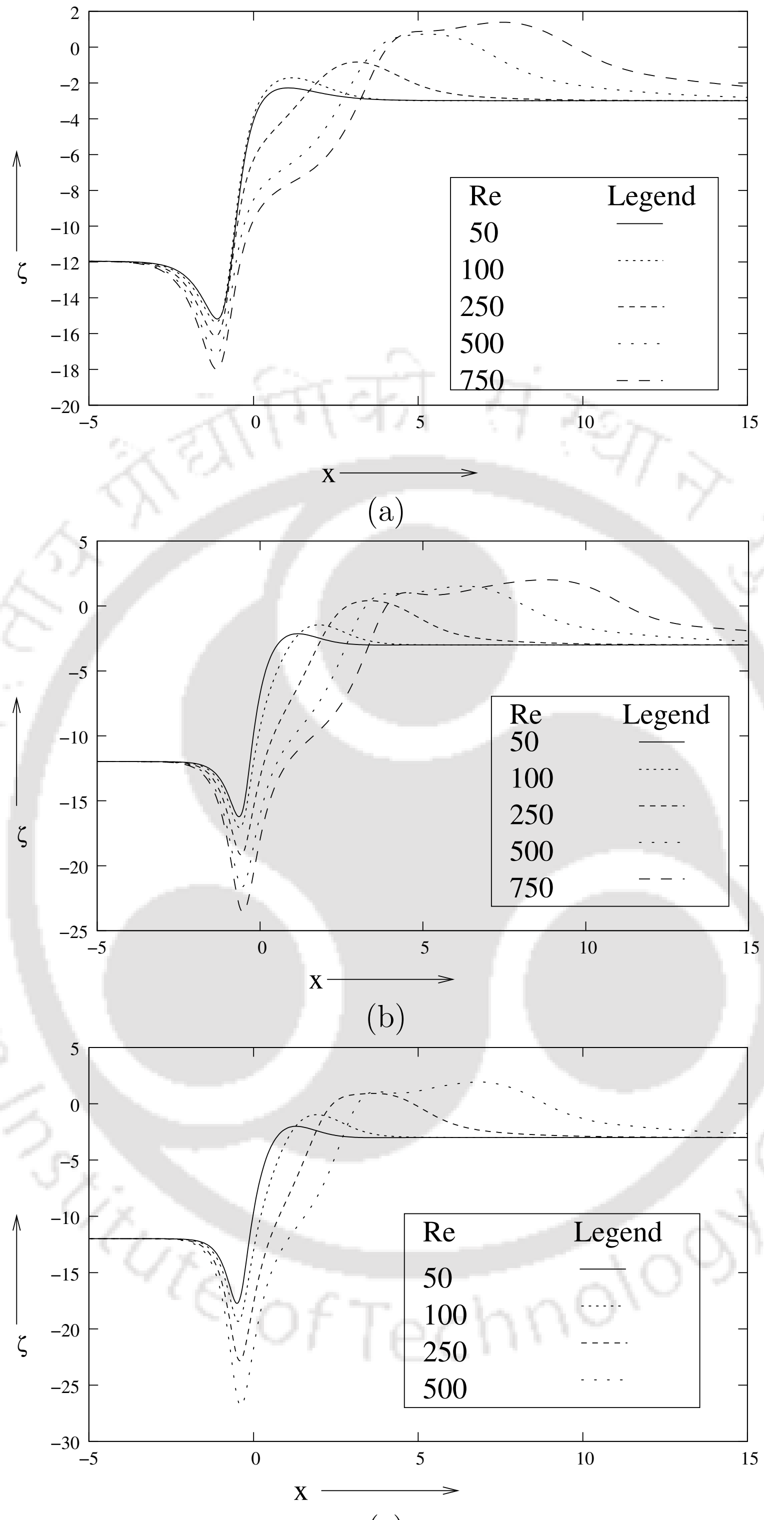

(a)

(b)

(c)

Figure 5.6: *In the asymmetric backward constricted channel (expansion ratio 1:2): lower wall shear-stress for (a) $\tau = 0.6$, (b) $\tau = 0.9$ and (c) $\tau = 1.0$.*

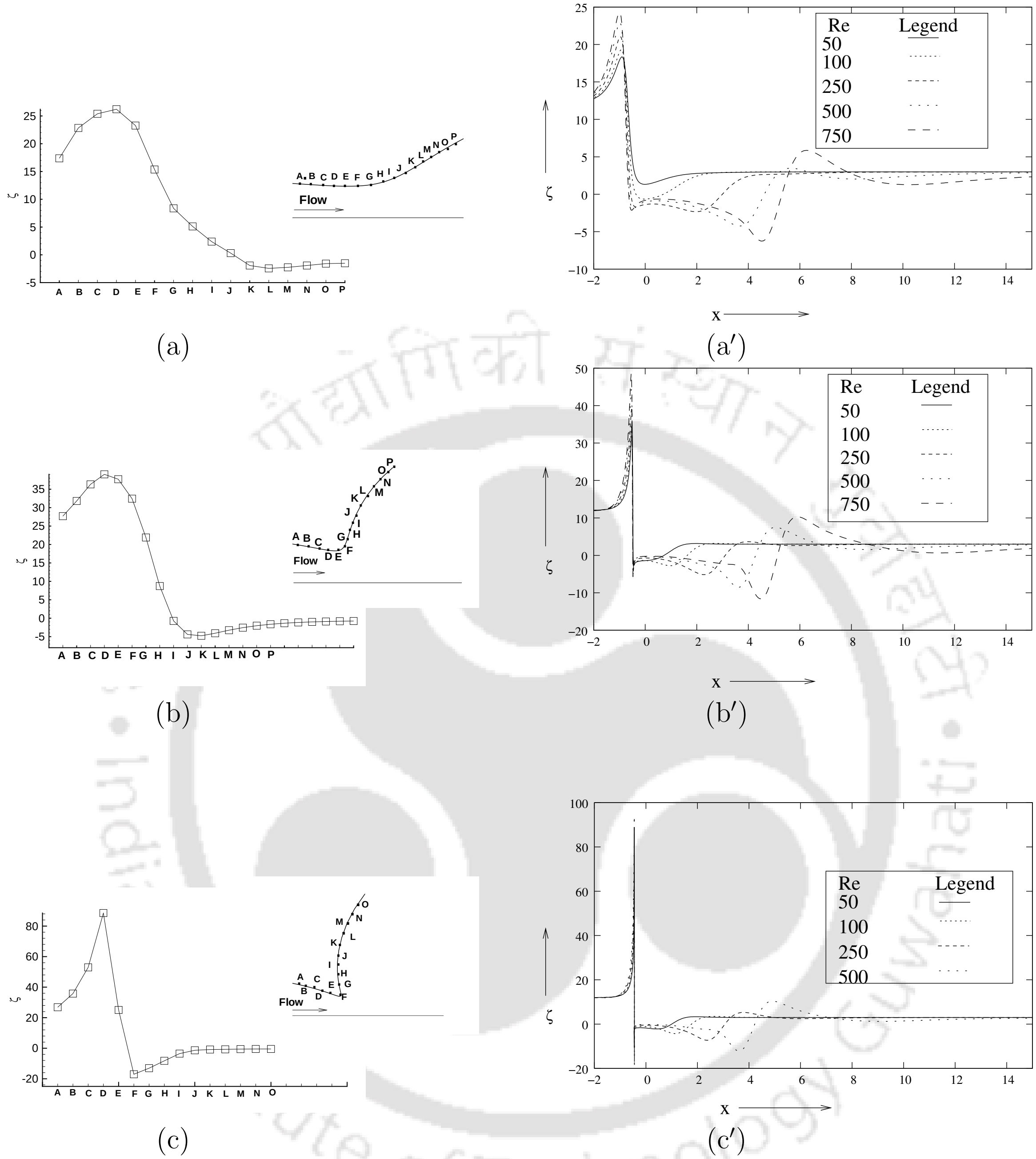

(a) (a′)

(b) (b′)

(c) (c′)

Figure 5.7: *In the asymmetric backward constricted channel (expansion ratio 1:2): (a), (b) and (c) respectively present the magnified view of the wall shear stress at the top wall around the throat for Re* $= 250$ *with* $\tau = 0.6$, $\tau = 0.9$ *and* $\tau = 1.0$, *and (a′), (b′) and (c′) respectively present the change of wall shear stress in a large part of the domain for different Res and different* τ ($\tau = 0.6$, $\tau = 0.9$ *and* $\tau = 1.0$).

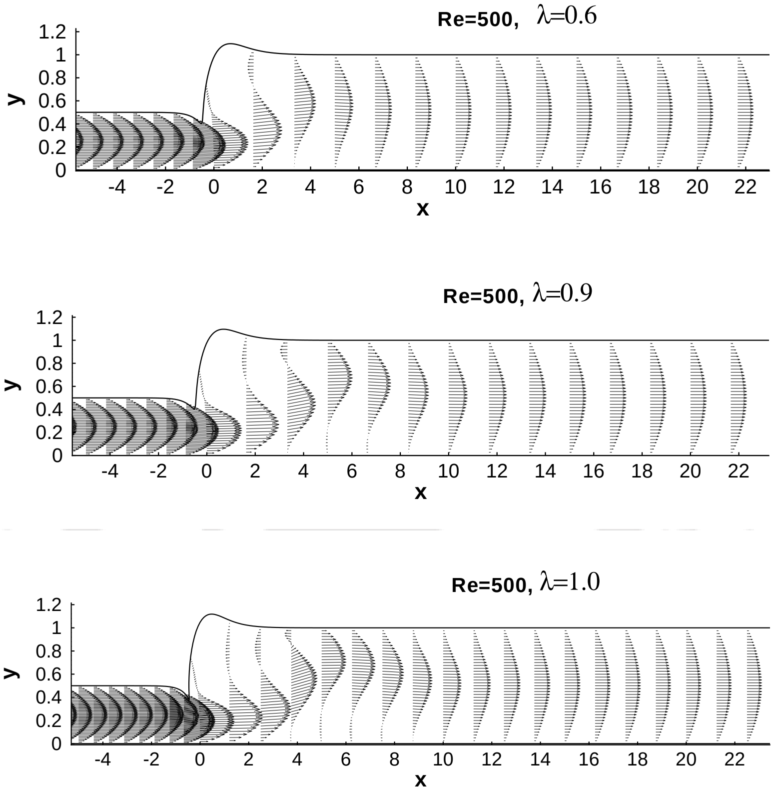

Figure 5.8: *In the asymmetric backward constricted channel (expansion ratio 1:2): velocity profile for re=500,* $\lambda = 0.6, 0.9$ *and 1.0.*

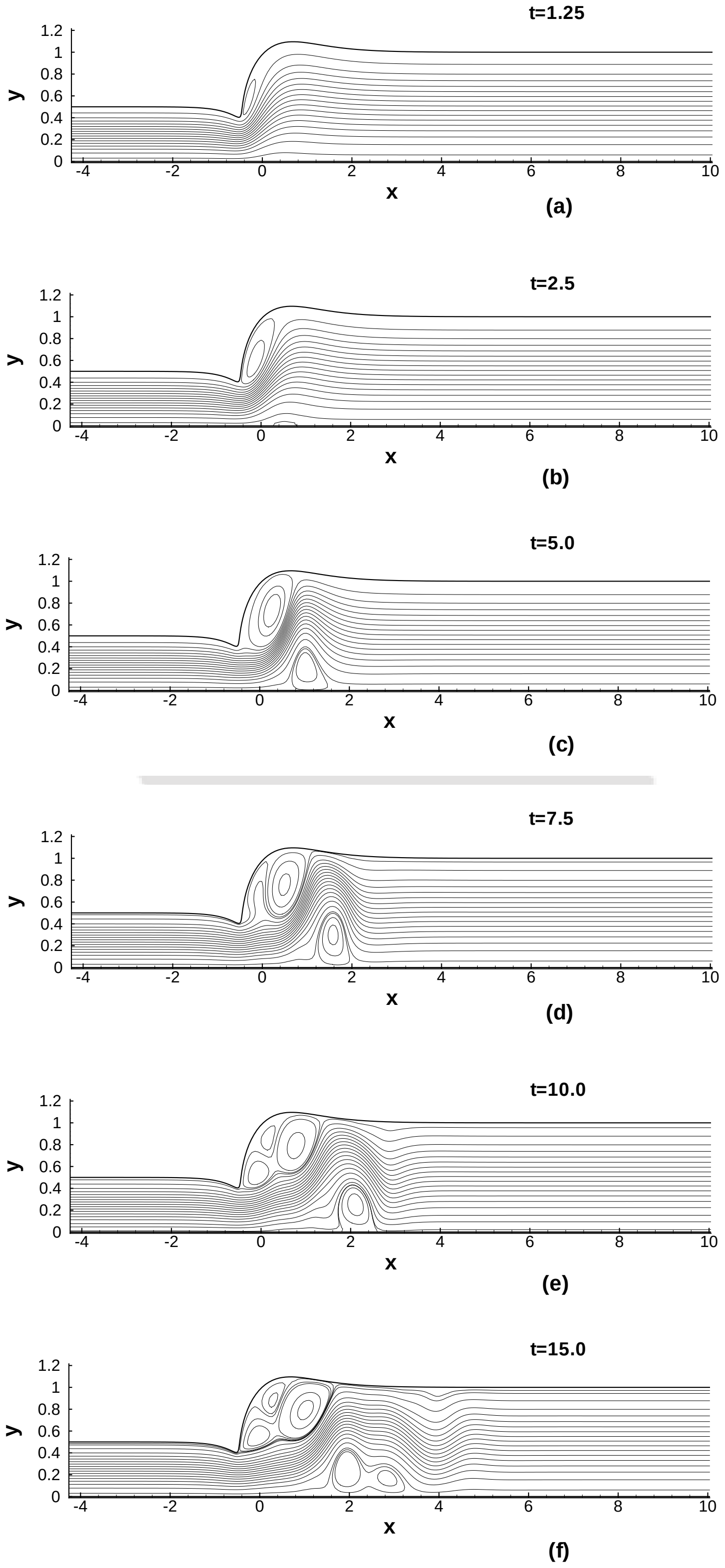

Figure 5.9. *For caption see next page.*

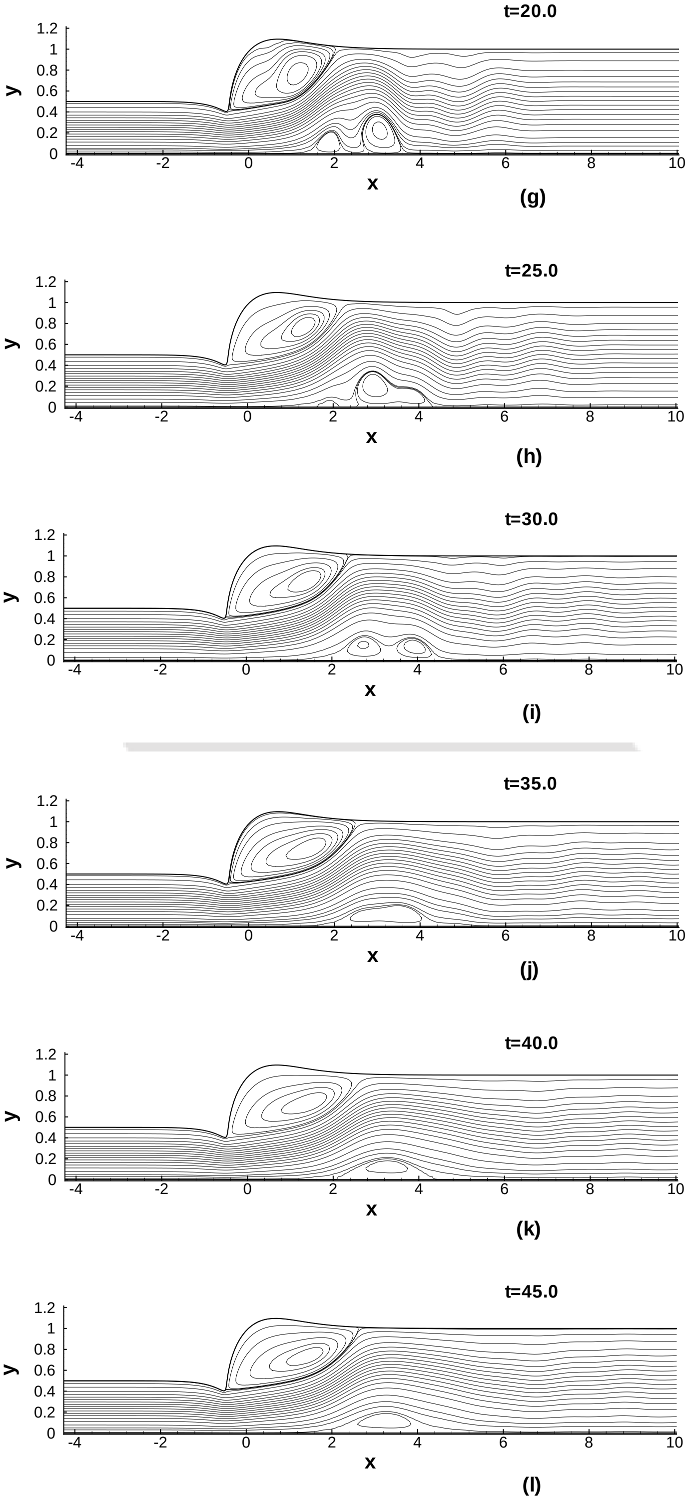

Figure 5.9: *In the asymmetric backward constricted channel (expansion ratio 1:2): evolution of streamlines for* $Re = 250$ $(\lambda = 0.9)$ *at different time stations.*

5.4.2 Expansion ratio 1:4

In this section, we have presented the steady-state solutions in figures (figure 5.10 and 5.11) and transient solutions in figure 5.12 for flow in an asymmetric channel with backward constriction having expansion ratio 1:4.

Figure 5.10 shows the streamline contours and corresponding vorticity contours for $\tau = 0.6$ with different Res. It is seen that as Re increases the number of vortices increases. As for example, at $\tau = 0.6$ the number of vortices developed for $Re = 50, 100$ and 250 are 1, 2 and 3 respectively. In comparison with the figure 5.2 for streamlines, it is seen that a drastic change in flow characteristics occurs in figure 5.10 for expansion ratio 1:4. In the constricted channel with expansion ratio 1:2, only one recirculation region develops for $Re = 250$ whereas in expansion ratio 1:4, the number of recirculation regions are three. This fact could be due to the lowering of expansion ratio. The flux at the upstream of the throat decreases for expansion ratio 1:4 in comparison with expansion ratio 1:2 but it diffuses in a large expansion region along the downstream of the throat. As a result pressure falls rapidly causing several recirculation regions. In the vorticity contours, the vortex lines pattern shows the increase in complexity of the flow with the increase in Res.

From figure 5.11, it is seen that the minimum wall shear stress at the lower wall occurs very close to the corner (throat) while the maximum occurs towards downstream. In comparison with the figures in 5.7 for expansion ratio 1:2, it is clearly observed (see figure 5.11) that at the lower wall, the minimum wall shear stress value further decreases and maximum wall shear stress value further increases. In the case of upper wall, the upper peak (maximum) occurs approximately at the same abscissa where the minimum shear stress occurs for lower wall. But the lower peak values occur at different location for different Res towards downstream. Again, this figure also reveals that for a fixed Re, the range of the wall shear stress values are high.

In figure 5.12 we have presented the time-wise evolution of the streamlines for $Re = 250$ with $\tau = 0.6$. It is noticed that a series of vortices appear at the lower time levels. This observation is in well agreement with the observation in [?]. As time evolves the vortices move downstream and elongated. The weaker vortices, which are far away from the corner move further downstream and smear out. Finally, towards steady-state, the flow domain contains only three vortices (see figure for t=30.0).

Thus, from the above discussions it can be concluded that expansion ratio plays an important role on the the behavior of flow characteristics.

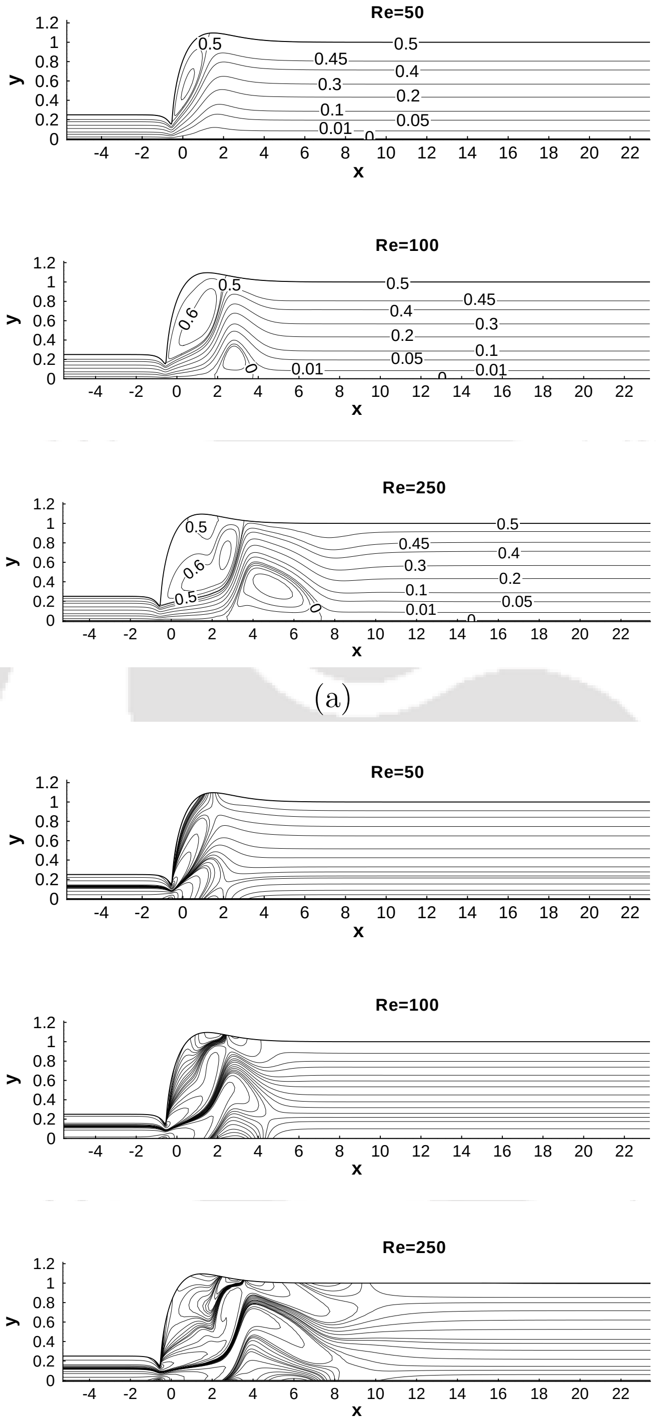

Figure 5.10: *In the asymmetric backward constricted channel (expansion ratio 1:4): streamlines contours at $\tau = 0.6$ for (a) Re=50, 100 and 250; and corresponding vorticity contours for (b) Re=50, 100 and 250.*

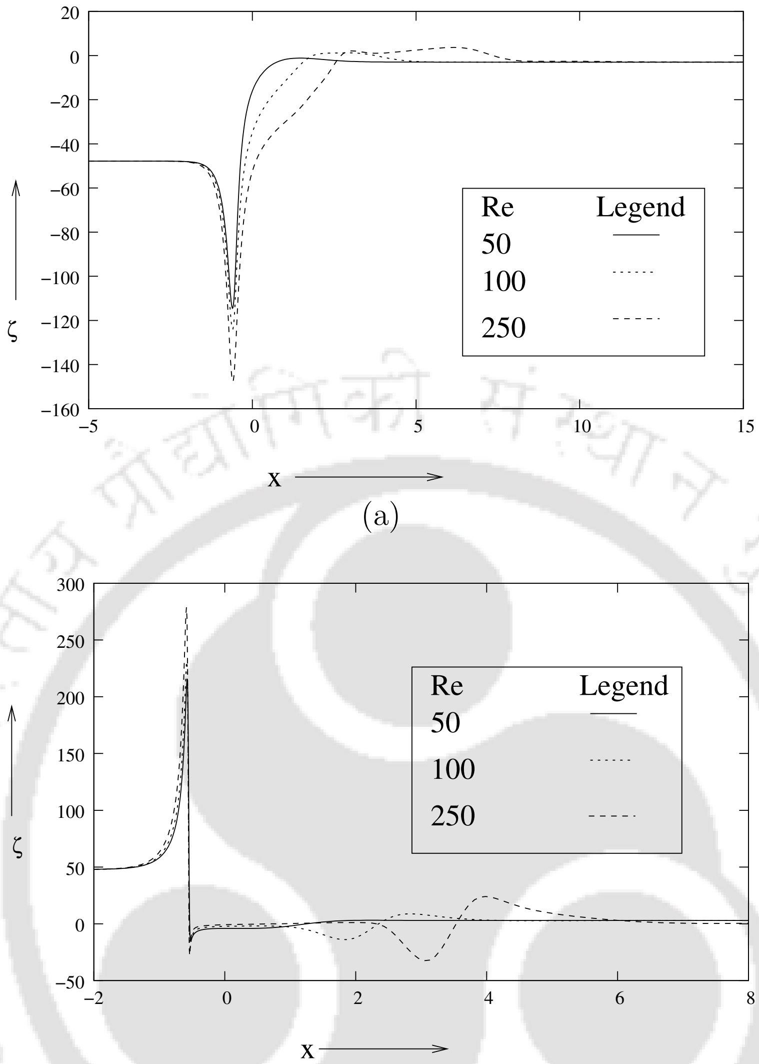

(a)

(b)

Figure 5.11: *In the asymmetric backward constricted channel (expansion ratio 1:4): wall shear stress (wall vorticity) at (a) lower wall, and (b) upper wall for* $Re = 50, 100$ *and* 250 *at* $\tau = 0.6$.

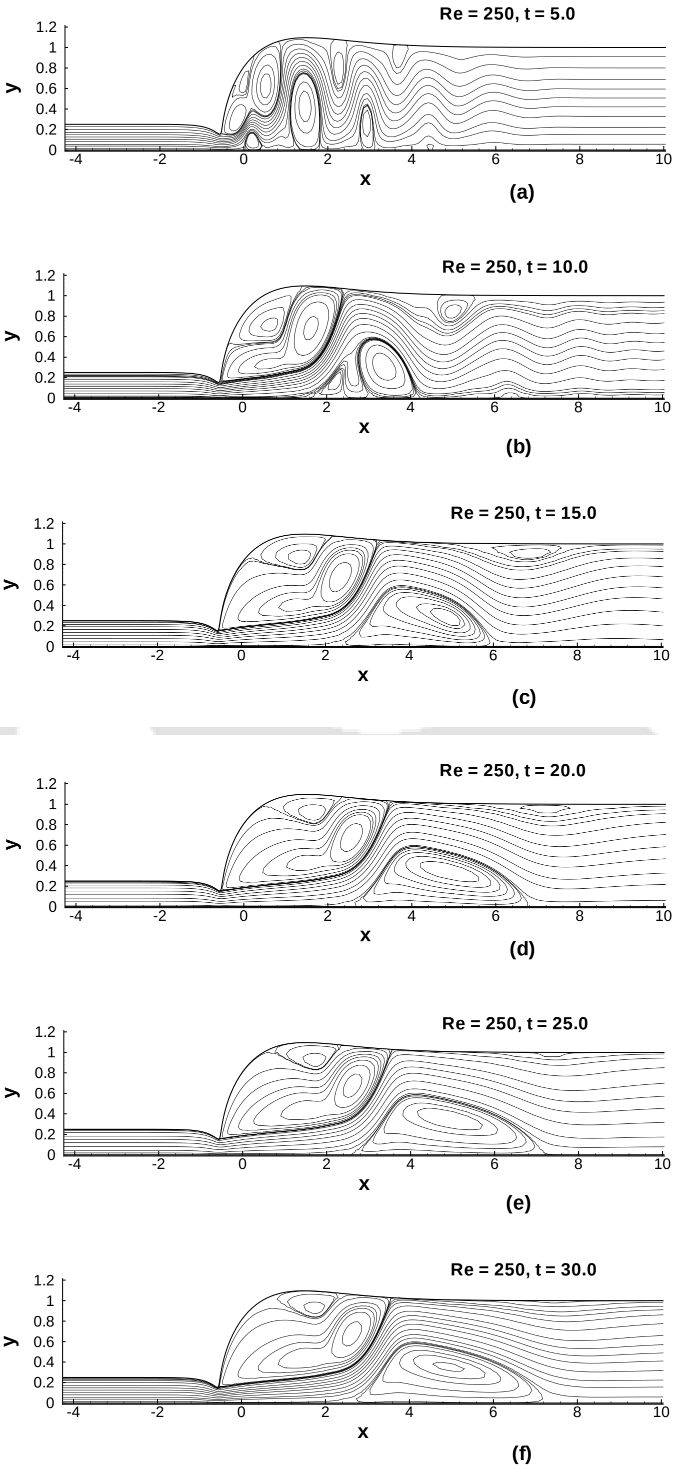

Figure 5.12: *In the asymmetric backward constricted channel (expansion ratio 1:4): evolution of streamlines for* $Re = 250$ $(\lambda = 0.6)$ *at different time stations (a) t=5.0, (b) t=10.0, (c) t=15.0, (d) t=20.0, (e) t=25.0 and (f) t=30.0.*

5.5 Conclusions

A numerical investigation has been carried out on both the steady-state and transient flow phenomena in an asymmetric channel with backward constriction through the (9,9) transient higher order compact (HOC) schemes proposed in chapter 3. The higher order accuracy of the scheme coupled with compactness of the computational stencils affords efficient computations for a wide range of parameters governing the flow on relatively coarser grids. Flow through the nonuniform asymmetric channel geometry with different degrees of sharpness of the reentrant corner is a new problem, and has not been numerically tested or validated before. The theories (results) produced for this asymmetric channel geometry agree reasonably well with the theories of backward facing constricted channel with right angled expansion. The channel geometry as well as sharpness of the throat of the channel along with Re are the important parameters to control the strength and size of the separation zone. The development of series of vortices, as observed in some other studies [130, 146], have also been observed in this study. The size of the vortex developed in the asymmetric backward constricted channel flow is small compared to that in axisymmetric case. In the next chapter we have discussed incompressible viscous flows through dilated channel.

Chapter 6

Flow analysis of incompressible viscous flows in a dilated channel

6.1 Introduction

Study of flows in dilated channels is of great importance in the field of hemodynamics. Flow phenomena in such channels resemble with the blood flow through aneurysmal vessels. It is well known that hemodynamics plays an important role for the genesis and progression of the arterial diseases. In this context, a brief history related to the aneurysm disease has been presented as follows:

As the human aorta is a relatively low resistance circuit for circulating blood in comparison to the lower extremities so the repeated trauma of a reflected wave on the distal aorta may injure a weaker aortic wall, the result is growth of a balloon-like bulge called a saccular aneurysm. Saccular aneurysms arising on the major arteries at one side of the arterial segment are called sidewall (lateral) aneurysms. It is a pathological dilation of an artery. An artery is considered aneurysmal when it grows more than 50% over its normal size. It may be pointed out that intracranial saccular aneurysm is a well known cerebrovascular disease. Intracranial saccular aneurysms are, in general, located along the cavernous segment of the intracranial arteries and may be of lateral, symmetric and bifurcation types. Over forty years, 5-6% of the population in Taiwan have been suffering from this disease [156]. Again, in the United States, approximately 15,000 people die annually due to aneurysm rupture, which is also recognized as the 13th leading cause of death in that country. Thus, the study of blood flow in diseased arteries is a challenging problem over the last century for which no satisfactory solution has yet been available.

Recent developments of techniques for the endovascular treatment of aneurysms have indicated the need of a better understanding of the relevant hemodynamic effects. In general, fluid flow in an aneurysmal artery depends upon its geometric configuration, the size of the orifice and volume of the aneurysm. An aneurysmal artery looks similar to a dilated channel. Flow in a channel with dilation provides an idealization of the flow through an aneurysmal vessel. Analytically, the solution of flow through a dilated channel is quite difficult. Computational fluid dynamics has revealed an useful, non-invasive tool to evaluate the flow characteristics in such geometries. Although it may be sometimes difficult to relate the assumed geometry and flow conditions to those seen clinically, as such often the simplifications used have helped to provide some understanding of the complexity of underlying physics.

The difficulties such as large computational requirements associated with the numerical solutions of the full three dimensional time-dependent Navier-Stokes equations motivate us to study the two dimensional version of this problem to throw some lights on steady and unsteady flow phenomena.

In the present work, we have considered rigid channel geometry with different shapes on the flow characteristics of Newtonian fluid as the effects of non-Newtonian fluid properties and wall elasticity are not prominent [88, 134–136]. We extensively discuss how the channel geometry with different shapes affects the flow. We have restricted our study up to $Re = 750$ because the Reynolds number in the intracranial arteries does not exceed 600 to 700 [87]. We have concentrated on numerical solutions of the flow characteristics in various lateral dilated channels and also those on symmetric nonuniform rigid channel having different degrees of dilatation since there is a limited literature available on these flow geometries.

6.2 Numerical procedure

6.2.1 The problem

We consider the incompressible viscous flows in a lateral (see figure 6.1 (a)) and in a symmetric (see figure 6.1 (b)) dilated channels. The schematic diagrams of channel geometry and related flow boundary conditions are shown in figure 6.1. Note that the dilation examined in the present study has a wide orifice with the neck close to it. We have considered the lateral channel geometry similar to that investigated by Lieber *et al.* [86]. This is an idealized model problem of a spherical sidewall saccular aneurysm emanating from a straight blood vessel.

For lateral channel geometry (see figure 6.1 (a)), the bottom wall is taken as x-axis and the line along the maximum height through the dilated region has been considered as y-axis. The point of their intersection has been considered as origin.

Similarly, the coordinate systems for symmetric channel geometry has been presented in figure 6.1 (b).

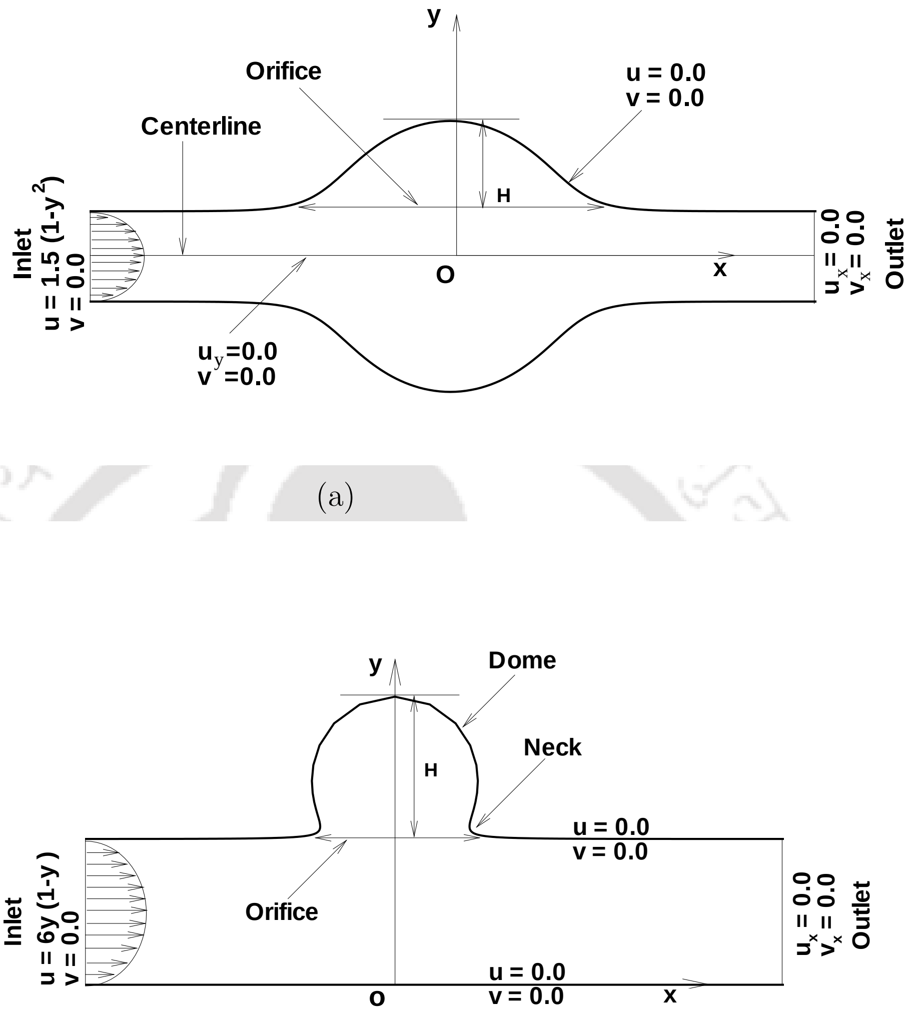

(a)

(b)

Figure 6.1: *Schematic diagrams of (a) lateral and (b) symmetric dilated channel geometries with flow boundary conditions.*

The governing equations are the two dimensional (2D) N-S equations which, in non-dimensional primitive variable formulation can be written as

$$\frac{\partial u}{\partial x} + \frac{\partial v}{\partial y} = 0, \tag{6.1}$$

$$\frac{\partial u}{\partial t} + u\frac{\partial u}{\partial x} + v\frac{\partial u}{\partial y} = -\frac{\partial p}{\partial x} + \frac{1}{Re}\nabla^2 u, \tag{6.2}$$

$$\frac{\partial v}{\partial t}+u\frac{\partial v}{\partial x}+v\frac{\partial v}{\partial y}=-\frac{\partial p}{\partial y}+\frac{1}{Re}\nabla^2 v. \tag{6.3}$$

For non-dimensionalization we have considered $x^*=\frac{x}{L}$, $y^*=\frac{y}{L}$, $u^*=\frac{u}{u_0}$, $v^*=\frac{v}{u_0}$, $t^*=t$, $p^*=\frac{p}{\rho u_0^2}$, where u, v are velocities along x-, y-directions respectively, p is the pressure, t is the time and Re is the Reynolds number given by $Re=\dfrac{Lu_0}{\nu}$, where L is the characteristic length (in case of lateral dilated channel it is the width and in symmetric channel it is half of the width at inlet), u_0 is the average velocity at the entrance and ν is the kinematic viscosity.

Instead of pressure and velocity, the derived quantities such as streamfunction $\psi(x,y,t)$ and vorticity $\zeta(x,y,t)$ can be introduced in terms of u, v as

$$u=\frac{\partial\psi}{\partial y},\qquad v=-\frac{\partial\psi}{\partial x}, \tag{6.4}$$

and

$$\zeta=\frac{\partial v}{\partial x}-\frac{\partial u}{\partial y}. \tag{6.5}$$

With these, the streamfunction-vorticity (ψ-ζ) form of the N-S equations (6.1)-(6.3) can be written as

$$-\frac{\partial^2\psi}{\partial x^2}-\frac{\partial^2\psi}{\partial y^2}=\zeta, \tag{6.6}$$

$$Re\frac{\partial\zeta}{\partial t}-\frac{\partial^2\zeta}{\partial x^2}-\frac{\partial^2\zeta}{\partial y^2}+uRe\frac{\partial\zeta}{\partial x}+vRe\frac{\partial\zeta}{\partial y}=0. \tag{6.7}$$

The boundary conditions are as follows:
On the top and bottom, a fixed rigid wall is considered and the usual no-slip condition is imposed i.e.

$$u=v=0. \tag{6.8}$$

Symmetry conditions are imposed along the horizontal centerline of the symmetric dilated channel which reads as

$$v=\frac{\partial u}{\partial y}=0. \tag{6.9}$$

At the entry section, a parabolic velocity profile is prescribed:
(a) For lateral dilated channel

$$\begin{aligned} v &= 0,\\ u &= 6y(1-y). \end{aligned} \tag{6.10}$$

(b) For symmetric dilated channel

$$\begin{aligned} v &= 0,\\ u &= 1.5(1-y^2). \end{aligned} \tag{6.11}$$

The boundary conditions for ψ and ζ can be easily obtained from the equations (6.4) and (6.5). At the outlet, fully developed flow is considered.

6.2.2 Mesh structure

We have constructed a grid (see figure 6.2) on curvilinear setting through the use of the conformal mapping which maps the nonuniform dilated channel (physical domain) to a straight rectangular channel (computational domain) as follows

$$z = w + B\tanh(\frac{\pi}{2}Cw), \tag{6.12}$$

where $z = x + iy$ and $w = \xi + i\eta$ ($i = \sqrt{-1}$) with

$$\begin{aligned} x &= \xi + \frac{B}{G}\sinh(C\pi\xi), & (6.13)\\ y &= \eta + \frac{B}{G}\sin(C\pi\eta). & (6.14) \end{aligned}$$

Here $G = \cosh(C\pi\xi) + \cos(C\pi\eta)$; B and C are the constants and determine the degrees of the

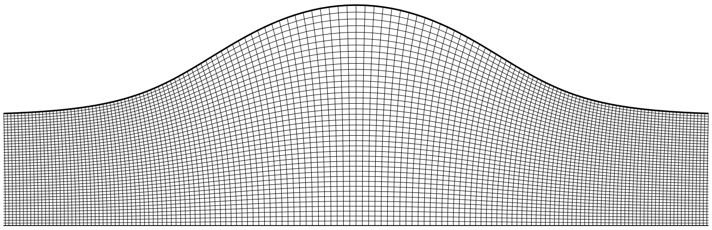

Figure 6.2: *Mesh structure.*

NOTE: The discretization of the transformed form of the governing equations and the solution procedure of the resulting algebraic equations are same as in problem of symmetric channel flow with forward and backward constriction [see chapter 4]. We have numerically experimented and accordingly we have considered the inlet position at $x \approx -6$ and $x \approx -10$ respectively for circular and concave shaped dilations in the dilated channel to eliminate the effects of dilation at the inlet. And to get fully developed flow at the outlet for different flow conditions and different degrees of dilations, we experimented numerically and accordingly we set the outlet at $x \approx 25$. In all the computations we have used step lengths $\Delta\xi = \frac{1}{25}, \frac{1}{50}$ and $\frac{1}{60}$ along the horizontal, and $\Delta\eta = \frac{1}{40}, \frac{1}{60}$ and $\frac{1}{80}$ along the vertical direction in the computational plane, and time step $\Delta t = 0.001$.

6.3 Results and discussions

In this section, numerical results of flows in a lateral and in an symmetric dilated channel have been presented.

6.3.1 Lateral dilated channel

General flow behavior in a lateral aneurysmal vessel

Most of the studies [48,50,140] show that the general patterns of blood flow in lateral aneurysms were similar i.e. three distinct zones characterize the blood flow behaviors. They are as follows:

1. An inflow entering the aneurysm from the distal side of the neck.
2. An outflow exiting the aneurysm at the proximal side of the neck.
3. A central slow flow vortex formed at the entrance to the aneurysm at each systole and circulated around the aneurysm during each cardiac cycle.

In this section, we have presented results for four model cases on the basis of the sectional area of the dilated region determined by the orifice length and height (=H, which is defined as the maximum vertical length from orifice to the dome.) of the dilation. They are such as model (a) m_1 for orifice length $-0.5 \leq x \leq 0.5$ and $H \approx 1$, (b) m_2 for orifice length $-1.0 \leq x \leq 1.0$ and $H \approx 2$, (c) m_3 for orifice length $-2.0 \leq x \leq 2.0$ and $H \approx 4$, and (d) m_4 for orifice length $-4.0 \leq x \leq 4.0$ and $H \approx 2$. Among these the first three are circular shaped dilation and the last one is concave shaped.

Figure 6.3 shows that the velocity vectors near the orifice of different sectional area of the dilated regions are deviated from the main path and gradually turn upward. The turning angle with respect to x-axis increases and becomes maximum at the distal lip of the orifice of the dilation. As a consequence, fluid starts to enter into the dilated part from the distal lip of the orifice and the fact that the stream layer rather adjacent to the upper wall of the parent channel has chance to enter into the dilated part. The upward vectors make turn again and move down along the proximal lip of the orifice. Thus, a counter-clockwise vortex is formed. It is also seen that a part of the fluid (mainly the outer part of the counter-clockwise vortex) at the interface between the main stream in the parent channel and the counterclockwise vortex, moves along downstream with the main flow in the parent channel and the rest returns into the dilated region. From the above discussion a conclusion can be made that the dilated region has little impact on the main flow both at upstream and downstream of the orifice in the parent channel. It must be mentioned that we have observed one dominant vortex in the dilated region for all the three models (m_1, m_2 and m_3) as observed by Lieber *et al.* [86] because the orifice and the neck are closely associated as stated in [50, 89, 90].

Table 6.1: *Vortex center of the lateral dilated channel flow.*

Orifice length and height of dilatation (H)	Re	Vortex center (x,y)	Max(ψ)
$-0.5 \leq x \leq 0.5$, $H \approx 1$	100	(0.1110, 1.2783)	1.0332
	250	(0.1615, 1.2612)	1.0302
	500	(0.1841, 1.3116)	1.0266
	750	(0.1277, 1.3344)	1.0244
$-1.0 \leq x \leq 1.0$, $H \approx 2$	100	(0.3407, 1.5637)	1.0897
	250	(0.2624, 1.7606)	1.0789
	500	(0.1787, 1.7857)	1.0687
	750	(0.2018, 1.8770)	1.0624
$-2.0 \leq x \leq 2.0$, $H \approx 4$	100	(0.5797, 2.6300)	1.2447
	250	(0.3846, 2.8159)	1.2197
	500	(0.2589, 2.8408)	1.1912
	750	(0.2589, 2.8409)	1.1731

Table 6.1 presents the location of the vortex center and the max(ψ) value thereat for different Res with different sectional areas determined by the orifice length and height (H) of the dilated region. It is seen that for a fixed sectional area of the dilated region, the strength of the vortex decreases with increase in Res and for a fixed Re the strength of the vortex increases with the increase in sectional area of the dilatation. It is also seen that the location of the vortex center in the dilated region fluctuates (along upstream and downstream direction) with increase in Re for models m_1 and m_2 whereas for model m_3 the vortex center remains fixed after $Re \approx 300$ (See figure 6.4). For higher degrees of dilation or for higher Res, vortex center generally moves away from the orifice.

Figure 6.5 shows the wall shear stress curves for models m_1, m_2 and m_3 of the lateral dilated channels. It is seen that for all the models, changes of wall shear stress values are mostly taken place around the necks of the dilated region. The maximum wall share stresses occur at or near the distal lip of the orifice (see point P in figure 6.5). This observation agrees reasonably well with the theory of lateral aneurysm models in [89–91, 135].

In figure 6.6 we have presented streamfunction and the corresponding vorticity contours along with the results of velocity fields and shear stress values for $Re = 500$. In this geometry, the orifice is too wide with respect to the height ($H \approx 2$) of the concavity of the dilation. It is seen that for a wide range of the orifice length ($-4.0 \leq x \leq 4.0$ approximately) two counter-rotating vortices develop, which is not observed in the previous models. The numerical experiments for smaller Res ($0 \leq Re \leq 250$) reveal that at most one vortex develops in the concavity of the dilation (though the figures are not presented here). However, in this case, a secondary vortex (smaller one) develops near the dome deforming the primary vortex (first large vortex). Figure 6.6(c) and (d) show the velocity fields in the flow domain and in the concavity of the dilation respectively. The magnified view of the vectors in 6.6(d) shows the developments of two counter-rotating vortices in the concavity of the dilation. The wall shear stress values at different points on the dilated wall are presented in figure 6.6(e), which shows a similar pattern to the figure 6.5(b). The heights of the dilated regions have been assumed to be equal (it has been considered as 2), though the orifice lengths are different.

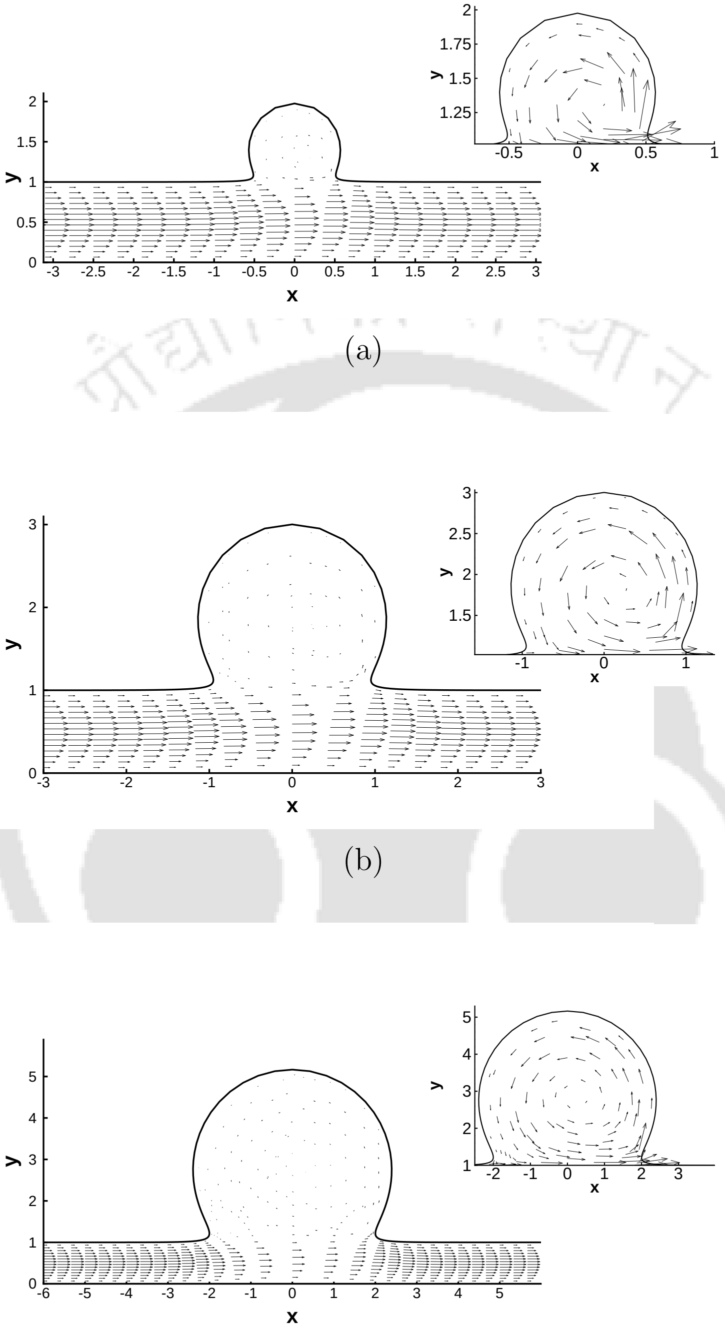

(a)

(b)

(c)

Figure 6.3: *In a lateral dilated channel: velocity fields for Re* = 500 *and models (a)* m_1 *(*$-0.5 \leq x \leq 0.5$*,* $H \approx 1$*), (b)* m_2 *(*$-1.0 \leq x \leq 1.0$*,* $H \approx 2$*) and (c)* m_3 *(*$-2.0 \leq x \leq 2.0$*,* $H \approx 4$*).*

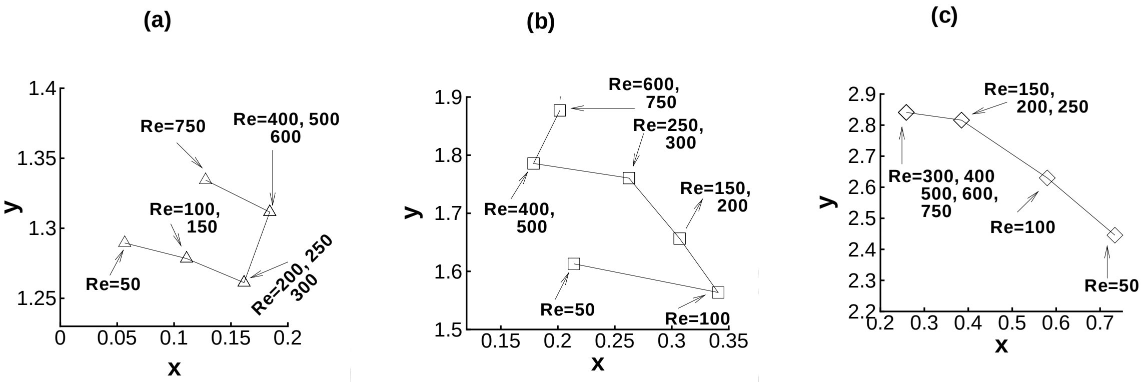

Figure 6.4: *In a lateral dilated channel: movement of the location of the vortex center for models (a)* m_1 *(*$-0.5 \le x \le 0.5$, $H \approx 1$*), (b)* m_2 *(*$-1.0 \le x \le 1.0$, $H \approx 2$*) and (c)* m_3 *(*$-2.0 \le x \le 2.0$, $H \approx 4$*).*

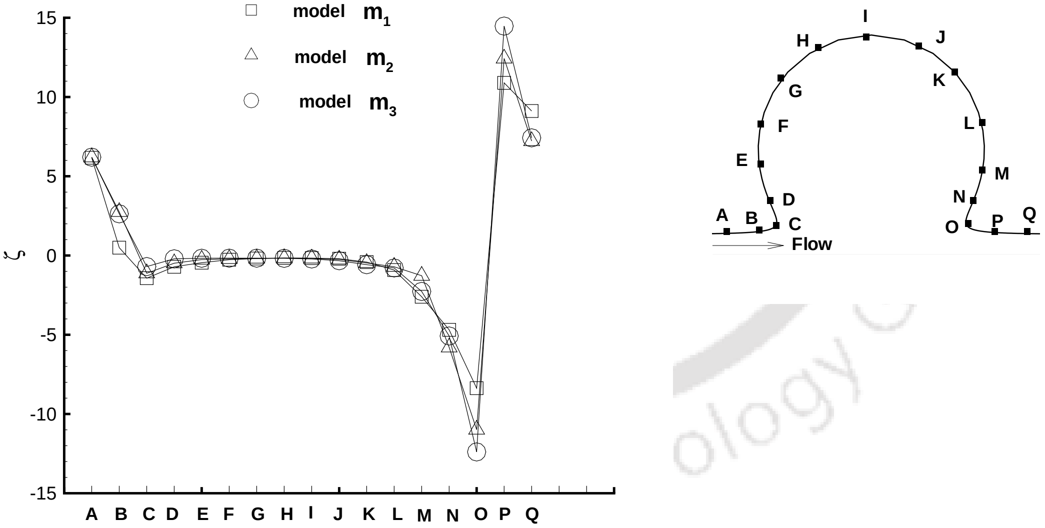

Figure 6.5: *In a lateral dilated channel: wall shear stress values for* $Re = 500$ *at the dilated wall for models* m_1 *(*$-0.5 \le x \le 0.5$, $H \approx 1$*);* m_2 *(*$-1.0 \le x \le 1.0$, $H \approx 2$*) and* m_3 *(*$-2.0 \le x \le 2.0$, $H \approx 4$*).*

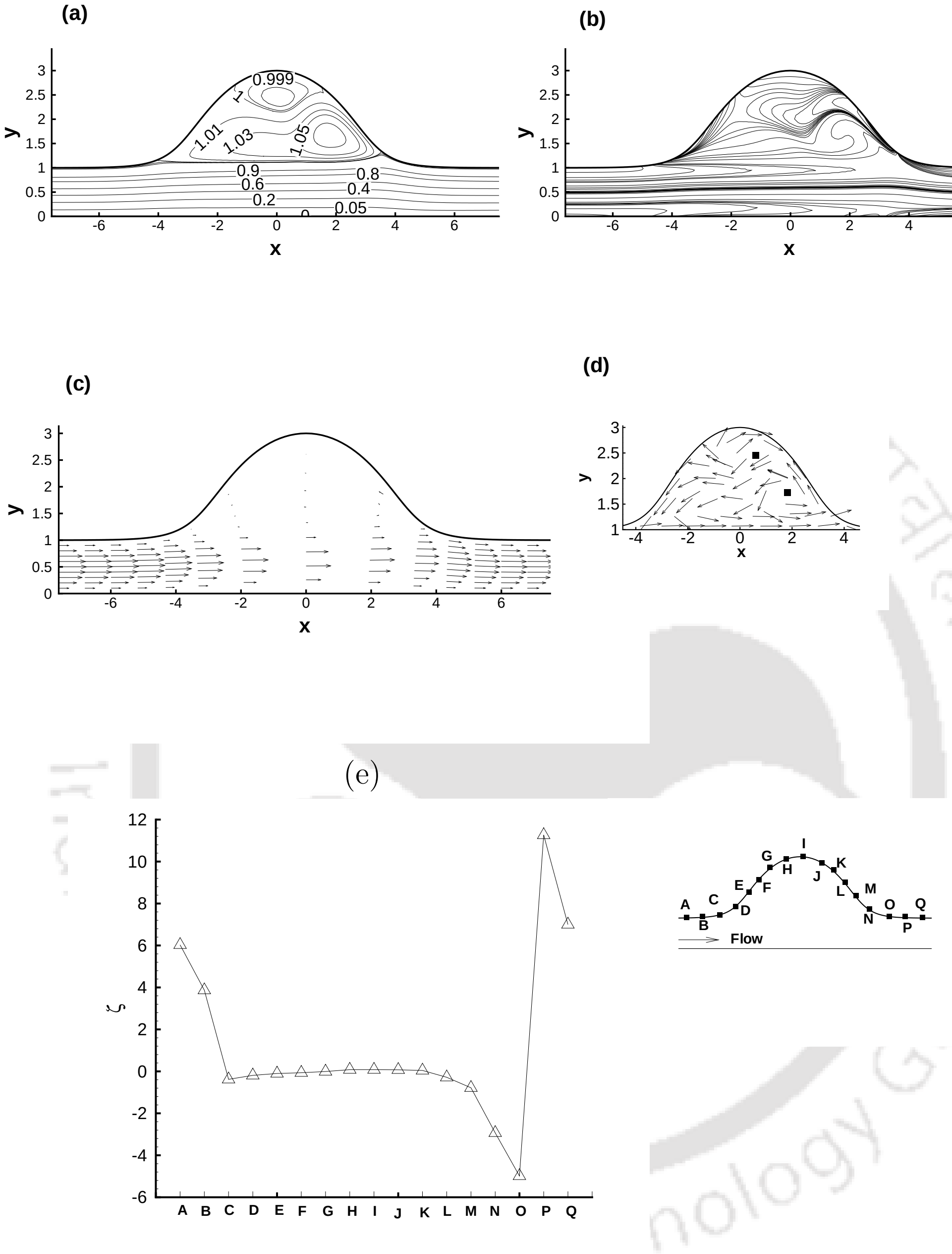

Figure 6.6: *In a lateral dilated channel: (a) Streamline contours, (b) Vorticity contours, (c) Velocity fields in the domain, (d) Magnified view of velocity fields in the dilated region, and (e) wall shear stress values at the top wall for* $Re = 500$*, and orifice length* $-4.0 \leq x \leq 4.0$ *and height* $H \approx 2$*.*

6.3.2 Symmetric dilated channel

We have numerically studied the flow patterns for different Res in the full dilated channel. In figure 6.7 we have presented the streamline contours for Re=100 and 600. It is seen that the curves of constant streamfunction values and the size of the recirculation zones are symmetrical with respect to the centerline. This flow phenomena confirms that the flow patterns in the symmetric dilated channel is symmetric. Therefore, we have considered one half plane (upper half plane) of the dilated channel for the numerical solutions and accordingly we have continued to discuss the following issues. For symmetric channel geometries, three model cases have been considered as given in table 6.2, in which M_1 ($-2.0 \leq x \leq 2.0$, $H = 0.5$) represents mild, M_2 ($-3.0 \leq x \leq 3.0$, $H =$) represents moderate, and M_3 ($-4.0 \leq x \leq 4.0$, $H = 2$) represents severe dilated channel. It should be mentioned here that for all the models convergent solutions have been obtained over a wide range of Reynolds numbers ($1 \leq Re \leq 750$). Time marching steady-state results with zero initial condition have been presented in the form of tables (table 6.3 - 6.5) as well as in the form of figures (figure 6.7 - 6.16). A description of the various possible steady-state laminar flow patterns is perhaps best rendered by a display of streamlines and vorticity contours for different degrees of constrictions as well as flow parameters. It has been numerically experimented that separation starts to occur at approximately Re = 66 for model M_1, whereas for model M_2 and M_3 separations start to occur at Re = 22 and 10 respectively (given in table 6.2).

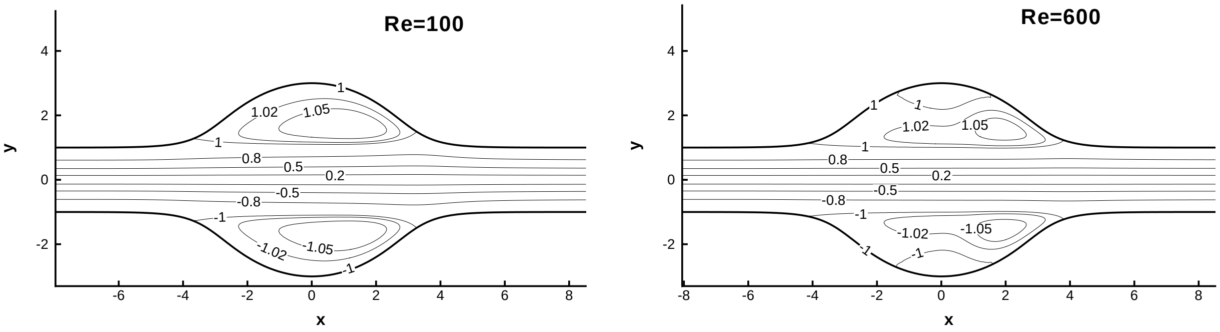

Figure 6.7: *Symmetric flow phenomena in a symmetric dilated channel having orifice length* $-4.0 \leq x \leq 4.0$ *and height of the maximum dilatation from the orifice* $H = 2.0$ *for Re=100 and 600.*

Table 6.2: *In an symmetric dilated channel: geometries of dilated channel and Reynolds number range studies.*

Model	Reynolds number range for calculations	Computed separation Reynolds number
M_1	1-750	66
M_2	1-750	22
M_3	1-750	10

Table 6.3: *In an symmetric dilated channel: grid independence study of the steady-state data at the center of the primary vortex for model* M_3 *(*$-4.0 \leq x \leq 4.0$*,* $H = 0.5$*).*

(h, k)	Re	Primary vortex center (x, y)	Max ψ
$(\frac{1}{25}, \frac{1}{40})$	100	(1.1767, 1.6377)	1.0880
	250	(1.6095, 1.5929)	1.0862
	500	(1.7068, 1.5623)	1.0744
$(\frac{1}{50}, \frac{1}{80})$	100	(1.1844, 1.6718)	1.0881
	250	(1.6095, 1.5929)	1.0861
	500	(1.7166, 1.5923)	1.0749

In table 6.3, we present grid independence data for ψ at the center of the primary vortex in model M_3 for $Re = 100$, 250 and 500 with two different grid sizes (h, k). Such grid sizes are $(\frac{1}{25}, \frac{1}{40})$ and $(\frac{1}{50}, \frac{1}{80})$, called as G_1 and G_2 respectively. With these grid sizes, we have presented the graph (see figure 6.8 for model M_3) for centerline velocity and the wall shear stress (wall vorticity) curves for $Re = 500$. These results confirm that the grid size finer than G_1 does not influence the numerical results.

In figures 6.9, 6.10 and 6.11, the first column illustrates the curves of constant streamfunctions with different Re values for the model M_1 ($-2.0 \leq x \leq 2.0$, $H = 0.5$), M_2 ($-3.0 \leq x \leq 3.0$, $H = 1$) and M_3 ($-4.0 \leq x \leq 4.0$, $H = 2$) respectively, and the second column represents corresponding vorticity contours. It has been numerically experimented that for lower Res (for example, $Re < 50$ in model M_1, $Re < 20$ in model M_2 and $Re < 9$ in model M_3) the streamlines contour show symmtrical patterns about the maximum height of the dilation (though the figures are not presented here). These symmetrical phenomena could be described by the fact that the effects of inertia do not dominate at these Re. A slight increase in Re stimulates the inertial effects

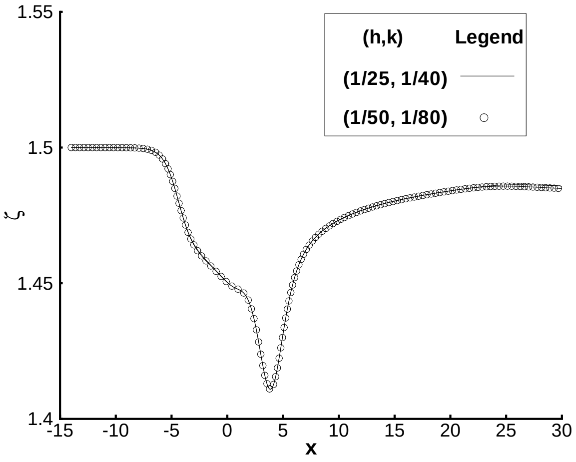

(a)

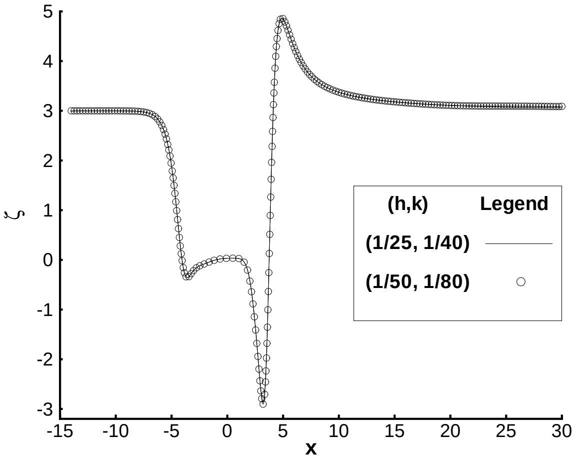

(b)

Figure 6.8: *In an symmetric dilated channel: grid independence test of (a) centerline velocity and (b) upper wall shear stress for* $Re = 500$ *in model* M_3 $(-4.0 \leq x \leq 4.0,$ $H = 2)$.

which result a slight perturbation in the streamlines (given in figure 6.9 for $Re = 50$, in figure 6.10 for $Re = 20$, in figure 6.11 for $Re = 9$) and the flow asymmetry starts to develop around the maximum cross-section of the channel. If Re values are increased further, recirculation zones (the large vortex called primary vortex) slowly develop because the pressure gradient across the dilated part of the channel is much higher in compared to the pressure gradient across the rest of the whole channel.

Table 6.4: *In a symmetric dilated channel: primary vortex center in the dilated channel flow for models M_1, M_2 and M_3.*

Model	Re	Primary vortex center (x, y)	Max ψ	Secondary vortex center (x, y)
M_1	100	(-0.2035, 1.3623)	1.0004	-
	250	(0.0654, 1.2435)	1.0043	-
	500	(0.2574, 1.1943)	1.0072	-
	750	(0.3837, 1.1832)	1.0081	-
M_2	100	(0.2590, 1.4629)	1.0205	-
	250	(0.6667, 1.3612)	1.0283	-
	500	(0.9724, 1.2997)	1.0278	-
	750	(1.1157, 1.2647)	1.0263	-
M_3	100	(1.1767, 1.6377)	1.0880	-
	250	(1.6095, 1.5929)	1.0862	-
	500	(1.7068, 1.5623)	1.0744	(0.1486, 2.6053)
	750	(1.8830, 1.5675)	1.0649	(0.1156, 2.3373)

For higher Res, a common observation is that the vortex rings nestled in the concavity of the dilated area and tend to grow in size with increase in Re, filling most of the dilated portion of the channel. It is also evident that for model M_3 ($-4.0 \leq x \leq 4.0$, $H = 2$) a large vortex develops even for $Re = 20$ (see figure 6.11).

In each model, it is seen that as Re increases, the center of the primary vortex moves towards distal side (see table 6.4 and figure 6.12). It is also seen from the table that for model M_1 ($-2.0 \leq x \leq 2.0$, $H = 0.5$), the $\psi_{\max}$ value increases with increase in Re but for higher degrees of dilation the general tendency is to decrease in $\psi_{\max}$ value with increase in Res. Another important observation for model M_3 ($-4.0 \leq x \leq 4.0$, $H = 2$) is that at higher Re (say for Re=500) (figure 6.11) a secondary vortex develops in the concavity of the dilatations deforming the shape of the primary vortex. The above facts conclude that the degree of dilatation i.e the area of the dilated region is more important for the development of recirculation zone than velocity (or Re).

In table 6.5 the separation and reattachment points have been cited for all the three model cases (see figure 6.13). The separation and reattachment points move further upstream and downstream respectively with the increase in Res resulting the growth and development of the vortices size. It is seen that for a constant Re, separation lengths increase with the increase in cross sectional area in the concavity of dilatations.

Table 6.5: *In a symmetric dilated channel: separation and reattachment points in the dilated channel flow for different degrees of dilatation.*

Model	Re	Separation points (x, y)	Reattachment points (x, y)
M_1	100	(-1.0219, 1.3227)	(0.4867,1.4552)
	250	(-1.4133, 1.2110)	(1.0744, 1.3073)
	500	(-1.6345, 1.1576)	(1.3674, 1.2233)
	750	(-1.7624, 1.1315)	(1.5033, 1.1881)
M_2	100	(-2.1549, 1.2968)	(1.7615, 1.4723)
	250	(-2.4610, 1.1937)	(2.1549, 1.2968)
	500	(-2.6285, 1.1513)	(2.3757, 1.2191)
	750	(-2.7110, 1.1336)	(2.4610, 1.1938)
M_3	100	(-3.6597, 1.2843)	(3.2577, 1.4952)
	250	(-3.9104, 1.1955)	(3.5739, 1.3219)
	500	(-4.0742, 1.1522)	(3.7860, 1.2358)
	750	(-4.1625, 1.1331)	(3.8553, 1.2125)

Figure 6.14 shows the variations of centerline velocity along axial direction for fixed *Re* with different degrees of dilation. It is seen that the effect of dilation on the centerline velocity is less along the upstream of the proximal side of the orifice compared to the distal side of the orifice. A drastic change of the centerline velocity occurs along the axial direction in the orifice. It is also noticed that for each *Re* the point at which minimum centerline velocity occurs, shifts towards the downstream with the increase in sectional area of the dilation. It should be mentioned that velocity decreases in the region around the maximum sectional area of the dilated channel. From physiological point of view, it can be mentioned that the dilated region leads to deposit lipids, proteins, fatty substances in the recirculation regions. This process is mainly responsible for the disease called "mural thrombogenesis". Thus, the thrombus completely occludes a blood vessel or a part of the thrombus may break off and moves downstream, which may enter in a smaller vessel and block it. This is a common disease in popliteal artery [62].

Figure 6.15 shows a comparative study on changes of wall vorticity along the x-direction for fixed *Re* with all the three models. The maximum wall shear stress occurs near to the distal lip of the orifice (see the tabular value of locations in figure 6.15). As *Re* increases, the location of the point at which shear stress is maximum slightly shifts towards distal side of the orifice (see the tabular values of locations in figure 6.15). The maximum change of the wall shear stress values occurs in the dilated region. Physiologically, it can be stated that this spatial variation in wall stresses lead to the damage of the vessel wall. i.e. endothelium. This may further weaken the wall and increase the possibility of aneurysm rupture. In addition to this, the high stress values in the ends of the dilatation (aneurysm lip) could be described as the cause of atherogenesis in the vicinity of aneurysms [62].

In figure 6.16 we have presented the axial velocity profile at the maximum cross section ($x = 0$) of the dilated channel. It shows that the parabolic shape of the profile has been disturbed towards the top wall indicating the development of negative shear stress values. Figure 6.16(a) and (b) show that the negative shear stress zone increases with increase in Re whereas the figure 6.16(c) shows a similar pattern up to $Re = 250$ but further increase in Re shows different behavior due to the development of another counter-rotating vortex in the sectional area.

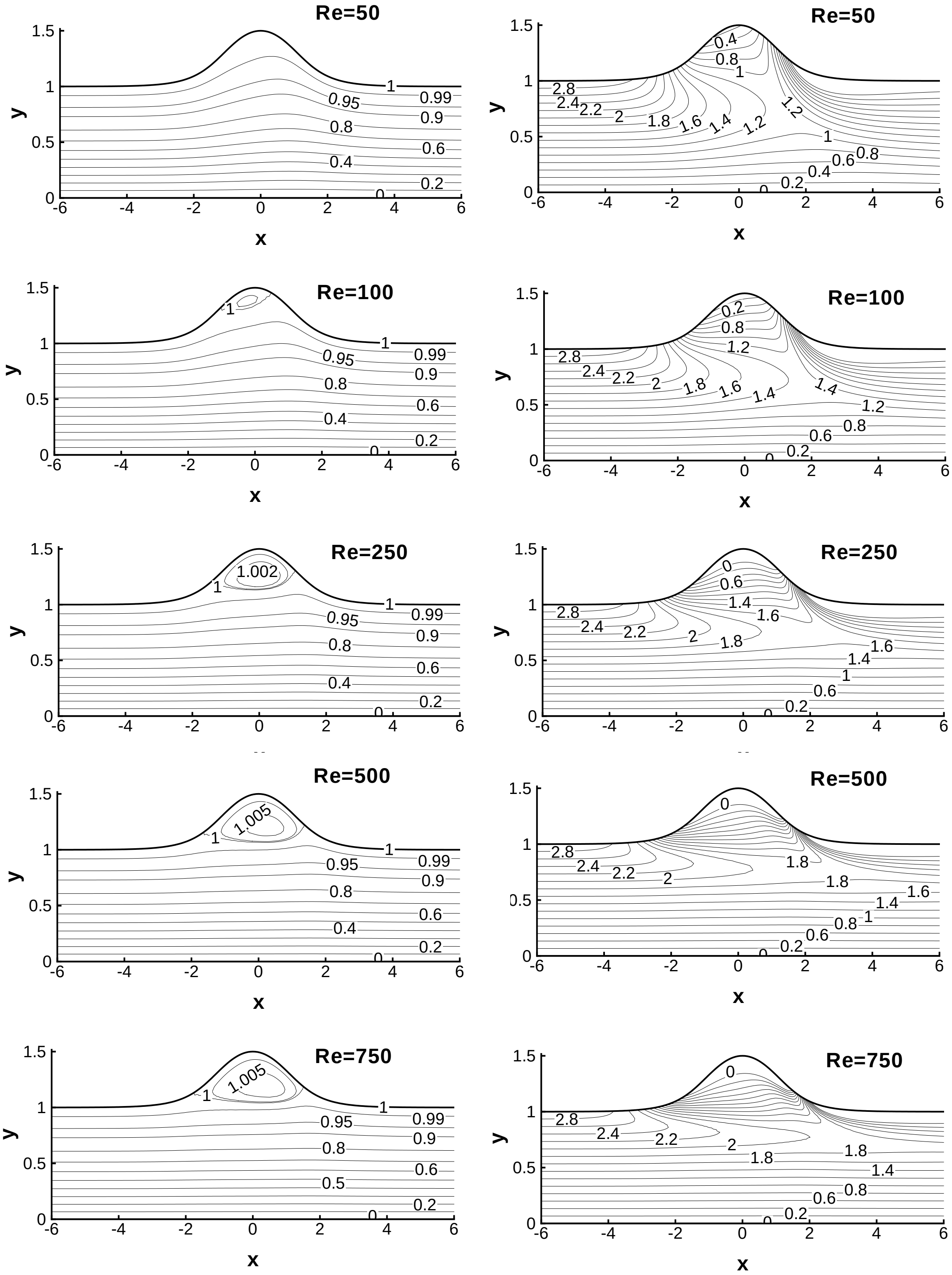

Figure 6.9: *In a symmetric dilated channel: streamline and corresponding vorticity contours for model* M_1 $(-2.0 \leq x \leq 2.0,\ H = 0.5)$ *at Re=50, 100, 250, 500 and 750.*

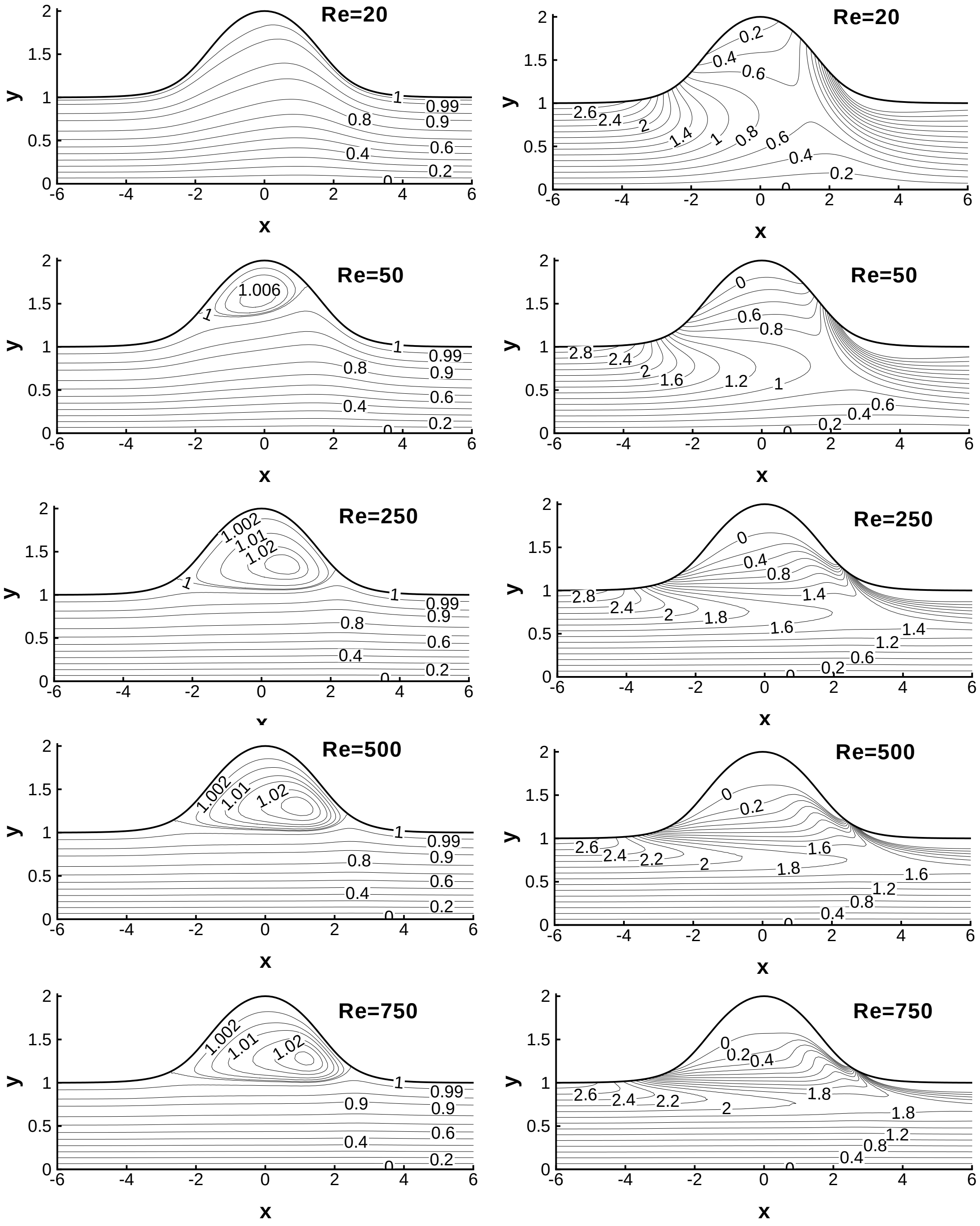

Figure 6.10: *In a symmetric dilated channel: streamline and corresponding vorticity contours for model* M_2 $(-3.0 \leq x \leq 3.0,\ H = 1)$ *at Re=20, 50, 250, 500 and 750.*

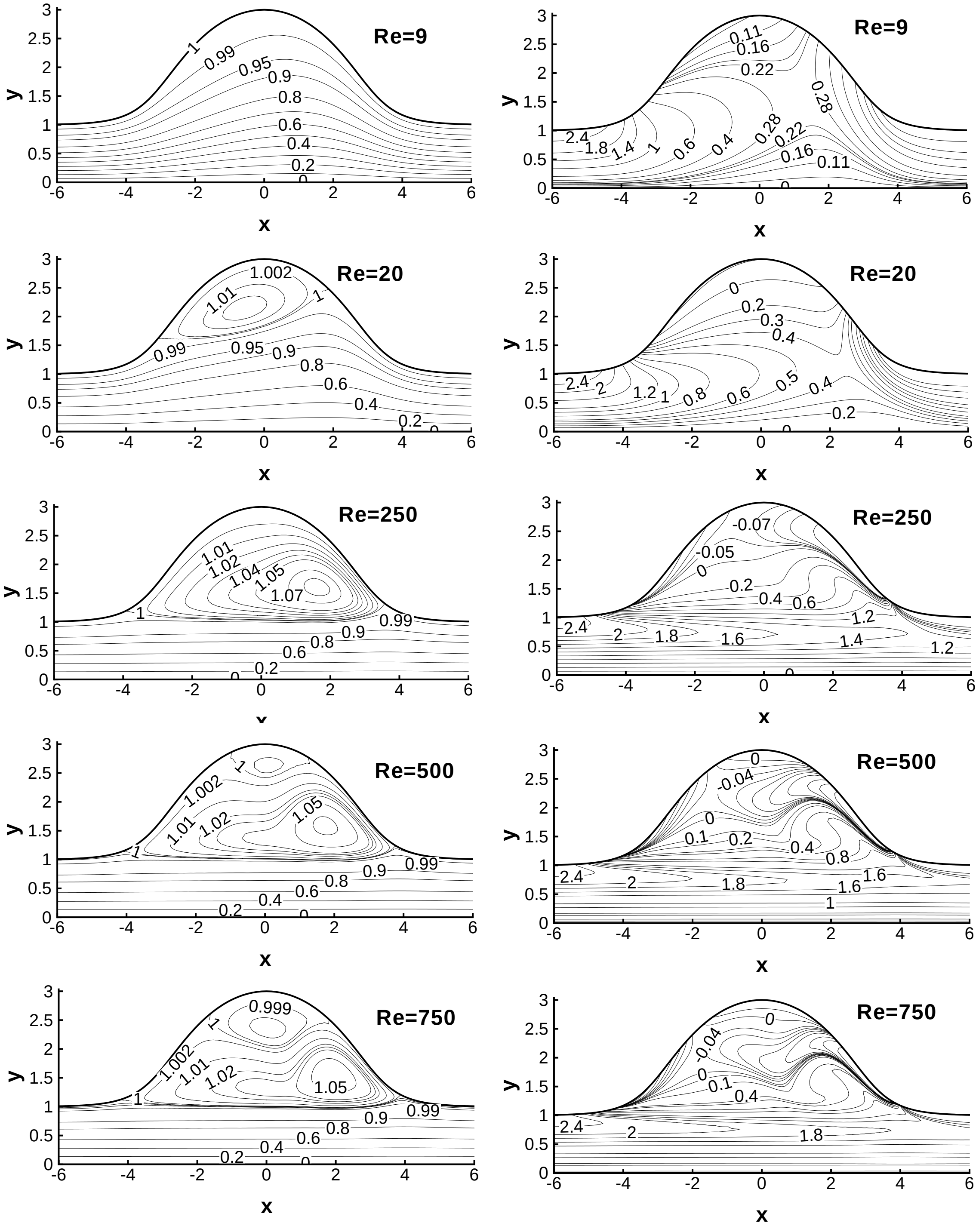

Figure 6.11: *In a symmetric dilated channel: streamline and corresponding vorticity contours for model* M_3 $(-4.0 \leq x \leq 4.0,\ H = 2)$ *at Re=9, 50, 250, 500 and 750.*

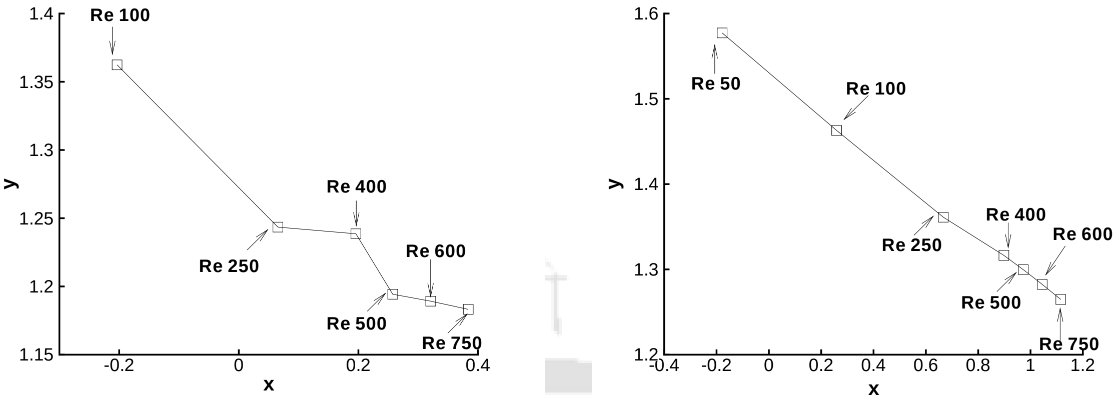

Figure 6.12: *In a symmetric dilated channel: movement of the location of the primary vortex center for models (a)* M_1 *(*$-2.0 \leq x \leq 2.0$, $H = 0.5$*), (b)* M_2 *(*$-3.0 \leq x \leq 3.0$, $H = 1.0$*).*

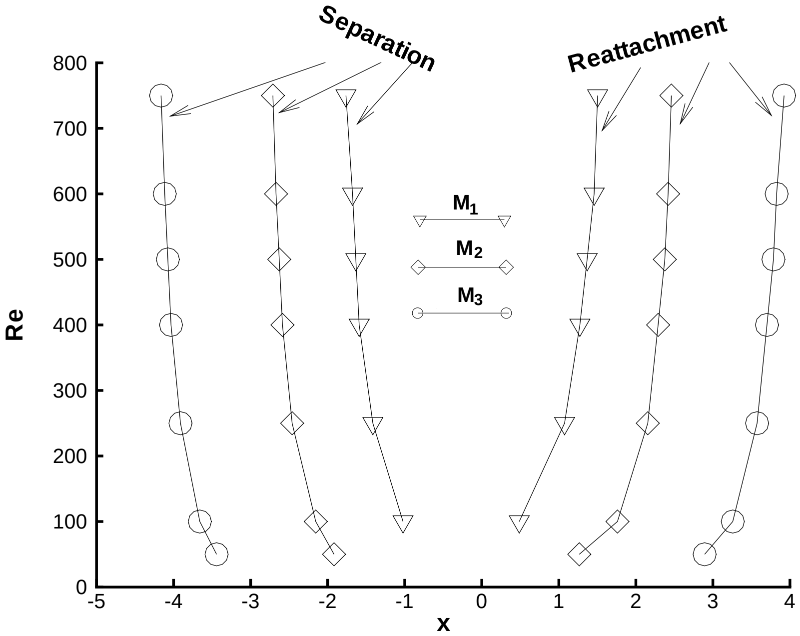

Figure 6.13: *In a symmetric dilated channel: separation and reattachment points of the primary vortex along the dilated wall for different degrees of dilatation.*

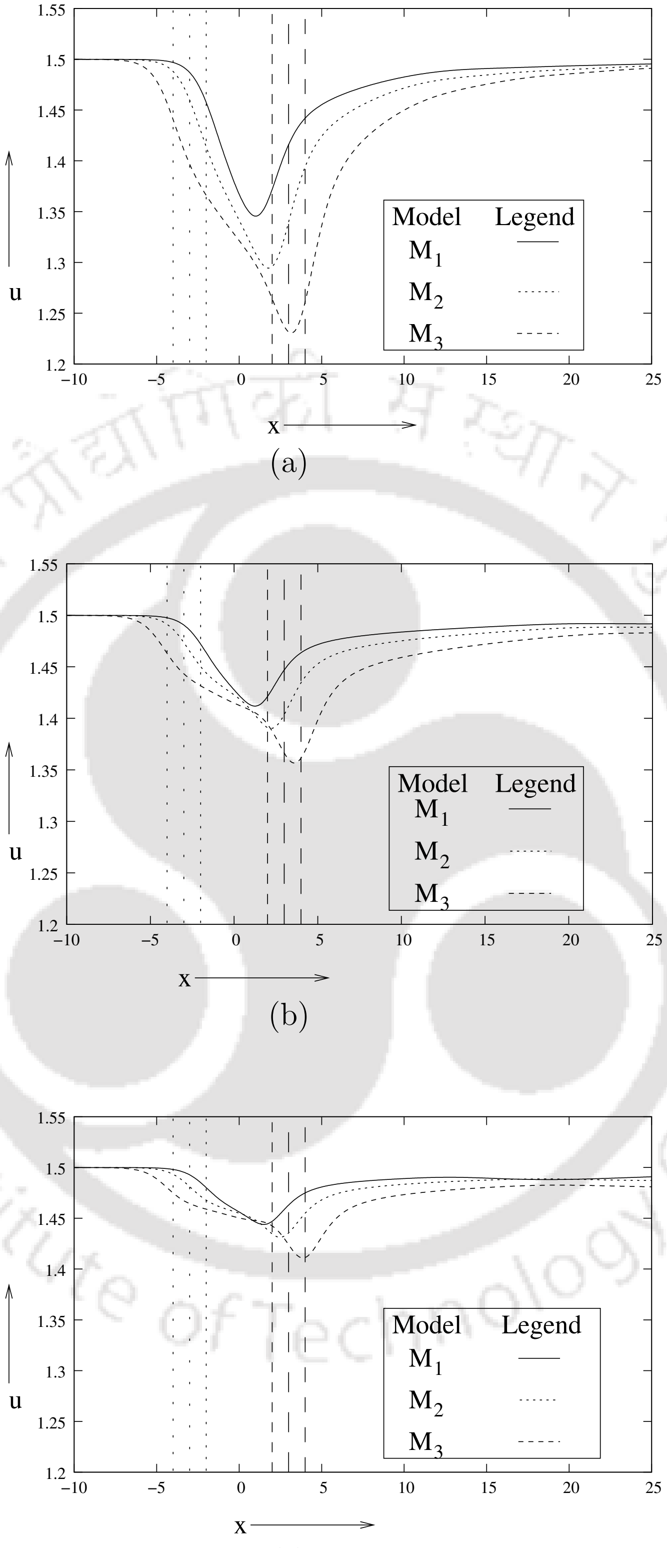

(a)

(b)

(c)

Figure 6.14: *In a symmetric dilated channel: Centerline axial velocity for (a) Re =* 100, *(b) Re =* 250 *and (c) Re =* 500.

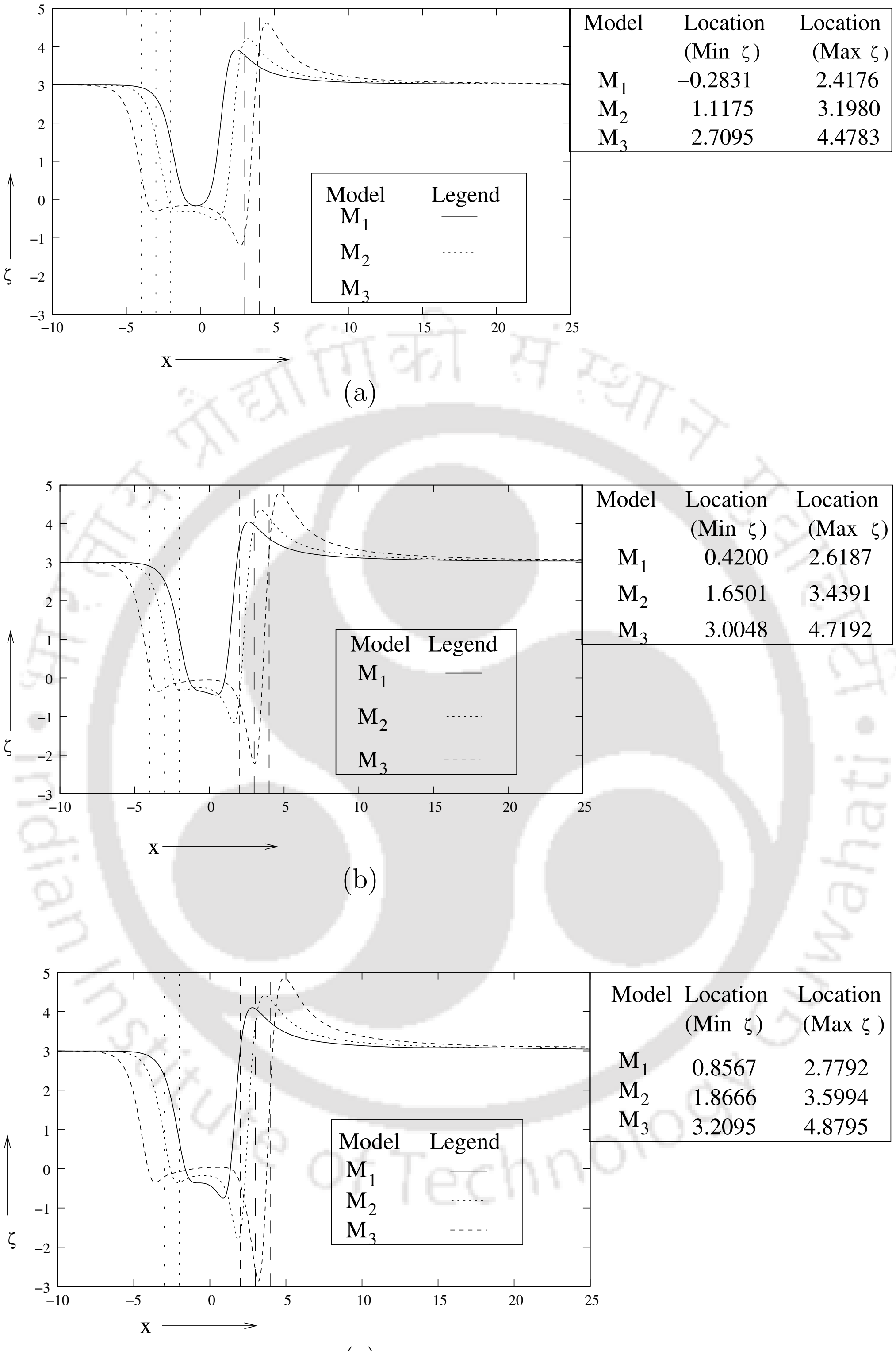

(a)

Model	Location (Min ζ)	Location (Max ζ)
M_1	−0.2831	2.4176
M_2	1.1175	3.1980
M_3	2.7095	4.4783

(b)

Model	Location (Min ζ)	Location (Max ζ)
M_1	0.4200	2.6187
M_2	1.6501	3.4391
M_3	3.0048	4.7192

(c)

Model	Location (Min ζ)	Location (Max ζ)
M_1	0.8567	2.7792
M_2	1.8666	3.5994
M_3	3.2095	4.8795

Figure 6.15: *In a symmetric dilated channel: Wall shear stress for (a)* $Re = 100$*, (b)* $Re = 250$ *and (c)* $Re = 500$*.*

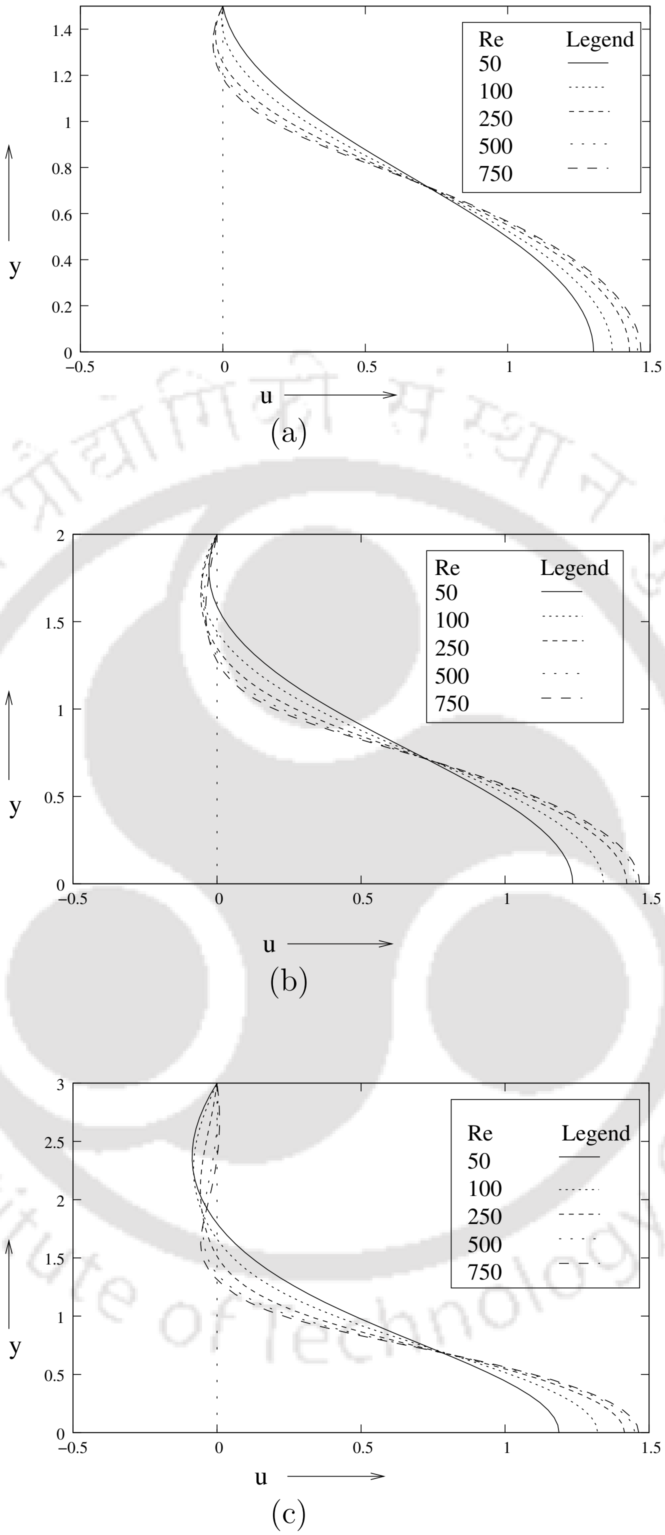

Figure 6.16: *In a symmetric dilated channel: axial velocity at the maximum cross-section for models (a)* M_1 *(*$-2.0 \leq x \leq 2.0$, $H = 0.5$*), (b)* M_2 *(*$-3.0 \leq x \leq 3.0$, $H = 1$*) and (c)* M_3 *(*$-4.0 \leq x \leq 4.0$, $H = 2$*).*

6.4 Conclusions

This study analyzes the steady-state solution of incompressible viscous flows in a lateral and a symmetric dilated channel with different degrees of dilatation using the proposed transient HOC schemes in chapter 3. We have studied a wide variety of model cases. The numerical solutions of these cases are performed to quantify the effect of the geometries upon the flow characteristics (separation and reattachment of points, stream lines, size and intensity of recirculation vortices). The following conclusions are drawn from the data presented:

Lateral dilated channel

1. In all the models, the flow patterns along upstream and downstream of the orifice are found to be similar.
2. One vortex in circular shaped dilated region and two vortices in concave shaped dilated region develop.
3. Generally, the wall shear stress is maximum at the distal lip or near it towards downstream.

Symmetric dilated channel

1. With the increase in area in the concavity of the dilatations, the critical Re for separation decreases.
2. Increase in Res show that the flow asymmetry exists about the maximum height of the dilated region of the channel.
3. Vorticity contours show that the gradients is high around the proximal and distal lip of the orifice.
4. The maximum wall share stress occurs near to distal lip of the orifice towards downstream.

It is obvious that neck of the aneurysm plays an important role for wall shear stress distribution. In the case of symmetric dilation the wall shear stress is comparatively low. It indicates that the spherical shaped aneurysm is more sensitive to aneurysm rupture. This flow analysis could predict the cause of some arterial diseases. Such as, the development of recirculation region can facilitate thrombogenesis in the case of dilatation of blood vessels. The high shear stress values in the vicinity of the end of aneurysms can lead to the atherogenesis. However, it is clear from our study that the area in the dilated part, the shape of the dilated region, Reynolds number are the important parameters to control the strength and the size of the recirculation zone without modifying the general flow patterns. However, the present study enriches various aspects of channel flows.

Chapter 7

Steady incompressible viscous flows in a constricted tube

So far we have confined our studies in the Cartesian coordinate systems. In this chapter, we have discussed our proposed scheme (given in chapter 2) for cylindrical coordinate systems. A calculation procedure for two dimensional (2D) incompressible viscous flows over curved boundaries, particularly flow in a constricted tube, is described.

7.1 Introduction

Like previous chapter, the study of flows in a constricted tube is an another important aspect in the field of physiological flow. Flow phenomena in such problems resemble with the blood flow through stenosed vessel. Stenosis is a generic medical term which means a narrowing of any body passage, tube or orifice. In physiology it is caused mainly due to atherosclerosis disease.

A considerable amount of work on arterial stenosis has been reported in the last few decades. Stenosis due to atherosclerosis causes the drastic change of the blood flow behavior. Hemodynamical perturbations induced by an atherosclerotic plaque have been continuously investigated over the past few decades. Changes in blood flows through diseased vessels generally depend on its geometric configurations and the percentage of area reductions. There are several literature about information pertinent to the genesis [4, 70, 117, 155], progression [12, 13, 15] and fluid dynamical effects [7, 22, 25, 26, 58, 61, 63, 99, 100, 107, 126, 142, 144] which has been acquired from autopsies and various in vivo, in vitro and numerical studies. Though there are several experimental studies available in the literature, but the number of theoretical studies is limited. This could be due to the complexity of simulation of the flow behaviour in reality as well as lower order accurate numerical schemes that have been used so far. So there is a great interest to solve this problem with higher order accurate schemes. Constantinescu and Lele [32] make a mark on cylindrical coordinate systems for higher order schemes.

Recent developments of techniques for the endovascular treatment of stenosis have indicated the need of a better understanding of the relevant hemodynamic effects. As the flow in a constricted tube is an ideal case of the flow through a stenosed vessel, the theoretical study of the flow in a constricted tube may give some basic informations and predictions about the flow through stenosed artery. It is very difficult to find analytical solution of the problem of fluid flows through a constricted tube. In addition to this, it may be sometimes difficult to describe mathematically the stenosed geometry and flow conditions seen in reality. In such cases often many simplifying assumptions make easier to find the approximate solution.

In the present work, we have applied our scheme proposed in chapter 2 on incompressible viscous flows through a constricted tube. In reality, vessels are elastic but due to the plaque formation, the local region of stenosis mostly behaves like a rigid tube. Again blood flow in a large artery shows Newtonian fluid flow behavior [152]. Therefore, in present study, we have considered the flow to be Newtonian and the tube to be rigid.

7.2 Numerical procedure

7.2.1 The problem

We consider incompressible viscous flows in a axisymmetric constricted tube with different degrees of area reductions. The schematic flow diagrams and corresponding boundary conditions are shown in figure 7.1. The geometry have been chosen for the present work because it has been studied experimentally and present suitable test case for the calculation method. In this figure the centerline is treated as z-axis and the line perpendicular on z-axis and passes through the throat with minimum cross section is donated as r-axis. The point of intersection of z and r-axes is called origin. Here, l is the half of stricture length (stenosis length) and δ the depth of the throat, as shown in figure 7.1.

The Navier-Stokes equations representing the axisymmetric steady flow in cylindrical coordinate system for a fluid, which is assumed to be homogeneous, incompressible, isothermal and Newtonian, can be written in non-dimensional form using the non-

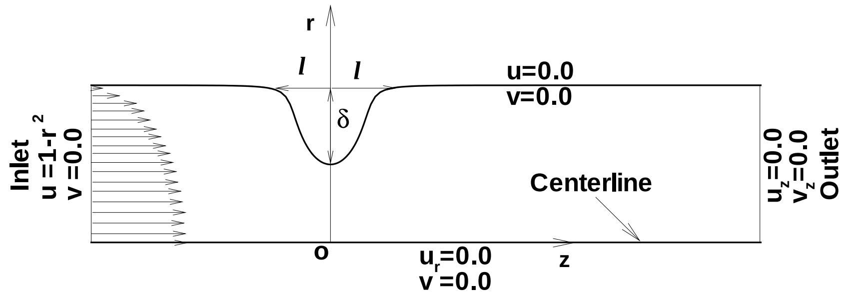

Figure 7.1: *Constricted tube flow configuration with boundary conditions.*

dimensional variables $r^* = \dfrac{r}{r_0}, z^* = \dfrac{z}{r_0}, u^* = \dfrac{u}{u_0}, v^* = \dfrac{v}{u_0}, p^* = \dfrac{p}{\rho u_0^2}$ as

$$\frac{\partial u}{\partial z} + \frac{\partial v}{\partial r} + \frac{v}{r} = 0, \tag{7.1}$$

$$Re\left(u\frac{\partial u}{\partial z} + v\frac{\partial u}{\partial r} + \frac{\partial p}{\partial z}\right) = \left(\frac{\partial^2 u}{\partial z^2} + \frac{\partial^2 u}{\partial r^2} + \frac{1}{r}\frac{\partial u}{\partial r}\right), \tag{7.2}$$

$$Re\left(u\frac{\partial v}{\partial z} + v\frac{\partial v}{\partial r} + \frac{\partial p}{\partial r}\right) = \left(\frac{\partial^2 v}{\partial z^2} + \frac{\partial^2 v}{\partial r^2} + \frac{1}{r}\frac{\partial v}{\partial r} - \frac{v}{r^2}\right), \tag{7.3}$$

where u, v are velocities along z-, r-directions respectively, p is the pressure and Re is the Reynolds number given by $Re = \dfrac{r_0 u_0}{\nu}$, where r_0 is called the characteristic radius, u_0 is the average velocity at the inlet and ν is the kinematic viscosity.

To formulate the governing equations (7.1), (7.2) and (7.3) in streamfunction $\psi(z, r)$ and vorticity $\zeta(z, r)$ form, we use the following definition of u, v such as

$$u = \frac{1}{r}\frac{\partial \psi}{\partial r}, \qquad v = -\frac{1}{r}\frac{\partial \psi}{\partial z}. \tag{7.4}$$

From definition of vorticity (ζ) it can be written as

$$\begin{aligned} \zeta &= \frac{\partial v}{\partial z} - \frac{\partial u}{\partial r} \\ &= -\frac{1}{r}\frac{\partial^2 \psi}{\partial z^2} + \frac{1}{r^2}\frac{\partial \psi}{\partial r} - \frac{1}{r}\frac{\partial^2 \psi}{\partial r^2}, \end{aligned}$$

i.e

$$\frac{\partial^2 \psi}{\partial z^2} + \frac{\partial^2 \psi}{\partial r^2} - \frac{1}{r}\frac{\partial \psi}{\partial r} = -\zeta r. \tag{7.5}$$

To eliminate p from the two non-dimensional momentum equations (7.2) & (7.3) by subtracting the differentiation of (7.2) w.r.t r from the differentiation of (7.3) w.r.t z and by continuity equation with simplification we get

$$Re\left[-\frac{v\zeta}{r}+u\frac{\partial\zeta}{\partial z}+v\frac{\partial\zeta}{\partial r}\right]=\left(\frac{\partial^2\zeta}{\partial z^2}+\frac{\partial^2\zeta}{\partial r^2}\right)+\frac{1}{r}\left(\frac{\partial\zeta}{\partial r}-\frac{\zeta}{r}\right). \qquad (7.6)$$

Therefore, the coupled equation for ψ and ζ in non-dimensional form can be written as

$$\psi_{zz}+\psi_{rr}-\frac{1}{r}\psi_r=-r\zeta, \qquad (7.7)$$

$$-\left(\zeta_{zz}+\zeta_{rr}\right)+uRe\zeta_z+\left(vRe-\frac{1}{r}\right)\zeta_r+\zeta\left(\frac{1}{r^2}-\frac{vRe}{r}\right)=0. \qquad (7.8)$$

These equations are the stream function and vorticity equation for incompressible viscous flows in a constricted tube. Equations (7.7) & (7.8) have the singularity at the centerline $r=0$. So it needs a special treatment at the centerline. Retaining the physics of the flow as unchanged, this singularity has been handled with care. The equations (7.7) & (7.8) can be brought under the umbrella of a general differential equation

$$\alpha(z,r)\frac{\partial^2\phi}{\partial z^2}+\beta(z,r)\frac{\partial^2\phi}{\partial r^2}+\gamma(z,r)\frac{\partial\phi}{\partial z}+\nu(z,r)\frac{\partial\phi}{\partial r}+\omega(z,r)\phi=\theta(z,r), \qquad (7.9)$$

where θ is the source term.

The same procedure as in chapter 2 has been followed to get the higher order compact scheme in cylindrical coordinate system.

The boundary conditions applied are as follows:

1. Symmetry line
   (a) $\psi=0,\zeta=0,v=0,\dfrac{\partial u}{\partial r}=0.$
2. Upper boundary
   (a) $u=v=0$ (usual no-slip conditions at the wall), $\psi=0.25$.
   (b) The vorticity ζ is obtained from governing equations.
3. Inflow
   (a) $\psi=\frac{1}{2}r^2(1-\frac{1}{2}r^2),\zeta=2r,u=(1-r^2),v=0.$
4. outflow
   The downstream location is assumed to be far enough so that the flow field does not change along the axis i.e the flow is assumed to be fully developed flow
   (a) $\psi_z=0,\zeta_z=0,u_z=0,v_z=0.$

7.2.2 Flow geometry and Mesh structure

Flow characteristics in the r-z half plane with respect to central line are computed as the flow is assumed to be axisymmetric. In vivo study reveals that the flow is very sensitive around the throat region. To capture the flow phenomena in a constricted tube accurately, a nonuniform mesh structure (see figure 7.2) on curvilinear setting has been provided through a conformal transformation [107] which produces a refined grid around the throat (see figure 7.2) as desired. This transformation maps the actual nonuniform geometry (physical domain) to a uniform rectangular geometry (computational domain) as follows:

$$\chi = w + B \tanh(\frac{\pi}{2} C w),$$

where $\chi = z + ir$ and $w = \xi + i\eta$ ($i = \sqrt{-1}$) with

$$\begin{aligned} \xi &= z + B\frac{\sinh(C\pi z)}{\cosh(C\pi z) + \cos(C\pi r)}, \\ \eta &= r + B\frac{\sin(C\pi r)}{\cosh(C\pi z) + \cos(C\pi r)}, \end{aligned} \tag{7.10}$$

where B and C are constants and determine the degrees of area reduction.

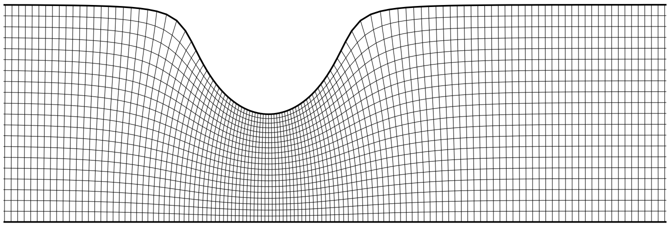

Figure 7.2: *Constricted tube's mesh structure.*

NOTE: The discretization of the transformed form of the governing equations (7.7) and (7.8), and the solution procedure of the resulting algebraic equations have been followed as in chapter 2. For the Neumann conditions at the outlet and along the horizontal centerline, we use a one-sided five point formula prescribed in [143]. For example, for a typical flow variable ϕ (which may represent u, v, ψ or ζ) at the outlet (denoted by the index b along z-axis), we use

$$\phi_{b,j} = 0.04\left[48\phi_{b-1,j} - 36\phi_{b-2,j} + 16\phi_{b-3,j} - 3\phi_{b-4,j} - 12h\left(\frac{\partial\phi}{\partial r}\right)_{b,j}\right] + O(h^5),$$

where h is the z-step length in the physical plane.

We have numerically experimented and accordingly we have found the minimum inlet distance from the throat of the constricted tube, which is $z \approx -10$ such that the stenosis effect at the inlet is negligible. And in order to get fully developed flow at the outlet for Reynolds numbers up to $Re = 1000$ we have numerically experimented and found a common minimum distance from the throat as $z \approx 30$. However these distances depend on the parameters (Re, degrees of constriction, etc.) In all the computations we have used step lengths $\Delta\xi = \frac{1}{20}, \frac{1}{25}$ and $\frac{1}{40}$ along the horizontal, and $\Delta\eta = \frac{1}{20}$ and $\frac{1}{40}$ along the vertical directions in the computational plane.

7.3 Results and discussions

Figure 7.3 shows the comparison of separation and reattachment points with Young and Tsai's experimental and Deshpande's numerical results for 56% area reduction. The present results for separation points are showing a very good agreement with both the experimental and numerical results but for reattachment points a disagreement is found with experimental results. It was mentioned that the experimental results for reattachment points were difficult to measure for Re higher than 300 due to flow instabilities [155]. It is seen that the separation length increases with the increase in Re.

The change in axial velocity (u) along radial direction (r) at different axial stations for 75% area reduction has been presented in figure 7.4 at $Re = 200$. Theoretically, it is well known that for a prescribed parabolic profile at the inlet of an symmetric tube the maximum axial velocity of each of the subsequent parabolic profile always occurs at the centerline. But our study shows that for a prescribed parabolic profile at the inlet of the constricted tube the maximum axial velocity generally does not occur on the centerline near the throat for severe area reductions (see figure 7.4 for velocity profile at the throat i.e. $z = 0$) whereas at inlet and outlet a parabolic profile is maintained. This observation agrees reasonably well with Deshpande *et al.* [34]. It could be due to severe area reduction that makes the flow field unstable around the throat.

Figure 7.5 reveals the effects of area reductions on velocity field around the throat. It is seen that for a fixed stricture length ($-1 \le l \le 1$) the parabolic profile prescribed

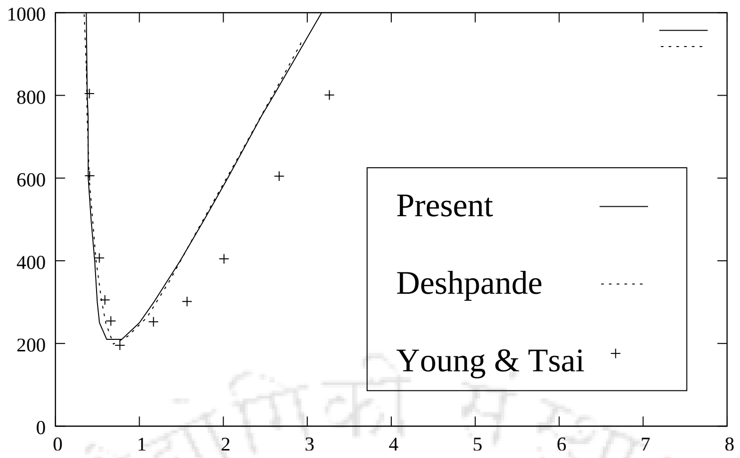

Figure 7.3: *In a constricted tube: separation and reattachment curve for steady flow with 56% area reduction with stricture length* $-4 \leq l \leq 4$.

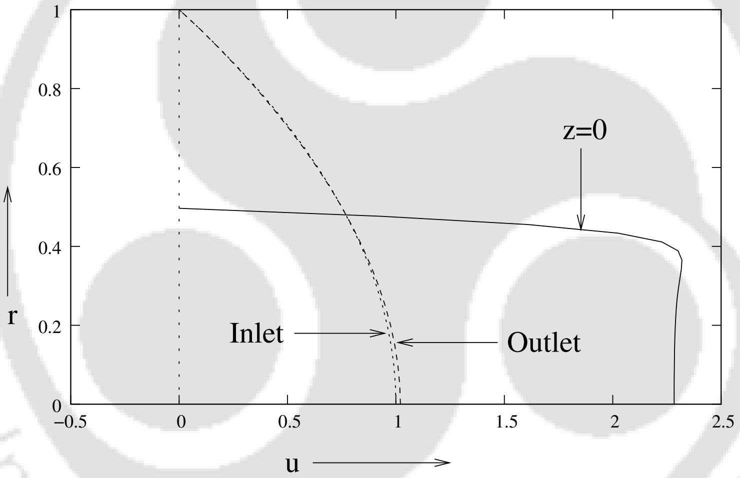

Figure 7.4: *In a constricted tube: velocity profiles for* $Re = 200$ *at three axial locations having stricture length* $-1 \leq l \leq 1$ *with 75% area reduction.*

at the inlet is no longer remains parabolic around the throat and it turns into blunt (non-parabolic) shaped at the throat with the increase in area reductions. It is also noticed that the velocity increases at the throat with the increase in area reductions as expected. After the throat of the constricted tube, a small negative velocity zone develops for 44% area reduction, which increases in size with the increase in area reduction (see figure 7.5 for 75% area reduction). This phenomenon can be explained

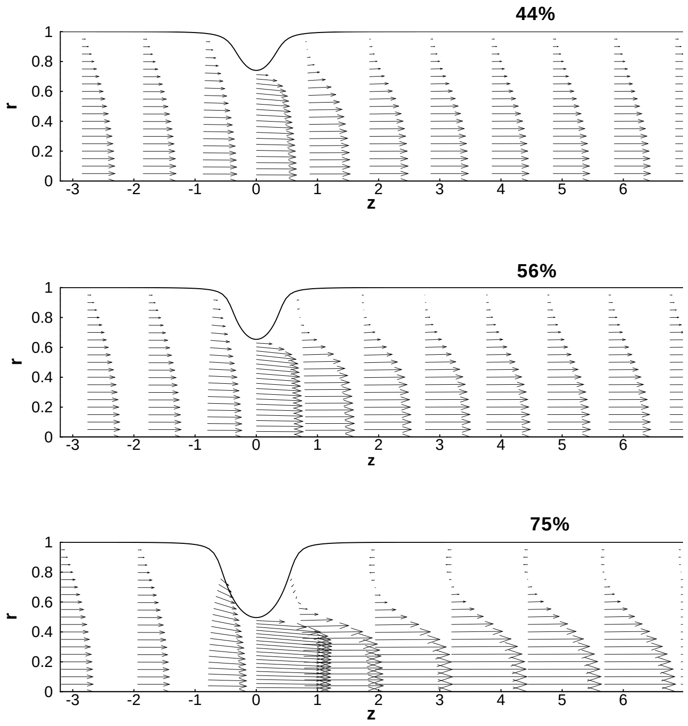

Figure 7.5: *In a constricted tube: velocity profiles around the throat for* $Re = 200$ *with different degrees of area reduction, having stricture length* $-1 \leq l \leq 1$.

as follows. Sudden expansion of the tube just after the throat causes pressure drop resulting recirculation of flows thereat. The area of the expanded region increases with higher degrees of area reduction resulting high pressure drops which causes large recirculation zone. From a physiological point of view, the decrease in velocity in this recirculation zone helps to deposit lipids, proteins, fatty substances there stimulating further stenosis.

In figure 7.6 the streamline contours for $Re = 200$ have been presented for different area reductions with the same stricture lengths ($-1 \leq l \leq 1$). It is seen that as the area reduction increases the size of the recirculation zone increases which has already been discussed in the previous paragraph. It is to be noted here that the strength of this recirculation zone increases with increase in area reduction.

Figure 7.7 shows the corresponding vorticity contours of figure 7.6. It shows that in the flow domain the patterns of the vortex line structures are basically same with different high gradient regions.

The variation of the axial velocity along the centerline is quite evident from figure 7.8 for different degrees of area reductions. In all cases, the stricture length is fixed $-1 \leq l \leq 1$. It reveals that for a fixed degree of area reduction the peak centerline velocity decreases with increase in Re. It is also seen that for a fixed Re, the peak velocity values increases with the increase in degrees of the area reduction as expected. For a fixed degree of area reduction the peak velocities occur for different Res nearer the throat towards downstream. The locations of the points (cited in the respective table) at which the peak velocities occur slightly shift towards downstream with increase in Re. In addition to this it is also noticed that, with the increase in Re the centerline velocity decreases linearly along the downstream. The above facts could be described as follows. Due to separation velocity gradients occur. For lower Re, this gradient is high in comparison with higher Re. For higher Re, velocity falls slowly and the maximum velocity is diminished due to resistance.

In figure 7.9 the results of wall shear stress due to area reductions 44 %, 56% and 75% respectively have been presented. The negative values of wall shear stress in the post stenotic region correspond to flow reversal in the separated flow region. It is seen that as the area reduction increases, the peak shear stress values increase for a fixed Re. For severe constriction, the rapid increase in wall vorticity is quite apparent. It is also seen that the location of the peak vorticity occurs at the upstream of the throat.

Figure 7.10 presents streamline contours determining the effect of varying stricture length. With the increase in stricture length, the recirculation zone becomes shorter and thinner. The separation point move further downstream from the throat.

In figure 7.11 the results of wall shear stresses for different Res in a 56% area reductions with different stricture lengths have been presented. It shows that with increase in stricture lengths the peak shear stress values are reduced and the peak does not rise sharply. However, all these three figures are showing the same patterns. The only difference is in peak vorticity values for different Res. The negative values of wall shear stresses after the throat correspond to flow reversal in the separated flow region. It also shows that as the stricture length increases, the region of negative shear stresses decreases which can be observed from figure 7.10.

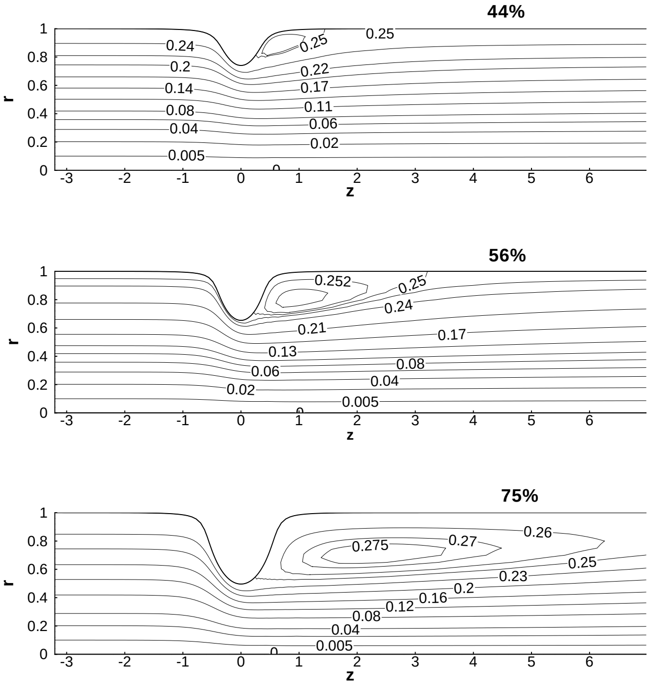

Figure 7.6: *In a constricted tube: streamline-contours for* $Re = 200$*, having stricture length* $-1 \le l \le 1$ *with different degrees of area reduction.*

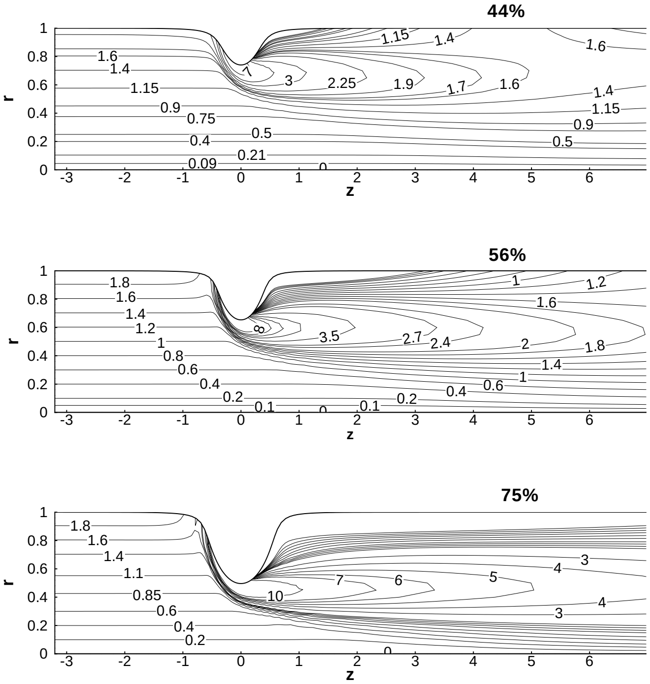

Figure 7.7: *In a constricted tube: vorticity contours for* $Re = 200$*, having stricture length* $-1 \le l \le 1$ *with different area reductions.*

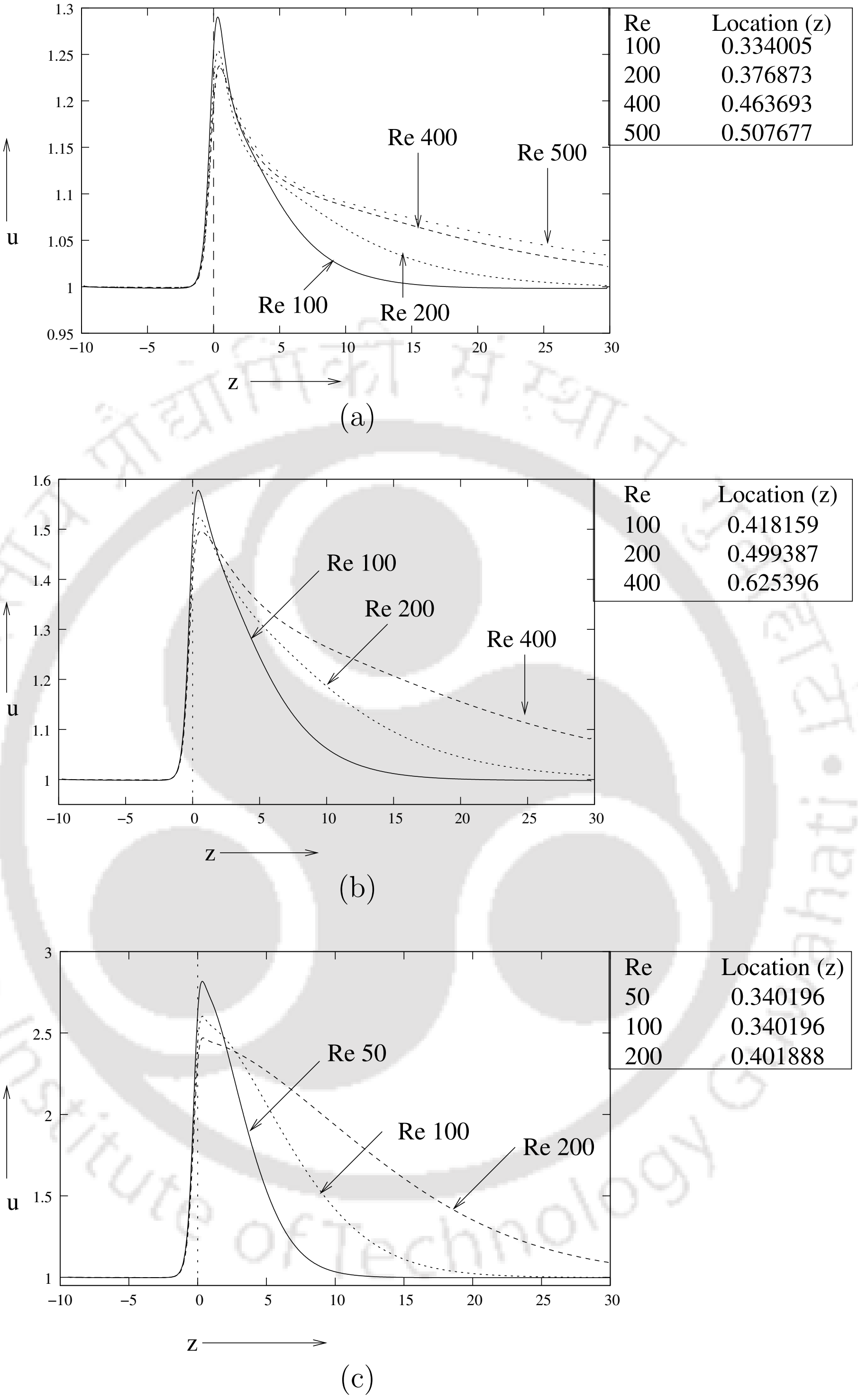

Re	Location (z)
100	0.334005
200	0.376873
400	0.463693
500	0.507677

Re	Location (z)
100	0.418159
200	0.499387
400	0.625396

Re	Location (z)
50	0.340196
100	0.340196
200	0.401888

Figure 7.8: *In a constricted tube: centerline velocity for stricture length* $-1 \leq l \leq 1$ *with area reduction (a) 44%, (b) 56% and (c) 75%.*

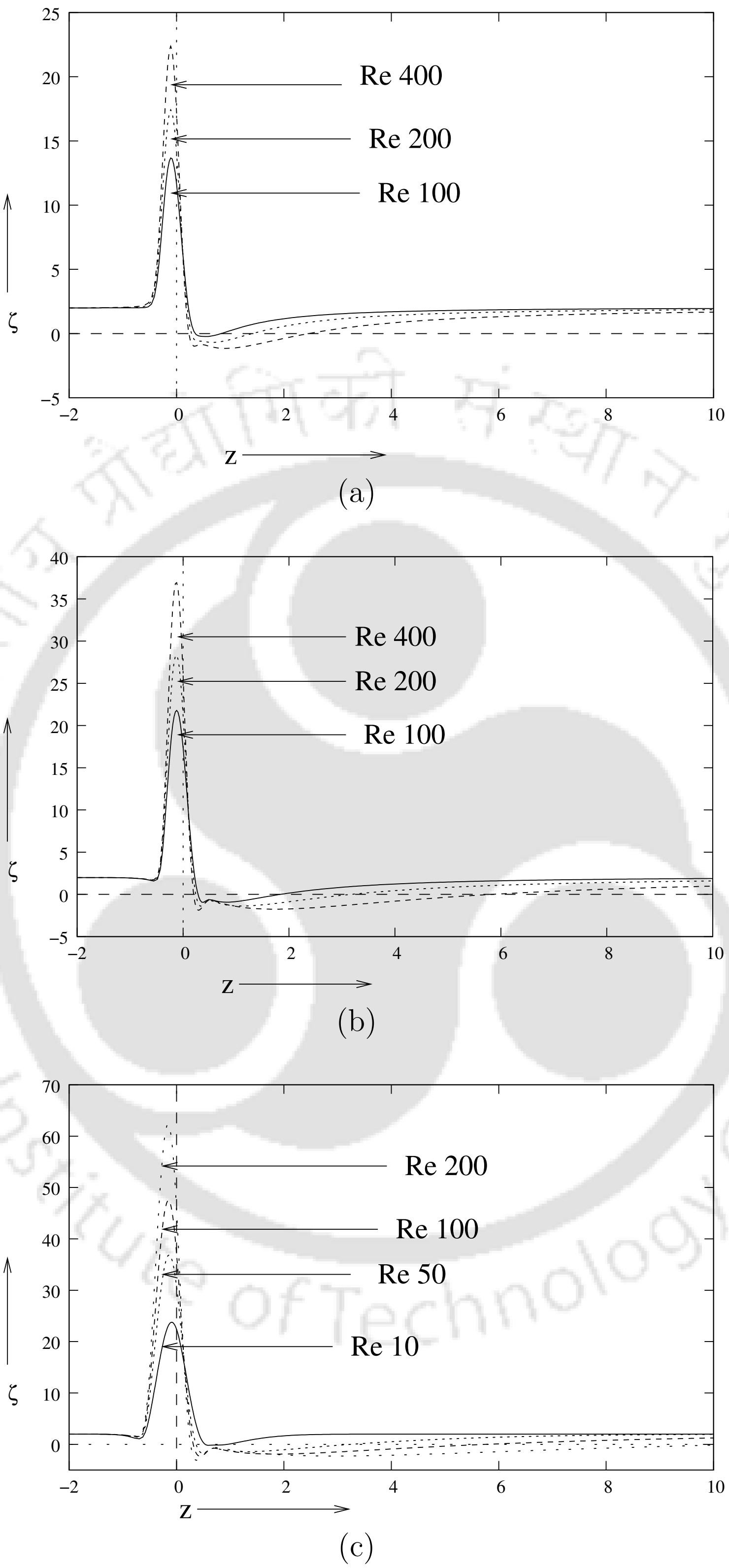

Figure 7.9: *In a constricted tube: wall vorticity for stricture length* $-1 \leq l \leq 1$ *with area reduction (a) 44%, (b) 56% and (c) 75%.*

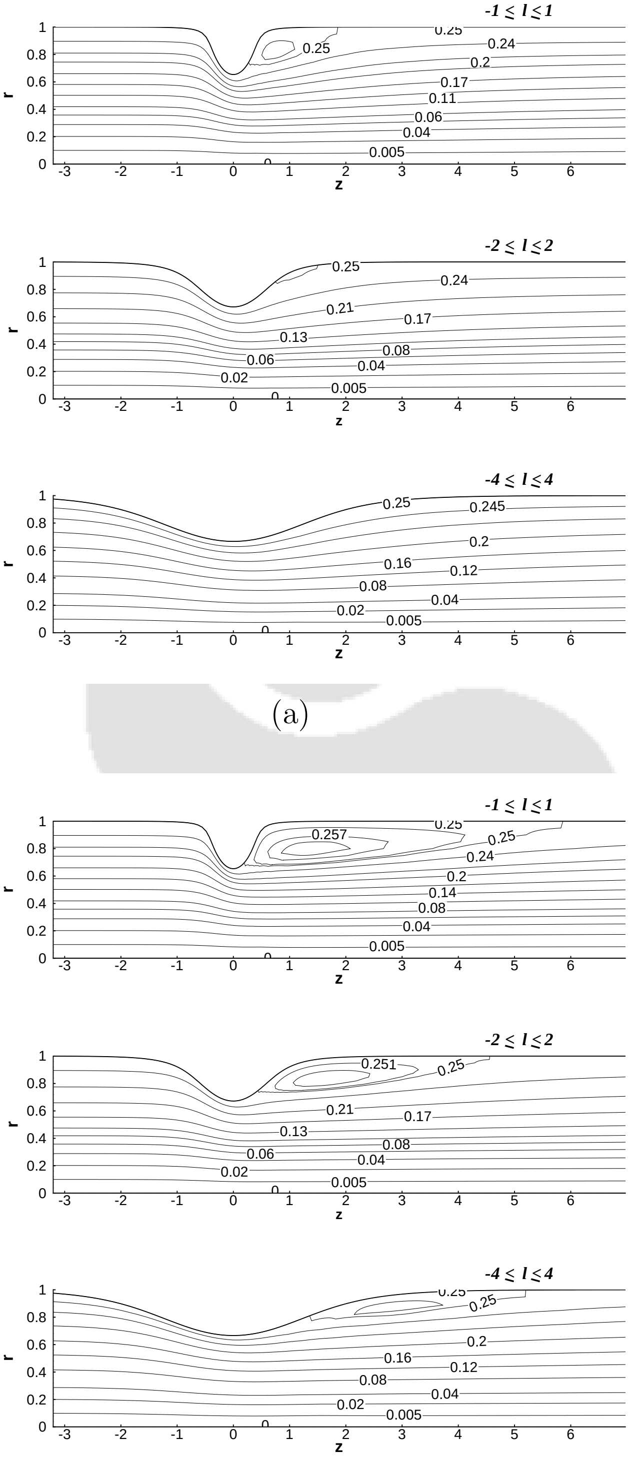

(a)

(b)

Figure 7.10: In a constricted tube with 56% area reduction and stricture length $-1 \leq l \leq 1$, $-2 \leq l \leq 2$ and $-4 \leq l \leq 4$: streamline contours for (a) $Re = 100$ and (b) $Re = 400$.

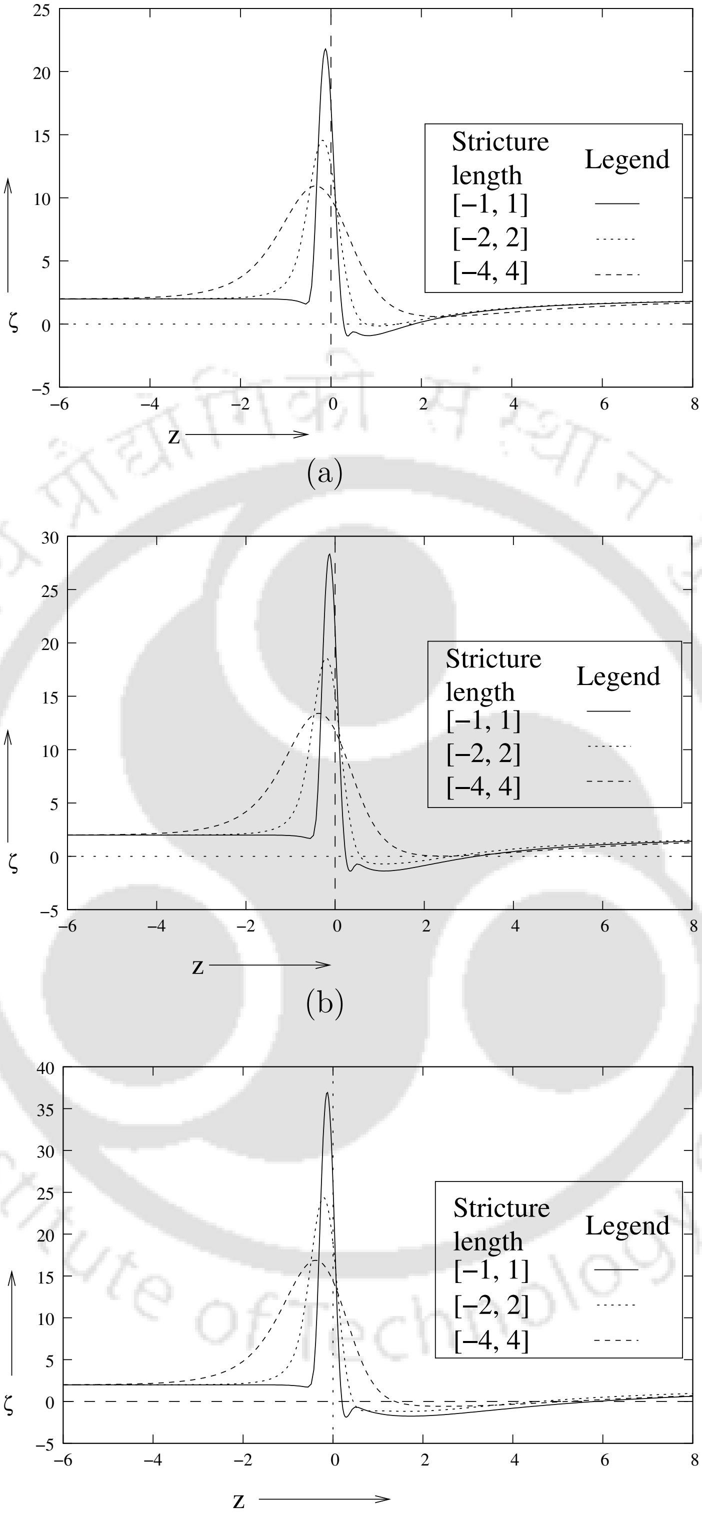

(a)

(b)

(c)

Figure 7.11: *In a constricted tube with 56% area reduction and stricture length* $-1 \le l \le 1$, $-2 \le l \le 2$ *and* $-4 \le l \le 4$*: Wall shear stress for (a)* $Re = 100$ *(b)* $Re = 200$ *and (c)* $Re = 400$*.*

7.4 Conclusions

In this chapter, we have extended the proposed higher order compact (HOC) scheme from cartesian coordinate systems (presented in chapter 2) to cylindrical coordinate systems. A constricted tube flow problem has been studied to realize the potential of the scheme. The numerical results are compared with both experimental and numerical results available in the literature. An excellent agreement has been found. For a prescribed parabolic profile at the inlet of the constricted tube the maximum axial velocity generally does not occur on the centerline near the throat for severe area reductions. The profile at the throat of the stenosis is blunt shaped for a prescribed parabolic profile at the inlet of the stenosed tube with higher degrees of area reduction. The maximum centerline velocity occurs along downstream of the throat. Unlike dilated channel, maximum wall shear stress occurs at the proximal side of the throat. In physiology, it is well known that stenosed artery sometimes collapses or plaque cap of the stenosis ruptures. From our study, it can be predicted that maximum and minimum wall shear stresses could be one of the important factors for such collapse and rupturing. However, our study captures all the well known flow features accurately confirming the code is right. It should be noted that to understand blood flow in atherosclerotic arteries, more realistic physiological conditions and geometry need to be considered. This model could be applied to analyze more complicated situations, such as multiple stenoses in a single vessel.

Chapter 8

Conclusions and Outlooks

8.1 Observations and Remarks

The aim of this dissertation is to enrich the scope of applications of HOC schemes by developing new generalized schemes for the simulation of fluid flows on geometries beyond rectangular. We have employed the proposed schemes not only to verify the order of accuracy, efficiency, effectiveness and robustness of these schemes on some well known problems (linear and nonlinear) having analytical solutions but also to explore new flow phenomena of some other complicated problems such as lid driven cavity flow problem, constricted channel as well as dilated channel problems, etc. However, these schemes can be applied to both convection-diffusion and reaction-diffusion equations, and can also be easily accommodated into solving problems of incompressible viscous flows through the geometries beyond rectangular governed by the N-S type equations with slight adjustment of the convection coefficients. Both Dirichlet and Neumann boundary conditions can be incorporated into the scheme with ease. Extensive validation exercise has been carried out by comparing the results obtained through these proposed schemes with analytical, numerical and experimental results available in the literature. In the following, the prominent features of the proposed HOC schemes and important physics of some flows through complex geometries obtained by our schemes have been summarized.

A new steady-state HOC scheme in the $\psi-\zeta$ formulation for solving incompressible viscous flow problems on non-uniform grids has been proposed. The scheme is fourth order accurate in space. To bring out different aspects of the scheme, we employed it to compute the steady-state solutions of a linear convection-diffusion problem, a problem governed by N-S equations with a constructed analytical solution, the 2D lid-driven cavity flow, and flow through constricted tube in cylindrical coordinate systems. We presented ample numerical evidence of its superiority over other established results.

The robustness of the scheme is illustrated by its applicability to problems of varying physical complexities, represented among others, by Reynolds numbers ranging from 0.01 to 5000 in the cavity problem and 1 to 1000 in the constricted tube flow problem. The results obtained in all the test cases by using the steady-state formulation of HOC schemes on relatively coarser grids are in excellent agreement with the analytical as well as established numerical results, underlining the high accuracy of the scheme.

One of the significant contributions of our work is the development of a class of implicit high order compact (HOC) finite difference schemes for solving the two-dimensional (2D) unsteady Navier-Stokes (N-S) equations on irregular geometries. From the above class, we have chosen a transient scheme which is second order accurate in time and fourth order accurate in space to simulate the complicated flow problems. To verify the effectiveness of the chosen scheme, we employed it to compute the transient solutions of the flow decayed by viscosity, the time marching steady-state as well as transient solutions of the 2D lid-driven cavity flow problem for Reynolds numbers ranging from 100 to 5000. However, the power of the proposed transient scheme is better realized when it is used to solve three complicated fluid flow problems, namely, the flow through (1) axisymmetric channels with forward and backward constrictions with different sharpness of the re-entrant corner, (2) an asymmetric channel with sudden expansion and different aspect ratios, (3) lateral and axisymmtric dilated channel. Our computed numerical results on relatively coarser grids are in excellent agreement with the analytical as well as established numerical and experimental results available in the literature.

Overall, the work has two major components, namely, (i) the development of generalized HOC schemes for efficient computation of steady-state and transient incompressible viscous flows on nonuniform grids, and (ii) their successful implementation to simulate flows through geometries beyond rectangular. In what follows the major achievements of the thesis will be highlighted in the form of observations and comments, further substantiating the claim of objectives having been achieved.

Most of the proposed earlier HOC approaches are confined to steady flow calculations on rectangular geometries with uniform grids. As such these schemes could not fully exploit the advantages associated with using nonuniform grids, particularly that of mesh grading to resolve smaller scales in the regions of large gradients in the physical domain. Our scheme efficiently handles the complex fluid flow problems on geometries beyond rectangular using nonuniform grids. So far we have not come across any work on transient HOC scheme on nonuniform curvilinear grids and our work could be the first one of this kind.

Since the proposed scheme is higher order accurate, it demands lesser number of grid points than other popular lower order schemes to reach a desired accuracy. Hence the required computational time (CPU time) is substantially reduced. Such savings of CPU time could be more effective in higher dimensions. Thus, in spite of complexities associated with transformation, our schemes preserve all the good features of existing HOC schemes and also show a better scale resolution even with coarser grids. The power of capturing tertiary vortices on a grid as coarse as 21× 21, even for Re=100, is one of such achievements through our proposed schemes. Again, on a grid of size 11× 11, a uniform grid fails to reproduce the secondary corner vortices at the bottom whereas this can be resolved easily when the grid is nonuniform. This clearly shows the advantage of nonuniform grids over uniform grids.

To the best of our knowledge, the transient evolution of vortex structures in the lid driven cavity flow problem for large values of aspect ratio (aspect ratio=5.0) could be the first work using HOC scheme. The deeper cavity gives rise to more interesting dynamics and the streamfunction contours show the dramatic extent of the effects due to the secondary vortex that begins to develop along the downstream wall near the lid. The intermediate steps show a clear picture of the development of the series of counter rotating vortices. We also tested the effects of aspect ratios of the cavity and found that the aspect ratios play an important role in the development of vortex structures.

Some prominent observations of the flow field in the backward constricted channel in comparison with the same in the forward constricted channel are as follows. For flow through a channel with forward constriction, it can be mentioned that flow separation does not occur for $\tau \leq 0.7$ even at higher Res (say Re=1000). The area of the negative velocity zone i.e separation zone in backward constricted channel is larger than that in the forward constricted channel. We also observe that the velocity profile at the throat of the forward constricted channel problem becomes blunter (non-parabolic profile) while in the backward constricted channel problem, it remains almost parabolic. In both the cases maximum wall shear stress values occur at the corner or near to corner along upstream. The evolution of vortex structures show that a series of vortices is observed in asymmetric backward constricted channel problem, the same is not seen in the axisymmetric case. This is perhaps the first study where the reentrant corner effects have been investigated thoroughly.

One of the important aspects in the study of dilated channel flow problem is the effects of the degrees of dilation. This is the idealization of blood flow through aneurysmal vessel. The increase of cross sectional area in the dilated region is seen to result in rapidly falling critical Reynolds number. Like lateral dilated channel, the maximum wall share stress in axisymmetric channel occurs at or nearer to the distal lip of the orifice along downstream, which agrees reasonably well with the experimental results. The development of secondary vortex in the dilated region depends more on the orifice length than the height of the dilated region. For higher *Re*s the dilated region is nestled by single or two counter-rotating vortex rings.

The study of constricted tube flow problem (similar to the study of blood flow through stenosed artery) could be the first one where cylindrical coordinate system has been introduced into the formulation of HOC. Our proposed scheme reproduces all the well known flow features. One of the important observation is that for a prescribed parabolic profile at the inlet of the constricted tube the maximum axial velocity of the velocity profile at the throat generally does not occur on the centerline and a blunter (non-parabolic) shaped profile develops thereat for severe area reductions. The degrees of area reduction and stricture lengths in the constricted tube flow problem show a significant change in the flow field.

In view of the successful implementation of our schemes over a wide variety of problems on irregular geometric settings, these schemes may be treated as the most generalized HOC schemes for incompressible viscous flows. However, the formulations of the proposed HOC schemes presented herein are limited to orthogonal grids only.

8.2 Scope for future work

In this section, we present some ideas for further research possibilities, stimulated by the work presented in this thesis. Of which, the major ones are listed below.

1. In most of the problems studied in this thesis, parabolic profiles have been prescribed at the inlet. It will be worthwhile to examine for oscillatory and pulsatile flows.

2. Three-dimensional study of the constricted channel and tube problems using HOC schemes will be an important and interesting area of research.

3. Study of blood-like fluid flows through stenosed and aneurismal vessel will be more realistic to use elastic wall removing the traditional rigid wall assumption.

4. Computation of the physiological flow considering the elastic properties of the arterial wall by using the proposed HOC schemes incorporating further modifications, if needed, will be more efficient and accurate. This study will be helpful to the medical practitioners.

Appendix I

Fundamentals of transformations

We can relate the metrics $x_\xi, x_\eta, y_\xi, y_\eta$ to the inverse metrics $\xi_x, \xi_y, \eta_x, \eta_y$ as follows:

$$\xi_x = \frac{y_\eta}{J}; \qquad \xi_y = -\frac{x_\eta}{J} \qquad \eta_x = -\frac{y_\xi}{J}; \qquad \eta_y = \frac{x_\xi}{J}. \tag{I.1}$$

where the jacobian (J) is $x_\xi y_\eta - y_\xi x_\eta$.

The inverse metrics can be calculated directly also by the inverse transformation (8). The differential operator in terms of inverse transformation as well as inverse metrics will be as follows.

$$\partial_x = \frac{1}{J}\left(y_\eta \partial_\xi - y_\xi \partial_\eta\right), \tag{I.2}$$

$$\partial_y = \frac{1}{J}\left(x_\xi \partial_\eta - x_\eta \partial_\xi\right). \tag{I.3}$$

For one-to-one mapping to exist, the determinant J should be finite and non-zero. Second derivatives are given by

$$\begin{aligned}\partial_{xx} &= \frac{1}{J^2}\Big[\left(y_\eta^2 \partial_{\xi\xi} - 2y_\eta y_\xi \partial_{\xi\eta} + y_\xi^2 \partial_{\eta\eta}\right) + \left(y_\eta y_{\xi\eta} - y_\xi y_{\eta\eta}\right)\partial_\xi + \left(y_\xi y_{\xi\eta} - y_\eta y_{\xi\xi}\right)\partial_\eta\Big] \\ &- \frac{1}{J^3}\Big[y_\eta^2 J_\xi \partial_\xi - y_\eta y_\xi J_\eta \partial_\xi - y_\xi y_\eta J_\eta \partial_\xi + y_\xi^2 J_\eta \partial_\eta\Big],\end{aligned} \tag{I.4}$$

$$\begin{aligned}\partial_{yy} &= \frac{1}{J^2}\Big[\left(x_\eta^2 \partial_{\xi\xi} - 2x_\eta x_\xi \partial_{\xi\eta} + x_\xi^2 \partial_{\eta\eta}\right) + \left(x_\eta x_{\xi\eta} - x_\xi x_{\eta\eta}\right)\partial_\xi + \left(x_\xi x_{\xi\eta} - x_\eta x_{\xi\xi}\right)\partial_\eta\Big] \\ &- \frac{1}{J^3}\Big[x_\eta^2 J_\xi \partial_\xi - x_\eta x_\xi J_\xi \partial_\eta - x_\xi x_\eta J_\eta \partial_\xi + x_\xi^2 J_\eta \partial_\eta\Big].\end{aligned} \tag{I.5}$$

where

$$\begin{aligned}J_\xi &= x_{\xi\xi} y_\eta + x_\xi y_{\xi\eta} - y_{\xi\xi} x_\eta - y_\xi x_{\xi\eta}, \\ J_\eta &= x_{\xi\eta} y_\eta + x_\xi y_{\eta\eta} - y_{\eta\xi} x_\eta - y_\xi x_{\eta\eta}.\end{aligned} \tag{I.6}$$

Appendix J

Derivation of the transformation

As described in section 5.2 in chapter 5, the transformation relation can be obtained as follows.

$$\begin{aligned}
\tanh(w) &= \tanh(\xi + i\eta) \\
&= \frac{\sin(\xi + i\eta)}{\cos(\xi + i\eta)} \\
&= \frac{\sinh\xi\cos\eta + i\cosh\xi\sin\eta}{\cosh\xi\cos\eta + i\sinh\xi\sin\eta} \\
&= \frac{\sinh\xi\cosh\xi + i\cos\eta\sin\eta}{\cosh^2\xi\cos^2\eta + \sin^2\xi\sin^2\eta} \\
&= \frac{\sinh(2\xi) + i\sin(2\eta)}{\cosh(2\xi) + \cos(2\eta)}
\end{aligned}$$

(by rationalization and after simplification)
NOTE:

$\cosh^2\xi - \sinh^2\xi = 1;$ $\cosh(2\xi) = 1 + 2\sinh^2\xi;$ $\sinh(2\xi) = 2\sinh\xi\cosh\xi.$

Let $H = \cosh(2\xi) + \cos(2\eta)$
Now substituting w and $\tanh(w)$ in

$$z = w(A + B\tanh(w))$$

we get

$$x = A\xi + \frac{B}{H}[\xi\sinh(2\xi) - \eta\sin(2\eta)],$$
$$y = A\eta + \frac{B}{H}[\eta\sinh(2\xi) + \xi\sin(2\eta)].$$

Bibliography

[1] Abarbanel, S. & Kumar, A. 1988 Compact higher order schemes for the Euler equations. *Journal of Scientific Computing* **3**, 275-288.

[2] Abu-Mulaweh, H. I. 2003 A review of research on laminar mixed convection flow over backward- and forward-facing steps. *International Journal of Thermal Sciences* **42**, 897-909.

[3] Adams, E. W. & Johnston, J. P. 1988 Effects of the separating layer on the reattachment flow structure. Part 2: Reattachment length and wall shear stress. *Experiments in fluids* **6**, 493-499.

[4] Ahmed, S. A. & Giddens, D. P. 1984 Pulsatile flow studies with Laser Doppler Anemometry. *J. Biomechanics* **17**, 695.

[5] American heart association. 2004 International cardiovascular disease statistics. *www.americanheart.org.*

[6] Anderson, H. I., Halden, R. & Glomsaker, T. 2000 Effects of surface irregularities on flow resistance in differently shaped arterial stenoses. *J. Biomechanics* **33**, 1257-1262.

[7] Ang, K. C. & Mazumdar, J. N. 1997 Mathematical modelling of 3-D flow through an asymmetric arterial stenosis. *Mathl. Compt. Modelling* **25**(1), 19-29.

[8] Armaly, B. F., Durst, F., Pereira, J. C. F. & Schonung, B. 1983 Experimental and theoretical investigation of backward-facing step flow. *Journal of Fluid Mechanics* **127**, 473-496.

[9] Aung, W. 1983 An experimental study of laminar heat transfer downstream of backsteps. *ASME Journal of Heat transfer* **105**, 823-829.

[10] Auteri, F., Quartapelle, L. & Vigevano, L. 2002 Accurate $\psi - \zeta$ Spectral solution of the singular driven cavity problem. *Journal of Computational Physics* **180**, 597-615.

[11] Back, L. H. & Roshke, E. J. 1972 Shear layer flow regimes and wave instabilities and reattachment lengths downstream of an abrupt circular channel expansion. *J. Appt. Mech. Trans. ASME,* **94**(3), 677-681.

[12] Back, L. D., Radbill, J. R. & Crawford, D. W. 1977 Analysis of pulsatile, viscous blood flow through diseased coronary arteries of man. *J. Biomechanics* **10**, 339-353.

[13] Bascom, P. A. J., Johnston, K. W., Cobbold, R. S. C. & Routh, H. F. 1993 On the Doppler signal from a steady flow asymmetrical stenosis model: effects of turbulence. *Ultrasound in medicine and biology* **19**, 197-210.

[14] Barragy, E. & Carey, G. F. 1997 Stream function-vorticity driven cavity solution using p finite elements. *Computers & Fluids* **26**(5), 453-468.

[15] Bascom, P. A. J., Johnston, K. W., Cobbold, R. S. C. & Ojha, M. 1997 Relation of the flow field distal to a moderate stenosis to the Doppler Power. *Ultrasound in medicine and biology* **23** (1), 25-39

[16] Bellhouse, B. & Bellhouse, F. 1969 Fluid mechanics of model normal and stenosed aortic valve. *Circulation Research* **25**, 693-704.

[17] Borgas, M. S. & Pedley, T. J. 1990 Non-uniqueness and bifurcation in annular and planar channel flows. *Journal of Fluid Mechanics* **214**, 229-250.

[18] Botella, O. & Peyret, R. 1998 Benchmark spectral results on the lid-driven cavity flow. *Computers & Fluids* **27**, 421-433.

[19] Bruneau, C. H. & Jouron, C. 1990 An efficient scheme for solving steady incompressible Navier-Stokes equations. *Journal of Computational Physics* **89**, 389-413.

[20] Bruneau, C. H. & Saad, M. 2005 The 2D lid-driven cavity problem revisited. *Comupters & Fluids* **35**, 326-348.

[21] Bruschke, A. V. G., Proudfit, W. L. & Sones, F. M. Jr. 1973 Clinical course of patients with normal, and slightly or moderately abnormal coronary arteriogram-a follow up study on patients. *Circulation* **47**, 936-945.

[22] Buchanan Jr., J. R., Kleinstreuer, C. & Comer, J. K. 2000 Rheological effects on pulsatile hemodynamics in a stenosed tube. *Computers & fluids* **29**, 695-724.

[23] Cassanova, R. A. & Giddens, D. P. 1978 Disorder distal to modelled stenosis in steady and Pulsatile flow. *J. Biomechanics* **11**, 441-453.

[24] Castillo, J. E. & Steinberg, S. 1995 The sensitivity and accuracy of fourth order finite-difference schemes on nonuniform grids in one dimension, DE-AC04-76DP00789.

[25] Cavalcanti, S. 1995 Hemodynamics of an artery with mild stenosis. *J. Biomechanics* **28**(4), 387-399.

[26] Cavalcanti, S., Bolelli, P. & Belardinelli, E. 1992 Pressure drops through arterial stenoses models in steady flow condition. *J. Bio-mechanical Engg. ASME,* **114**, 416-418.

[27] Chen, Y. N., Yang, S. C. & Yang, J. Y. 1999 Implicit weighted essentially non-oscillatory schemes for the inconpressible Navier-Stokes equations. *Int. J. Numer. Meth. Fluids* **31**, 747-765.

[28] Cheng, M. & Hung, K. C. 2006 Vortex structure of steady flows in a rectangular cavity. *Computers & Fluids* **35**(10), 1046-1062.

[29] Cherdron, W., Durst, F. & Whitelaw, J. H. 1978 Asymmetric flows and instabilities in symmetric ducts with sudden expansions. *Journal of Fluid Mechanics* **84**, 13-31.

[30] Chorin, A. J. 1968 Numerical solution of the Navier-Stokes equation. *Mathematics of Computation* **22**, 745-762.

[31] Chudanov, V. V., Popkov, A. G., Churbanov, A. G., Vabishchevich, P. N. & Makarov, M. M. 1995 Operator-splitting schemes for the streamfunction-vorticity formulation. *Computers & Fluids* **24**(7), 771-786.

[32] Constantinescu, G. S. & Lele, S. K. 2002 A highly accurate technique for the treatment of flow equations at the polar axis in cylindrical coordinates using series expansions. *Journal of Computational Physics* **183**, 165-186.

[33] Dennis, S. C. R. & Hudson, J. D. 1989 Compact explicit h^4 finite difference approximations to operators of Navier-Stokes type. *Journal of Computational Physics* **85**, 390-416.

[34] Deshpande, M. D., Giddens, D. P. & Mabon, R. F. 1976 Steady laminar flow through modelled vascular stenoses. *J. Biomechanics* **9**, 165-174.

[35] Dukowicz, J. K. & Ramshaw, J. D. 1979 Tensor viscosity method for convection in numerical fluid dynamics. *Journal of Computational Physics* **32**, 71-79.

[36] Durst, F., Melling, A. & Whitelaw, J. H. 1974 Low Reynolds number flow over a plane symmetrical sudden expansion. *Journal of Fluid Mechanics* **64**, 111.

[37] Durst, F. & Pereira, J. C. F. 1988 Time dependent laminar backward-facing step flow in a two dimensional duct. *Trans. ASME 1: Journal of Fluids Engineering* **110**, 289-296.

[38] Durst, F., Pereira, J. C. F. & Tropea, C. 1993 The plane symmetric sudden-expansion flow at low Reynolds numbers. *Journal of Fluid Mechanics* **248**, 567-581.

[39] Dvinsky, A. & Ojha, M. 1994 Simulation of 3-D pulsatile flow through an asymmetric stenosis. *Med. and Biol. and Eng. Computer* **12**, 1601-1612.

[40] Eaton, J. K., Jeans, A. H., Ashjaee, J. & Johnston, J. P. 1979 A wall flow direction probe for use in separating and reattaching flows. *ASME Journal of Fluids Engineering* **101**, 364-366.

[41] Ferziger, J. H. & Peric, M. 2002 *Computational Methods for Fluid Dynamics.* Springer.

[42] Finlay, H. M., Whittaker, P. & Canham, P. B. 1998 Collagen organization in the branching region of human brain arteries. *Stroke* **29**, 1595-601.

[43] Gartland Jr., E. C. G. 1982 Discrete weighted mean approximation of a model convection-diffusion equation. *SIAM Journal On Scientific and Statistical Computing* **3**(4), 460-472.

[44] Gartling, D. K. 1990 A test problem for outflow boundary conditions-flow over a backward facing step. *Int. J. Numer. Meth. Fluids* **11**, 953-967.

[45] Ge, L. & Zhang, J. 1999 Accuracy iterative solution of convection diffusion equation with boundary layers on nonuniform Grids. *Technical Report*, University of Kentucky, Lexington, KY. 288-99.

[46] Ghia, U., Ghia, K. N. & Shin, C. T. 1982 High resolution for incompressible Navier-Stokes equation and a multigrid method. *Journal of Computational Physics* **48**, 387-411.

[47] Goldstein, R. J., Eriksen, V. L., Olson, R. M. & Eckert, E. R. G. 1970 Laminar separation, reattachment and transition of the flow over a downstream facing step. *ASME Journal of Basic Engineering* **92**, 732-741.

[48] Gobin, Y. P., Counord, J. L., Flaud, P. & Duffaux, J. 1994 In vitro study of haemodynamics in a giant saccular aneurysm model: Influence of flow dynamics in the parent vessel and effects of coil embolisation. *Neuroradiology* **36**, 530-536.

[49] Gonzalez, C. F., Cho, Y. I., Ortega, H. V. & Moret, J. 1992 Intracranial Aneurysms: Flow analysis of their origin and progression. *AJNR* **13**, 181-188.

[50] Graves, V. B., Strother, C. M., Partington, C. R. & Rappe, A. 1992 Flow dynamics of lateral carotid artery aneurysms and their effects on coils and balloons: An experimental study in dogs. AJNR: *Am. J. Neurorad.* **13**, 189-196.

[51] Gupta, M. M., Manohar, R. M. & Stephenson, J. W. 1984 A single cell high order scheme for the convection-diffusion equation with variable coefficients. *Int. J. Numer. Meth. Fluids* **4**, 641-651.

[52] Gupta, M. M. 1991 High accuracy solutions of incompressible Navier-Stokes equations. *Journal of Computational Physics* **93**, 343-357.

[53] Gupta, M. M. & Kalita, J. C. 2005 A new paradigm for solving Navier-Stokes equation: streamfunction-velocity formulations. *Journal of Computational Physics* **207**, 52-68.

[54] Gustafson, K. & Halasi, A. 1986 Vortex dynamics of cavity flows. *Journal of Computational Physics* **64**, 279.

[55] Guzman, A. M. & Amon, C. H. 1994 *Phys. of Fluids* **6**.

[56] Hoffman, J.D. 1982 Relationship between the truncation errors of centered finite-difference approximations on uniform and nonuniform meshes. *Journal of Computational Physics* **46**, 469-474.

[57] Hou, S., Zou, Q., Chen, S., Doolen, G. & Cogley, A. 1995 Simulation of cavity flows by the lattice boltzmann method. *Journal of Computational Physics* **118**, 329-347.

[58] Huang, H., Modi, V. J. & Seymour, B. R. 1995 Fluid mechanics of stenosed arteries. *Int. J. Engg. Sc.*, **33**(6), 815-828.

[59] Hunt, R. 1990 The numerical solution of the laminar flow in a constricted channel at moderately high Reynolds number using Newton iteration. *Int. J. Numer. Meth. Fluids* **11**, 247-259.

[60] Ishikawa, T., Oshima, S. & Yamane, R. 2000 Vortex enhancement in blood flow through stenosed and locally expanded tubes. *Fluid Dynamics Research* **26**, 35-52.

[61] Ishikawa, T., Oshima, S., Yamane, R. & Gimaraes, L. F. R. 1998 Effects on non-Newtonian property of blood on flow through a stenosed tube. *Fluid Dynamics Research* **22**, 251-264.

[62] Johansen, K. 1982 Aneurysms. *Sci. Am.*, 110-125.

[63] Johnston, P. R. & Kilpatrick, D. 1991 Mathematical modelling of flow through an irregular arterial stenosis. *J. Biomechanics*, **24**(11), 1069-1077.

[64] Kalita, J. C., Dass, A. K. & Dalal, D. C. 2001 Fully compact higher order computation of steady-state natural convection in a square cavity. *Physical Review E* **64**(6), 066703:1-13.

[65] Kalita, J. C., Dalal, D. C. & Dass, A. K. 2002 A class of higher order compact schemes for the unsteady two-dimensional convection-diffusion equation with variable convection coefficients. *Int. J. Numer. Meth. Fluids* **38**, 1111-1131.

[66] Kalita, J. C., Dass, A. K. & Dalal, D. C. 2004 A transformation-free HOC for steady convection-diffusion on nonuniform grids. *Int. J. Numer. Meth. Fluids* **44**, 33-53.

[67] Karageorghis, A. & Philips, T. N. 1989 Chebyshev spectral collocation methods for laminar flow through a channel contraction. *Journal of Computational Physics* **84**, 114-133.

[68] Kelley, C. T. 1995 *Iterative Methods for Linear and Nonlinear Equations.* SIAM Publications, Philadelphia.

[69] Kennedy, C. A. & Carpenter, M. H. 1994 Several new numerical methods for compressible shear-layer simulations. *Appl. Numer. Math.* **14** (4), 397-433.

[70] Khalifa, A. M. A. & Giddens, D. P. 1981 Characterization and evolution of post stenotic flow disturbances. *J. Biomechanics* **14**(5), 279-296.

[71] Kim, B. M. & Corcoran, W. H. 1974 Experimental measurements of turbulence spectra distal to stenosis. *J. Biomechanics* **7**, 335-342.

[72] Kim, J. & Moin, P. 1985 Application of fractional step method to incompressible Navier-Stokes equation. *Journal of Computational Physics* **59**, 308-323.

[73] Ku, D. N. 1997 Blood flow in arteries. *Annual Rev. Fluid Mech.* **29**, 399-434.

[74] Kuen, D. M. 1980 Effects of adverse pressure gradient on the incompressible reattaching flow over a rearward- facing step. *AIAA J.* **18**(3), 343-344.

[75] Kumar, A. & Yajnik, K. 1980 Internal separated flows at large Reynolds numbers. *Journal of Fluid Mechanics* **97**, 27-51.

[76] Kumar, B. V. R. & Kundu, K. B. 1995 Finite element analysis of nonlinear pulsatile suspension flow dynamics in blood vessels with aneurysm. *Computers and Biomedical Research* **25**, 1-20.

[77] Kumar, B. V. R. & Kundu, K. B. 1996 Hemodynamics in Aneurysm. *Computers and Biomedical Research* **29**, 119-139.

[78] Kupferman, R. A. 2001 A central-difference scheme for a pure stream function formulation of incompressible viscous flows. *SIAM J. Sci. Comp.* **23**(1), 1-18.

[79] Lax, P. D. & Wendroff, B. 1960 *Comm.Pure Appl.Math.* 13, 217-237.

[80] Lee, J. S. & Fung, Y. C. 1970 Flow in locally constricted tubes at low Reynolds Numbers. *J. Appl. Mech. Trans. ASME.* **37**, 9-16.

[81] Lele, S. K. 1992 Compact finite difference schemes with spectral like resolution. *Journal of Computational Physics* **103**, 16-42.

[82] Leonard, B. P. 1991 The Ultimate conservative difference scheme applied to unsteady one-dimensional advection. *Comput. Methods Appl. Mech. Eng.* **88** (1), 17-74.

[83] Li, Z. & Kleinstreuer, C. 2005 Blood Fflow and structure interactions in a stented abdominal aortic aneurysm model. *Medical Engineering and Physics* **27**, 369-382.

[84] Li, M., Tang, T. & Fornberg, B. 1995 A compact fourth order finite difference scheme for the steady incompressible Navier-Stokes equations. *Int. J. Numer. Meth. Fluids* **20**, 1137-1151.

[85] Li, M. & Tang, T. 2001 A compact fourth order finite difference scheme for unsteady viscous incompressible flows. *Journal of Scientific Computing* **16**(1), 29-45.

[86] Lieber, B. B., Livescu, V., Hopkins, L. N. & Wakhloo, A. K. 2002 Particle image velocimetry assessment of stent design influence on intra-aneurysmal flow. *Ann. Biomed. Eng.* **30**, 768-777.

[87] Liepsch, D. W. 1986 Flow in tubes and arteries - a comparison. *Biorheology* **23**, 395-433.

[88] Liepsch, D. W., Poll, A. & Steiger, H. J. 1991 Fluid dynamics studies in terminal aneurysms. *Medical & Biological Engineering & computing* **29** (supplement), 19.

[89] Liou, M. T. & Liao, C. C. 1997 Flowfields in lateral aneurysm model arising from parent vessels with different curvatures using PTV. *Experiments in Fluids* **23**, 288-298.

[90] Liou, M. T., Chang, W. C. & Liao, C. C. 1997 LDV measurements in lateral model aneurysms of various sizes. *Experiments in Fluids* **23**, 317-324.

[91] Low, M., Perktold, K. & Rauning, R. 1993 Hemodynamics in rigid and distensible saccular aneurysms: a numerical study of pulsatile flow characteristics. *Biorheology* **30**, 287-298.

[92] Luchini, P. 1991 Higher-order difference approximations of the Navier-Stokes equations. *Int. J. Numer. Meth. Fluids* **12**, 491-506.

[93] Mackinnon, R. J. & Johnson, R. W. 1991 Differential equation based representation of truncation errors for accurate numerical solution. *Int. J. Numer. Meth. Fluids* **13**, 739-757.

[94] Mancera, P. F. De. A. & Hunt, R. 1997 Fourth order method for solving the Navier Stokes equations in a constricted channel. *Int. J. Numer. Meth. Fluids* **25**, 1119-1135.

[95] Mancera, P. F. A. 2003 A study of numerical solution of the steady two dimensional Navier-Stokes equations in a constricted channel problem by a compact fourth order method. *Applied Mathematics and Computation* **146**, 771-790.

[96] Mehta, U. B. & Lavan, Z. 1969 Flow in a two dimensional channel with a rectangular cavity. *J. Applied Mechanics* **36**, 897-901.

[97] Miller, W. 1995 Flow in the driven cavity calculated by Lattice Boltzmann method. *Physical Review E* **51**(4), 3659.

[98] Misra, J. C. & Chakravarty, S. 1986 Flow in arteries in the presence of stenosis. *J. Biomechanics* **19**(11), 907-918.

[99] Moayeri, M. S. & Zendehbudi, G. R. 1999 Comparison of physiological and simple pulsatile flows through stenosed arteries. *J. Biomechanics* **32**, 559-565.

[100] Moayeri, M. S. & Zendehbudi, G. R. 2003 Effects of elastic property of the wall on flow characteristics through arterial stenosis. *J. Biomechanics* **36**, 525-535.

[101] Moffat, M. K. 1964 Viscous and resistive eddies near a sharp corner. *Journal of Fluid Mechanics* **18**, 1-18.

[102] Nakamura, M. & sawada, T. 1988 Numerical study on the flow of a non-Newtonian fluid through an asymmetric stenosis. *J. Biomechanical Engg.*, **110**, 137-143.

[103] Nakamura, M. & Sawada, T. 1990 Numerical study on the unsteady flow of non-Newtonian fluid. *J. Biomech. Engg.,* **112**, 100-103.

[104] Nerem, R. M., Rumberger, J. A., Gross, D. R, Jr., Hamlin, R. L. & Geiger, G. L. 1974 Hot film anemometer velocity measurements of arterial blood in horses. *Circulation research* **34**, 193-203.

[105] Nishimura, T., Arakawa, S., Murakami, S. & Kawamura, Y. 1989 Oscillatory viscous flow in symmetric wavy-walled channels. *Chemical Engineering Science* **44**(10), 2137-2148.

[106] Noye, B. J. & Tan, H. H. 1988 Finite difference methods for solving two-dimensional advection-diffusion equation. *Int. J. Numer. Meth. Fluids* **9**, 75-98.

[107] O'Brien, V. & Ehrlich, L. W. I. 1985 Simple Pulsatile Flow in an Artery with a constriction. *J. Biomechanics* **18**, 117-127.

[108] Pan, F. & Acrivos, A. 1967 Steady flows in rectangular cavities, *J Fluid Mechanics* **28**(4), 643.

[109] Pandit, S. K., Kalita, J. C. & Dalal, D. C. 2007 A fourth order accurate compact scheme for the solution of steady Navier-Stokes equations on nonuniform grids, *Computer & Fluids* (In Press).

[110] Pandit, S. K., Kalita, J. C. & Dalal, D. C. 2007 A transient higher order compact scheme for incompressible viscous flows on geometries beyond rectangular, *Journal of Computational Physics* doi:10.1016/j.jcp.2007.01.016.

[111] Patil, D. V., Lakshmisha, K. N. & Rogg, B. 2006 Lattice Boltzmann simulation of lid-driven flow in deep cavities. *Computers & Fluids* **35**(10), 1116-1125 .

[112] Pedrizzetti, G. 1996 Unsteady tube flow over an expansion. *Journal of Fluid Mechanics* **310**, 89-111.

[113] Perktold, K., Peter, R. & Resch, M. 1989 Pulsatile non-Newtonian blood flow simulation through a bifurcation with an aneurysm. *Biorheology* **26**, 1011-1030.

[114] Ralph, M. E. 1986 Oscillatory flows in wavy-walled tubes. *Journal of Fluid Mechanics* **168**, 515-540.

[115] Restivo, A. & Whitelaw, J. H. 1978 Turbulence characteristics of the flow downstream of a symmetric, plane sudden expansion. *Trans. ASME 1: Journal of Fluids engineering* **100**, 308.

[116] Roache, R. J. & Mueller, T. J. 1970 Numerical solutions of laminar separated flows. *AIAA J.* **8**, 520-538.

[117] Ross, R. 1993 The Pathogenesis of Atherosclerosis, a perspective for the 1990s. *Nature* **362**, 801-809.

[118] Saad, Y. 1996 *Iterative Methods for Sparse Linear Systems.* PWS Publishing Company.

[119] Samarskii, A. A., Tishkin, V. F., Favorskii, A. P. & Shashkov, M. Yu. 1981 Operational Finite Difference Schemes. *Diff. Eqns.* **17**, 863-885.

[120] Schreiber, R. & Keller, H. B. 1983 Driven cavity flows by efficient numerical techniques. *Journal of Computational Physics* **49**, 310-333.

[121] Sesterhenn, J. 2001 A characteristic-type formulation of Navier-Stokes equations for high order upwind schemes. *Computer & Fluids* **30**(1), 37-68.

[122] Shankar, P. N. 1993 The eddy structure in Stokes flow in a cavity. *Journal of Fluid Mechanics* **250**, 371-383.

[123] Shankar, P. N. & Deshpande, M. D. 2000 Fluid mechanics in the driven cavity. *Annual Review Fluid Mechanics* **32**, 93-136.

[124] Shapira, M., Degani, D. & Weihs, D. 1990 Stability and existence of multiple solutions for viscous flow in suddenly enlarged channels. *Computers & Fluids* **18**, 239-258.

[125] Shen, C. & Floryan, J. M. 1985 Low Reynolds number flow over cavity. *Phys. of Fluids* **28**, 3191-202.

[126] Siouffi, M., Deplano, V. & Pellisier, R. 1998 Experimental analysis of unsteady flow through a stenosis. **31**(1), 11-19.

[127] Spotz, W. F. 1995 High order compact finite difference scheme for computational mechanics. *PhD Thesis,* University of Texus at Austin, December.

[128] Spotz, W. F. & Carey, G. F. 1998 Formulation and experiments with High Order Compact schemes for nonuniform grids. *The International Journal of Numerical Methods for Heat and Fluid Flow* **8**(3), 288-303.

[129] Spotz, W. F. & Carey, G. F. 1995 High-order compact scheme for the steady stream-function vorticity equations. *Int. J. Numer. Meth. Eng.* **38**, 3497-3512.

[130] Sobey, I. J. 1980 On flow through furrowed channels. Part 2. Observed flow patterns. *Journal of Fluid Mechanics* **96**, 27-32.

[131] Sobey, I. J. 1983 The occurence of separation in oscillatory flow. *Journal of Fluid Mechanics* **134**, 247-257.

[132] Sobey, I. J. 1985 Dispersion caused by separation during oscillatory flow through a furrowed channel. *Chemical engineering science* **40**(11), 2129-2134.

[133] Sobey, I. J. & Drazin, P. G. 1986 Bifurcations of two dimensional channel flows. *Journal of Fluid Mechanics* **171**, 263-287.

[134] Steiger, H. J., Poll, A., Liepsch, D. & Reulen, H. J. 1987a Basic flow structure in saccular aneurysms: a flow visualization study. *Heart & vessels* **3**, 55-65.

[135] Steiger, H. J., Poll, A., Liepsch, D. & Reulen, H. J. 1987b Haemodynamic stress in lateral saccular aneurysms. *Acta Neurochir* **86**, 98-105.

[136] Steiger, H. J., Poll, A., Liepsch, D. & Reulen, H. J. 1987b Haemodynamic stress in terminal aneurysms. *Acta Neurochir* **93**, 18-23.

[137] Stephanoff, K. D., Sobey, I. J. & Bellhouse, B. J. 1980 On flow through furrowed channels. Part 1. Calculated flow patterns. *Journal of Fluid Mechanics* **96**, 1-26.

[138] Stone, K. & Vanka, S. P. 1999 Numerical steady of developing flow and heat transfer in a wavy passage. *Journal of Fluids Engineering* **121**, 713-719.

[139] Strikwerda, J. C. 1997 High-order accurate schemes for incompressible viscous flow. *Int. J. Numer. Meth. Fluids* **24**, 715-734.

[140] Strother, C. M., Graves, V. B. & Rappe, A. 1992 Aneurysm hemodynamics: An experimental study. *AJNR: Am. J. Neurorad.* **13**, 1089-1095.

[141] Taneda, S. 1979 Visualization of separating Stokes flows. *J. Phys. Soc. Jpn.* **46**, 1935-42.

[142] Tang, D., Yang, C. & Ku, D. N. 1999 A 3-D thin wall model with fluid structure interactions for blood flow in carotid arteries with symmetric and asymmetric stenoses. *Computers and Structures* **72**, 357-377.

[143] Tannehill, J. C., Anderson, D. A. & Pletcher, R. H. 1984 *Computational Fluid Mechanics and Heat Transfer.* Hemisphere Publishing Corporation, New York.

[144] Tu, C., Deville, M., Dheur, L. & Vanderschuren, L. 1992 Finite element simulation of pulsatile flow through arterial stenosis. *J. Biomechanics* **25**(10), 1141-1152.

[145] Tutty, O. R. 1992 Pulsatile flow in a constricted channel. *Journal of Biomechanical Engineering* **114**, 50-54.

[146] Tutty, O. R. & Pedley, T. J. 1993 Oscillatory flow in a stepped channel. *Journal of Fluid Mechanics* **247**, 179-204.

[147] Ujiie, H., Liepsch, D. W. et al. 1996 Hemodynamic study of the anterior communicating artery. *Stroke* **27**, 2086-2094.

[148] Vanka, S. P. 1986 Block-implicit multigrid solution of Navier-Stokes equations in primitive variables. *Journal of Computational Physics* **65**, 138-158.

[149] Visbal, M. R. & Gaitonde, D. V. 2002 On the Use of Higher-Order Finite-Difference Schemes on Curvilinear and Deforming Meshes. *Journal of Computational Physics* **181**, 155185.

[150] Vorst, H. V. D. 1992 BiCGSTAB: A fast and smoothly converging variant of BiCG for the solution of nonsymmetric linear systems. *SIAM J. Sci. Comput.* **13**, 631-644.

[151] Webster, J. S., Moberg, C. & Rincon, G. 1974 Natural history of severe proximal coronary artery disease and documented by coronary Cineangiography. *American J. Cardiol.* **33**, 195-200.

[152] Whitmore, R. L. 1968 *Rheology of the circulation*. Peramon Press, Oxford.

[153] Wille, R. & Fernholz, H. 1965 Report on the first European Mechanics Colloquium on the Coanda effect. *Journal of Fluid Mechanics* **23**, 801-819.

[154] Yanwen, M., Dexun, F., Kobayashi, T. & Taniguchi, N. 1999 Numerical solution of the incompressible Navier-Stokes equations with an upwind compact difference scheme. *Int. J. Numer. Meth. Fluids* **30**, 509-521.

[155] Young, D. F. & Tsai, F. Y. 1973a Flow charecteristics in models of arterial stenoses -I. Steady flow. *Journal of Biomechanics* **6**, 395-410.

[156] Zamani, A. 1997 MRA of intracranial aneurysms. *Clin. Neurosci.* **4**, 123-129.